N° d'ordre NNT : 2018LYSE1002

THESE de DOCTORAT DE L'UNIVERSITE DE LYON
opérée au sein de
l'Université Claude Bernard Lyon 1

École Doctorale 206
(Chimie, Procédés, Environnement)

Spécialité de doctorat : Procédés

Soutenue publiquement le 16/01/2018, par :

Sónia Ferreira

Modélisation du transport intragranulaire dans un réacteur catalytique

---

Devant le jury composé de :

Mme TAYAKOUT-FAYOLLE Mélaz	UCBL	Examinatrice
M. COPPENS Marc-Olivier	UCL	Rapporteur
M. FAVRE Eric	ENSIC	Rapporteur
Mme JULCOUR Carine	ENSIACET	Examinatrice
M. JALLUT Christian	UCBL	Directeur de Thèse
M. VERSTRAETE Jan	IFPEN	Promoteur
Mme JOLIMAITRE Elsa	IFPEN	Invitée
M. LEINEKUGEL-LE-COCQ Damien	IFPEN	Invité

UNIVERSITE CLAUDE BERNARD - LYON 1

Président de l'Université	**M. le Professeur Frédéric FLEURY**
Président du Conseil Académique	M. le Professeur Hamda BEN HADID
Vice-président du Conseil d'Administration	M. le Professeur Didier REVEL
Vice-président du Conseil Formation et Vie Universitaire	M. le Professeur Philippe CHEVALIER
Vice-président de la Commission Recherche	M. Fabrice VALLÉE
Directrice Générale des Services	Mme Dominique MARCHAND

COMPOSANTES SANTE

Faculté de Médecine Lyon Est – Claude Bernard	Directeur : M. le Professeur G.RODE
Faculté de Médecine et de Maïeutique Lyon Sud – Charles Mérieux	Directeur : Mme la Professeure C. BURILLON
Faculté d'Odontologie	Directeur : M. le Professeur D. BOURGEOIS
Institut des Sciences Pharmaceutiques et Biologiques	Directeur : Mme la Professeure C. VINCIGUERRA
Institut des Sciences et Techniques de la Réadaptation	Directeur : M. X. PERROT
Département de formation et Centre de Recherche en Biologie Humaine	Directeur : Mme la Professeure A-M. SCHOTT

COMPOSANTES ET DEPARTEMENTS DE SCIENCES ET TECHNOLOGIE

Faculté des Sciences et Technologies	Directeur : M. F. DE MARCHI
Département Biologie	Directeur : M. le Professeur F. THEVENARD
Département Chimie Biochimie	Directeur : Mme C. FELIX
Département GEP	Directeur : M. Hassan HAMMOURI
Département Informatique	Directeur : M. le Professeur S. AKKOUCHE
Département Mathématiques	Directeur : M. le Professeur G. TOMANOV
Département Mécanique	Directeur : M. le Professeur H. BEN HADID
Département Physique	Directeur : M. le Professeur J-C PLENET
UFR Sciences et Techniques des Activités Physiques et Sportives	Directeur : M. Y. VANPOULLE
Observatoire des Sciences de l'Univers de Lyon	Directeur : M. B. GUIDERDONI
Polytech Lyon	Directeur : M. le Professeur E. PERRIN
École Supérieure de Chimie Physique Électronique	Directeur : M. G. PIGNAULT
Institut Universitaire de Technologie de Lyon 1	Directeur : M. le Professeur C. VITON
École Supérieure du Professorat et de l'Éducation	Directeur : M. le Professeur A. MOUGNIOTTE
Institut de Science Financière et d'Assurances	Directeur : M. N. LEBOISNE

Remerciements

Ce projet de recherche a été réalisé au sein de l'IFP Énergies nouvelles (IFPEN) à Solaize dans la direction "Conception Modélisation Procédés" et je tiens à remercier Messieurs Christophe Boyer, Luc Nougier et Pierre Porot, ainsi que l'ensemble de la direction de m'avoir accueilli dans la réalisation de cette thèse.

Je tiens à exprimer tout d'abord mes sincères remerciements aux membres du jury, qui ont accepté d'évaluer ce travail de thèse. Merci à Mme Mélaz Tayakout-Fayolle, professeure au LAGEP - Université Claude Bernard Lyon 1, d'avoir accepté de présider le jury de cette thèse. Merci également à M. Marc-Olivier Coppens, professeur de l'University College of London et M. Eric Favre, professeur des universités à l'Université de Lorraine, d'avoir accepté d'être les rapporteurs de ce manuscrit. Leurs remarques et suggestions lors de la lecture de mon rapport m'ont permis d'apporter des améliorations à la qualité de ce dernier. Merci également à Mme Carine Julcour-Lebigue, directrice de recherche au CNRS et l'ENSIACET (Toulouse) d'avoir accepté d'examiner mon mémoire et de faire partie de mon jury de thèse.

Je souhaite exprimer ma profonde gratitude à Christian Jallut, professeur des universités au LAGEP - Université Claude Bernard Lyon 1, dont l'aide sur le plan scientifique tout au long de ce travail a permis de mener à bien cette thèse. J'ai largement profitée de sa rigueur scientifique, de sa patience, de ses qualités humaines mais aussi de son inépuisable précision lors de la relecture de ce manuscrit.

Je remercie tout particulièrement Jan Verstraete, ingénieur de recherche à l'IFPEN, pour son encadrement, sa pédagogie, ses conseils méthodologiques et scientifiques, et son analyse critique de mon travail lors des nombreuses discussions. En outre, j'aimerais profiter de cette occasion pour lui adresser mes sincères remerciements pour la relecture et la correction linguistique et scientifique de cette thèse, faite avec beaucoup de rigueur et de soins.

Je tiens également à exprimer ma profonde reconnaissance à Elsa Jolimaître, ingénieure de recherche à l'IFPEN, avec qui j'ai eu le grand plaisir de mener mon projet de recherche. Je lui adresse ma gratitude pour sa disponibilité, sa rigueur scientifique, ses qualités humaines, l'encouragement, la patience et l'amabilité dont elle a fait preuve tout au long de notre collaboration.

Je tiens à remercier Damien Leinekugel-Le-Cocq, ingénieur de recherche à l'IFPEN, pour sa rigueur scientifique et pour son aide précieuse à la réussite de ce travail.

J'exprime toute ma reconnaissance aux personnes qui m'ont aidée dans ces travaux de recherche. Parmi celles-ci, je tiens à citer tout particulièrement Isabelle Pitault, Françoise Couenne, Maxime Moreaud, Luis Pereira, Jean-Marc Schweitzer, Tiago Sozinho, Victor Costa pour leur soutien, disponibilité et sympathie tout au long de ces trois années.

Une pensée spéciale à mes co-bureaux préférées «Rosa», «Caro dans l'eau» et Charlotte, à l'équipe «cheucheux» : Leonor, Ruben, Leonel & Magalie, Prates, Alberto, Mafalda, Pedro, Marisa, um Muito Obrigada mais aussi à Edouard, Dina, Guillaume, Rim, Rémi, Luigi, et Romain.

Enfin, merci aux thésards : Matthieu, Sylvie, Esther, Nadia, Clément, Kévin, Moms, Cora, Zlatko, Fabien, Etienne, Wei, Benoît, Amir, Daniel, Florian, Robin, Charlotte, Damien, Ana Sofia, Ana Teresa et Florine pour les nombreuses sorties, beach-volley et repas thésards à l'IFPEN.

À mon plus profond bonheur d'être soutenue et encouragée par la douceur, la patience et le charme de Svetan…
À mes amis et à ma famille…

Dedicado aos meus pais e ao meu irmão pela enorme paciência e apoio incondicional,
sem esquecer o meu bochechas Svetan…

Résumé

La R&D sur les catalyseurs s'est longtemps focalisée sur la formulation de la phase active, conduisant ainsi à une influence accrue des limitations diffusionnelles internes. Dans cette thèse, une meilleure représentation microscopique de catalyseurs poreux a été développée. En représentant simultanément les propriétés texturales et diffusionnelles, ce modèle pourra quantifier ces limitations dans le but d'optimiser la conception des catalyseurs.

En s'appuyant sur une approche de Monte Carlo, des réseaux en 2D ou 3D, constitués de pores cylindriques interconnectés, sont générés de façon à reproduire la porosité, la surface spécifique et le volume poreux des supports d'alumine-gamma. Cet outil performant est capable de générer des réseaux contenant jusqu'à 18000×18000 nœuds en 2D et 600×600×600 en 3D avec 2 milliards de pores.

Un modèle 1D du transport de matière est utilisé à l'échelle du pore en supposant une diffusion fickienne. Avec cet outil, des réseaux de taille 200×200 peuvent être simulés. La confrontation des tortuosités simulées aux données de la littérature montre un bon accord. Cependant, la comparaison avec les valeurs expérimentales issues d'études par chromatographie inverse, montre des valeurs expérimentales plus élevées, probablement dû à la présence de deux niveaux de porosité.

L'algorithme a par conséquent été modifié afin de générer des réseaux à deux niveaux de porosité et a ainsi permis de reproduire les propriétés texturales et de transfert de matière d'une alumine. Concernant les propriétés texturales, des erreurs relatives inférieures à 10% ont été obtenues, tandis qu'un bon accord a été trouvé pour les tortuosités, 2.34 pour 2.40 expérimentalement.

Mots-clés : supports d'alumine-gamma, modèles de réseaux poreux aléatoires, diffusion en 1D dans des réseaux poreux, tortuosité.

Abstract

Catalyst R&D has long focused on the formulation of the active phase, leading to an increased influence of internal diffusion limitations. In this Ph.D. thesis, a better discrete representation of porous catalysts has been developed. By simultaneously accounting for the correct textural and diffusional properties, such catalyst support models can be used to quantify internal mass transfer in order to optimize catalyst design.

Both 2D and 3D pore networks, constituted by interconnected cylindrical pores, are generated by a Monte Carlo approach to reproduce the porosity, specific surface area and pore volume of gamma-alumina supports. This highly efficient tool is capable of generating 2D networks of 18000×18000 and 600×600×600 nodes in 3D, containing up to 2 billion pores.

Mass transfer is simulated by a 1D Fick's diffusion model within each pore of the network. 200×200 networks, containing up to 80,000 pores, can be simulated. The confrontation of the calculated tortuosities as a function of porosity to theoretical correlations shows a good agreement. However, when comparing to experimental values from fixed-bed tracer experiments, actual aluminas exhibit higher tortuosities, probably due to the organisation of the pore structure in two levels.

Hence, by modifying the model to generate networks with two-levels of porosity, we have been able to simultaneously reproduce both the textural and diffusion properties of an actual alumina. Relative errors less than 10% were obtained for the textural properties, while a good agreement was found for the tortuosity values, with a calculated value of 2.34 against the experimental value of 2.40.

Keywords: gamma alumina supports, random pore network models, 1D diffusion within pore networks, tortuosity.

Table of Contents

STATE OF THE ART 5

CHAPTER I – CHARACTERISATION OF THE TEXTURAL PROPERTIES OF POROUS CATALYSTS 6

I.1 Preparation of gamma-alumina catalysts 6

I.1.1 SUPPORT SYNTHESIS 7

I.1.2 DISPERSION OF THE ACTIVE PHASE 9

I.1.3 AGEING, DRYING AND THERMAL TREATMENT (CALCINATION) 10

I.1.4 ACTIVATION 10

I.2 Porous catalyst supports and their textural properties 10

I.3 Experimental characterisation of the textural properties 14

I.3.1 ELECTRON MICROSCOPY 14

I.3.2 SORPTION TECHNIQUES 16

I.4 Conclusions 28

CHAPTER II – MASS TRANSFER WITHIN POROUS CATALYSTS 30

II.1 Description of the mass transfer phenomena 30

II.1.1 EXTERNAL MASS TRANSFER 31

II.1.2 DIFFUSION IN MACRO/MESOPORES - DIFFUSION REGIMES 31

II.1.3 MODELLING THE MOLECULAR DIFFUSION PROCESS 32

II.2 Experimental characterisation of mass transfer properties in porous media 36

II.2.1 EXPERIMENTAL MICROSCOPIC METHODS FOR DIFFUSION PROPERTIES 36

II.2.2 EXPERIMENTAL MACROSCOPIC METHODS FOR DIFFUSION PROPERTIES: INVERSE CHROMATOGRAPHY 37

II.3 Conclusions 38

CHAPTER III - IMPACT OF PORE STRUCTURE ON MASS TRANSFER PROPERTIES .. 40

III.1 Continuum approaches 40

III.1.1 CONVENTIONAL APPROACH 41

III.1.2 Random Spheres Model (RSM) 46

III.2 Discrete approaches - combined description of pore structure and mass transfer 47

III.2.1 Analytical models 47

III.2.2 Numerical models 50

III.3 Conclusions 54

DESCRIPTION OF THE MODELS 57

CHAPTER IV - PORE NETWORK MODEL: MONTE CARLO ALGORITHM AND MASS TRANSFER DESCRIPTION 58

IV.1 Introduction 58

IV.2 Random pore network generation 59

IV.2.1 Output data from the network generation model 61

IV.2.2 Network generation algorithm diagram 64

IV.2.3 Inaccessible volume suppression algorithm 66

IV.3 Mass transfer description within each cylindrical pore of a random pore network 67

IV.3.1 Initial and boundary conditions at the nodes 68

IV.3.2 Numerical resolution diagram for the mass transfer model 70

IV.4 Conclusions 71

SENSITIVITY ANALYSES 73

CHAPTER V - NETWORK GENERATION ALGORITHM ANALYSIS 74

V.1 Introduction 74

V.2 Inaccessible volume suppression 75

V.3 Monte Carlo algorithm variability 76

V.3.1 Required minimum network size 76

V.3.2 Required number of simulations 79

V.4 Influence of the network generation model parameters 81

V.4.1 Influence of the aspect ratio N_X/N_Y with an equal maximum number of nodes 81

V.4.2 Influence of the pore existence probability: P 83

V.4.3 Influence of the pore diameter: D_P 85

V.4.4 Influence of the pore length: L_P 86

V.4.5 Relation between the average connectivity and the textural properties 88

V.5 Conclusions 91

CHAPTER VI - MASS TRANSFER MODEL ANALYSIS 92

VI.1 Introduction 92

VI.1.1 Estimation of the effective diffusion coefficient 92

VI.2 Monte Carlo algorithm variability 94

VI.2.1 Required number of simulations 94

VI.3 Influence of the network generation model parameters 95

VI.3.1 Influence of the aspect ratio N_X/N_Y with a constant maximum number of nodes...95

VI.3.2 Influence of the pore existence probability: P 97

VI.3.3 Influence of the pore diameter: D_P 98

VI.3.4 Influence of the pore length: L_P 99

VI.3.5 Relation between the average connectivity and the mass transfer properties..100

VI.3.6 Comparison of the predicted tortuosities with the effective medium theory for constant pore diameters.....101

VI.3.7 Comparison of the predicted tortuosities with the effective medium theory for pore diameter distributed networks 102

VI.4 Conclusions 103

DYNAMIC STUDY 105

CHAPTER VII - DYNAMIC BEHAVIOUR OF THE SYSTEM 106

VII.1 Introductory case studies for the discrete model 106

VII.1.1 Effect of the network volume 107

VII.1.2 Effect of a dead volume 109

VII.2 Comparison of the transient responses for the discrete model and the continuum model 112

VII.2.1 Simple case studies for the comparison of the transient responses of the discrete model and the continuum model 114

VII.2.2 Simple case studies with dead volumes for the comparison of the transient responses of the discrete model and the continuum model.....116

VII.2.3 Simple case studies with an increased porous media length ΔL for the comparison of the transient responses of the discrete model and the continuum model.....117

VII.2.4 Periodic 2D networks for the comparison of the transient responses of the discrete model and the continuum model 119

VII.3 Conclusions 123

COMPARISON TO ACTUAL ALUMINAS 125

CHAPTER VIII - REPRESENTATIVENESS OF 2D NETWORKS 126

VIII.1 Introduction 126

VIII.2 Construction of two-level pore networks 128

VIII.3 Sensitivity analyses on two-level pore networks 130

VIII.3.1 Influence of the pore existence probability 130

VIII.3.2 Influence of the pore diameter 133

VIII.3.3 Influence of the pore length 137

VIII.4 Generation of a two-level network for alumina C 140

VIII.5 Conclusions 148

THESIS CONCLUSIONS 149

PERSPECTIVES 153

BIBLIOGRAPHIC REFERENCES 161

APPENDICES 169

Glossary

BC	Boundary condition
BDDT	Brunauer-Deming-Deming-Teller classification system for adsorption isotherms
BET	Brunauer-Emmet-Teller method for the determination of the surface area
BJH	Barret-Joyner-Halenda method for the determination of the pore size distribution
CPU	Central processing unit
CS	Case study
DFG	Driving force gradient
DV	Dead volume
EMT	Effective medium theory
H1	Type 1 adsorption/desorption hysteresis
H2	Type 2 adsorption/desorption hysteresis
HDM	Hydrodemetallization
HDS	Hydrodesulphurization
IUPAC	International Union of Pure and Applied Chemistry
PDE	Partial derivative equations
PFG-NMR	Pulsed field gradient nuclear magnetic resonance
PSD	Pore size distribution
QENS	Quasi-elastic neutron scattering
RAM	Random access memory
RHS	Right hand side
RSM	Random spheres model
SEM	Scanning electronic microscopy
TEM	Transmission electron microscopy

Nomenclature

B	Maxwell-Stefan matrix B $(m^{-2} \cdot s)$; empirical constant used in the Iversen and Jorgensen correlation relating the tortuosity with the catalyst porosity
C	Empirical BET constant
CF	Correction factor that is given by the ratio of the pore volume to the volume of a single pore from the continuum (macroscopic) representation
CF_{global}	Correction factor that is given by the ratio of the pore volume to the volume of pores that have a projection on the diffusion axis
c_i	i species fluid concentration $(mol \cdot m^{-3})$
$c_{i\ bulk}$	i species fluid concentration in the bulk phase $(mol \cdot m^{-3})$
$c_{i\ initial}$	i species fluid concentration at time t_0 $(mol \cdot m^{-3})$
$c_{i\ interface}$	i species fluid concentration at the particle outer surface $(mol \cdot m^{-3})$
c_{node}	Concentration of a given component at a given node of the network $(mol \cdot m^{-3})$
c_t	Total molar concentration of the fluid mixture $(mol \cdot m^{-3})$
D_{AB}^{∞}	Molecular diffusion coefficient determined by the Stokes-Einstein equation $(m^2 \cdot s^{-1})$
D_1	Pore diameter from the first level of porosity of a given two levels pore network (nm)
D_2	Pore diameter from the second level of porosity of a given two levels pore network (nm)
D_{avg}	Mean pore diameter (nm)
D_{im}	i species molecular diffusion coefficient $(m^2 \cdot s^{-1})$
$D_{i\ eff}$	i species effective diffusion coefficient $(m^2 \cdot s^{-1})$i
D_p	Pore diameter (m)
E_x	Network thickness in the x direction (m)
E_y	Network size in the y direction (m)
E_z	Network size in the z direction (m)
F	Percolation probability
F_{ip}	Molar flow of component i for a given pore p $(mol \cdot s^{-1})$
f	Shape factor used in the BJH equation to account for the liquid-vapour shape during adsorption $(f = 1)$ and desorption $(f = 2)$; occupation probability

f_c	Percolation threshold for the Seaton method
g_1, g_2, g_3	Polynomial functions used in the Seaton method
$HETP$	Height Equivalent to Theoretical Plate (m)
J_{Ay}	Continuum (macroscopic) molar flux in the y direction taking the Johnson and Stewart approach
J_i	Molar flux of component i $(mol \cdot m^{-2} \cdot s^{-1})$;
J_{ip}	Molar flux of component i and for a given pore p $(mol \cdot m^{-2} \cdot s^{-1})$
${J_{Ay}}^p$	Projection of the molar flux along a single pore in the y direction taking the Johnson and Stewart approach
K_i	Component Henry's adsorption constant
k_B	Boltzmann constant $(1.3807 \times 10^{-23} J \cdot K^{-1})$
k_{if}	External mass transfer coefficient of component i $(m \cdot s^{-1})$
L	Average linear dimension of microparticles used In the Seaton method (m), column length (m); thickness of the infinite plate (m)
L_1	Pore length for the first level of porosity of a given two levels pore network (nm)
L_2	Pore length for the first level of porosity of a given two levels pore network (nm)
L_p	Pore length (m)
l	Spatial coordinate along the pore axis (m)
M	Molar mass $(g \cdot mol^{-1})$
M_B	Atomic molar mass of solvent B $(g \cdot mol^{-1})$
M_{total}	Total catalyst mass (g)
N	Number of samples
N_A	Avogadro number (mol^{-1})
N_{colloc}	Number of collocation points
N_{nodes}	Number of nodes
N_p	Number of pores
$N_{p\ outlet}$	Number of pores at the outlet of the infinite plate
$N_{pores\ diffusion}$	Number of pores that have a diffusion projection on the flux direction
N_x	Network size as in the number of nodes along the x direction
N_y	Network size as in the number of nodes along the y direction
N_z	Network size as in the number of nodes along the z direction

$n(r_p)$	Pore number distribution
n_m	Monolayer capacity per unit of solid mass $(mol \cdot g^{-1})$
n^a	Amount of adsorptive present in the pores per unit of solid mass $(mol \cdot g^{-1})$
P	Pressure of the system (Pa); pore existence probability
P_0	Saturated vapour pressure (Pa)
P_1	Pore existence probability for the first level of porosity of a given two levels pore network
P_2	Pore existence probability for the second level of porosity of a given two levels pore network
q_v	Volumetric fluid flow rate $(m^3 \cdot s^{-1})$
R	Ideal gas constant $(J \cdot mol^{-1} \cdot K^{-1})$
R_i	Mass transfer resistance $(s \cdot m^{-3})$
R_h	Hydrodynamic radius of the solute molecule (m)
$rand$	Random number
r_K	Kelvin radius obeying the BJH method (cm)
r_p	Pore radius (m)
$r_{p\,max}$	Maximum pore radius (m)
$r_{p\,min}$	Minimum pore radius (m)
S_p	Pore surface (m^2)
S_{pores}	Total pore surface (m^2)
s_{BET}	Specific surface area obtained using the BET monolayer capacity $(m^2 \cdot g^{-1})$
s_{BJH}	Pore surface area per unit of solid mass obtained via the BJH method $(m^2 \cdot g^{-1})$
T	Temperature of the system (K)
t	Thickness of the adsorbed multilayer film for the BJH method (cm, nm), time (s), simulation time (s)
t_0	Initial time (s)
$\overline{t_s}$	Mean residence time of the component within the column (s)
u_1	Diffusion velocity of component 1 $(m \cdot s^{-1})$
u_2	Diffusion velocity of component 2 $(m \cdot s^{-1})$
V_p	Pore volume (m^3)
V_{pores}	Total pore volume (m^3)

V_{total}	Total catalyst volume (m^3)
v_A	Molar volume of solute A at its normal boiling point $(m^3 \cdot mol^{-1})$
v_L	Molar volume of the adsorbate in the liquid state $(cm^3 \cdot mol^{-1})$
v_{int}	Interstitial velocity $(m \cdot s^{-1})$
v_p	Specific pore volume or pore volume per unit of mass $(ml \cdot g\ cat^{-1})$, $(m^3 \cdot g\ cat^{-1})$
x	Non-dimensional pore aspect ratio for the effective medium theory x; axis
x_i	Molar fraction of species i $(mol \cdot m^{-3})$
y	y axis
Z	Coordination number
Z_{avg}	Average coordination number or connectivity
Z_{max}	Maximum coordination number
z	z axis

Subscripts and superscripts

0	In the absence of a porous medium
1	First level of porosity for a given two levels pore network
2	Second level of porosity for a given two levels pore network
eff	Effective parameter i.e. in the presence of a porous medium
i	Species i
ij	Step ij
NC	Number of components
$n+1$	Represents the solid when using the Maxwell-Stefan model
p	Pore p

Greek letters

Δn	Number of moles of the component that is accumulated within the column during the breakthrough experiment (mol)
Δt_{ij}	Decrease in thickness of the adsorbed film at the pore surface and already empty for step ij (cm)
ΔV_{ij}	Desorbed gas volume during step ij $(cm^3 \cdot g^{-1})$

$Đ_{ij}$	Binary diffusion coefficient used in the Maxwell-Stefan model $(m^2 \cdot s^{-1})$
Φ	Dimensionless association coefficient of solvent B for the Wilke and Chang empirical correlation
α	Slope of the BET equation $(g \cdot mol^{-1})$
β	Intercept on the y axis of the BET equation; critical exponent for the Seaton method $\beta = 0.41$
γ_o	Surface tension of the liquid-vapour interface $(N \cdot cm^{-1})$
ε	Catalyst porosity
ε_{int}	Interstitial porosity which is the bulk porosity
η_B	Solvent viscosity $(kg \cdot m^{-1} \cdot s^{-1})$
θ	Contact angle between the liquid and the solid surface (°); pore inclination in the Johnson and Stewart approach (°)
λ	Pore conductance $(m^3 \cdot s^{-1})$
λ_{eff}	Effective medium conductance $(m^3 \cdot s^{-1})$
μ_i	Molar chemical potential of species i $(J \cdot mol^{-1})$
μ_n	n^{th} moment used to exploit data from the inverse chromatography using the moments method $[\mu_1] = (s), [\mu_2] = (s^2)$,
ν	Critical exponent for the Seaton method $\nu = 0.88$
ρ_{ap}	Apparent density or mass per unit of catalyst volume $(g.ml^{-1})$
ρ_s	Solid phase or skeletal density $(g \cdot ml^{-1})$
σ	Molecular cross-sectional area (average area occupied by each molecule in a monolayer) (m^2); standard deviation; pore surface ratio related to the continuum (macroscopic) representation
τ	Tortuosity factor
τ_{geom}	Geometrical tortuosity

GENERAL INTRODUCTION

In the refining industry, hydroprocessing, catalytic reforming and isomerization processes all use catalysts that are dispersed on gamma-alumina supports. These supports are highly complex porous structures due to their scales of porosity and heterogeneity. The activity and selectivity of catalysts is therefore not only determined by the active phase, but also by the mass transfer occurring within the porous structure of the support. Moreover, the mass transfer resistance is in particular related to the pore structure and to the nature and size of the diffusing molecules that will define the diffusion regime.

Intra-particle diffusion is an essential aspect in the research field of heterogeneous catalysis. In the case of catalytic conversion of complex fractions, it has been established that intra-particle diffusional resistance can be highly limiting for certain applications. Therefore, during the preparation of heterogeneous porous catalysts, slight variations in the textural properties of the support (porosity, pore diameter) can lead to significant variations in the catalytic activity.

Hence, the adequate evaluation of the diffusion phenomena is crucial in order to correctly predict the influence of operating conditions during reactor design and optimisation. It is also important to have a good understanding of these aspects in order to optimise the catalyst pore structure and therefore mass transfer through the catalyst network.

When modelling mass transfer phenomena within catalyst particles, one is confronted with two main steps. First, one has to describe the pore structure of the pellet in a realistic way, since the diffusion kinetics is highly dependent on the pore network geometry. Secondly, one has to model mass transfer within the catalyst particle. Comparing the simulation results to experimental data is also essential in order to validate the models and/or estimate unknown parameters (textural or diffusion properties).

Several representations of porous catalysts can be found in the literature. They can be classified into two main types, continuum models and discrete representations. Typically, a continuum description of mass transfer in porous media is based on global textural parameters, such as the porosity and the tortuosity (Ruthven, 1984). The main shortcoming of continuum descriptions is related to the representation of the catalyst pore structure as a pseudo-homogeneous medium, which does not allow to explicitly account for the contributions of neither the pore network topology (interconnectivity, coordination, etc.) nor the pore morphology (pore size distribution, pore shape, pore surface roughness, etc.). This assumption also implies the use of average or effective mass transfer properties.

On the other hand, discrete models, which describe the pore structure by using a network of connected pores, have now been highlighted for several years, as can be seen in the literature review. These models are able to define the pore structure on the microscopic level, by means of a discrete network, taking profit of experimental characterisation data to reproduce the pore structure of a given sample. The prediction of mass transfer through the previously constructed porous medium is also possible, simulating mass transfer within each pore of the network. An interesting property of the direct simulation of mass transfer within each pore is that it only requires the use of molecular diffusion coefficients and hence, no fitting parameters are needed. However, at the present, the actual barriers for this kind of models are the memory restrictions and the CPU performance. Indeed, only small networks can be simulated. Rieckmann and Keil (1999), for instance, used a 30×30×30 network corresponding to 27 thousand nodes and 60 thousand pores.

However, up to now none of these discrete models have been able to correctly reproduce the textural properties at a representative (grain) scale and validate the predictions on the diffusion phenomena occurring at the level of a catalyst grain of an actual solid.

Hence, this thesis will focus on a better representation of the influence of the topology on the mass transfer properties by using a discrete approach and will apply such techniques to gamma-alumina supports.

OUTLINE OF THE THESIS

As mentioned above, gamma-alumina supports are highly complex porous structures therefore requiring a special care for their representation. The first part of this thesis (**State of the Art**) includes three chapters. General information on the supports is given in Chapter I, to provide the reader an insight into the geometrical complexity of gamma-aluminas. An overview on the experimental characterization of the textural properties within porous catalysts is as well depicted (Chapter I).

The main mass transfer phenomena occurring within a pore network are discussed in Chapter II, as well as, techniques for the experimental characterisation of mass transfer within porous catalysts. In Chapter III, several approaches found in the literature, either discrete or pseudo-homogeneous/continuous, to study the impact of the pore structure topology on the mass transfer properties are described.

The second part of the manuscript (**Description of the models** - Chapter IV) contains the description of the model developed during this thesis project. Firstly, the algorithm that represents the pore structure of gamma-alumina supports by means of a discrete pore network is presented. This discrete representation is simply based on a random pore network physically constituted by interconnected cylindrical pores. The explanation of the network generator algorithm is followed by the description of the model accounting for mass transfer within pore networks.

The third part of the manuscript (**Sensitivity Analyses**) includes two chapters. The sensitivity analyses were performed on different parameters of the generation algorithm. We have expressively separated the impact on the textural properties presented in Chapter V from the impact on the mass transfer properties that can be found in Chapter VI.

The fourth part of the manuscript (**Dynamic Study**) is dedicated to the mass transfer properties in transient regime (Chapter VII). A dynamic study is presented that compares the transient diffusion properties in a discrete pore network to those obtained in the pseudo-homogeneous model.

The last part of the manuscript (**Comparison to Actual Aluminas**) contains Chapter VIII that is dedicated to the reproduction of both textural and mass transfer properties using 2D periodic pore networks. The simulated data is confronted to the textural and mass transfer properties of 5 samples of gamma-alumina supports, which were previously characterized via physisorption and inverse chromatography techniques, during an experimental PhD thesis at IFP Energies Nouvelles (Kolitcheff, 2017).

Finally, the thesis conclusions and perspectives are given at the end of the manuscript.

STATE OF THE ART

CHAPTER I – CHARACTERISATION OF THE TEXTURAL PROPERTIES OF POROUS CATALYSTS

The present chapter will give a brief introduction on the literature review devoted to catalyst supports, specifically within the frame of our work devoted to gamma-alumina supports. The complexity of gamma alumina supports and the impact of the operating conditions during catalyst preparation on their textural properties are described.

To improve the design and preparation of more efficient materials as catalyst supports, several textural properties have been used over the years, to characterize the performances of these catalyst supports. This chapter will be dedicated to these features. The experimental techniques and methods used for the textural properties estimation are also discussed.

I.1 PREPARATION OF GAMMA-ALUMINA CATALYSTS

We have listed below different aspects that underlie the performance and lifetime of catalysts and that are related to the characteristics of supports (Poncelet and Grange, 1983):

- the mechanical resistance;
- the specific surface area;
- the dispersion of the metal nanoparticles/active sites;
- the possibility for the support to become a reactive support and participate in the catalytic reaction.

Catalyst preparation is an important step that aims to produce at industrial scale catalysts with high activity, selectivity and stability conditions. In general, the main characteristic of a gamma-alumina support is related to a large specific surface area on which the active material can be dispersed. Depending on its final application, other characteristics may come into play, such as the pore size distribution and the pore volume. The catalyst support creates resistances to mass transfer that are related to the support morphology and can remarkably decrease the catalyst performances. It is then important to give an overview of the techniques used for their formulation and synthesis.

Let us consider the example of a hydrotreating process where the use of gamma-alumina supports prevails due to its mechanical properties, low costs and good knowledge of its textural properties. The gamma-alumina supports are generally used in the form of beads or extrudates.

Supported catalysts are prepared in several steps. The general procedure consists in depositing the precursor onto the support surface and transforming the precursors into the required active compounds (oxide, sulphide, metal). The main preparation steps are listed below:

- support formulation and synthesis;
- dispersion of the active phase;
- drying;
- calcination;
- activation of the precursor species.

I.1.1 SUPPORT SYNTHESIS

In Fig. I-1, an overview on the gamma alumina support synthesis for a hydrotreating catalyst is presented.

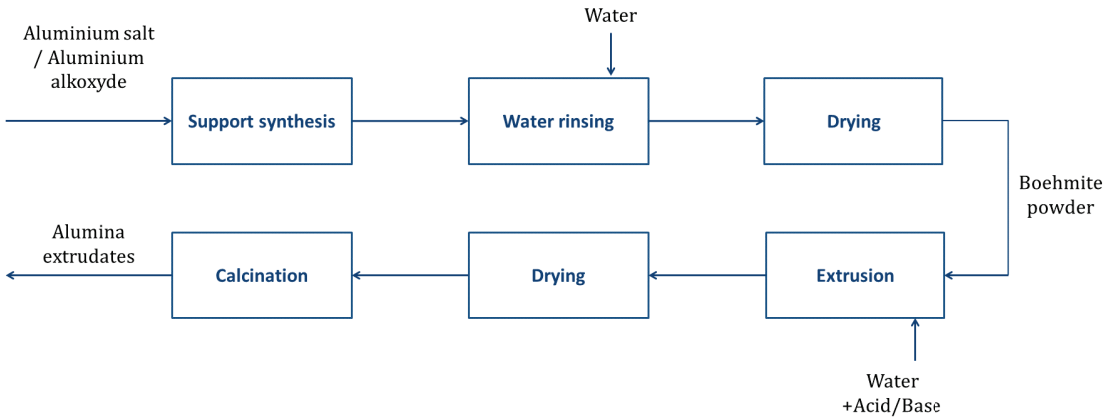


Fig. I-1. Support formulation of an alumina catalyst support. Adapted from Kolitcheff (2015).

A first mixing step is performed to obtain a suspension of metal salt solution, either via precipitation using an aluminium salt, or via a sol-gel route using an aluminium alcoxyde. The metal salt suspension is then water rinsed and dried, obtaining thereby a boehmite powder. A post-treatment is then performed to settle the support formulation, by means of forming, drying and decomposition (calcination).

The final sizes of the platelets depend on the balance between the nucleation rate and the particle growth rate that is controlled by the supersaturation (ratio between the solute concentration and its solubility) and therefore on the concentration of the suspension and the operating conditions. As supersaturation increases, the formation of smaller platelets is favoured and when the temperature increases, larger platelets are formed. It is important to note that the size of the platelets determines the size of the voids inside the catalyst, i.e. the pore sizes. When larger platelets are formed then larger pores are as well formed.

During extrusion, the boehmite powder is transformed into millimetre size particles. This step first consists on mixing the boehmite powder with an acid phase under mechanical agitation. Afterwards, an alkaline solution is added, the particles flocculate, giving the material a certain consistency. The paste obtained is then extruded through a die of a given shape (cylinder, trilobe, quadrilobe, etc.). For catalytic applications, polylobed geometries are generally preferred, as they increase the external surface to volume ratio of the extrudates, and hence reduce the characteristic length of internal and external mass transfer.

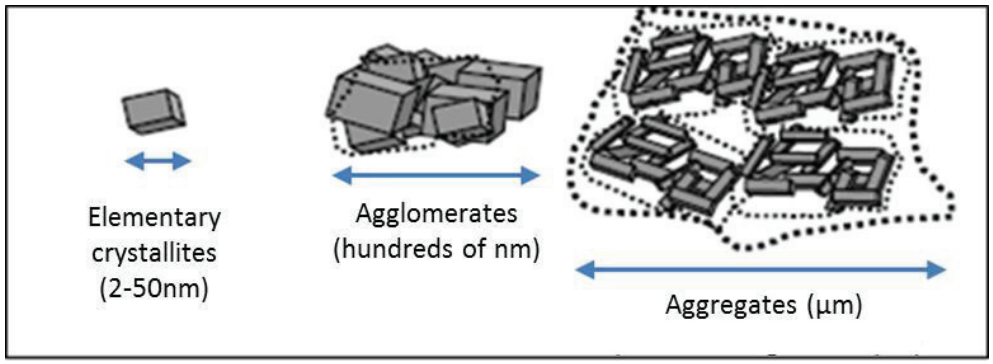


Fig. I-2. Schematic representation of an elementary crystallite, agglomerates and aggregates.

During the course of the support synthesis, the platelets (elementary crystallites) of 2 to 50 nm form aggregates (hundreds of nm) and agglomerates (µm) (Fig. I-2), which produce a very complex porous system characterized by different spatial organizations at different scales.

In order to remove the residual water remaining within the extrudates, a drying step is required before reinforcing the textural and mechanical properties via a calcination process.

The operating conditions of the support synthesis govern the arrangement of the aluminium oxides conditioning the network, the structure and the pores and/or platelets, agglomerates and aggregates dimensions. These different aspects can be partially quantified by the textural properties of the support. A further section is presented towards the understanding of these textural properties.

I.1.2 DISPERSION OF THE ACTIVE PHASE

After the preparation of the catalyst support (extrusion – drying – calcination), the active phase needs to be added and dispersed inside the catalyst support. This step is considered to have only a small influence on the structure of the support.

There are different techniques to perform the dispersion of the active phase, such as impregnation, ion exchange/equilibrium adsorption, grafting, anchoring, deposition/precipitation, spreading and wetting, immobilization of metal particles and agglomerates and chemical vapour deposition. Amongst these, impregnation is the most common one (Köhler, 2006).

Impregnation consists in the deposition of precursors (salts in aqueous phase) belonging to the active phase over the catalyst support. There are two main impregnation techniques: dry and diffusional impregnations.

During dry impregnation, one controls the exact amount of deposited species in the solvent volume to cover the available pore volume. The migration of precursors into the pores of the support is promoted by capillary pressure. The diffusional impregnation makes use of a greater amount of solvent and requires a concentration gradient in order to the precursors to migrate, as the support is immersed in the impregnation solution.

Under a chemical regime, the more dispersed the active phase, the greater the catalyst activity. A large surface area allows the active phase to be deposited in the most dispersed form possible (Balakrishnan and Gonzalez, 1993). Thus, the best way to improve chemical reactivity, apart from using a highly efficient active phase, is to increase the specific surface area. However, the pore diameter can also be extremely impacting on the overall activity:

- in the case where the size of the molecules is larger than the diameters of certain pores, the molecules cannot access a part of the solid. Since the molecules cannot reach the active phase located in this porosity, the latter becomes useless for the reaction. This is usually observed for bulky molecules, such as asphaltenes for instance;
- if the molecules have access to the entire porosity of the solid, the size of the pores could have an influence on the diffusion regime of the molecules.

After the dispersion of the active phase, several other steps come into play: an ageing stage, a drying step, followed by a thermal treatment using calcination or reduction and finally, the activation step.

I.1.3 AGEING, DRYING AND THERMAL TREATMENT (CALCINATION)

In the course of the ageing step, a slow migration of the metal precursors into the catalyst grains occurs, usually with the help of a water-saturated atmosphere at ambient temperature and pressure. At the drying stage, the evaporation of the solvents used during the active phase dispersion takes place.

During the thermal treatment, the textural properties, the activity and the stability of the catalyst will be modified. This stage is usually performed with the introduction of an inert gas flow and promoted at high temperatures, leading to the following transformations:

- precursors decomposition, with the formation of active sites;
- textural modifications by sintering, increasing the aggregate dimensions and therefore the pore sizes, thus lowering the specific surface area and leading to greater internal diffusional resistances.

At the end of these steps, the final form of the active species is obtained and in the case of precursors with low interaction with the support, a better dispersion is obtained. Also, the final structure of the catalyst is obtained.

I.1.4 ACTIVATION

During this step, precursors are transformed into the catalytically active phase submitted to a thermal treatment, with a gas flow, where the following phenomena occur:

- decomposition and desorption of volatile compounds;
- chemical bonding of the precursors to the support;
- chemical transformation generating new phases, by means of a thermal treatment under inert, oxidizing, reducing, sulphur-containing or reaction gas atmosphere: calcination (O_2/N_2), reduction (H_2), sulphidation (H_2/H_2S).

I.2 POROUS CATALYST SUPPORTS AND THEIR TEXTURAL PROPERTIES

The preparation of gamma-alumina supports occurs in several successive and individual steps. Each step may impact the textural and mechanical properties of the material. The porosity of gamma-aluminas is originated by the voids in the different levels of organization of the pore structure. As we may recall, the morphology of a gamma-alumina support is considered to contain three main scale structures.

From the same sizes of elementary crystallites, it is possible to synthetize gamma-alumina supports with a great variation of the textural properties. In the work of Morin (2014), the influence of the solvent used during the catalyst preparation was investigated. As we can see in Fig. I-3, the pore size distributions are very different depending on the solvent that is used: in the presence of an organic solvent (t-butanol) a second level of porosity with larger pores is created. Since the organic solvent exerts repulsive forces between the different scale structures, reducing their capacity to agglomerate and delivering more porous supports.

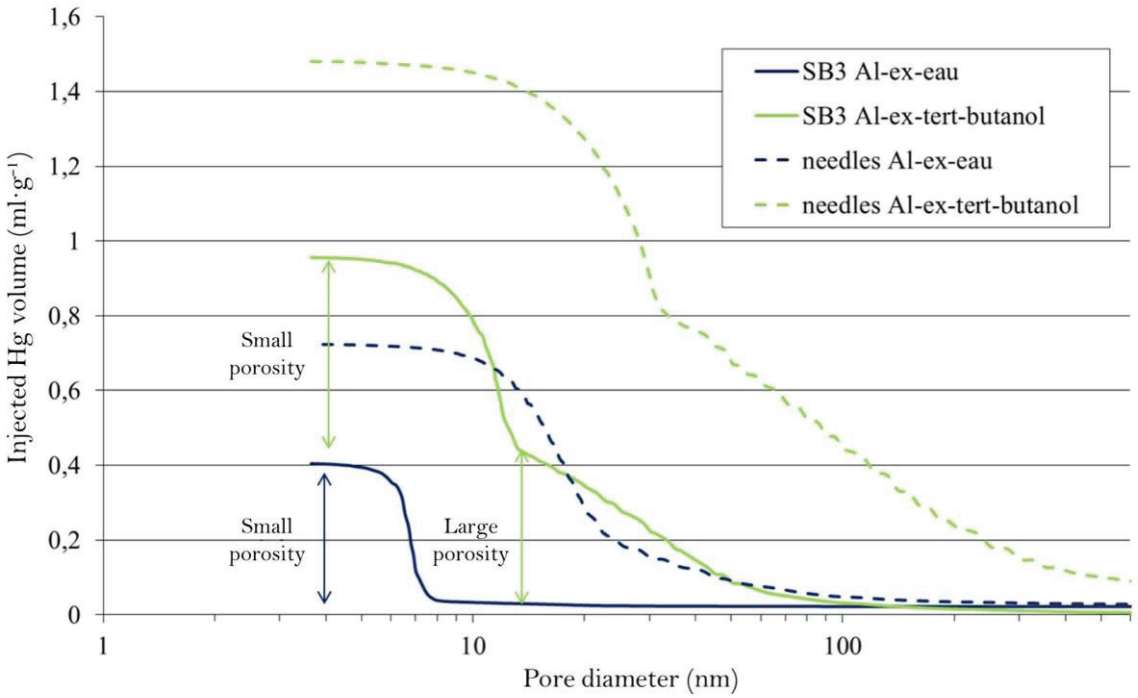


Fig. I-3. Cumulated pore size distributions measured via Hg porosimetry and obtained for gamma-alumina supports prepared using two different solvents and two different shaping processes (Morin, 2014).

This means that aluminas porosity is not only linked to the morphology and/or size of the elementary crystallites but there is also the possibility to obtain different pore structures depending on the supports preparation method.

Weiland (2015) studied Xenon diffusion in a bimodal alumina using NMR spectroscopy. Different levels of confinement have been identified and can be attributed to different porosities characterized by different diameters, which is in agreement with Morin (2014). Weiland (2015) also showed that these different porous levels are hierarchically organized: only the larger porous domain is in direct contact with the external fluid, i.e. to access the small porosity, molecules have first to pass through the larger porous domain.

In order to develop a model to correctly represent a gamma-alumina support, one should understand the main textural properties. We will therefore be dedicating to the available

structural information on porous catalysts, the experimental characterisation techniques used and the data obtained, as well as, their interpretation.

Among the most commonly used textural properties are the specific surface area, the specific pore volume, the porosity and the pore size distribution (Klobes *et al.*, 2006).

The porosity of the support is the fraction of pore volume of a particle. This parameter is given by the ratio of the accessible void space volume to the total volume of the catalyst particle and can be related to other properties:

$$\varepsilon = \rho_{ap} . v_p \quad \text{(I-1)}$$

where v_p is the pore volume per unit of mass or specific pore volume ($ml \cdot g_{cat}{}^{-1}$) and ρ_{ap} is the mass per unit of catalyst volume or apparent density (expressed in $g_{cat} \cdot ml^{-1}$). The latter also depends on the pore volume, as follows:

$$\rho_{ap} = \frac{1}{v_p + \frac{1}{\rho_s}} \quad \text{(I-2)}$$

with ρ_s the solid phase or skeletal density expressed in $g_{cat} \cdot ml^{-1}$.

The average pore diameter is also an important property of the support, since it determines the diffusional regime. Besides the classification of pores according to their availability, their shape and dimension are also pore characteristics. Pore shapes have been systematically defined as cylindrical, funnel or slit-shaped. For pore dimensions, the IUPAC (International Union of Pure and Applied Chemistry) classification proposes three categories:

- micropores, with a diameter inferior to $2\,nm$;
- mesopores, having a diameter ranging from 2 to $50\,nm$;
- macropores, with a diameter higher than $50\,nm$.

Generally, gamma-alumina supports are essentially constituted by mesopores and macropores corresponding respectively to the voids between crystallites/clusters and by the voids between agglomerates. Depending on the formulation of the support, several structures and pore size distributions of aluminas can be obtained. However, the increase in the mean pore diameter is generally to the detriment of the specific surface area due to the growth of the elementary crystallites.

Hence, the pore structure depends on the size, shape and the aggregation of the particles (crystallites, clusters and agglomerates) giving rise to the textural properties.

The total specific surface area is defined as the accessible area of a solid surface per unit mass of material (for reasons of brevity the word "accessible" will be dropped in the

remainder of the report). The specific surface area of alumina-supported catalysts typically ranges from 50 to $400\, m^2 \cdot g^{-1}$.

The pore size distribution $PSD(r_p)$ when normalized by the solid mass is defined as follows:

$$dv_p = PSD(r_p)dr_p \tag{I-3}$$

where dv_p is the specific pore volume corresponding to the pores having a radius comprised between r_p and $r_p + dr_p$. The total specific pore volume is then given by:

$$v_p = \int_{r_{p\,min}}^{r_{p\,max}} PSD(r_p)dr_p \tag{I-4}$$

where $[r_{p\,min}, r_{p\,max}]$ is the range of radii in the porous medium.

Another important feature characterising the pore structure of a catalyst support is the connectivity (Z_{avg}). This is simply the average coordination number in the pore network. With the coordination number defined as the number of pores emanating from each branching site.

Table I-1 gathers the main textural properties of five aluminas used in hydrotreating processes, giving an idea of the order of magnitude of the textural features: average diameter, BET surface area, specific pore volume and support's porosity. These aluminas were experimentally characterised in the work of Kolitcheff (2017) and will be interesting to validate the proposed model.

Table I-1. Textural properties obtained for 5 samples of actual porous aluminas using nitrogen sorption (Kolitcheff, 2017).

Alumina	$\boldsymbol{D_{avg}}$ $(\boldsymbol{nm})$	$\boldsymbol{s_{BET}}$ $(\boldsymbol{m^2 \cdot g^{-1}})$	$\boldsymbol{v_p \times 10^6}$ $(\boldsymbol{m^3 \cdot g^{-1}})$	**ε**
A	7.1	340	0.71	0.72
B	8.0	300	0.72	0.70
C	9.0	290	0.78	0.72
D	9.6	270	0.74	0.71
E	17.6	160	0.77	0.73

I.3 EXPERIMENTAL CHARACTERISATION OF THE TEXTURAL PROPERTIES

In the following, a description of two experimental techniques of characterization and some general methods used to treat the data are given: electron microscopy and sorption techniques.

I.3.1 ELECTRON MICROSCOPY

Transmission Electron Microscopy (TEM) and Scanning Electron Microscopy (SEM) are generally employed as qualitative techniques for experimental characterization. With these techniques, one can observe and detect the local properties of the physical structure. It should be stressed however that these local properties are not always representative of the global structure of the support. From the images of the TEM/SEM techniques, we can evaluate the homogeneity of the porous structure, the main defects, the size of the elementary particles, and also their shape.

The following SEM images were taken on bimodal gamma-alumina supports exhibiting macro- and mesopores. During the preparation of the solids that are submitted to SEM experiments, it is necessary to fill the samples with resin and polish them mechanically. The black spots in Fig. I-4 to Fig. I-6 represent the added resin and therefore the void space and the grey space represents the gamma-alumina structure.

The SEM images (Fig. I-4 and Fig. I-5) were taken on a bimodal catalyst support at a scale of $100\,nm$ and $20\,\mu m$. Fig. I-4 shows some visible mesopores, macropores and agglomerates. The SEM image in Fig. I-5 simultaneously shows macropores, agglomerates and clusters, while the SEM image in Fig. I-6 shows a mono-modal alumina support obtained at a scale of $1\,\mu m$.

It can be concluded from these SEM images that the gamma-alumina structure is highly disordered and complex, showing different levels of porosity. Therefore, the development of a representative network for the real structure of a gamma-alumina support is a quite difficult task and remains a simplified version of the real system.

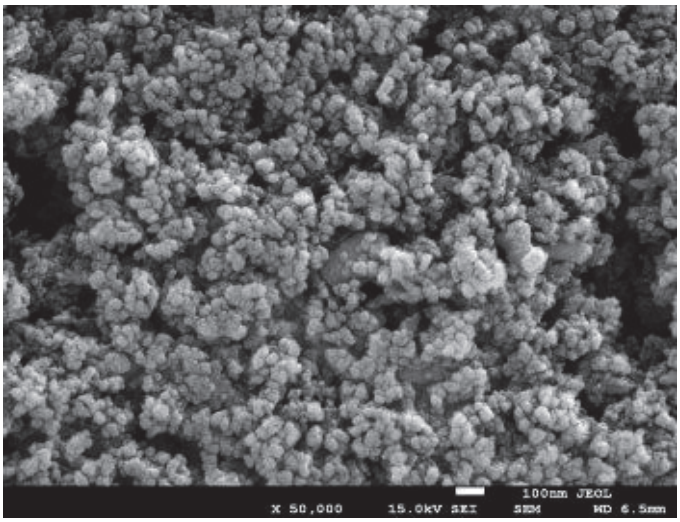


Fig. I-4. SEM image at a scale of 100 nm of a bimodal alumina (Direction Physique et Analyse - Groupe de travail texture et Polissage Ionique 2014).

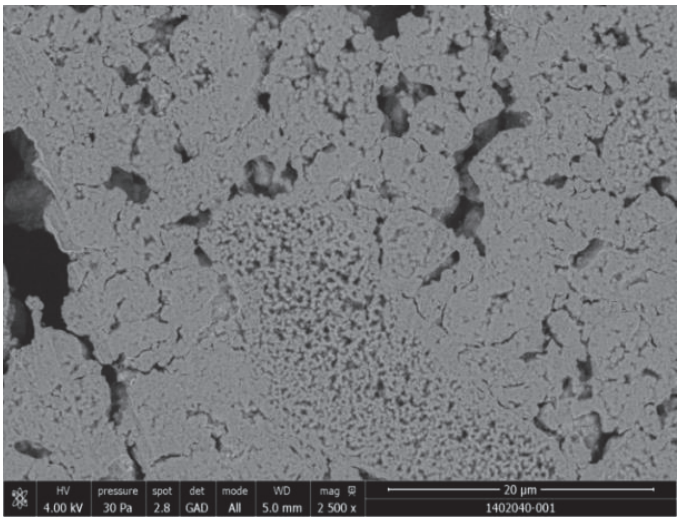


Fig. I-5. TEM image from a bimodal alumina with a macro and mesoporosity at a $20\,\mu m$ scale (Direction Physique et Analyse - Groupe de travail texture et Polissage Ionique 2014).

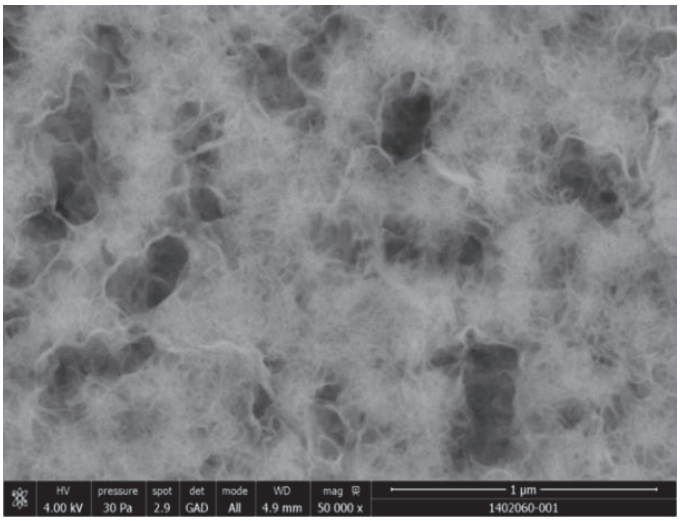


Fig. I-6. TEM image of a monomodal alumina with a mesoporosity scale and shot at $5\,\mu m$ (Direction Physique et Analyse - Groupe de travail texture et Polissage Ionique 2014).

I.3.2 SORPTION TECHNIQUES

Numerous sorption techniques using probe molecules have been developed to characterize powders and porous solids (Sing *et al.*, 1984; Rouquerol *et al.*, 1994). These sorption techniques can only detect open pores because of the inaccessibility of the fluid to closed pores. Similarly, if the probe molecules are too large, they will not reach all the accessible porosity.

We will focus on the description of the physisorption technique and the underlying methods used to determine the textural properties.

I.3.2.1 SORPTION ISOTHERMS AND HYSTERESIS LOOPS

Physical sorption occurs when a species, the adsorptive, is brought into contact with the surface of a solid, the adsorbent. The fluid-wall and fluid-fluid interactions govern the physical sorption process. The technique consists in measuring the quantity of adsorptive that is present within the pores at a given temperature and pressure. The measurements can be performed by increasing or decreasing the relative pressure P/P_o, where P_o is the saturation pressure of the bulk adsorptive. At a value of $P/P_o \sim 1$, the porous sample is totally filled with liquid. The sorption measurements are usually performed by using nitrogen at its boiling temperature of 77K.

One will choose the probe molecule according to the diameter of the pores to be studied. These molecules should be small enough so that they can reach all the porosity. An alternative to nitrogen is for instance, the argon molecule due to its greater stability (chemically inert).

Although sorption techniques can only detect open pores, the total volume of closed pores can be derived knowing the experimental apparent density and the theoretical skeletal density.

At a given temperature, the experimental isotherms are generally represented by the amount of adsorptive present in the pores per unit of solid mass n^a as a function of the relative equilibrium pressure P/P_o (Rouquerol *et al.*, 2014):

$$n^a = f(P/P_o)_T \qquad \text{(I-5)}$$

As illustrated in Fig. I-7 (Kuchta, 2010; Bobin, 2010), depending on the relative pressure P/P_o, the sorption process is due to several consecutive steps. By increasing the relative pressure, one successively finds:

Domain A - Located adsorption: at low relative pressures, from 10^{-6} to 10^{-4}, adsorption occurs on the solid sites of adsorption that are the most strongly attractive (defaults, imperfections, etc.);

Domain B - After increasing the pressure, but still at low relative pressures, the filling of narrow micropores occurs according to an adsorption process;

Domain C - At a relative pressure around 10^{-4} to 10^{-1}, micropores continue to be filled. Simultaneously, the solid surface is covered by a number of adsorbed molecules that is increasingly significant. At the end of this domain $(P/P_o \sim 0{,}15)$, the whole surface of the solid is statistically covered by a dense adsorbed monolayer that allows to determine the specific surface area of the porous solid according to the BET method (see section I.3.2.2);

Domain D - On top of the monolayer, several layers are progressively formed by multi-molecular adsorption. Then, the adsorption process is replaced by a liquid phase filling process of mesopores, the capillary condensation. The Kelvin equation (I-11) relates the pressure to the curvature radius of the liquid-vapour interface. According to a geometrical model of the pore, the curvature radius can be related to the pore radius that is being filled. By increasing the pressure, all pores are finally filled with liquid at the boundary limit of approximately $P/P_o \sim 1$.

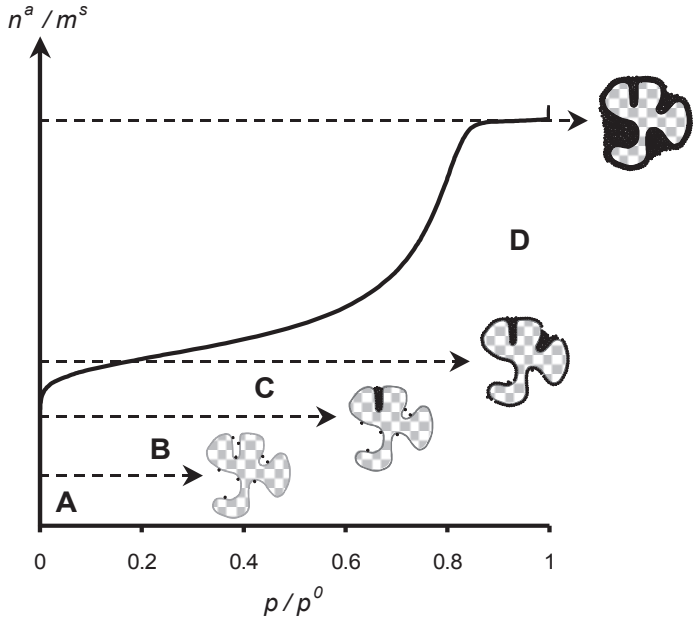


Fig. I-7. Main adsorption steps on a physical adsorption isotherm.

For different porous materials, the shape of the isotherms differs. In 1940, five types of adsorption isotherms were identified, as proposed by Brunauer *et al.* (1940). The classification is referred to as the BDDT or Brunauer classification. Afterwards, Halsey (1948) documented a sixth adsorption isotherm. Later on, in the 80's, Sing *et al.* (1984)

joined by Rouquerol *et al.* (1999), reformulated the adsorption isotherms classification as represented in Fig. I-8 by adding the hysteresis loop that appears in the isotherms of type IV and V.

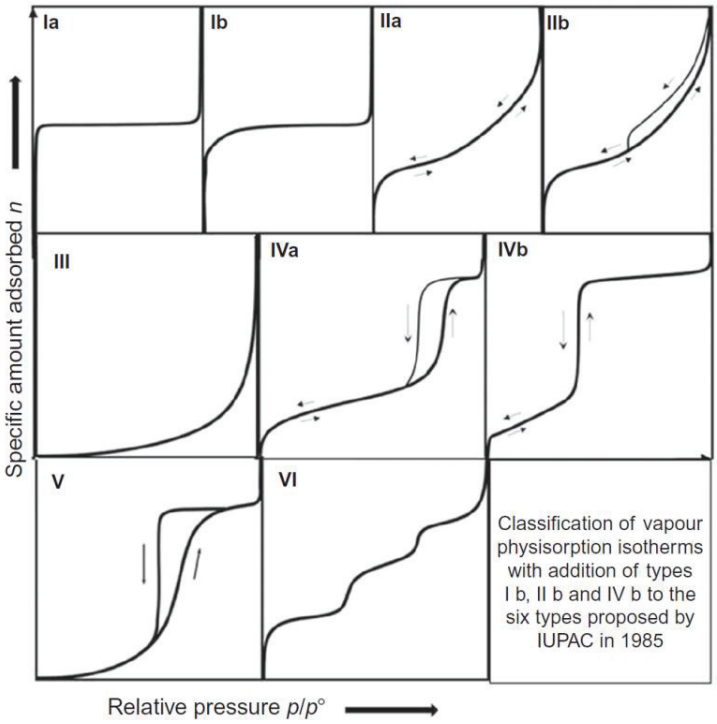


Fig. I-8. Classification of adsorption isotherms defined by IUPAC (Sing *et al.*, 1984; Rouquerol *et al.*, 1999; Rouquerol *et al.*, 2014).

These six types of adsorption isotherms are generally accepted by the scientific community and documented by the International Union of Pure and Applied Chemistry (IUPAC) and published in Sing *et al.* (1984):

Type I: Microporous materials (e.g. zeolites and activated carbon);

Type II: Non-porous and macroporous materials (e.g. non-porous alumina and silica);

Type III: Non-porous and macroporous materials with weak interactions between adsorbate and adsorbent (e.g. graphite/water);

Type IV: Mesoporous materials (e.g. mesoporous alumina and silica);

Type V: Porous materials having weak interactions with the adsorbate (e.g. activated carbon/water);

Type VI: Homogeneous surface materials (e.g. graphite/Kr and NaCl/Kr).

Nitrogen sorption is only suitable to characterize micro and mesopores. Furthermore, the specific surface area has to be greater than $1\,m^2 \cdot g^{-1}$. In the case of gamma-alumina supports, *Type IV isotherms,* which correspond to mesoporous materials, are usually observed.

When the adsorption and desorption curves follow a different path, the sorption isotherm is said to have a hysteresis loop. These hysteresis loops are linked to the capillary condensation that occurs in the mesopores and can be described by the Kelvin equation (I-11). Based on the hypothesis of the capillary condensation mechanism, Barrett, Joyner and Halenda (1951) were able to determine pore size distributions, leading to the so-called BJH method.

In the following sections, we present a brief description of the methods used to exploit physisorption data in order to estimate the specific surface area, the pore size distribution and the connectivity.

I.3.2.2 DETERMINATION OF THE SPECIFIC SURFACE AREA - BET METHOD

The theory proposed by Brunauer, Emmett and Teller (1938), known as the BET method, is based on the principle of multimolecular adsorption that is applied to the domains A to C (see Fig. I-7). The first layer formation mainly depends on the fluid-wall interaction while the formation of the following layers mainly depends on the fluid-fluid interactions.

In a first step, the physisorption data has to be translated into a BET plot that is assumed to be linear according to the BET model (Rouquerol *et al.*, 2014):

$$\frac{1}{\left[n^a\left(\frac{P_o}{P}-1\right)\right]}=\frac{1}{n_m C}+\left[\frac{C-1}{n_m C}\right]\left(\frac{P_o}{P}\right) \tag{I-6}$$

where n^a corresponds to the amount of gas adsorbed per unit of solid mass $(mol\cdot g^{-1})$ and n_m to the monolayer capacity per unit of solid mass $(mol\cdot g^{-1})$, C is an empirical constant indicating the order of magnitude of the adsorbent-adsorbate interactions. From the slope $\alpha=(C-1)/(n_m C)$ and the intercept on the *y* axis $\beta=1/(n_m C)$ of this plot, one obtains the monolayer capacity n_m and constant C:

$$n_m=\frac{1}{\alpha+\beta} \tag{I-7}$$

$$C=(\alpha+\beta)+1 \tag{I-8}$$

In the absence of other factors, for instance, the presence of microporosity or highly active sites, the BET plot applied to a Type II or Type IV isotherm is capable of providing a fairly reliable assessment of the monolayer capacity, as long as the curvature of the first plateau of the isotherm is distinguishable.

The second step consists in calculating the specific surface area that is obtained using the BET monolayer capacity, n_m:

$$s_{BET}=n_m\cdot N_A\cdot\sigma \tag{I-9}$$

with $s_{BET}(m^2 \cdot g^{-1})$ the specific surface area obtained from the BET method, $N_A(mol^{-1})$ the Avogadro number and $\sigma(m^2)$ the molecular cross-sectional area (average area occupied by each molecule in a monolayer). This parameter may be already known or estimated by other methods or even calculated from the density of the adsorptive in a bulk liquid state (Rouquerol *et al.*, 2014). Thus,

$$\sigma = f\left(\frac{M}{\rho \cdot}\right)^{2/3} \quad \text{(I-10)}$$

where f is a packing factor, ρ the density of the adsorptive liquid at the operating temperature and M the molar mass of the adsorptive. Nitrogen adsorption occurs at 77K and the value of $0.162\ nm^2$ is usually taken for σ (Emmett and Brunauer, 1938).

I.3.2.3 DETERMINATION OF PORE SIZE DISTRIBUTION – BJH METHOD

In the case of mesoporous materials, such as silica alumina supports, the pore size distribution can be obtained by using the desorption branch of the isotherm for relative pressures comprised between 0.4 and 1.0, according to the BJH method (Barrett *et al.*, 1951). It is admitted that each step of the desorption process at a given relative pressure P/P_o is due to two phenomena:

- liquid emptying of a category of pores having a radius lower than a radius r_K obeying to the Kelvin equation (I-11) that are condensed by capillarity and leaving behind an adsorbed film in the pore walls according to equation (I-12);
- desorption contribution from a category of pores already emptied and having a radius greater than r_K, where the thickness Δt of the adsorbed multilayer decreases.

Applying the Kelvin equation to the desorption branch and taking the hypothesis of cylindrical and open pores, Barret and his co-workers were able to obtain a quantitative analysis of porosity (Barrett et al., 1951). The Kelvin equation relates the pore dimensions to the vapour phase pressure that corresponds to the liquid-vapour equilibrium within the pore. For a cylindrical pore shape, the *modified Kelvin equation* is:

$$ln\left(\frac{P}{P_o}\right) = -\frac{f \cdot \gamma_o \cdot v_L \cdot \cos(\theta)}{R \cdot T \cdot r_K} \quad \text{(I-11)}$$

f is a shape factor, that takes the value of 1 for adsorption and 2 for desorption;

γ_o is the surface tension of the liquid-vapour interface and is equal to $8.85 \times 10^{-5} N \cdot cm^{-1}$ for nitrogen at $T = 77.4\ K$ (Bobin, 2010);

v_L is the molar volume of the adsorbate in the liquid state (for nitrogen $v_L = 34.65\ cm^3 \cdot mol^{-1}$);

θ is the contact angle between the liquid and the solid surface, which takes a maximum value of $90°$ during pore condensation;

r_K is the Kelvin radius which is related to the pore radius r_p by $(r_p - t)$, where t is the thickness of the adsorbed multilayer film (cf. Fig. I-9).

During desorption in a set of cylindrical mesopores with exactly the same radii r_p, it seems reasonable to assume that the condensate has a meniscus of hemispherical form and radius r_K. However, as some adsorption has already occurred, the thickness of the adsorbed multilayer needs to be accounted for, so that, r_K is smaller than r_p. If the thickness of the adsorbed multilayer is given by t, the radius of the cylindrical pore is:

$$r_p = r_k \cos(\theta) + t \tag{I-12}$$

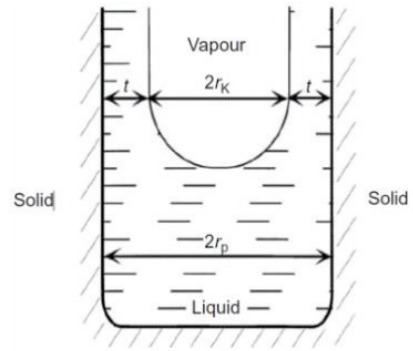


Fig. I-9. Schematic representation of the relation between the Kelvin radius, r_k and the pore radius r_p in a cylindrical mesopore (Rouquerol *et al.*, 2014).

The BJH method is therefore based on an adapted Kelvin equation in order to take into account a layer of adsorbed molecules, with thickness t. These adsorbed molecules are present on the pore's surface before capillary condensation takes place, but they are also present after the evaporation (Bobin, 2010). Given that for most liquid-solid systems the contact angle is low, it is generally assumed that $\cos(\theta) \sim 1$. We may therefore define the adapted Kelvin equation by:

$$ln\left(\frac{P}{P_o}\right) = -\frac{f.\gamma_o.V_L}{R.T.(r_p - t)} \tag{I-13}$$

In addition, there are also several correlations that were established experimentally for the layer thickness t. The most used correlations in the determination of the pore size are from Halsey presented in equation (I-14) and Harkins-Jura-de Boer (equation (I-15)) (Hammond and Conner, 2013).

$$t(nm) = 0.354\left(\frac{-5}{ln\left(\frac{P}{P_o}\right)}\right)^{1/3} \tag{I-14}$$

$$t(nm) = 0.1\left(\frac{13.99}{0.034 - log\left(\frac{P}{P_o}\right)}\right)^{1/2} \tag{I-15}$$

The two expressions for the layer thickness are compared in the following figure (Fig. I-10):

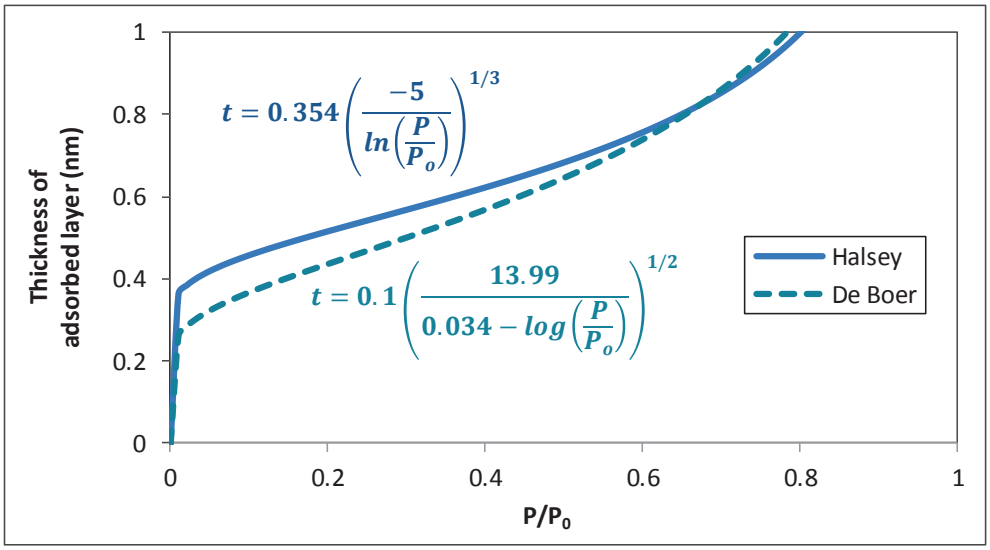


Fig. I-10. Adsorbed layer thickness as a function of relative pressure from Halsey and Harkins-Jura-de Boer works.

Knowing the adsorbed volume, the thickness t and the pore radius, as well as, assuming a cylindrical pore shape with $S_p = 2\pi r_p L_p = 2V_p/r_p$, one can determine the volume and surface of the different categories of pores.

On Fig. I-11 is represented the specific pore volume corresponding to $r_{p\,min} < r_p < r_{p\,max}$ for three catalyst supports.

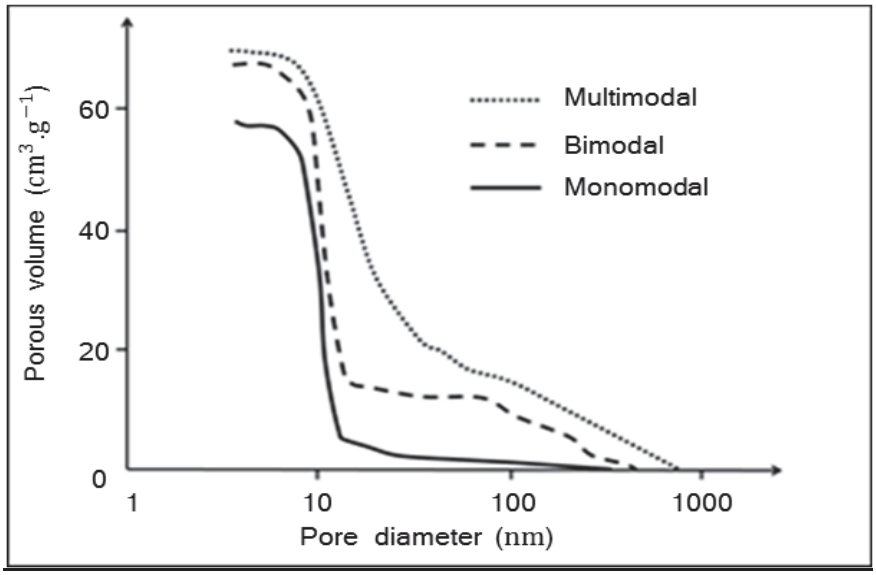


Fig. I-11. Specific pore volume of different catalyst supports used in hydrotreating. Adapted from Leprince (1998).

The quantity that is measured and represented on Fig. I-11 is in fact $v_p(r_p) = \int_{r_p}^{r_{p\,max}} PSD(r_p)dr_p$ so that, the *PSD* is obtained by taking the derivative of this

quantity. An example of a pore size distribution (*PSD*), obtained for a $\gamma - Al_2O_3$ support, used in hydrotreating applications, is presented on Fig. I-12.

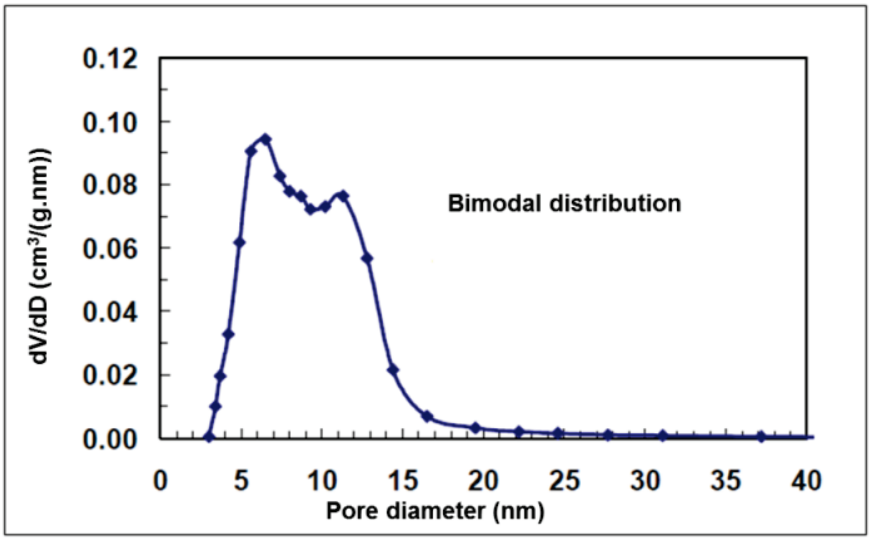


Fig. I-12. PSD obtained by the BJH method for a gamma-alumina support (Bobin, 2010).

From the PSD obtained by the BJH method, the total pore surface area per unit of solid mass s_{BJH} can be calculated and compared to the s_{BET} in order to get information on the shape and morphology of the pores present in the porous material:

- if $s_{BJH} \sim s_{BET}$: pores have a shape similar to that assumed in the BJH method, i.e. tubular pores opened at both extremities;
- if $s_{BJH} > s_{BET}$: pores may be of a cylindrical shape but closed on at least one of the extremities, or presenting constraining regions or of ink-bottle shaped. This situation is the most frequent;
- if $s_{BJH} < s_{BET}$: pores contain several spherical cavities. If the discrepancy is high, it may indicate the possibility of having a microporosity region.

Other approaches also exist, such as the Corrugated Pore Structure Model (Androutsopoulos and Salmas, 2000) which is dedicated to the *PSD* characterisation, using nitrogen hysteresis data and accounting for the evolution of the shape of the interface. This method was extended to estimate non-biased mass transfer tortuosity factor - τ_{CPSM} in Salmas *et al.* (2003).

I.3.2.4 SEATON METHOD FOR THE PSD AND CONNECTIVITY DETERMINATION

Different numerical approaches propose enhanced characterization models accounting for the connectivity factor, a factor that is left aside by conventional models. These models go beyond simple parallel and regular cylindrical pores.

The Seaton method (Seaton, 1991), used to determine the connectivity, is described here. This method is based on the use of both the desorption and the adsorption branches of the sorption isotherm for relative pressures comprised between 0.4 and 1.0.

The adsorption branch is used to determine the *PSD* by the method developed by Seaton and his co-workers (Seaton *et al.*, 1989) or conventional methods like the BJH method. On the other hand, a percolation model is applied to analyse the desorption branch. The simultaneous use of the two branches allows to determine the mean connectivity of the porous material as well as a characteristic dimensionless length of the micro/meso porous domains. As mentioned before, the connectivity is defined as the average coordination number i.e. on the total number of pores meeting at a junction.

The hysteresis phenomenon can be due to three mechanisms. It is either associated to thermodynamic effects, in the presence of a metastable liquid and at a pressure below the condensation pressure, or considered to be due to the curvature difference of the liquid-vapour interface between the condensation and the vaporisation and leading to factor 2 from the Kelvin equation (I-11). The third mechanism, the one studied by Seaton, is related to the interconnectivity of the network as illustrated in Fig. I-13.

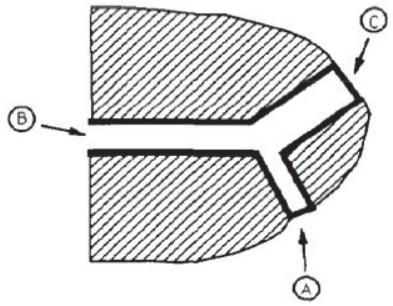


Fig. I-13. Illustration of the percolation theory. Taken from Seaton (1991).

Three pores A, B and C are supposed to be filled with liquid at the end of the adsorption branch. For the liquid to vaporize it must be in contact with the vapour phase (meniscus formation). If the three pores were in contact with the external surface, the order in which liquid nitrogen should vaporize is C, B, A when the pressure decreases according to the Kelvin equation. If only pore B is in contact with the external surface, the interconnectivity factor comes into play, and the sequence of vaporization will be: B at the vaporization pressure of pore B and C at the vaporization pressure of pore B, and finally, A at the vaporization pressure of pore A. The delay of pore C emptying will give rise to the hysteresis phenomenon.

As illustrated above, for emptying or vaporization to occur, a percolation threshold has to be reached within the pore network. This percolation threshold is characterized by the existence of a percolation cluster that is necessarily full of vapour. From that point of

view, each pore of the network can be occupied or non-occupied according to the following rules:

- a pore containing **liquid** nitrogen at an applied pressure greater than its condensation pressure corresponds to a **non-occupied bond**: it cannot participate in the percolation process;
- a pore containing **metastable liquid** or **vapour phase nitrogen** at an applied pressure inferior to its condensation pressure is an **occupied bond**;
- a pore containing a vapour phase is associated to an occupied bond belonging to the percolation cluster.

In the experimental isotherm taken from Seaton (1991) and given in Fig. I-14, different steps of desorption can be identified. At the relative pressure P/P_o of approximately 1, all pores are filled with liquid nitrogen. From A to B (Fig. I-14), only the pores located nearby the external surface can start evaporating followed by their immediate neighbours. At point B, a sufficient number of pores contain vaporized nitrogen in order to form the first percolation cluster, which crosses the entire catalyst particle. From point B to point C, desorption will occur, as shown in Fig. I-14. From point C onwards, all pores have access to the vapour phase via the percolation cluster, and the adsorption and desorption isotherms coincide.

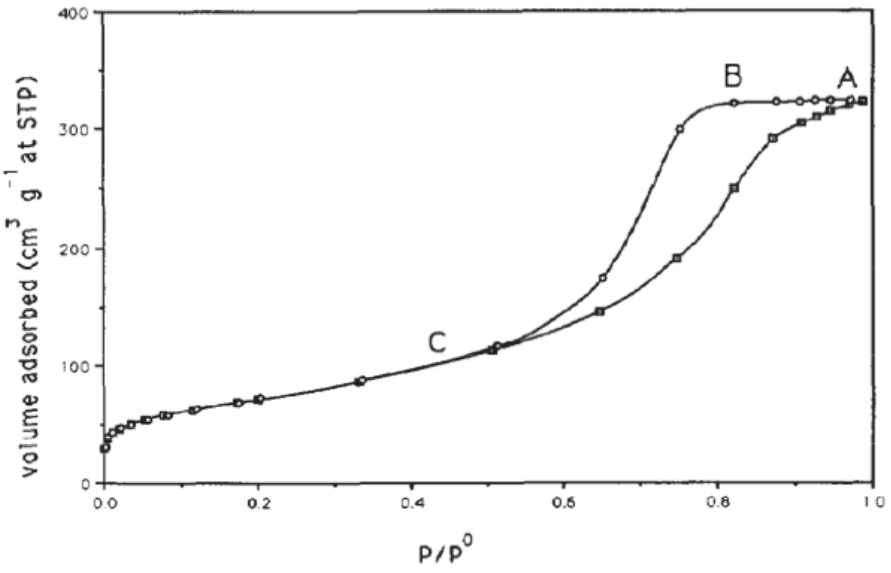


Fig. I-14. Adsorption and desorption isotherms for a silica alumina catalyst support (Seaton, 1991).

It should be stressed that Seaton's method is only consistent with *Type H1* and *Type H2* hysteresis. The percolation process is described by the following variables:

- f is the occupation probability that is calculated by the ratio between the number of pores which are submitted to a pressure below their condensation

pressure (that contain a metastable liquid or vapour phase) and the total number of pores;

- F is the percolation probability or accessibility that is calculated by the ratio between the number of pores from which nitrogen has vaporised and the total number of pores. Put otherwise, F is the probability for a pore to belong to the percolation cluster;
- Z_{avg} is the connectivity or mean coordination number, i.e. the mean number of bonds to which a node is connected;
- L is the average linear dimension of the micro/mesoporous structure.

Fig. I-15 represents the evolution of two main parameters derived from the percolation theory. A parallel can be made with the desorption branch presented in Fig. I-14.

From point A to point B (Fig. I-14 and Fig. I-15), f increases as the pressure is reduced but F remains equal to 0: percolation does not occur. At point B from Fig. I-14, a percolation cluster is formed by a pathway of metastable pores connected to the external surface of the catalyst, so that $F > 0$ and $f = f_{cluster}$. Between points B and C, f continues to increase as well as F since, the number of occupied bonds continues to increase by decreasing the applied pressure. A decompression of the liquid in the mesopores occurs, emerging the vapour phase in a few pores at the catalyst surface and pores with metastable liquid. When point C is reached, $F \longrightarrow f$ and $f \longrightarrow 1$: the percolation process is totally achieved.

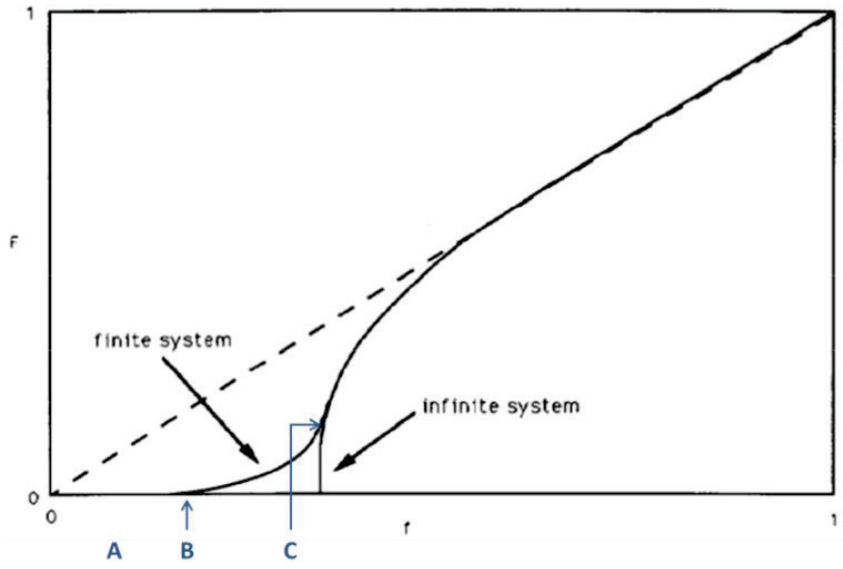


Fig. I-15. Variation of F (percolation probability) as a function of f (occupation probability) during desorption (Seaton, 1991).

In the literature devoted to the percolation theory, many models have been proposed to relate $Z_{avg}\,F$, the number of accessible connections, i.e. the number of connections that

belong to the percolation cluster and $Z_{avg}\, f$, the number of occupied connections, i.e. the number of pores filled with metastable liquid or vapour phase. Jarzbeski and Lorenc (1995), Uzio (1997) and Uzio and Euzen (2000) proposed the following relation on the basis of the work of Kirkpatrick (1973). Kirkpatrick's equation to determine $Z_{avg}\, F$ as a function of $Z_{avg}\, f$ is:

$$Z_{avg}\, \cdot F = Z_{avg}\, \cdot f \times tanh\left[h(Z_{avg}\, f)\right] \tag{I-16}$$

with the function $h\left(Z_{avg}f\right)$ using Kirkpatrick's equation for $Z_{avg}F$ dependence on $Z_{avg}f$

$$h\left(Z_{avg}f\right) = g_1(L) \cdot Z_{avg}\, \cdot f^{g_2(L)} + g_3(L) \tag{I-17}$$

where $g_1(L)$, $g_2(L)$ and $g_3(L)$ are polynomial functions that depend on L. The coefficients of these polynomial functions are then adjusted to match the experimental data. Stauffer and Aharony (1985) proposed another relation for $Z_{avg}F$ as a function of $Z_{avg}f$ near the percolation threshold, and for sufficiently large systems, which is given by:

$$L^{\beta/\nu} Z_{avg}F = h\left[\left(Z_{avg}f - \frac{3}{2}\right) \cdot L^{1/\nu}\right] \tag{I-18}$$

with the critical exponents, β and ν, taking the values of 0.41 and 0.88, respectively. However, in order to define the h function, this relation uses the universal relation between Z_{avg} and the value of f at the percolation threshold f_c, that is $Z_{avg}f_c = 1.5$.

The proposed characterization method is as follows (see also Liu *et al.* (1992), and Liu and Seaton (1994)):

1) Firstly, one determines the pore number distribution $n\left(r_p(P)\right)$ by using the adsorption branch. From this distribution, one can calculate the occupation probability $f(P)$ for each pressure P according to the pore size distribution:

$$f(P) = \frac{\sum_{r_p(\mathrm{P})}^{\infty} n\left(r_p(P)\right) dr_p}{\sum_0^{\infty} n\left(r_p(P)\right) dr_p} \tag{I-19}$$

where $r(P)$, is the pore size at pressure P_i at which nitrogen vaporizes and given by the Kelvin equation.

2) Secondly, for each pressure P, the ratio F/f is determined from the experimental isotherm according to the following expression (see Fig. I-16).

$$\frac{F(P_i)}{f(P_i)} = \frac{\overline{EF}}{\overline{EG}} \tag{I-20}$$

One should note that $f(P_i)$ is the number of moles that would vaporize if all pores at a pressure below their condensation pressure had access to the vapour phase. And so, it is also the number of moles required to fill pores, in which nitrogen

has not yet condensed at a given pressure, during the adsorption experiment. Regarding $F(P_i)$ it is the number of moles that were able to desorb to the detriment of the network connectivity (Liu *et al.*, 1992).

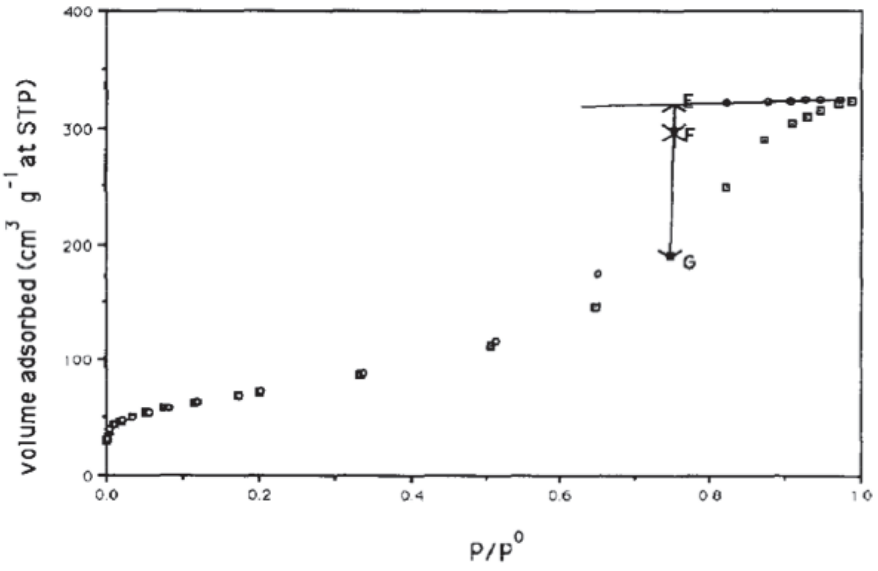


Fig. I-16. Illustration of $F(P)/f(P)$ determination.

3) The third step consists in obtaining the average coordination number Z_{avg} and the characteristic dimension L by fitting a model expressing $Z_{avg}F$ as a function of $Z_{avg}f$ to the experimental data $F(P_i)\ vs.\ f(P_i)$. From this set of equations, Z_{avg} and L are recursively obtained (see equations (I-16) and (I-18)).

For the isotherm curve presented in Fig. I-14/Fig. I-16, the fitting using equation (I-16) takes only into account the domain of application near the percolation threshold. This means that only experimental points where F is significantly different from 0 and from f are accounted for. For the isotherm presented in Fig. I-14/Fig. I-16, only the 3 data points between point B and C are in the valid range, $F(P_i) \neq 0$ and $F(P_i) \neq f(P_i)$.

I.4 CONCLUSIONS

From the SEM images, we are able to detect the major disorders present in the physical structure of alumina supports. This leads us to conclude that there is no easy way of replacing a complex porous structure by a simple geometrical representation that actually corresponds to the physical structure of alumina. It is also clear from the images presented that we are not in the presence of cylindrical pores, as it is generally assumed.

For the physisorption techniques, we concluded that they can be used to determine the structural parameters (*PSD*, surface area, porosity) of the porous solid. It should be stressed that the textural properties obtained always describe the catalyst from a pseudo-homogeneous viewpoint. Focusing on the Seaton model, that makes use of physisorption data, we may conclude that this model can be an important tool to extract

additional structural parameters for gamma-alumina samples, specifically the average connectivity of the porous catalyst.

CHAPTER II – MASS TRANSFER WITHIN POROUS CATALYSTS

This chapter is dedicated to the description of mass transfer phenomena that occur inside the pore structure of a catalyst particle. We first discuss the general phenomena occurring in the catalyst particle followed by a brief description of the most significant ones for this project. We also introduce the key models found in the literature to represent diffusion phenomena occurring inside porous structures, i.e. the well-known and largely used Fick's model and the Maxwell-Stefan model.

After identifying the main mass transfer properties used to characterise mass transfer through porous catalysts, we present some experimental techniques used for mass transfer properties estimation and determination.

II.1 DESCRIPTION OF THE MASS TRANSFER PHENOMENA

This section contains a short description of the mass transfer phenomena involved in a catalytic reactor at the particle scale. Enclosed mass transfer phenomena at the particle scale may be categorized into three main mechanisms:

- mass transfer resistance in the vicinity of the extrudates/particles external walls;
- diffusion in macro and mesopores;
- adsorption and surface diffusion.

A general schematic representation of these three mechanisms is illustrated in Fig. II-1:

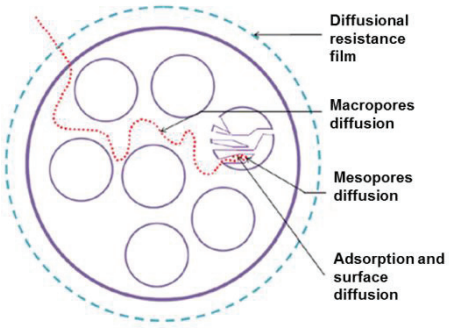


Fig. II-1. Illustration of the three mass transfer mechanisms present in a bimodal catalyst support. Adapted from Gaulier (2014).

II.1.1 EXTERNAL MASS TRANSFER

Before entering into the grain, molecules must be transferred from the bulk fluid to the surface of the catalyst particle. The corresponding mass transfer resistance is represented by the film model that is based on the assumption that the external mass transfer resistance is concentrated in the vicinity of the outer surface of the catalyst particles. This resistance is related to the hydrodynamic conditions prevailing in the catalytic reactor, as well as, to diffusion within the fluid. The i component flux is expressed as follows:

$$J_i = k_{if}(c_{i\ interface} - c_{i\ bulk}) \qquad \text{(II-1)}$$

with k_{if}, the external mass transfer coefficient of component i $(m \cdot s^{-1})$, $c_{i\,interface}$ and $c_{i\,bulk}$ respectively the fluid concentration of the i species at the grain outer surface and in the bulk phase.

II.1.2 DIFFUSION IN MACRO/MESOPORES - DIFFUSION REGIMES

The mass transfer phenomena occurring inside the porous catalyst particles depend on the physical and geometrical characteristics of the system. There are three different diffusion regimes: molecular diffusion, Knudsen diffusion and surface diffusion that may be combined with a viscous flow. The mass transfer by diffusion in porous media is a consequence of the molecule-molecules collisions and/or the molecule-wall collisions.

Both bulk/molecular and Knudsen diffusion regimes occur according to a serial arrangement of resistances (see Fig. II-2). In the case of a liquid phase, the resistance due to the wall is generally negligible (molecular diffusion) while it can be significant in the case of a gas phase. Indeed, this resistance can become the limiting step when the mean free path of the molecules (i.e. the average distance between molecular collisions) is large compared to the pore diameter – and is called Knudsen diffusion (Krishna and Wesseling, 1997).

Surface diffusion occurs in parallel with the molecular and Knudsen processes and its contribution to the total species flow may be quite significant within micropores, in the presence of strong adsorption. In those cases, the limiting diffusion is therefore the surface diffusion (Krishna and Wesseling, 1997). If a pressure gradient exists within the porous medium, a global convective flow can also exist, generally in the laminar regime, that acts in parallel with molecular and Knudsen diffusion mechanisms.

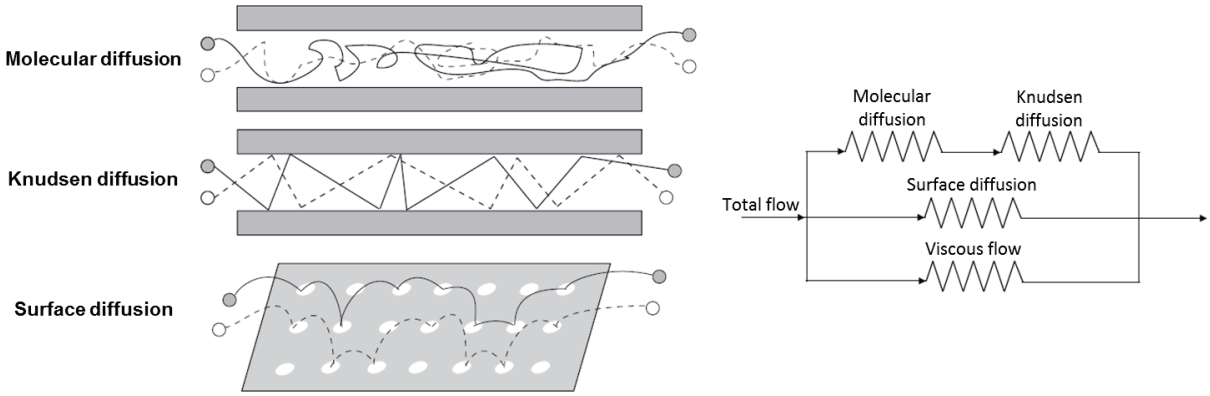


Fig. II-2. Representation of different mass transfer mechanisms in porous media and the equivalent electric resistivity scheme. Adapted from Krishna and Wesseling (1997).

In the framework of our project, the mass transfer data that we dispose, was obtained using representative molecules of different sizes (n-heptane and squalene) diffusing under molecular diffusion in a liquid phase over a gamma-alumina catalyst support (Kolitcheff *et al.*, 2017). Hence, the next subsection will be only dedicated to a brief description regarding the molecular diffusion regime, even though for very large molecules surface diffusion cannot be ruled out.

In conclusion, as our system is considered to be in the molecular diffusion regime, the mean free path of the molecules is small compared to the pore diameter and so, inter-molecular collisions are much more frequent than molecule-wall collisions. Therefore, one can consider that diffusion is only due to the Brownian motion of the molecules and to the geometrical properties of the porous media.

II.1.3 MODELLING THE MOLECULAR DIFFUSION PROCESS

In the following sections, two models are presented to describe isobaric diffusion transport, Fick's model and Maxwell-Stefan's model. At the end, a brief comparison of the two models is given, specifying their ranges of application and their flaws.

II.1.3.1 THE FICK MODEL

This model is often used due to its simplicity and is defined as follows:

$$J_i = -D_{im} c_t \nabla x_i \quad \text{(II-2)}$$

J_i, diffusive flux of the i species $(mol \cdot m^{-2} \cdot s^{-1})$;
c_t, total concentration $(mol \cdot m^{-3})$;
D_{im}, molecular diffusion coefficient of species i in the mixture $(m^2 \cdot s^{-1})$;
∇x_i, molar fraction gradient of species i.

In this model, it is assumed that the mass transfer driving force is the composition gradient, D_{im} representing the friction between species i and the remaining components of the fluid considered as a whole. It should be stressed that this model has been derived and should in principle only be applied to binary mixtures or at high levels of dilution of component i.

Within the framework of the Fick model, one can find some theoretical or empirical equations for the calculation of the Fick binary diffusion coefficients. In the case of large spherical molecules, highly diluted in a low molecular weight liquid solvent, the molecular diffusion coefficient can be estimated by the Stokes-Einstein equation (Krishna and Wesseling, 1997):

$$D_{im} = D_{AB}^{\infty} = \frac{k_B T}{6 \cdot \pi \cdot \eta_B \cdot R_h} \quad \text{(II-3)}$$

with,
D_{AB}^{∞}, Fick binary diffusion coefficient in a diluted solution $(m^2 \cdot s^{-1})$;
k_B, Boltzmann constant $(1.3807 \times 10^{-23} J \cdot K^{-1})$;
T, temperature of the system (K);
η_B, solvent viscosity $(kg \cdot m^{-1} \cdot s^{-1})$;
R_h, hydrodynamic radius of the solute molecule (m).

Wilke and Chang developed an empirical correlation for diluted binary solvent/solute liquid mixtures accounting for the steric hindrance of solutes and solvents, as well as an association parameter for the solvent (Chang and Wilke, 1955).

$$D_{im} = D_{\mathrm{AB}}^{\infty} = 7.4 \times 10^{-8} \cdot \frac{T \cdot (\Phi M_B)^{1/2}}{\eta_B \cdot {v_A}^{0.6}} \quad \text{(II-4)}$$

where,
Φ, dimensionless association coefficient of solvent *B*;
M_B, molar mass of solvent *B* $(g \cdot mol^{-1})$;
v_A, molar volume of solute *A* at its normal boiling point $(m^3 \cdot mol^{-1})$.

II.1.3.2 THE MAXWELL-STEFAN MODEL

Let us first consider a binary mixture at a fixed pressure. If the motion of components 1 and 2 is considered at steady state, the momentum balance equation of component 1 for example, can be written as follows (Krishna and Wesseling, 1997):

$$-\frac{1}{RT}\frac{d\mu_1}{dz}=\frac{x_2(u_1-u_2)}{Đ_{12}} \tag{II-5}$$

with μ_1 the chemical potential of species 1 of which the gradient accounts for a distance from equilibrium. The right-hand side of equation (II-5), where u_1 and u_2 are the diffusion velocities of the components, represents the friction force exerted on species 1 by species 2 characterised by the binary diffusion coefficient $Đ_{12}$. This friction force is proportional to x_2, the molar fraction of component 2 and to the relative velocity (u_1-u_2). Multiplying by x_1/RT and using the diffusion flux definition, $J_1=c_t x_1 u_1$ we obtain the momentum balance for species 1 expressed according to the diffusive fluxes:

$$-\frac{x_1}{RT}\nabla_{T,P}\mu_1=\frac{x_2J_1-x_1J_2}{c_tĐ_{12}} \tag{II-6}$$

Since by definition $J_1+J_2=0$, then equation (II-6) allows to calculate J_1. Equations (II-5) and (II-6) can be easily extended to any multicomponent mixture as follows:

$$-\frac{\nabla_{T,P}\mu_i}{RT}=\sum_{\substack{j=1\\ j\neq i}}^{NC}\frac{x_j\left(u_i-u_j\right)}{Đ_{ij}},i=1,\dots,NC \tag{II-7}$$

And, according to the diffusion fluxes and for a multicomponent ideal mixture:

$$-x_i\frac{\nabla_{T,P}\mu_i}{RT}=\sum_{\substack{j=1\\ j\neq i}}^{NC}\frac{x_jJ_i-x_iJ_j}{c_tĐ_{ij}},i=1,\dots,NC \tag{II-8}$$

Among equations (II-8), only $(NC-1)$ equations are independent. As a matter of fact, due to the Gibbs-Duhem equation and the fact that $Đ_{ij}=Đ_{ji}$, the following equation holds:

$$\sum_{i=1}^{NC}-x_i\frac{\nabla_{T,P}\mu_i}{RT}=0 \tag{II-9}$$

$$\sum_{i=1}^{NC}\sum_{\substack{j=1\\ j\neq i}}^{NC}\frac{x_jJ_i-x_iJ_j}{c_tĐ_{ij}}=0 \tag{II-10}$$

For an isothermal, isobaric diffusion process in an ideal multicomponent solution and taking a multicomponent mixture, we have:

$$\begin{aligned}&-c_t\nabla x=[B](J)\\&(J)=-c_t[B]^{-1}\nabla x\end{aligned} \tag{II-11}$$

where ∇x and (J) are the molar fraction gradient vector and diffusion fluxes vector respectively, and the $(NC-1)(NC-1)$ matrix $[B]$ elements are:

$$B_{ii} = \frac{x_i}{Đ_{iNC}} + \sum_{\substack{k=1 \\ k\neq i}}^{NC} \frac{x_k}{Đ_{ik}}$$
$$B^e_{ij(i\neq j)} = -x_i\left(\frac{1}{Đ_{ij}} - \frac{1}{Đ_{iNC}}\right) \qquad \text{(II-12)}$$
$$i,j = 1,2,\dots,NC-1$$

In the case of a non-ideal solution, a thermodynamic model of the mixture has to be used in order to express the chemical potential of each component.

II.1.3.3 MAIN FEATURES OF FICK'S MODEL

The substantial difference found comparing the Maxwell-Stefan model with Fick's model resides in the driving force that is used. The Maxwell-Stefan approach is based on a more realistic driving force, the chemical potential gradient and bases the mass transfer properties on irreversible thermodynamic considerations, whereas Fick's model uses a concentration gradient as driving force. Since thermodynamic equilibrium is driven by chemical potential, Fick's model is therefore less realistic.

Moreover, the Maxwell-Stefan diffusivities are clearly binary diffusion coefficients and are less dependent on concentration. The Maxwell-Stefan formulation also takes naturally into account the coupling effects between components. As far as the binary diffusion coefficients are concerned, it should always be remembered that the applicability of Fick's law is limited to binary mixtures or for a highly diluted component in a mixture. The extension of the Fick's model to multicomponent mixtures, that can take into account coupling between the fluxes and forces, is based on diffusion coefficients that are complex functions of the binary diffusion coefficients and of the solute composition (Bird *et al.*, 2007).

Despite all the constraints and warnings concerning Fick's model, it continues to be extensively used due to its simplicity.

On the opposite side, the Maxwell-Stefan model is thermodynamically consistent, since its driving force is the chemical potential. The Maxwell-Stefan diffusivities are clearly binary diffusion coefficients and are less dependent on concentration. The Maxwell-Stefan formulation also takes naturally into account the coupling effects between the various concentration gradients and fluxes. The main drawback resides in the resolution of the equations.

Since within the framework of this study, the main point is the geometrical representation of porous media, we will restrict ourselves to Fick's model.

II.2 EXPERIMENTAL CHARACTERISATION OF MASS TRANSFER PROPERTIES IN POROUS MEDIA

The characterisation of physical structures and the morphology of pores plays an important role in the determination of mass transfer properties since they lead to the definition of the effective diffusion coefficient in porous media. As mentioned before, several experimental techniques used in the determination of this mass transfer property can be found in the literature. Among them we can cite, the Pulsed Field Gradient Nuclear Magnetic Resonance (PFG-NMR) (Kortunov *et al.*, 2005) which is a microscopic technique. We can also cite macroscopic techniques that lead to an indirect estimation of the tortuosity (Shen and Chen, 2007): either measuring the diffusion coefficient of a chosen nonreactive species both, in free solution and in a porous material of known porosity, the Inverse Chromatography technique (Ruthven, 1984) - a time-consuming process, or relating the tortuosity to a measured quantity that is obtained from electrical resistivity measurements (Barrande *et al.*, 2007).

The results obtained from the so-called macroscopic and microscopic methods can be very different. Microscopic methods are based on the measurement of physical phenomena occurring at the molecular level. Macroscopic methods are, however, measuring an overall property.

Moreover, measurements by self-diffusion (PFG-NMR) and diffusive transport (Inverse Chromatography) lead to a difference in the expression of the relationship between the molecular diffusion and the effective diffusion, and hence on the tortuosity. When measuring the flux as in the case of the inverse chromatography, the correction by the accessible porosity is required. On the other hand, during a mean square displacement measurement, as it is the case of PFM-NMR, this correction is not necessary since the molecules are already in the accessible porosity.

II.2.1 EXPERIMENTAL MICROSCOPIC METHODS FOR DIFFUSION PROPERTIES

The microscopic methods that can be found in the literature are for instance, the PFG-NMR and the quasi-elastic neutron scattering (QENS). The QENS technique can measure both transport and self-diffusivities at individual pore space level, but requires a careful sample preparation exempted of water and a single component measurement. Concerning the use of the PFG-NMR technique, we can list several advantages (Mantle, 2010):

- simple sample technique;

- isothermal system;
- multicomponent systems are possible;
- spatial resolution is also possible.

It was shown that the PFG-NMR technique is able to estimate mass transfer properties that are comparable to those from the chromatography technique. However, the main disadvantage is the fact that with the NMR technique it is difficult to reach high temperatures and pressures. Also, commercial catalysts, containing paramagnetic metals, generally cannot be studied by PFG-NMR. Finally, the measured mass transfer properties are pure molecular self-diffusivities instead of transport diffusivities, since the measurements are performed at equilibrium conditions (under a system with no chemical potential gradient).

II.2.2 EXPERIMENTAL MACROSCOPIC METHODS FOR DIFFUSION PROPERTIES: INVERSE CHROMATOGRAPHY

Since we dispose a set of results obtained by the inverse chromatography technique, the following section will only be devoted to the description of this technique. The available results were obtained during a PhD thesis at IFP Energies Nouvelles (Kolitcheff, 2017) and focused on gamma-alumina supports used in hydrotreating processes.

One of the main advantages of the inverse chromatography technique is the wide temperature and pressure operating ranges that can be chosen close to reaction conditions. It can also be used with commercial catalysts and is a rather simple technique, when compared for instance to the NMR technique.

Inverse Chromatography is generally used to study the diffusion and adsorption process in porous media. The basis of this technique relies on the concentration outlet time response of a column filled with a porous material (fixed-bed) and initially at equilibrium, to a concentration perturbation of one component diluted in a carrier fluid applied at the inlet stream.

The propagation and deformation of a given perturbation along the column depends on the fluid velocity, as well as, on the equilibrium and transport properties of the porous material with respect to the component that is used. In the case of an inlet concentration step (see Fig. II-3), the outlet concentration time variation is called breakthrough curve. In this case, when the concentration perturbation completely leaves the column, the inlet and outlet concentrations become equal. The experiments are generally performed within the linear domain.

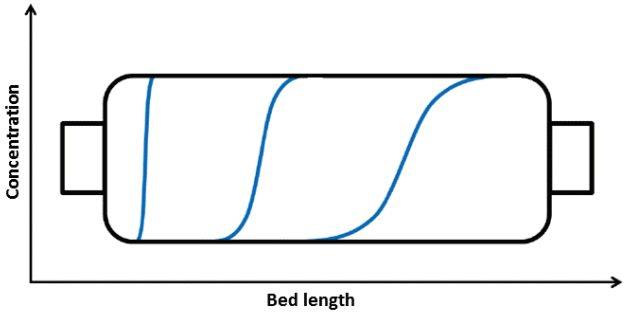


Fig. II-3. Schematic representation of a breakthrough curve – evolution in time and space of the radial average concentrations in the packed bed. Adapted from Kolitcheff (2017).

In order to extract the mass transfer and equilibrium parameters from breakthrough curves, one uses a linear dynamic model of the column (Ruthven, 1984). The moments technique can be used to obtain these parameters (Haq and Ruthven, 1986). With this technique, the transport and equilibrium parameters are obtained by matching the experimental moments to those obtained from the model. The models that are commonly used for the inverse chromatography technique are 1D models with respect to the axial coordinate of the column. Fig. II-3 represents the average radial concentration profiles as a function of time and axial position for a given column. As far as the porous medium is concerned, mono- or bi-disperse models are used depending on its structure (Ruthven, 1984).

During his PhD thesis, Kolitcheff (2017) used the moments method based on a mono disperse model: the expression of the first and second theoretical moments of this model have been derived previously (Haynes and Sarma, 1973). Then, in order to obtain the mass transfer properties, the plate theory of chromatography is employed relating the HETP to the first and second theoretical moments. It should be stressed, however, that the expressions of the theoretical moments are only known for some linear models (Ruthven, 1984). Hence, the experiments have to be performed within a linear response domain. If adsorption occurs, for example, the isotherm has to be linear with respect to the component fluid phase concentration.

II.3 CONCLUSIONS

Concerning the intra-particle mass transport, it should be stressed that, within the framework of our project, the diffusion process through macropores and mesopores is considered to occur according to the molecular diffusion regime. For the available experimental data, Kolitcheff showed during his PhD thesis that the experiments were indeed carried out under the molecular diffusion regime.

Assuming that the total concentration is uniform and that the diffusing species is highly diluted, Fick's model is going to be mainly used for the sake of simplicity.

Comparing Inverse Chromatography to NMR techniques has shown us that similar mass transfer properties can be obtained by both techniques. Yet, inverse chromatography is a more time-consuming technique. Even so, it has a wide application given its range of possible operating conditions, in contrast to NMR techniques that cannot be used under high pressures and temperatures. On the other hand, it must also be stressed that the main disadvantage of the Inverse Chromatography technique concerns the fact that its application to multicomponent systems is difficult.

CHAPTER III - IMPACT OF PORE STRUCTURE ON MASS TRANSFER PROPERTIES

The influence of the pore structure on mass transfer can be accounted for in two different ways: in a pseudo-homogeneous approach or discretely.

A pseudo-homogeneous description of mass transfer in porous media is based on a representation of the porous medium by a continuous pseudo-homogeneous system and requires the definition of global and average textural parameters, such as porosity and tortuosity. On the other hand, a discrete description can be based on the generation of a pore network or simply by accounting for the pore size distribution, as we will see further on (for instance on section III.2.1.2). But most importantly, the mass transfer modelling within the porous structure is based on the mass transfer description occurring within each pore of the network. Instead of using an effective diffusion coefficient as for pseudo-homogeneous representations, the discrete representation uses a molecular diffusion coefficient, thereby avoiding the use of the tortuosity factor as an adjustable parameter.

III.1 CONTINUUM APPROACHES

As we cite from Coppens and Bhatt (2017): "the most utilised representation for modelling phenomena in porous media are continuum models that do not explicitly consider the pores or the solid, but they average their impact on properties by way of effective values. For example, transport by diffusion and flow, with or without reaction, is modelled using partial differential equations (PDEs) over a continuum, bounded by the external surface of the medium, in which the transport and reaction parameters are

assumed to take effective values. These values account explicitly for porosity, but condense topological (connectivity) and morphological effects into a single parameter (for transport: tortuosity), which is assumed constant or could change over the spatial domain and over time (in case of dynamic processes, like catalyst deactivation). For anisotropic media, the effective properties could vary in different directions as well".

The conventional approach to account for the pore network on mass transfer properties considers a correction of the molecular diffusion coefficients. The Random Spheres Model (Toulhoat *et al.*, 2005; Rao and Coppens, 2012) used to describe mass transfer in hydrodemetallisation catalysts is one of the examples found in the literature that uses the somewhat different, but still conventional approach.

III.1.1 CONVENTIONAL APPROACH

First, in the description of mass transfer within a conventional approach, the concept of a continuous and pseudo-homogeneous medium requires to account for the macroscopic influence of the pore network morphology on the mass transfer properties.

Indeed, the solid structure introduces geometrical constraints to diffusion within the fluid phase that are conventionally accounted for by the particle porosity and by the so-called tortuosity factor τ. The latter is usually considered as an adjustable parameter in pseudo-homogeneous mass transfer models developed for porous media. When using a Fick or Maxwell-Stefan model for molecular diffusion, their diffusion coefficients must be corrected as follows in order to obtain the effective diffusion coefficient (Ruthven, 1984):

$$D_{i\,eff} = D_{im} \times \frac{\varepsilon}{\tau} \qquad \text{(III-1)}$$

with D_{im} $(m^2 \cdot s^{-1})$ the molecular diffusion coefficient, ε and τ, respectively the particle porosity and the tortuosity factor. Equation (III-1) is valid if it is assumed that the diffusing molecules have to cross the external surface area of the catalyst particle in order to access the pore volume. However, if it is assumed that the diffusing molecules are already inside the catalyst pore volume, then the catalyst porosity ε must be removed from equation (III-1) (see Appendix I for more details on this subject).

Regarding the tortuosity factor, it has been, over the years, extensively studied. The next section is devoted to the empirical and theoretical models that have been developed for the prediction of this feature.

III.1.1.1 THE TORTUOSITY FACTOR

The tortuosity factor can be defined in two different ways: either geometrically or by relating the flux to the driving force gradient. From a geometric point of view, the

tortuosity is given by the ratio between, the total length of the diffusion path of a species diffusing in a porous medium, and the straight-line distance between starting and finishing points. This geometric tortuosity factor therefore only depends on the support porosity and the network structure.

From the open literature, one observes that several correlations for the tortuosity factor give τ^2, the exponent 2 being related to the definition of a geometric tortuosity, which is given by $\tau = \sqrt{\frac{\Delta l}{\Delta y}}$, the square root of the ratio of the actual distance travelled by the species per unit length of the medium (Shen and Chen, 2007). For the sake of brevity and common usage among the chemical engineering community, the τ^2 will be addressed to as τ, the tortuosity factor.

However, it should also be highlighted that the path followed may depend on the diffusion regime, i.e. on the size of the diffusing particles or molecules compared to that of pores. Another definition of tortuosity therefore uses the true path length of diffusing particles. Hence, according to Barrande *et al.* (2007), the tortuosity factor is entirely linked to the ratio of the flux to the driving force with and without the presence of a porous medium:

$$\left(\frac{J}{DFG}\right)_{eff} = \frac{\varepsilon}{\tau}\left(\frac{J}{DFG}\right)_0 \qquad \text{(III-2)}$$

J is the transport variable as a flux of matter, velocity or current, DFG is the driving force gradient and the indices eff and 0 refer respectively to the measurement of the flux in the presence and in the absence of the porous solid.

Under a molecular diffusion regime, equation (III-2) is equivalent to equation (III-1). However, the extent of this equation is not constrained to the molecular diffusion regime. Indeed, it can be applied in the presence of Knudsen and surface diffusion, which implies that if the system is submitted to a variation of the operating conditions (temperature or pressure), the tortuosity factor changes, due to the fact that it will gather contributions from the variation of the operating conditions on the Knudsen and surface diffusivities. On the other hand, under a molecular diffusion regime, the measured tortuosity is similar to a geometric tortuosity and therefore only depends on the network porosity and organization.

The tortuosity is a parameter used in many fields such as, heterogeneous catalysis, medicine and rheology. According to Shen and Chen (2007), one of the approaches that can be found to indirectly measure tortuosity is based on measurements of diffusion coefficients of selected nonreactive species, both in free solution and in a porous medium. The methods using the diffusional characteristic times, can be divided in two

types, microscopic, such as Pulsed Field Gradient Nuclear Magnetic Resonance (PFG-NMR) (Kortunov *et al.*, 2005) and macroscopic, for example inverse chromatography.

The tortuosity factor is usually represented as a function of the porosity. The main theoretical relations available in the literature are listed below. The first three equations refer to the constraints that these models have to satisfy:

$$\tau \geq 1 \tag{III-3}$$

The constraint presented in equation (III-3) means that the actual (average) path crossed by the species while diffusing within the interstitial fluid in a porous medium is longer than in the absence of the solid. The second constraint implies no hindrance to diffusion in the absence of the porous solid:

$$\lim_{\varepsilon \to 1} \tau = 1 \tag{III-4}$$

The third constraint is related to the fact that diffusion mass transfer is not supposed to occur in the solid itself:

$$\lim_{\varepsilon \to 0} \tau = \infty \tag{III-5}$$

The fundamental **theoretical relations** developed and taken from Petersen (1958), Bhatia (1985), and Dykhuizen and Casey (1989), accounting for diffusion in porous media begin with the derivation of the tortuosity factor in dilute suspensions of particles of simple geometric shapes, i.e. a collection of randomly oriented capillaries cutting through a solid body. Maxwell (1873) dedicated his work to uniform spheres and Rayleigh (1892) to infinite cylinders normal to the direction of flow, leading respectively to the following expressions:

$$\tau = \frac{3 - \varepsilon}{2} \tag{III-6}$$

$$\tau = 2 - \varepsilon \tag{III-7}$$

Bhatia (1985), and Dykhuizen and Casey (1989) defined the tortuosity factor by $3/F$, where F depends on the angle between successive pores. If the successive steps are truly randomly oriented, or if we are in the presence of a regular lattice, or even if we are in the presence of randomly oriented cylindrical pores, *F*=1 and therefore:

$$\tau = 3 \tag{III-8}$$

On the other hand, if the pore size is distributed than $\tau > 3$. In the work of Bhatia (1985), it is mentioned that for capillary networks, factor *F* may actually depend on the pore lengths and diameters, as well as, on the connectivity of the network *Z*. For constant diameter and length, τ is given by:

$$\tau = 3\left(\frac{Z+1}{Z-1}\right) \quad \text{(III-9)}$$

Several other theoretical relations of tortuosity as a function of porosity have been proposed in the literature (Akanni and Evans, 1987; Shen and Chen, 2007). For example, systems of overlapping spheres, random arrays of freely overlapping cylinders and a mathematical description for heterogeneous catalysts taking two- and three dimensional porous structures where a large number of travellers walk throughout the structure, can be respectively retrieved from the works of Weissberg (1963), Tomadakis and Sotirchos (1993) and Beeckman (1990):

$$\tau = 1 - \frac{1}{2}\ln(\varepsilon) \quad \text{(III-10)}$$

$$\tau = 1 - \ln(\varepsilon) \quad \text{(III-11)}$$

$$\tau = \frac{\varepsilon}{1-(1-\varepsilon)^{1/3}} \quad \text{(III-12)}$$

Both equations (III-13) and (III-14) were obtained for the diffusion within gamma-alumina pellets and are respectively from the works of Wakao and Smith (1962) and Weisz and Schwartz (1962). In the work of Weisz and Schwartz (1962), the developed model takes the simulation of diffusion within a random cylindrical porous structure, and where the solid structure is represented by a random structure of overlapping spheres.

$$\tau = 1/\varepsilon \quad \text{(III-13)}$$

$$\tau = \sqrt{3}/\varepsilon \quad \text{(III-14)}$$

It should be stressed that these theoretical models are highly idealized and based on a given structure of the porous medium and that they do not contain any adjustable parameter.

Empirical correlations have also been proposed and may depend on one or several adjustable parameters, such as the ones proposed in the critical review from Shen and Chen (2007). With one adjustable parameter we can find the work of Iversen and Jorgensen (1993) dedicated to soils and catalysts:

$$\tau = \varepsilon + B(1-\varepsilon) \quad \text{(III-15)}$$

The work of Boudreau (1996) and of Weissberg (1963) dedicated to the diffusive transport in fine-grained sediments, proposed the following correlation:

$$\tau = 1 - C \cdot ln(\varepsilon) \quad \text{(III-16)}$$

where *B* and *C* are adjustable parameters, the default values being respectively equal to 3.79 and 2.02.

The main theoretical and empirical correlations are graphically represented in Fig. III-1. As we observe from Fig. III-1, the tortuosity globally decreases with the porosity. Within the framework of our project, the alumina is formulated by the crystallites stacking giving rise to aggregates. These aggregations are governed by the formulation conditions of the supports. In the case of random stacking, the relationships presented below (Fig. III-1) show that for porosities between 0.4 and 0.8, the associated tortuosity values should be comprised between 4.3 and 1.1. In the literature, however, for aluminas having the same porosity, values of tortuosity ranging from 1.8 to 7.1 are found (Carniglia, 1986). Moreover, the aluminas studied in the work of Kolitcheff *et al.* (2017) that have a porosity around 0.7, present values of tortuosity ranging from 2 to 3.

The works of Weisz and Schwartz (1962) and of Beeckman (1990) take a special interest due to their high values of tortuosity. For instance, the work of Beeckman (1990) is actually based on Monte Carlo simulations taking a large amount of travellers that go throughout a two- or three-dimensional porous structure. The underlying tortuosity calculated in this work implies a diffusional definition.

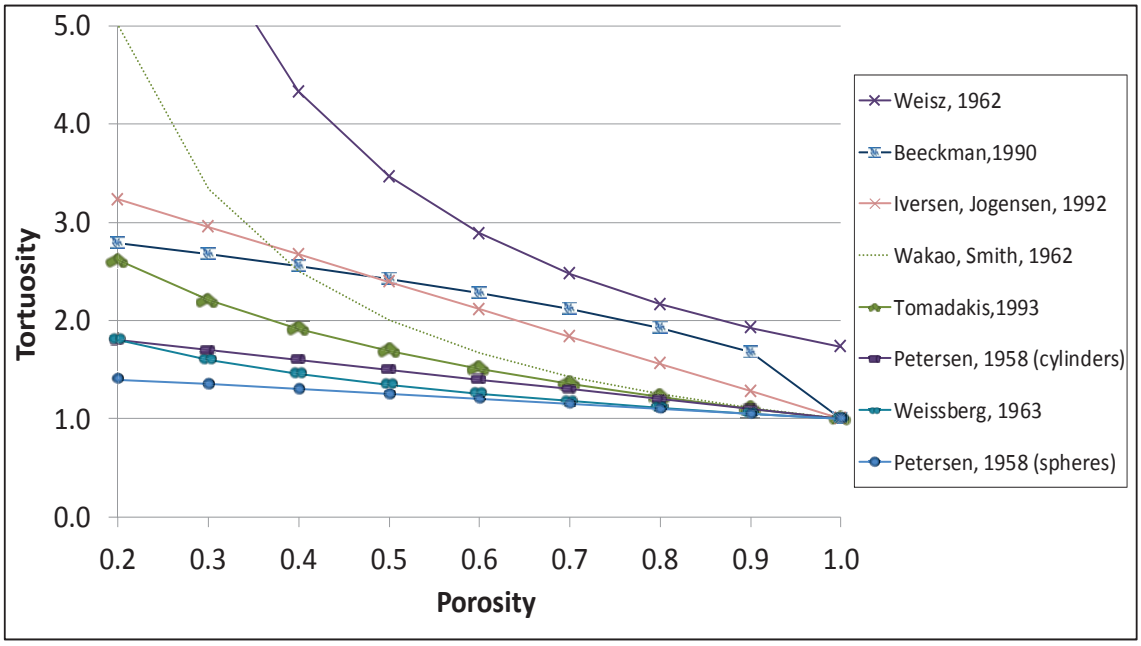


Fig. III-1. Tortuosity as a function of the porosity given by some theoretical models or empirical correlations.

As mentioned before, a special application of this conventional approach found in the literature to describe the influence of the morphology of the support on mass transfer properties in a continuous way is the Random Spheres Model. A brief description of this model will be presented below.

III.1.2 RANDOM SPHERES MODEL (RSM)

The random spheres model presented in Toulhoat *et al.* (2005) is inspired from the work of Weissberg (1963), and of Van Eekelen (1973).

In the work of Toulhoat *et al.* (2005), several porous catalysts were studied: the hydrodemetallisation (HDM) catalysts for instance, the chestnut bur with large meso and macropores, as well as hydrodesulphurization (HDS) catalysts.

In residue hydrotreating units, catalyst deactivation is very fast and is due to coking and deposition of metal sulphides, Ni and V sulphides. Hence, it strongly affects the intrinsic catalytic activities and the textural properties. To account for this major operating issue, any residue hydroprocessing simulator needs a description of the catalyst deactivation. The main idea of Toulhoat *et al.* (2005) consisted in providing a detailed description of the fresh catalyst and of the evolution of the catalyst during fouling. The schematic representation of porous media, subject to coking and to metal sulphide deposition is represented in Fig. III-2:

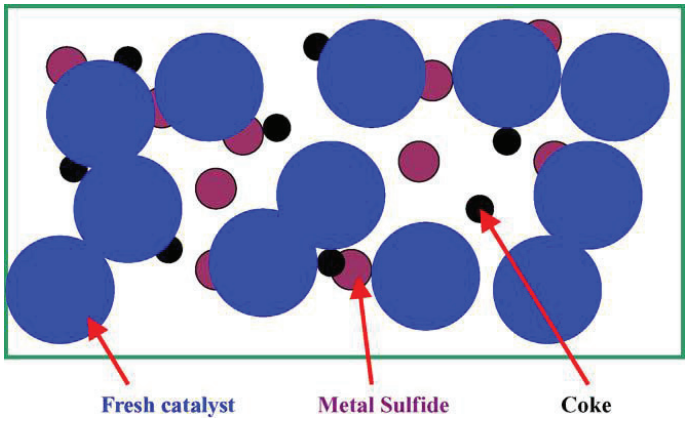


Fig. III-2. Porous media schematic representation considering catalysts ageing and superposing three different porous media: fresh catalyst (blue), metal sulphides (violet) and coke deposits (black) (Toulhoat *et al.*, 2005).

The first step consisted in finding a representation of the fresh catalyst. With the RSM model, proposed by Van Eekelen (1973), alumina platelets or alumina clusters are defined as spheres with a given particle radius and a volumetric density. The spheres are randomly positioned and allowed to overlap. For given values of these two parameters, the porosity and the surface area can be calculated. Subsequently, the appearance of coke and the deposition of metal sulphides create additional objects that reduce the available pore space, the available surface area and the average pore radius.

Intra-particle mass transfer is accounted for by Fick's model using a local effective diffusion coefficient $D_{i\,eff}$. This coefficient depends on the local porosity and the average pore radius. Both parameters were defined as a function of the amount of metal sulphides and coke locally deposited in the catalyst structure.

Numerous other applications of the RSM model can be found in the literature. In the work of Rao and Coppens (2012), a Random Spheres Model was constructed in order to take into account the deactivation of porous catalysts used in hydrodemetallisation processes.

III.2 DISCRETE APPROACHES - COMBINED DESCRIPTION OF PORE STRUCTURE AND MASS TRANSFER

Several approaches have been found in the literature combining the description of the porous structure of the pellet in a realistic way, and the multicomponent diffusion of reactants into and out of the pores of the catalyst support. The optimization of the pore geometry is an important tool to design a support with minimum diffusional resistances and leading to a higher catalyst performance. For that matter, in this section, we propose a brief review of the models used to investigate the transport in disordered porous materials using diffusion models at the single pore level. Besides the more correct description of mass transport, the following approaches account for the real porous structure taking their experimental textural data and constructing a pore network reproducing these features, in contrast to continuum models.

The following sections are hence dedicated to two different types of approaches, analytical and numerical approaches defining implicitly and explicitly the pore structure. With either, some methods that do not take into account the connectivity effect, such as the cross-linked pore network models, while other models are able to account for this network property: the effective medium theory, the Bethe networks, the Rieckman's approach and the Pore-Cor Model.

III.2.1 ANALYTICAL MODELS

Keil (1999) mentions the great amount of works dedicated to diffusion-reaction systems in pore networks. For instance, the random pore model developed by Wakao and Smith (1962) is dedicated to pellets containing a bi-disperse pore system. The pore structure of the pellets is simulated by an assembly of small particles. If these particles are allowed to contain pores, then both a macro and micro void-volume distribution exist. The drawback of this model is the absence of connections between pores. In fact, it is a refined version of a parallel pore model. An enhanced model was created by Johnson and Stewart (1965) that employs randomly oriented capillary axes that are cross-linked, as briefly described in the following section.

III.2.1.1 CROSS-LINKED PORE NETWORK MODELS

The model created by Johnson and Stewart (1965) represents the porous structure according to Fig. III-3.



Fig. III-3. Pore model developed by Johnson and Stewart (1965).

In their work, the flux in the *y* direction is obtained by averaging the flux in the pores over the void and solid area of the particle. For that matter, they use the pore size distribution and the inclination of each pore with respect to *y* likewise:

$$J_{Ay} = \int_0^{\infty} \int_0^{\pi/2} {J_{Ay}}^{p} \cdot f(\theta, r_p)\, d\theta dr_p \qquad \text{(III-17)}$$

where ${J_{Ay}}^{p}$ is the projection of the flux along a single pore in the *y* direction and J_{Ay} the macroscopic flux in the *y* direction. The inclination of pores is the phenomenon leading to the definition of the tortuosity factor as described in Friedman and Seaton (1995) and taking a value of 3. Even though in the latter a correction may be considered in order to take into account for the finite aspect ratio of the pores.

The Johnson and Stewart (1965) work was then extended by Feng and Stewart (1973). Indeed, equation (III-17) was put in 3 different working forms, based on various approximations of the diffusion integral for isotropic pore networks (i.e. randomly oriented), such as:

- 1st approach: uniform pore radius;
- 2nd approach: the tortuosity is independent of the pore radius;
- 3rd approach: the integral from equation (III-17) is reduced to a summation.

Their results infer that the 2nd approach is the less accurate, the 3rd approach being the most reliable and recommended for accurate work. Even though the 1st approach is less accurate than the 3rd one, it is mentioned that it gives shorter computation times.

III.2.1.2 EFFECTIVE MEDIUM THEORY

The effective medium theory (EMT) adapted by Kirkpatrick (1973) to electric resistivities is here discussed. It offers a convenient route to model transport in disordered mesoporous materials, while considering the entire pore size distribution, by replacing the actual pore network with an effective one, having a uniform conductance in each pore. One advantage of this method is that it enables a rigorous analysis of the relationship between apparent tortuosity and the pore structure, as well as, properties of the diffusing fluid taking a special interest on the network connectivity.

In the work of Gao *et al.* (2014), the EMT was implemented for the case of diffusion in a gaseous phase. First, for a pore radius r_p, the conductance λ is defined as the ratio of the molecular current to the driving force (pseudo-bulk density gradient), i.e.:

$$\lambda = \frac{\pi \cdot {r_p}^2 \cdot D_{im}(r_p) K(r_p)}{L_p} \tag{III-18}$$

with $D_{im}(r_p)K(r_p)$ the apparent diffusivity where *K* is the equilibrium constant based on the relevant pore radius.

Taking as hypothesis, the independence of the bulk pressure drop on the pore size, the effective medium conductance λ_{eff} is given by the solution of:

$$\left\langle \frac{\lambda - \lambda_{eff}}{\lambda + (Z_{avg}/2 - 1) \cdot \lambda_{eff}} \right\rangle = 0 \tag{III-19}$$

with $\langle\ \rangle$ an average over the pore number distribution, Z_{avg} the mean coordination number or connectivity of the network.

After having determined the effective medium conductance, Gao *et al.* (2014) are able to estimate the pore flux by the given equation:

$$J(r_p) = \frac{\lambda_{eff} \cdot L_p}{\pi \cdot {r_p}^2 \cdot R \cdot T} \times \left(\frac{Z_{avg} - 1}{Z_{avg} + 1}\right) \times \overline{cos^2(\theta)} \times \left(-\frac{dP}{dy}\right) \tag{III-20}$$

with R the ideal gas constant, y the coordinate along the macroscopiccontinuum flux direction, $\left(\frac{Z_{avg}-1}{Z_{avg}+1}\right)$ stands for a correlation effect due to the finite possibility that a diffusing molecule re-enters a pore that it has just left, cf. Bhatia (1995), and $cos^2(\theta)$ accounts for the orientation of pores depending on the pore aspect ratio $x = r_p/L_p$.

Upon integration over the pore volume of equation (III-20), it results:

$$J = \frac{\varepsilon \cdot \lambda_{eff} \cdot \langle L_p^2 g(x) \rangle}{\pi \cdot \langle {r_p}^2 L_p \rangle \cdot R \cdot T} \times \left(\frac{Z_{avg} - 1}{Z_{avg} + 1}\right) \times \left(-\frac{dP}{dy}\right) \tag{III-21}$$

with $\overline{cos^2(\theta)} = g(x) = 1 + \frac{4x}{3(1+4x^2)} - \frac{2}{3(1+4x^2)^{0.5}}$

Comparing with experimental data based on $D_{i\,eff}$ at a mean pore radius yield on equation (III-22) an apparent tortuosity can be easily obtained, like so:

$$J = \frac{\varepsilon \cdot D_{im}}{\tau_{app} \cdot R \cdot T} \times \left(-\frac{dP}{dy}\right) \tag{III-22}$$

$$\tau_{app} = \frac{\pi \cdot \langle {r_p}^2 L_p \rangle \cdot D_{im}}{\langle L_p^2 \cdot g(x) \rangle \cdot \lambda_{eff}} \times \left(\frac{Z_{avg} + 1}{Z_{avg} - 1}\right) \tag{III-23}$$

An interesting study performed under the Knudsen regime for different temperatures and network connectivities, to study the impact on the apparent tortuosity factor, is available

in the work of Gao *et al.* (2014). They observed very high values of the tortuosity factor, up to a value of 12.

III.2.2 NUMERICAL MODELS

In order to account for the influence of the morphology of the porous structure on mass transfer properties, a representative pore network is created. The mass transfer is then described within the representative simulated pores. Several models are presented below: the Bethe networks, the Rieckman's approach and finally, the Pore-Cor model.

Many other models could be cited for instance, a recent one proposed by Ye *et al.* (2017) that is also based on a construction of a pore network. In their work, the pore network is cut in the desired shapes of the catalysts and so, it is capable of explicitly accounting for the pore network topology and for the pore connectivity. The pore networks have been simulated with mass transfer and reaction for a network size of 1152 nodes around 10×10×10. The effectiveness factor for different catalyst shapes was compared.

III.2.2.1 BETHE NETWORKS

Another interesting representation of porous structures is that of random pore networks (Bethe networks), first introduced by Beeckman and Froment (1980) and Reyes and Jensen (1985), see Fig. III-4.

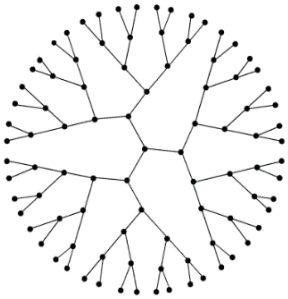


Fig. III-4. Bethe lattice pore network representation.

In Bethe networks, a well-defined topological network is the departure point. The network created is then modified to match the porosity and pore size distribution of a given structure. Bethe networks consist of infinite branching trees and are fully characterised by a mean coordination number or connectivity Z_{avg} (Fig. III-5).

These random Bethe networks are therefore able to reproduce many of the properties of more complex three-dimensional model structures. In particular, the remaining fraction of the original branches reflects the experimental porosity, and the pore size distribution function is given by the experimentally measured pore size distribution. The connectivity Z_{avg} remains to be specified, but it could be either used as an adjustable parameter or experimentally obtained by the Seaton method (Seaton, 1991) for instance.

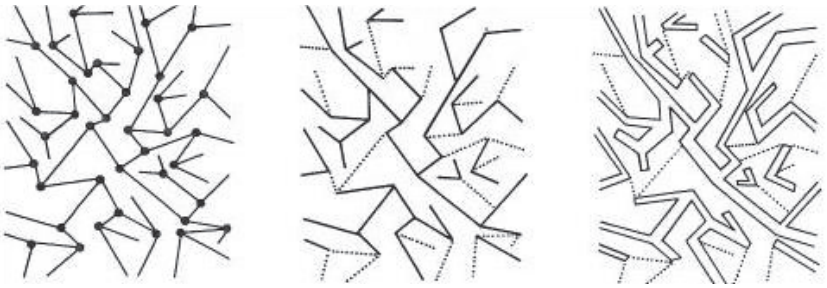


Fig. III-5. From the left to the right: Bethe lattice with Z=3; related Bethe network having a fraction of bonds randomly removed; coordinated Bethe network with arbitrary values of porosity and pore sizes (Becker and Pereira, 1993).

In addition, a very useful property of Bethe networks is that they exhibit classical percolation behaviour: a minimum fraction of bonds or percolation threshold is required to find a connected path spanning a large region of space – percolation threshold. This can be related to the connectivity factor by the following expression:

$$f_c = \frac{1}{Z_{avg} - 1} \tag{III-24}$$

As mentioned before, the percolation threshold gives the minimum fraction of bonds required for the network to have macroscopic transport. Stated otherwise, we could say that f_c is a measure of the interconnectivity between the pores of the network.

Similarly, to the Seaton's method, the Bethe network is able to quantify the pore accessibility within the network. With, the accessible porosity that is the fraction of pores in the network that can be reached from a distant peripheral location.

The description of mass transfer using the Bethe network is based on the evaluation of a continuum effective diffusion coefficient in a porous solid, with a given porosity and average connectivity, and by integrating single pore diffusivities over all accessible pores present in the network structure (Reyes and Jensen, 1985; Becker and Pereira, 1993).

III.2.2.2 RIECKMAN AND KEIL'S APPROACH

The model constructed by Rieckmann and Keil (1999) can be divided in two main parts: description of the pore structure and definition of mass transfer through the network. First of all, the definition of the pore network was obtained by representing a 3D random cubic network (Fig. III-6). Different aspects are taken into account: the type of pores, type of pore walls (e.g. smooth or fractal), the effect of connectivity, local heterogeneities, distribution of active centres, time-dependent changes and percolation phenomena (Rieckmann and Keil, 1997). This part of the model adopts a predefined pore radii and porosity distributions meeting experimental data obtained via nitrogen

physisorption or mercury porosimetry and a connectivity factor obtained by the Seaton's method.

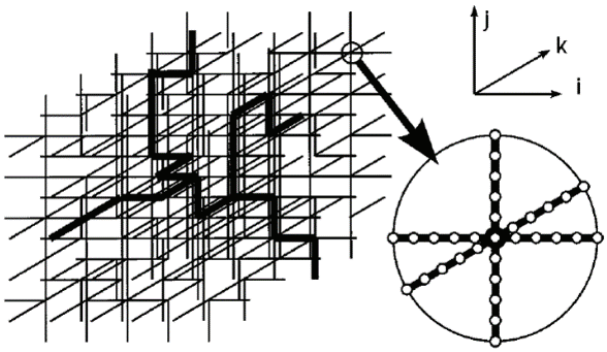


Fig. III-6. Discretization of the pore network (Rieckmann and Keil, 1997).

Concerning mass transport occurring in the porous medium, its description is based on the dusty-gas model for each pore and with an enhanced factor regarding the chemical reactions (Krishna and Wesseling, 1997). The dusty-gas model comprehends the description of both the molecular diffusion, the Knudsen diffusion, the surface diffusion and finally, the viscous flow. In the work of Rieckmann and Keil (1999), they used power-law rate equations, as well as Langmuir-Hinshelwood or Eley-Rideal equations to model the chemical reaction rates.

In the work of Rieckmann and Keil (1999), the pores are connected at the nodes, where it is assumed that no chemical reaction neither adsorption nor accumulation occurs. So, the overall balance in a node must be equal to 0. It should be noted that inner and outer surface nodes have specific boundary conditions. In order to solve the mass balance equations within the entire network, the mass balance equations for individual pores have to be solved simultaneously, since these mass balances are coupled by the boundary conditions at the nodes of the network. In their work, Rieckmann and Keil (1999) were able to simulate mass transfer within a grid of 30×30×30 network size averaged over 10 realisations to compare calculated to measured concentrations, in order to validate their model.

III.2.2.3 PORE-COR MODEL

The "Pore-Cor" network model has been used to model a range of materials such as soil, sandstone, catalysts and paper coating (Johnson *et al.*, 2003; Spearing and Matthews, 1991; Laudone *et al.*, 2005). It represents the void structure of a porous medium as a series of identical interconnected unit cells with periodic boundary conditions. Each unit cell comprises an array of 1000 nodes equally spaced in a Cartesian cubic-close-packed array, i.e. a 10×10×10 network. Cubic pores are positioned with their centres at each node, and are connected by smaller cylindrical pores (Fig. III-7).

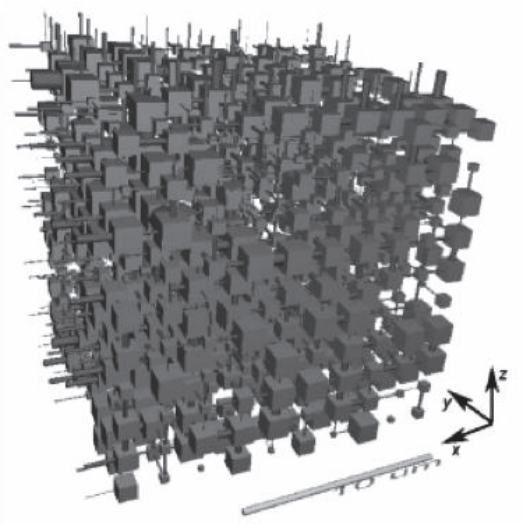


Fig. III-7. Usual cell unit obtained from the Pore-Cor model (Laudone *et al.*, 2008).

In the work of Spearing and Matthews (1991), 1000 cubes configured in a $10 \times 10 \times 10$ array and connected by a network of cylinders in 3D were used. The model was able to quantify the essential features of a porous material, the surface area, porosity and the pore size distribution from mercury porosimetry experiments. It can also quantify the tortuosity factor and the connectivity.

To describe the pore network, the lengths and radii of the pores must be known. The model uses a specific pore size distribution obtained experimentally, going from the larger size to the lowest from the limits of the mercury porosimetry curve. Diameters are considered uniformly spaced from 1 to $100\,\mu m$. The pore size distribution can be skewed by a parameter known as "pore skew". These 100 radii sizes are then assigned randomly to the total amount of pores. The largest pore intersecting a given node then determines the node size (cube size). As the pore size governs the cube size, there is at least a strong correlation between node and pore sizes for any particular cube (node).

In order to model the void spaces of the pore network, the Pore-Cor model reproduces the experimental percolation phenomenon within the sample during mercury porosimetry experiments by fitting the simulated characteristics with the mercury intrusion experimental data (Johnson *et al.*, 2003; Laudone *et al.*, 2007). To construct a realistic pore network, a best-fit is obtained for the values of four geometric modelling parameters included in a distance function between two neighbour data points, from the simulated and the experimental mercury intrusion curves (Johnson *et al.*, 2003). To this end, node and pore size distributions, specifically the node and pore skew, the connectivity factor and a correlation between nodes and pores sizes are used (Laudone *et al.*, 2007):

- the connectivity, the coordination numbers of the nodes may vary from 0 to 6 and the connectivity factor is generally lower than 5, often taking the value of 3 (Laudone *et al.*, 2005; Bobin, 2010);
- pore skew, defined as the percentage of pores of the smallest size in a distribution of 100 sizes which is linear when plotted on a logarithmic size axis;
- the node skew, which is a sort of a shape-scaling factor that bulks up the sizes of the nodes (cubes) to achieve the experimental porosity;
- the correlation level between nodes and pores sizes is also fitted. The pore lengths are determined by the distance between the node edges that they connect. These distances are determined not only by the node size, but also by the spacing between the row of nodes, which is determined by equalizing the simulated to the experimental porosity.

In order to adjust the simulated to the experimental porosity, the spacing of the nodes is varied. This means that the length of the pores joining the nodes is varied while keeping the node sizes and pore diameters unchanged.

The modelling of diffusion from simulated pore structures obtained from the Pore-Cor model was also tested and one of these cases is described in the work of Laudone *et al.* (2008). The diffusive flux of species *A* through a single cylindrical pore of length l and radius r is given by Fick's model, being the concentration profiles obtained via the resolution of a one-dimensional diffusion problem. However, in the work of Laudone *et al.* (2008), the mass transfer description was not compared to experimental data.

It must be mentioned that at IFPEN (Bobin, 2010), alumina supports were simulated using the Pore-Cor model, starting from mercury porosimetry experiments and using the Pore-Cor model to obtain Z_{avg} and τ. From the latter study, the influence of the four Pore-Cor parameters on the steepness of the simulated mercury intrusion curve was confirmed. At IFPEN, the Seaton's method was also tested to quantify L and Z_{avg} with the help of physisorption data.

III.3 CONCLUSIONS

The use of a discrete representation of the pore network with modelling mass transfer by diffusion within each pore (either using the Fick or the Maxwell Stefan model, the latter being a more realistic approach) appears to be the preferred method for representing the influence of the topoly of porous catalysts on mass transfer (Keil, 1999).

As stated before, the random spheres model gives a continuum description of the influence of the solid morphology on mass transfer properties, even though a local

effective diffusion coefficient, a local porosity and a local pore radius are used. It is therefore of less interest when it comes to compare this model with a discrete approach. As mentioned in the first section of this chapter, a discrete representation of the pore network of a given solid would be more realistic and is more helpful in the understanding and the optimization of the structure of the gamma-alumina supports. As stated by Keil (1999), a discrete approach is preferable for such a study in comparison to a continuum approach.

Concerning the analytical methods from the discrete representation, the Johnson and Stewart (1965) model was a first introduction for the account of the network phenomena related to the different pore sizes and to the orientation of pores, nevertheless the connectivity phenomena is not studied. On the other hand, the effective medium theory, accounts for both phenomena related to the different pore sizes, the orientation of pores and the connectivity over the pore structure. In the work of Gao *et al.* (2014), they were able to estimate a tortuosity factor, even though extremely high values for the tortuosity factor are found.

Concerning the Bethe network, we should underline the use of percolation concepts and the fact that it is a discrete approach based on diffusivities obtained from single cylindrical pores.

Rieckmann and Keil (1999) proposed a very inspiring work in terms of the creation of a pore network accounting for the connectivity of the system. The way the pore structure meets the characteristics of a real solid is also highly relevant. However, in their work, only the pore size distribution is fitted. The description of mass transfer in this approach uses the Dusty Gas model to simulate the pore network. This allows to accurately predict mass transfer phenomena occurring inside the particle grains of a catalytic reactor.

Concerning the Pore-Cor model, the simulation of a pore network of cubes and cylinders closely matches data, such as porosity and percolation properties, obtained experimentally by mercury porosimetry. Diffusion is well simulated in the work of Laudone *et al.* (2008) for a given porous material taking this discrete approach but still, not compared to available experimental data.

The present work is very similar to this kind of models that, as we have seen, are able to correctly account for both textural and mass transfer properties. The developed model is based on the Rieckman's approach. Indeed, in order to represent the pore structure of gamma-alumina supports, an algorithm capable of generating random pore networks of interconnected cylindrical pores is developed and mass transfer by diffusion is simulated within each pore of the network. The main goal of the developed tools is to reproduce the textural features and the tortuosity of actual aluminas.

DESCRIPTION OF THE MODELS

CHAPTER IV - PORE NETWORK MODEL: MONTE CARLO ALGORITHM AND MASS TRANSFER DESCRIPTION

IV.1 INTRODUCTION

In this chapter are described the numerical tools used within the framework of the Ph.D. thesis. A first tool is used to generate random pore networks by means of a Monte Carlo algorithm. Then, a second tool is used to simulate transient mass transfer within the network by considering one-dimensional diffusion within each pore of the network.

The Monte Carlo algorithm generates pore networks in order to represent the textural structure of gamma alumina supports. The pore network is constituted by interconnected cylindrical pores. The textural properties such as the specific surface area, the pore volume and the catalyst porosity are calculated.

A second tool is dedicated to the 1D transient simulation of mass transfer through each single pore of the pore network. Diffusional mass transfer description either using the Fick model or the Maxwell-Stefan model is possible. From this model, we are able to extract an effective diffusion coefficient that can be compared with experimental data obtained from fixed bed tracer experiments (Kolitcheff, 2017) as well as, with available information in the open literature. On the following figure (Fig. IV-1), a schematic description of the process of generating, treating and simulating mass transfer within the pore networks is provided.

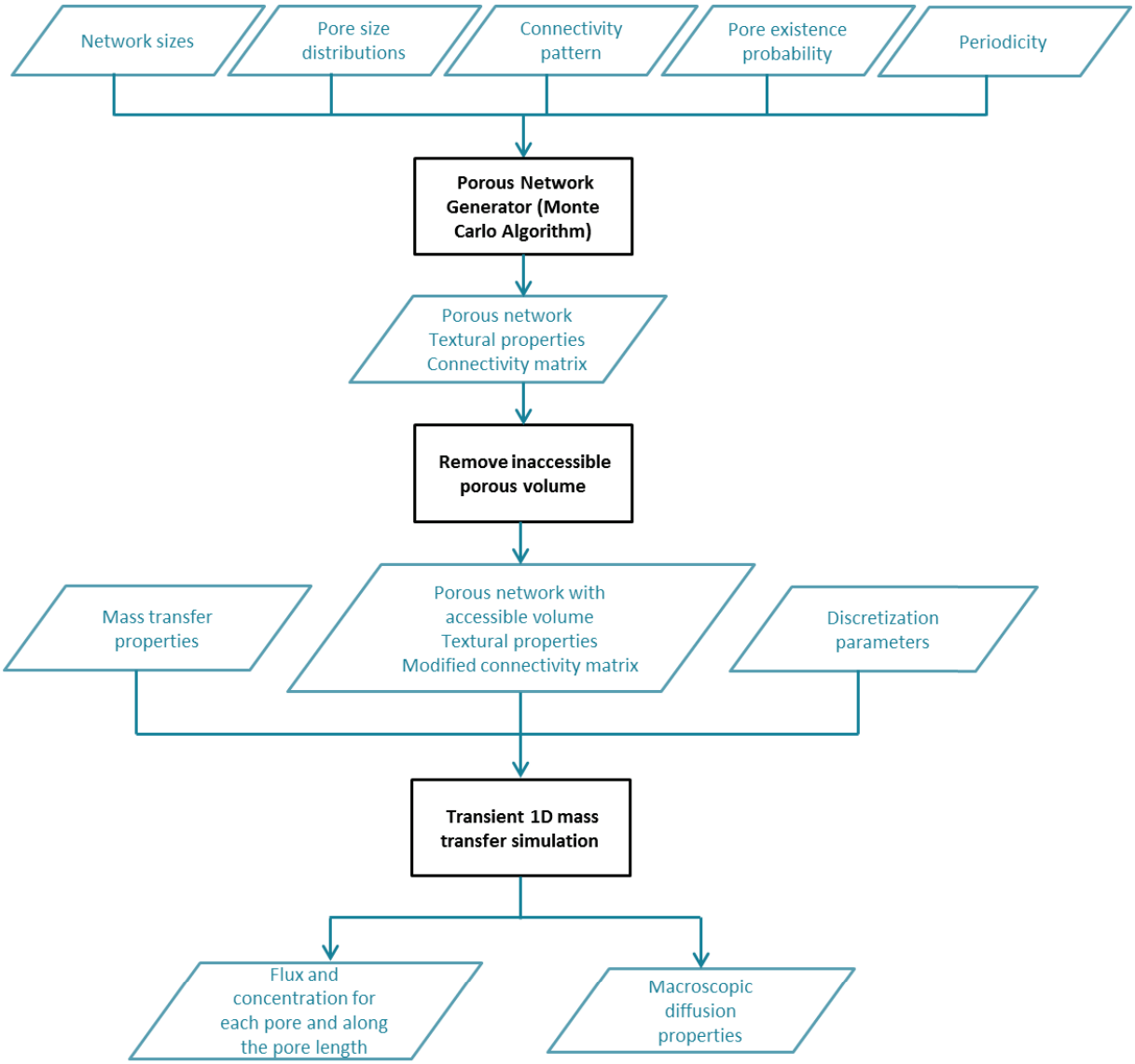


Fig. IV-1. Flowchart describing the pore network modelling process from its generation and treatment to mass transfer simulation.

IV.2 RANDOM PORE NETWORK GENERATION

The network is structurally constituted by interconnected cylindrical pores of given diameter and length. The generation is based on the following inputs: the network sizes, a connectivity pattern, pore diameter and pore length distributions and finally, a pore existence probability, P, that defines if a given pore exists based on a generated random number. The pore connectivity pattern repeats an elementary unit of pore connections along the network and gives the maximum number of pores connected to a node.

The initial condition of the network is a pre-defined grid of nodes positioned in 2D or 3D, with N_x, N_y and N_z nodes along each axis, resulting in a maximum number (or initial number) of nodes in the network of $N_x \times N_y \times N_z$.

A Monte Carlo algorithm walks through the grid and randomly creates pores based on the connectivity pattern and on the pore existence probability. At a given node, a random number uniformly distributed between 0 and 1 is drawn for each initially connected pore (given the connectivity pattern, see section IV.2.1) in order to determine whether the pore is retained in the network. The existence of a given node is thereby a consequence of the connection of at least one pore. Given the pore size distributions specified as input, a randomly drawn diameter (D_p) is attributed to each existing pore. While the developed algorithm also allows randomly drawing a pore length for a distribution, in this work, we restrict ourselves to the case of a fixed pore length (L_p).

The following table (Table IV-1) illustrates the role of the connectivity pattern. For each configuration, we define the vectors that constitute the connectivity pattern and that will reproduce different pore network configurations, when repeating the elementary unit. The connectivity pattern will dictate the maximum connectivity of the network. For instance, if we take a 2D configuration for square networks, each node is initially connected to 4 pores corresponding to a maximum coordination number of Z_{max}=4.

Table IV-1. Examples on how the connectivity pattern works.

Configuration	Vectors (x,y,z)	Elementary unit	Pores configuration
1D Z_{max}=2	(1,0,0)		
2D Z_{max}=4 (squared)	(1,0,0) (0,1,0)		
2D Z_{max}=6 (triangular)	(1,0,0) (0,1,0) (1,1,0)		
2D Z_{max}=8	(1,0,0) (0,1,0) (1,1,0) (-1,1,0)		
3D Z_{max}=6 (cubic)	(1,0,0) (0,1,0) (0,0,1)		

By changing the connectivity pattern, we can therefore generate different types of pore networks in 2D (square, triangular, hexagonal) or in 3D (simple cubic, body-centred cubic, face-centred cubic, diamond, tetrahedral), each having a different maximum connectivity Z_{max}.

The networks can also be created with a periodicity along the *x*, *y*, and/or *z* axis. For example, to introduce a periodicity along the *x* axis into a given pore network, we must

simply connect the nodes on the "left" of the network to the nodes on the "right" by adding a pore.

At the external surface of a given pore network, we have expressly removed the perpendicular pores with respect to the surface normal vector.

At the end of the procedure, dead volumes of inaccessible pores are eliminated since they do not contribute to the experimental textural properties neither to the diffusion paths. Then, the textural properties of the support are recalculated (see section IV.2.1). The next section is dedicated to the output data obtained from the Monte Carlo algorithm.

IV.2.1 OUTPUT DATA FROM THE NETWORK GENERATION MODEL

The textural properties are a part of the output data generated by the pore network model. Here follows the way they are calculated. **Hypothesis 1** considers a parallelepiped particle shape, with dimensions E_x, E_y and E_z, in which there are initially a number of nodes that are equidistantly spaced in all directions. The parallelepiped dimensions are given by:

$$\begin{aligned} E_x(m) &= N_x \cdot L_p \\ E_y(m) &= N_y \cdot L_p \\ E_z(m) &= N_z \cdot L_p \end{aligned} \qquad \text{(IV-1)}$$

with N_x, N_y and N_z the initial number of nodes along each axis and L_p, the pore length. Within 2D pore networks N_z=1 and the above definitions are still used. These definitions lead to a representation of a random pore network with fixed and equidistant nodes within the matrix. The total catalyst support volume (V_{total}) and mass (M_{total}) are simply given by:

$$V_{total}(m^3) = N_x \cdot N_y \cdot N_z \cdot {L_p}^3 \qquad \text{(IV-2)}$$

$$M_{total}(g) = \rho_{Al_2O_3} \cdot V_{total} \cdot (1 - \varepsilon) \qquad \text{(IV-3)}$$

where $\rho_s = \rho_{Al_2O_3}(g \cdot m^{-3})$ is the alumina skeletal density. The initial or maximum number of nodes $N_{nodes\,max}$ in the parallelepiped particle is given by:

$$N_{nodes\,max} = N_x \cdot N_y \cdot N_z \qquad \text{(IV-4)}$$

Hypothesis 2 considers that a pore network is constituted by cylindrical pores. In equations (IV-5), (IV-6) and (IV-7) we present the expressions that allow to calculate the catalyst porosity, the specific surface area and the specific pore volume.

$$\varepsilon = \frac{V_{pores}}{V_{total}} = \frac{\sum_{p=1}^{Np} \pi \cdot \frac{D_p^2}{4} \cdot L_p}{E_x \cdot E_y \cdot E_z} \quad \text{(IV-5)}$$

$$s_{BET}(m^2 \cdot g^{-1}) = \frac{S_{pores}}{M_{Total}} = \frac{\sum_{p=1}^{Np} \pi \cdot D_p \cdot L_p}{E_x \cdot E_y \cdot E_z \cdot \rho_{Al2O3} \cdot (1-\varepsilon)} \quad \text{(IV-6)}$$

$$v_p\ (m^3 \cdot g^{-1}) = \frac{V_{pores}}{M_{Total}} = \frac{\varepsilon}{\rho_{Al2O3} \cdot (1-\varepsilon)} = \frac{\sum_{p=1}^{Np} \pi \cdot \frac{D_p^2}{4} \cdot L_p}{E_x \cdot E_y \cdot E_z \cdot \rho_{Al2O3} \cdot (1-\varepsilon)} \quad \text{(IV-7)}$$

The above equations are used in the code to calculate the values for the textural properties. It should be mentioned that the latter equation is not independent of the first one, as $v_p = \varepsilon / \left(\rho_{Al2O3} \cdot (1-\varepsilon)\right)$.

In order to illustrate the effect of each parameter, one can further simplify the equations with some additional hypotheses. In case the pore network has a constant pore diameter and a constant pore length (**Hypothesis 3**), the above equations reduce to:

$$\varepsilon = \frac{V_{pores}}{V_{total}} = \frac{N_p \cdot \pi \cdot \frac{D_p^2}{4} \cdot L_p}{E_x \cdot E_y \cdot E_z} \quad \text{(IV-8)}$$

$$s_{BET}(m^2 \cdot g^{-1}) = \frac{S_{pores}}{M_{Total}} = \frac{N_p \cdot \pi \cdot D_p \cdot L_p}{E_x \cdot E_y \cdot E_z \cdot \rho_{Al2O3} \cdot (1-\varepsilon)} \quad \text{(IV-9)}$$

$$v_p\ (m^3 \cdot g^{-1}) = \frac{V_{pores}}{M_{Total}} = \frac{\varepsilon}{\rho_{Al2O3} \cdot (1-\varepsilon)} = \frac{N_p \cdot \pi \cdot \frac{D_p^2}{4} \cdot L_p}{E_x \cdot E_y \cdot E_z \cdot \rho_{Al2O3} \cdot (1-\varepsilon)} \quad \text{(IV-10)}$$

The maximum connectivity for a node is equal to Z_{max}, except for the nodes at the surface, where the pores can only be oriented inside the material. However, if the network is sufficiently large, the effect of this lower connectivity for the nodes placed at the catalyst surface on the average connectivity becomes negligible (**Hypothesis 4**). Hence, we can approximate the number of pores by:

$$N_p \approx N_{nodes\,max} \cdot \frac{Z_{max}}{2} \cdot P \approx N_{nodes\,max} \cdot \frac{Z_{avg}}{2} \quad \text{(IV-11)}$$

with the average connectivity $Z_{avg} = Z_{max} \cdot P$. Given equation (IV-4), one obtains:

$$V_{pores} = N_{nodes\,max} \cdot \frac{Z_{max}}{2} \cdot P \cdot \pi \frac{D_p^2}{4} L_p \quad \text{(IV-12)}$$

And since $V_{total} = N_x \cdot N_y \cdot N_z \cdot {L_p}^3$, one obtains:

$$\varepsilon = \frac{V_{pores}}{V_{total}} = \frac{\frac{Z_{max}}{2} \cdot P \cdot \pi \cdot \frac{D_p^2}{4}}{L_p^2} \quad \text{(IV-13)}$$

$$s_{BET}(m^2 \cdot g^{-1}) = \frac{S_{pores}}{M_{Total}} = \frac{\frac{Z_{max}}{2} \cdot P \cdot \pi \cdot D_p}{L_p^2 \cdot \rho_{Al2O3} \cdot (1-\varepsilon)} \quad \text{(IV-14)}$$

$$v_p\ (m^3 \cdot g^{-1}) = \frac{V_{pores}}{M_{Total}} = \frac{\varepsilon}{\rho_{Al2O3} \cdot (1-\varepsilon)} = \frac{\frac{Z_{max}}{2} \cdot P \cdot \pi \cdot \frac{D_p^2}{4}}{L_p^2 \cdot \rho_{Al2O3} \cdot (1-\varepsilon)} \quad \text{(IV-15)}$$

It should be stressed that

$$(1-\varepsilon) = 1 - \frac{\frac{Z_{max}}{2} \cdot P \cdot \pi \cdot \frac{D_p^2}{4}}{L_p^2} = \frac{L_p^2 - \frac{Z_{max}}{2} \cdot P \cdot \pi \cdot \frac{D_p^2}{4}}{L_p^2} \quad \text{(IV-16)}$$

Hence, one finally obtains:

$$\varepsilon = \frac{\frac{Z_{max}}{2} \cdot P \cdot \pi \cdot \frac{D_p^2}{4}}{L_p^2} \quad \text{(IV-17)}$$

$$s_{BET}(m^2 \cdot g^{-1}) = \frac{\frac{Z_{max}}{2} \cdot P \cdot \pi \cdot D_p}{\rho_{Al2O3} \cdot \left(L_p^2 - \frac{Z_{max}}{2} \cdot P \cdot \pi \cdot \frac{D_p^2}{4}\right)} \quad \text{(IV-18)}$$

$$v_p\ (m^3 \cdot g^{-1}) = \frac{V_{pores}}{M_{Total}} = \frac{\varepsilon}{\rho_{Al2O3} \cdot (1-\varepsilon)} = \frac{\frac{Z_{max}}{2} \cdot P \cdot \pi \cdot \frac{D_p^2}{4}}{\rho_{Al2O3} \cdot \left(L_p^2 - \frac{Z_{max}}{2} \cdot P \cdot \pi \cdot \frac{D_p^2}{4}\right)} \quad \text{(IV-19)}$$

It is clear that if the diameter, the maximum connectivity or the pore existence probability increase, then ε, v_p and s_{BET} will increase as well. However, if the pore length increases then the values of these textural properties decrease. A sensitivity analysis regarding the model parameters is presented in section V.4.

Moreover, in order to perform the transient mass transfer simulation within the network, the information on the structure of the pore network must be handed over to the mass transfer model. To this aim, we have developed a connectivity matrix that contains all the required information on the network. Indeed, the connectivity matrix is a simple matrix, where it is possible to store information concerning not only pores and nodes but also information related to the boundary conditions of the mass transfer model. Indeed, certain pores are linked to nodes placed on the external surface of the porous catalyst, while others are interior pores.

As an example, let us take a simple network constituted by two pores A and B and 3 nodes: 1, 2 and 3. A schematic and illustrative representation of this network is shown in Fig. IV-2. Even though nodes are here illustrated with a small volume, the volume of the generated pore networks is exclusively contained in the pores.

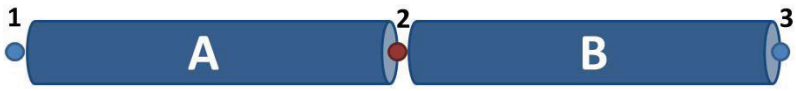


Fig. IV-2. Schematic network used to exemplify data storage. Each node is represented by a circle. Blue circles for nodes at the external surface of the grain, red circles for interior nodes.

The following matrix (Table IV-2) illustrates the connectivity matrix obtained for the network example presented in Fig. IV-2.

Table IV-2. Connectivity matrix defining the pore network represented in Fig. IV-2 with $Z_{max} = 2$.

Nodes	**Connectivity, Z**	**$Z = 1$**	**$Z = 2$**	**B.C.**
1	1	$+A$	0	-1
2	2	$-A$	$+B$	0
3	1	$-B$	0	$+1$

The first column lists the node labels, while the second column gives the connectivity of each node, Z. The 3rd and 4th columns contain the label of each pore connected to a given node. The number of columns of this part of the connectivity matrix can vary from Z=1 to Z_{max}. In the example depicted in Fig. IV-2, the maximum connectivity of the network is $Z_{max} = 2$ (a node can be connected up to two pores, at the most) therefore, only two columns are required for this network. If the node connectivity of a given node is lower than Z_{max}, the subsequent columns are filled with 0. The +/- sign before each pore label in the 3rd and 4th columns imposes the sign convention of the flow inside each pore.

The last column refers to the boundary conditions applied to each node or to each pore boundary. Any value differing from (0) corresponds to nodes that are located at the external surface of the particle and that allow to distinguish inlet and outlet nodes, respectively (-1) and (+1) for the example presented in Fig. IV-2. For such external nodes, the concentrations of the species are fixed as boundary conditions during the diffusion simulations. On the other hand, (0) means that we have an internal node. For such nodes, a conservation condition of each species is used. The latter will be explained further on. The next section will give a global overview of the Monte Carlo algorithm.

IV.2.2 NETWORK GENERATION ALGORITHM DIAGRAM

The following diagram presented in Fig. IV-3 illustrates the network generation model based on a Monte Carlo approach, from the selection of the network size and configuration of the pore network to the determination of the textural properties. As

shown in Fig. IV-3, several inputs are used to generate the pore network, such as the connectivity pattern and the pore existence probability.

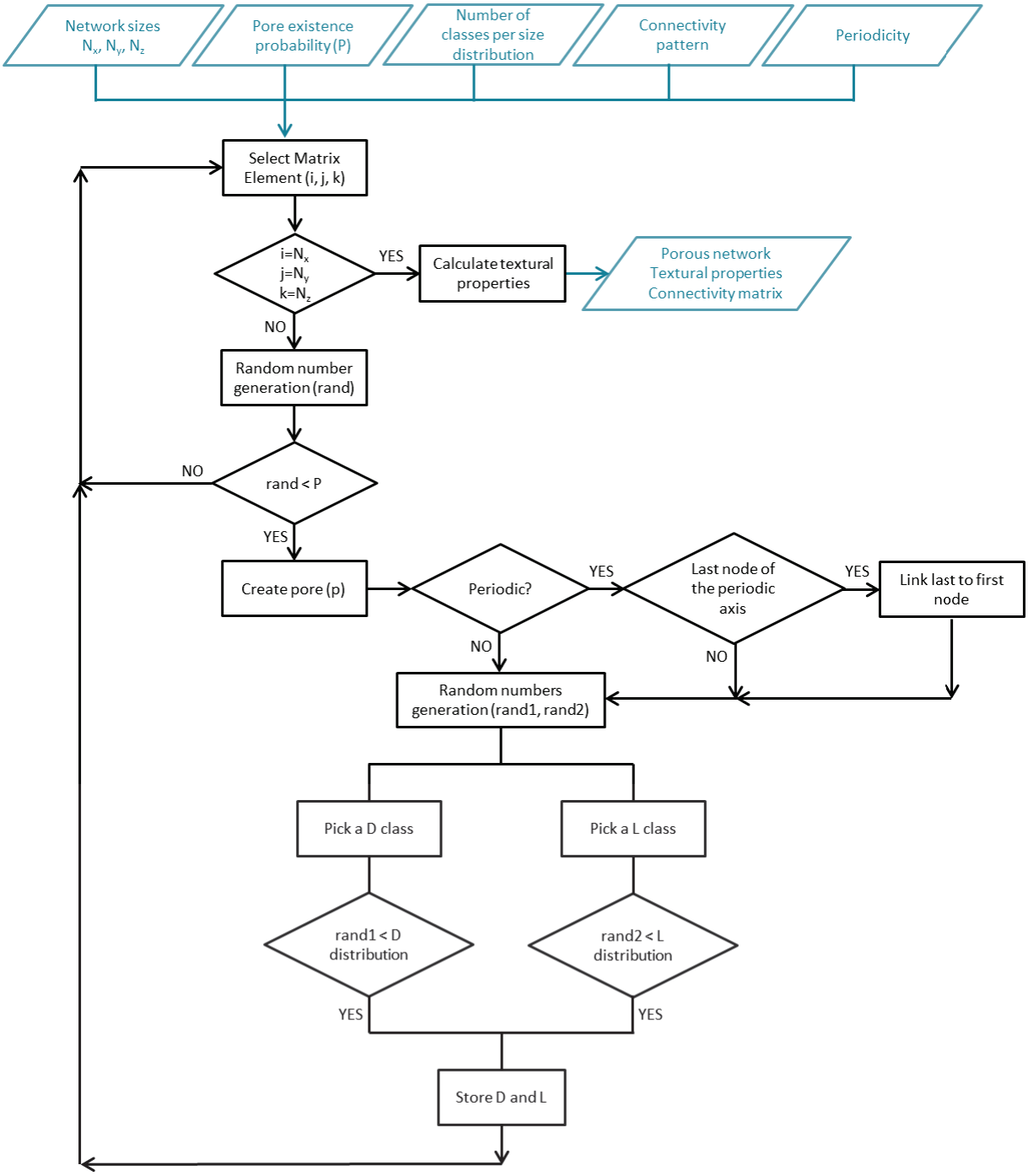


Fig. IV-3. Flowchart describing briefly the pore network generation.

An initial grid is taken as departure point. A given element (node) from the initial grid is selected. Taking the connectivity pattern, a potential pore is considered and a uniformly distributed random number selected. If the random number is lower than the pore existence probability then the pore exists and is connected to the node. A pore diameter and length are attributed in accordance with the pore size distributions specified as input. When generating a periodic network, additional pores may connect the network from one

side to the other along the periodicity axis. These extra pores are of course added according to the connectivity pattern and the pore existence probability.

The procedure ends when all elements from the initial grid have been covered. Then, the textural properties, such as the average diameter and average length of the pores, the specific surface area, the catalyst pore volume and the porosity, are calculated and stored. The connectivity matrix that contains the required information on the pore network structure for further mass transfer simulation is also stored.

As mentioned before, in order to simulate mass transfer by diffusion through the pore network, the network must be submitted to the removal of possible inaccessible pores. The next section contains a brief description on the inaccessible volume removal.

IV.2.3 INACCESSIBLE VOLUME SUPPRESSION ALGORITHM

To simulate mass transfer within a pore network, the inaccessible pore volume is first removed. This inaccessible pore volume is made of pores for which there is no path linking them to the external surface of the pore network. Therefore, these inaccessible volumes will not contribute to the textural properties nor participate to the mass transfer and shall be removed. They are nevertheless used to evaluate the catalyst textural properties with and without the inaccessible pore volume (see section V.2).

A flowchart is presented in Fig. IV-4 in order to illustrate the process of removing the inaccessible volume. In order to remove this inaccessible volume, the inaccessible pores must be found within the pore network. To this end, the paths that can be found from the external nodes are systematically marked by walking from node to node. An inaccessible pore does not belong to any of these paths. The global outcome will allow us to save all pores having a path to the external surface of the catalyst (accessible volume).

After having removed the inaccessible volume, the connectivity matrix and the textural properties are saved. These data are subsequently used to simulate mass transfer within the pore network.

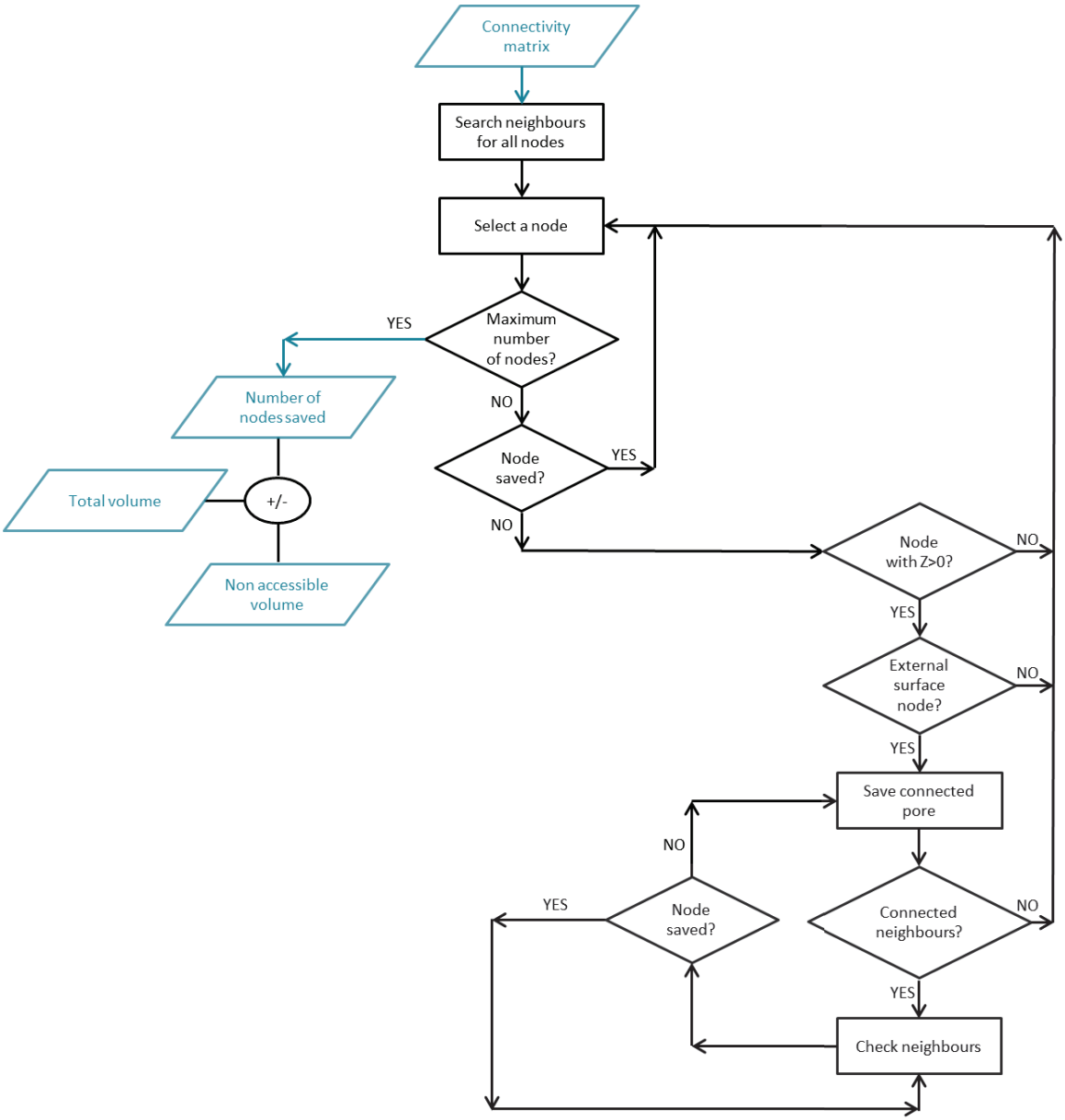


Fig. IV-4. Flowchart summarizing the inaccessible volume suppression.

IV.3 MASS TRANSFER DESCRIPTION WITHIN EACH CYLINDRICAL PORE OF A RANDOM PORE NETWORK

The mass transfer within the pore network is simulated based on the connectivity matrix and additional inputs, such as the initial and boundary conditions, the molecular diffusion coefficient and some discretization parameters.

According to Friedman and Seaton (1995), for intersecting capillary models, if it is assumed that the pores are much longer than wide, diffusion and reaction are effectively one dimensional in individual pores and the solution of the network diffusion problem reduces to satisfying a mass balance at each node. Therefore, in order to simulate mass

transfer by diffusion within a pore network, a 1D isothermal transient mass transfer model is assumed since the length of each pore is high with respect to its diameter. For species i, the mass balance within each pore of the network under isothermal conditions is given as follows:

$$\frac{\partial c_{ip}}{\partial t} + \frac{\partial J_{ip}}{\partial l} = 0 \qquad \text{(IV-20)}$$

where c_{ip} and J_{ip} are respectively the concentration and flux of species i in a given pore p and l is the spatial coordinate along the pore axis.

In order to calculate J_{ip}, we use the Fick model, considering a constant total concentration binary mixture and constant molecular diffusion coefficient D_{im}. Hence, J_{ip} is then defined by:

$$J_{ip} = -D_{im}\frac{\partial c_{ip}}{\partial l} \qquad \text{(IV-21)}$$

with D_{im}, the molecular diffusion coefficient of species i, which for small concentrations of the diffusing species can be considered independent from the concentration. The combination of the mass balance of species *i* with the Fick model leads to:

$$\frac{\partial c_{ip}}{\partial t} = D_{im}\frac{\partial^2 c_{ip}}{\partial l^2} \qquad \text{(IV-22)}$$

The discretization over time and space of equation (IV-22) is performed using respectively the DASPK routine created by Petzold (1982) and an orthogonal collocation method developed by Villadsen and Michelsen (1978) (cf. Appendix II). It is important to mention that the majority of the simulations were performed using for each pore, 3 collocation points. The next section is dedicated to the initial and boundaries conditions applied to the system.

IV.3.1 INITIAL AND BOUNDARY CONDITIONS AT THE NODES

With the information stored in the connectivity matrix (example given in Fig. IV-2 and Table IV-2) and the length and diameter of each pore of the network, one can describe the mass transfer process within the pores. By checking the connectivity matrix, one observes that the only inlet of the network represented in Fig. IV-2 is node 1, since its boundary condition takes the value of -1.

The procedure adopted to define the initial conditions and the boundary conditions of pores and nodes will now be described.

As initial condition for the pores, a fixed concentration in every position of all pores is used. Hence, we have for a given species:

$$c_{ip}(l, t_0) = c_{i\ initial} \quad \text{(IV-23)}$$

The boundary conditions for the pores are expressed at the nodes of the network. Since we consider that nodes do not accumulate matter, these boundary conditions were inspired from the Kirchhoff's junction rule (or nodal rule) and by the Kirchhoff's loop (or mesh) rule that are used for the modelling of electrical circuits. Kirchhoff's first law or junction rule derives from the mass conservation law and implies that, at any node (junction), the sum of the flows entering into that node is equal to the sum of the flows leaving that node, or, stated differently, the algebraic sum of flows is zero. Kirchhoff's second law requires that the chemical potential (or the concentration in the case of Fick's law) at the pore end connected to a node equals the chemical potential (or concentration) of the node.

The initial condition for the nodes is the same as those for the pores. According to the position of the nodes in the network, their boundary conditions can be different. Indeed, for the external nodes, the concentrations of the species are fixed at a given value during the diffusion simulations.

We list below the boundary conditions for our system of interconnected pores with some exceptions that can be found in the course of diffusion through the pore network. For a given node, the number of boundary conditions is equal to its connectivity, i.e. the number of connected pores. To the first pore considered (from those connected to the node), a flow continuity is imposed: the flow is calculated and the concentration at the node is therefore known. For the remaining pores, the concentration at the pore end connected to a node is imposed.

- If a given node is located at the external surface of the catalyst grain then, the concentration is given by the concentration at the catalyst surface:

$$c_{ip}\left(l = \pm L_p, t\right) = c_{i\ bulk}, \quad \forall\, t > t_0 \quad \text{(IV-24)}$$

- For inner nodes, the boundary condition invokes that the sum of all the flows entering and leaving pores connected to the node must be equal to 0. For a given node, we have:

$$\sum_{p=1}^{Np} F_{ip}\left(l = \pm L_p, t\right) = \sum_{p=1}^{Np} J_{ip}\left(l = \pm L_p, t\right) \cdot \frac{\pi D_p^2}{4} = 0, \quad \forall\, t > t_0 \quad \text{(IV-25)}$$

- The node concentration of species i is common to all connected pores to the node:

$$c_{ip}\left(l = \pm L_p, t\right) = c_{node}, \qquad \forall\, t > t_0 \quad \text{(IV-26)}$$

- In the particular case where the node is a dead-end, the flow at the node must be equal to $F_{ip}\big|_{\pm L_p} = 0$ and so, taking the Fick model, the concentration gradient must simply fulfil:

$$\frac{\partial c_{ip}}{\partial l}(l = \pm L_p, t) = 0, \qquad \forall\, t > t_0 \tag{IV-27}$$

with $l = \pm L_p$, depending on the extremity of the pore that is considered.

IV.3.2 NUMERICAL RESOLUTION DIAGRAM FOR THE MASS TRANSFER MODEL

A global overview of the 1D mass transfer simulation within each pore, from the spatial and time discretization to the flux determination, is presented in Fig. IV-5.

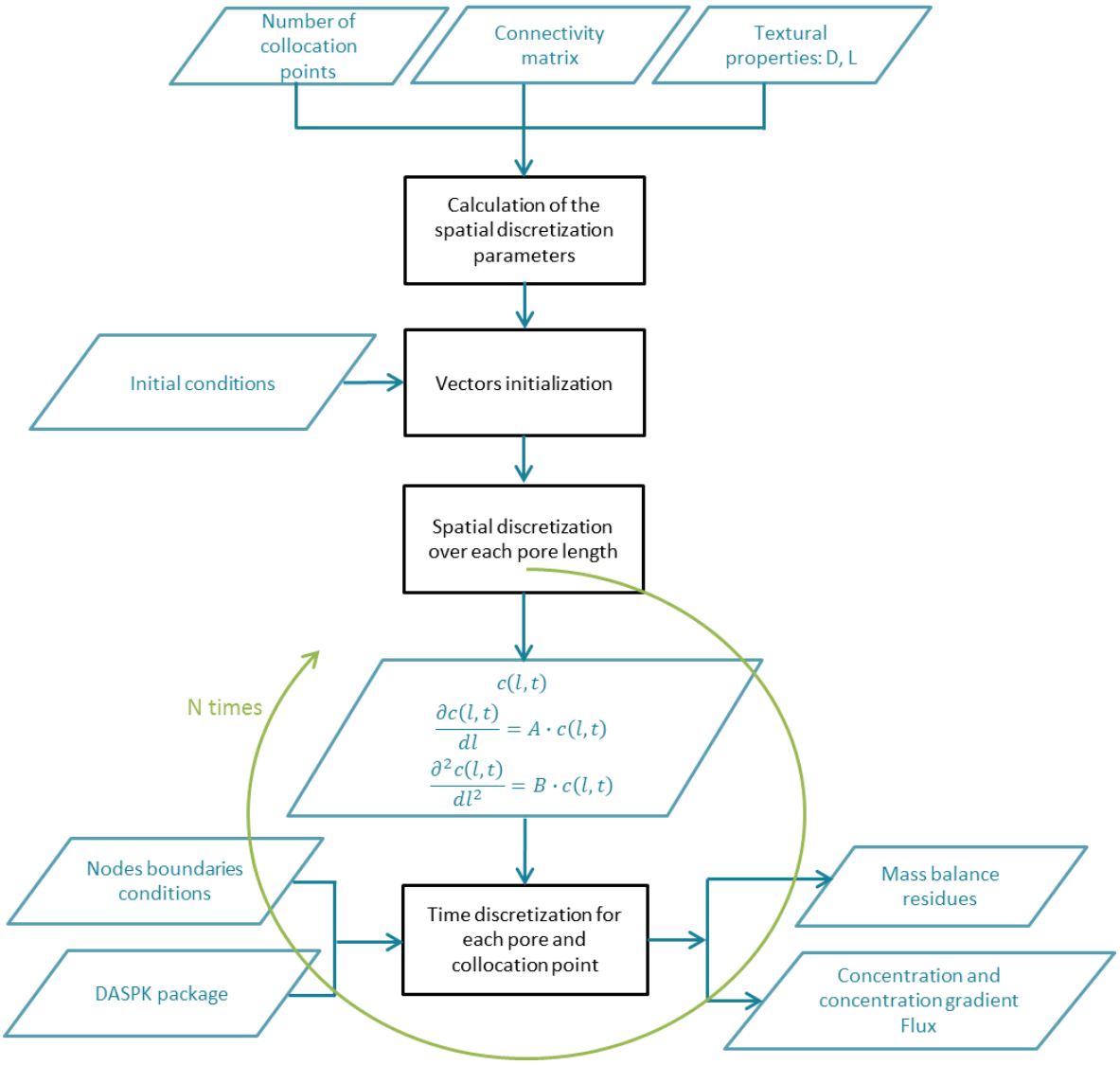


Fig. IV-5. Flowchart describing in summary the mass transfer simulation procedure.

For the mass transfer simulation and as mentioned before, an orthogonal collocation is used with respect to the spatial discretization (Villadsen and Stewart, 1967) and for the

time discretization the DASPK package is used and based on a modified Newton's method Petzold (1982). Further information can be found in Appendix II.

The first step of the mass transfer simulation is the calculation of certain spatial discretization parameters, such as the weighting functions and the Jacobi polynomial roots. The reader should know that the mentioned Jacobi polynomials roots are simply the position of each collocation point along the pore length and are of course reliant on to the spatial discretization. The weighting functions are also relative to the spatial discretization, they are part of the determination of the concentration and concentration derivatives at each collocation point of a given pore. Extended information can be found in Appendix II.

Then, a combination of the spatial and time discretization is required in order to obtain both, the concentration and the 1^{st} and 2^{nd} derivatives at each time and over each collocation point of a given pore based on the initial and boundary conditions and the calculation of the mass balance residual errors.

IV.4 CONCLUSIONS

A major building block of our work has been presented here. It illustrates a method to generate random pore networks and to obtain its textural properties and its connectivity information. The combination of the generation of random networks along with the description of mass transfer will allow us to simulate large size pore networks.

By modifying the input parameters, various networks with different structures can now be generated and their textural properties can be calculated. These networks will have to correctly represent the textural properties of actual alumina supports. Moreover, the determination of effective mass transfer properties from the simulation of mass transfer by diffusion in 1D of each pore of the network will allow us to compare the simulated effective diffusivity and tortuosity with experimental and correlated data.

Nevertheless, a numerical validation of the mass transfer model as well as a sensitivity analysis to the model parameters of the network algorithm and their impact on both textural and mass transfer properties must be investigated. The validation of the mass transfer model is available in Appendix III. The next chapters will be dedicated to the sensitivity analyses.

SENSITIVITY ANALYSES

CHAPTER V - NETWORK GENERATION ALGORITHM ANALYSIS

V.1 INTRODUCTION

One of the outstanding features of the developed network generation algorithm is related to its capacity and highly efficient data storage. Indeed, it was proven possible to create extremely large networks: 15000×15000 nodes in 2D and 600×600×600 nodes in 3D, containing up to 340 million pores connecting 225 million nodes. The algorithm also has a very low computation time: on a Dell desktop computer with a 3.5 GHz Intel Xeon E5 CPU and 16GB of RAM, it takes about 2 s to build a square pore network with 200×200 nodes (40 thousand nodes and 56 thousand pores), and about 30 min to build a cubic network with 400×400×400 nodes (64 million nodes and 115 million pores).

In order to test the network generation algorithm, we have studied the textural properties of several networks starting from different inputs. Since the networks may contain some inaccessible volumes, the first study was dedicated to the impact of the inaccessible volume removal on the textural properties. Then, several sensitivity analyses were performed towards the impact of the Monte Carlo algorithm variability. Finally, we have studied as well the influence of the network parameters, such as the pore diameter, the pore length, the maximum connectivity, the dimensionality (2D or 3D), and the pore existence probability.

We have used a range of model parameters capable of generating pore networks within the range of the textural properties of actual aluminas textural properties and that are presented in Table I-1.

V.2 INACCESSIBLE VOLUME SUPPRESSION

During the network generation, inaccessible pores may have been created. Since these pores will not participate on the mass transfer process, their suppression allows reducing the computational burden of the dynamic mass transfer simulations. In the present study, we intend to check if whether the textural properties change significantly after the removal of the inaccessible volume.

We have represented in Fig. V-1 and Fig. V-2, the catalyst porosity and specific surface area obtained for thirty 2D triangular pore networks of maximum connectivity Z_{max}=6 for each tested network size. We have used network sizes of 50x50 and 100x100 and a pore existence probability of P=0.7.

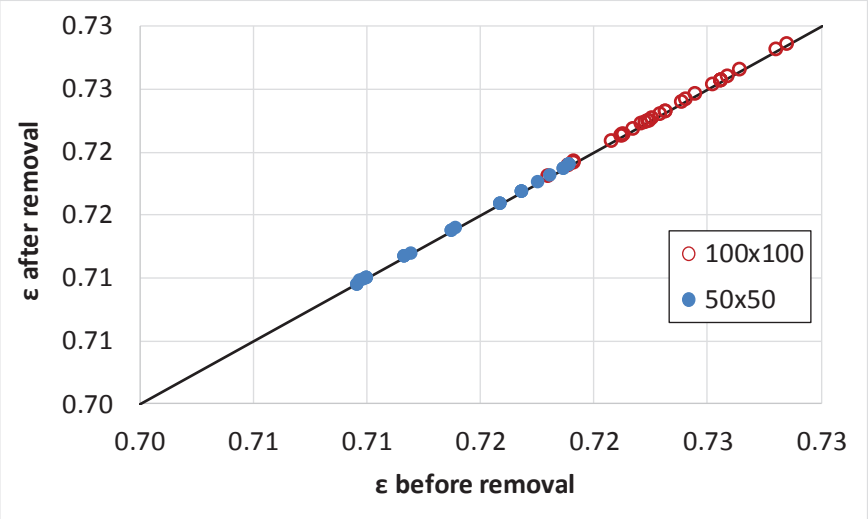


Fig. V-1. Catalyst porosity calculated for 2D Z_{max}=6 networks with P=0.7 before and after the inaccessible volume removal.

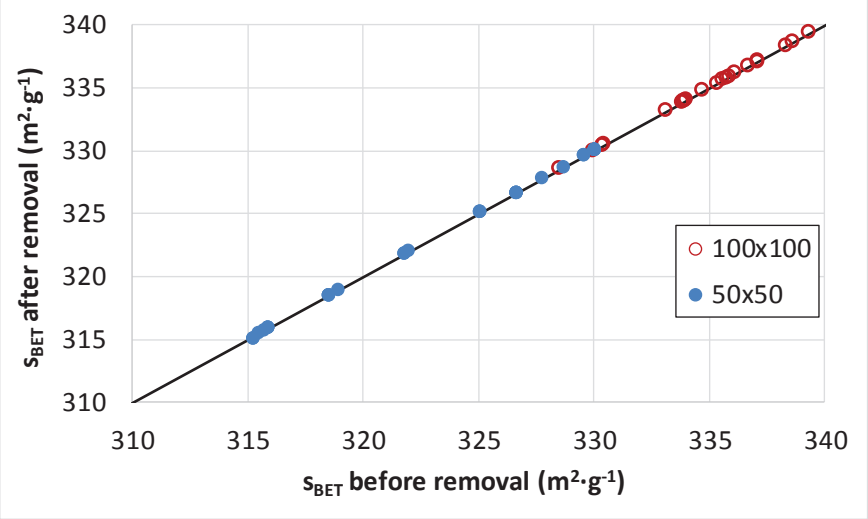


Fig. V-2. Catalyst specific surface area calculated for 2D triangular networks with P=0.7 before and after the inaccessible volume removal.

For a pore existence probability of P=0.7, we observe that the textural properties remain identical for almost all 30 networks generated. We have calculated the maximum relative deviations comparing the textural properties before and after removal (see Table V-1) for the two tested network sizes and for the pore existence probability of 0.7 and also at P=0.6. It is clear that the inaccessible pore volume that can appear occasionally in some of the generated pore networks does not significantly impact their textural properties.

Table V-1. Maximum relative deviations of the textural properties before and after the inaccessible pores removal for 2D networks with Z_{max}=6.

Network size	Probability	S_{BET}	V_p	ε	Z
100×100	P=0.7	0.02%	0.02%	0.005%	0.005%
	P=0.6	0.07%	0.07%	0.03%	0.06%
50×50	P=0.7	0.07%	0.07%	0.02%	0.06%
	P=0.6	0.12%	0.12%	0.05%	0.12%

V.3 MONTE CARLO ALGORITHM VARIABILITY

To test the network generation tool, several sensitivity analyses on the calculated textural properties were performed. In what follows, the influence of the Monte Carlo algorithm variability on the required minimum network size and on the number of simulations is studied. The corresponding mass transfer properties with respect to the required number of simulations are presented in Chapter VI.

V.3.1 REQUIRED MINIMUM NETWORK SIZE

Due to the Monte Carlo algorithm variability, a sensitivity analysis is performed to determine the minimum network size to use in order to get constant textural properties. The analysis was performed for constant D_p and L_p at 10 and 15 nm, respectively. To investigate this effect, 1000 networks were generated for several pore existence probabilities and network sizes $N_x \times N_y \times N_z$. Different connectivity patterns were also tested, with maximum connectivities Z_{max} ranging from 4 to 12.

As an example, Fig. V-3 - Fig. V-6 contain the results obtained for 2D triangular networks (Z_{max}=6) using P=0.7. The porosity (ε), the connectivity (Z), the specific surface area (s_{BET}) and the specific pore volume (v_p) are graphically represented for several network sizes as a function of the number of nodes. The three curves in each figure correspond to the minimum, maximum and average values found among the 1000 networks generated.

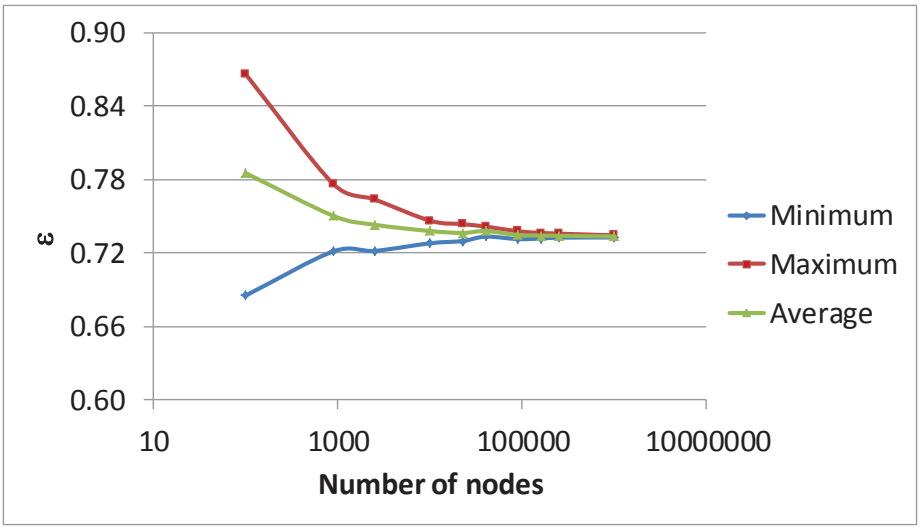


Fig. V-3. Porosity obtained for different network sizes $N_x \times N_y \times N_z$ with $N_x = N_y$ and $N_z = 1$.

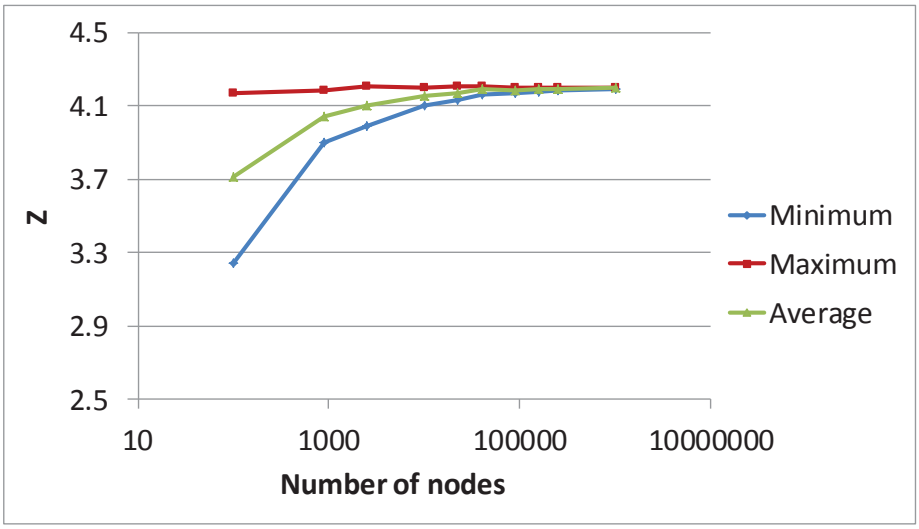


Fig. V-4. Connectivity obtained for different network sizes $N_x \times N_y \times N_z$ with $N_x = N_y$ and $N_z = 1$.

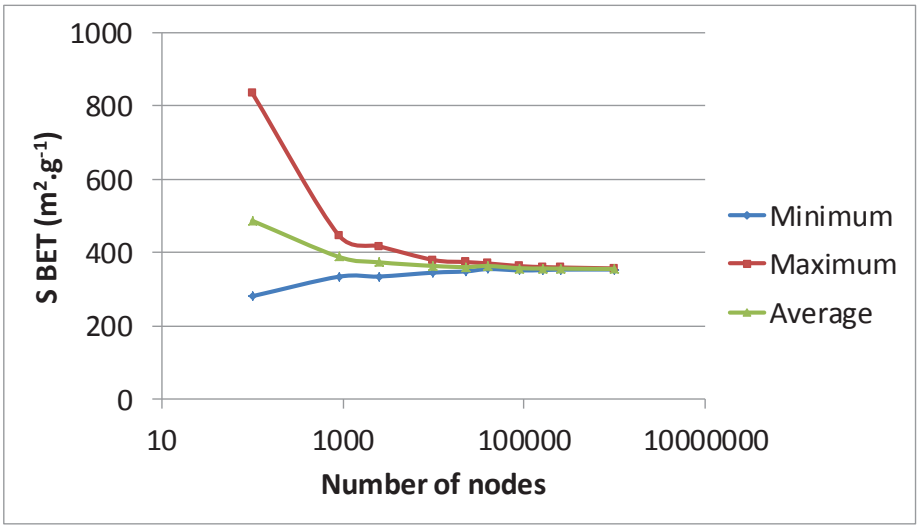


Fig. V-5. Specific surface area obtained for different network sizes $N_x \times N_y \times N_z$ with $N_x = N_y$ and $N_z = 1$.

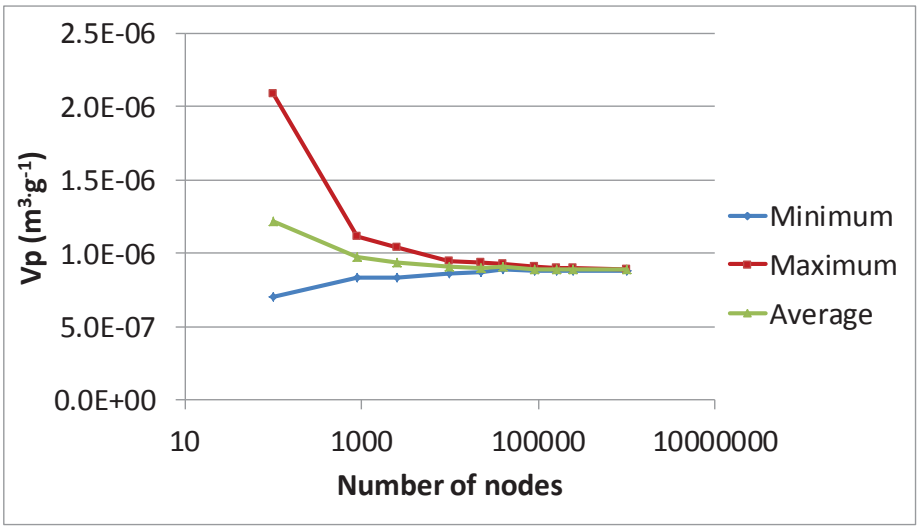


Fig. V-6. Pore volume obtained for different network sizes $N_x \times N_y \times N_z$ with $N_x=N_y$ and $N_z=1$.

From Fig. V-3 to Fig. V-6, one observes that the minimum, average and maximum values converge as the number of nodes increases, meaning that the Monte Carlo variability can be reduced by increasing the number of nodes of a pore network. Taking a 5% maximum relative variation on the textural properties leads to a required network size of 10,000 nodes (100×100 network) for a 2D $Z_{max}=6$ network using $P=0.7$.

Table V-2 contains the required minimum network sizes obtained for several pore existence probabilities and connectivity patterns in 2D and 3D. The minimum network sizes were selected at a 5% relative deviation on the textural properties. From Table V-2, we may conclude that, from a global point of view, as pore existence probability and maximum connectivity increase, so does the required number of nodes of the network. Extended data can be found on Appendix IV.

Table V-2. Required network size for several pore existence probabilities and maximum connectivities.

	2D		**3D**	
Connectivity pattern	**$Z_{max}=4$ (square)**	**$Z_{max}=6$ (triangular)**	**$Z_{max}=6$ (cubic)**	**$Z_{max}=8$ (tetrahedral)**
***P*=0.5**	100×100	100×100	20×20×20	30×30×30
***P*=0.7**	100×100	100×100	20×20×20	80×80×80
***P*=0.9**	50×50	200×200	40×40×40	-

V.3.2 REQUIRED NUMBER OF SIMULATIONS

Since a single Monte Carlo simulation provides a single random network, its textural properties correspond to a single value inside their distribution. To compensate for this randomness, several simulations are generally averaged when one uses Monte Carlo-based algorithms. With several Monte Carlo simulations, one can calculate an average value and a standard deviation for each property, and hence a confidence interval for the estimated properties. It is often more convenient to use a relative deviation to characterize the range of the confidence interval:

$$Relative\ deviation(X) = \frac{\sigma(X)}{E(X)} = \frac{\sqrt{\frac{1}{n} \cdot \sum_{i=1}^{n}(x_i - \overline{x})^2}}{\overline{x}} \quad \text{(V-1)}$$

The goal of this sensitivity analysis is to assess the number of simulations that are required in order to obtain textural and mass transport properties with a chosen precision. To this aim, 1000 2D networks of size 50×50 with a maximum connectivity of Z_{max}=6, a pore existence probability of P=0.7 and constant D_p and L_p (10 and 15 nm, respectively) were generated. The textural properties obtained are represented in Fig. V-7 to Fig. V-10.

For the sample of 1000 simulations, we obtain the following results as average values and standard deviations: catalyst porosity ε of 0.71±0.005, an average connectivity Z_{avg} of 4.11±0.03, an average specific surface area s_{BET} of 322±9$m^2 \cdot g^{-1}$, and a pore volume v_p of $0.8\times10^{-6}\pm0.02\times10^{-6} m^3 \cdot g^{-1}$. As illustrated in Fig. V-7 to Fig. V-10, the relative deviations initially decrease rapidly, and show almost constant values of 0.8%, 0.8%, 2.7% and 2.7% respectively are obtained for the Monte Carlo variability for large numbers of simulations. After approximately thirty simulations, the relative deviations already reach similar values.

A confidence interval on an averaged property not only depends on the standard deviation of the sample, but also on the sample size. For a sample with N values, the standard deviation of the mean is calculated as $s/\sqrt{N-1}$, while the 95% confidence interval for the average is given by $\bar{X} \pm t_{0.95}(N-1) \cdot s/\sqrt{N-1}$, where $t_{0.95}$ is the critical value given by Student's t-distribution.

For a sample of thirty simulations, we therefore obtain, given as 95% confidence intervals, a porosity of 0.71±0.001, an average connectivity Z_{avg} of 4.11±0.01, an average specific surface area s_{BET} of 322±3.25 $m^2 \cdot g^{-1}$, and a mean pore volume v_p of 0.80×10^{-6} $\pm0.01\times10^{-6}$ $m^3 \cdot g^{-1}$. Expressed as relative deviations, the ranges of the confidence intervals are therefore equal to 0.3%, 0.3%, 1.0% and 1.0% respectively.

Compared to the experimental errors, these deviations are considered to be sufficiently adequate.

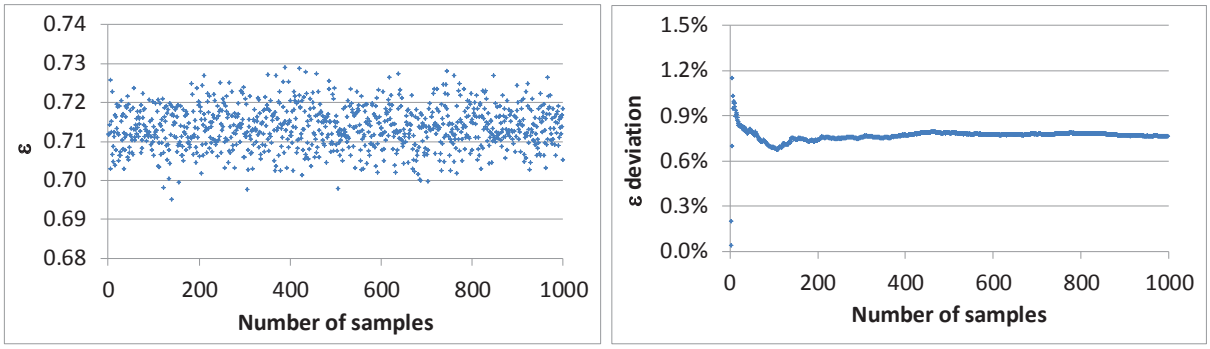


Fig. V-7. Porosity obtained from 1000 2D 50×50 networks with Z_{max}=6 and P=0.7.

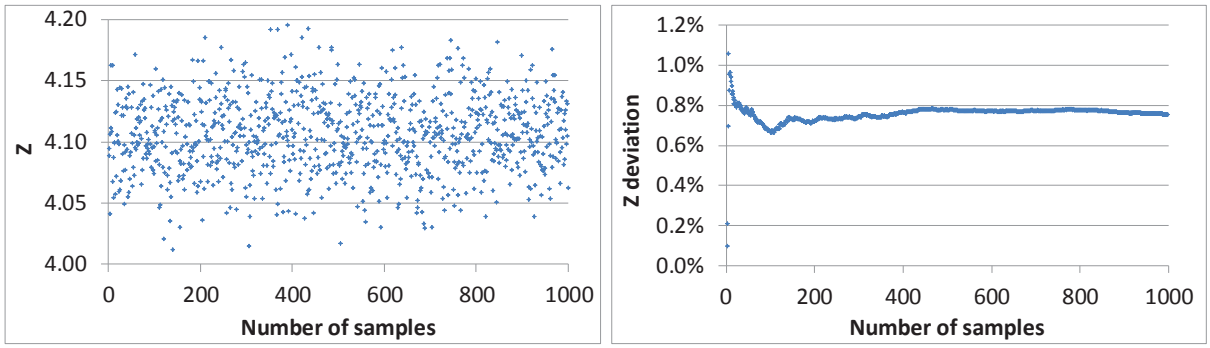


Fig. V-8. Predicted connectivity of all 1000 2D networks of size 50×50 with Z_{max}=6 and P=0.7.

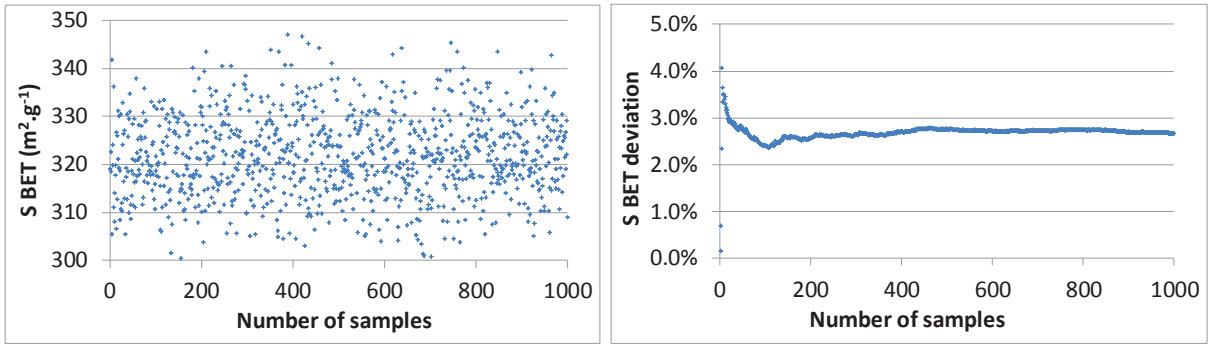


Fig. V-9. Predicted specific surface area of all 1000 2D networks of size 50×50 with Z_{max}=6 and P=0.7.

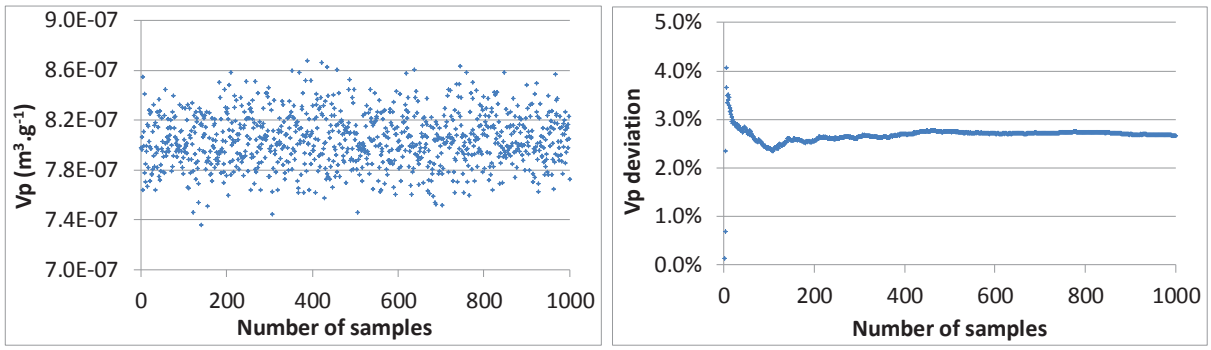


Fig. V-10. Predicted pore volume of all 1000 2D networks of size 50×50 with Z_{max}=6 and P=0.7.

V.4 INFLUENCE OF THE NETWORK GENERATION MODEL PARAMETERS

In this section, we intend to illustrate the influence of the model parameters on the textural properties of the generated pore networks. Several network parameters were tested, such as the parallelepiped particle dimensions (N_x and N_y), the pore existence probability P, the pore diameter distribution D_p and the pore length L_p. We have also put in evidence the relation between the textural properties and the average connectivity.

These sensitivity studies are performed using 2D networks (N_z = 1) generated from a maximum connectivity Z_{max}=6 with constant D_p and L_p of 10 and 15 nm respectively, and a pore existence probability of 0.7. If for instance the sensitivity analysis is performed to the pore diameter then, of course, the diameter is varied, otherwise it is fixed to the values listed above. The corresponding mass transfer properties will be presented in section VI.3.

V.4.1 INFLUENCE OF THE ASPECT RATIO N_X/N_Y WITH AN EQUAL MAXIMUM NUMBER OF NODES

We have first tested separately the influence of the particle dimensions N_x and N_y (the corresponding data is available in Appendix V).

We have selected five network sizes of constant maximum number of nodes so that, the Monte Carlo variability (see section V.3.1) does not interfere in this particular study. Since we are using 2D triangular networks with P=0.7, at least 10,000 nodes are required (cf. Table V-2). The following $N_x \times N_y$ sizes with N_z=1 were chosen: 10×1000, 20×500, 50×200, 200×50 and 500×20. The mean and standard deviations of the main textural properties are graphically represented on Fig. V-11 to Fig. V-14.

As can be seen in Fig. V-12, the mean connectivity varies from 4.2 to 3.96. Concerning the average porosity, specific surface area and pore volume (Fig. V-13 and Fig. V-14), they decrease from 0.73 to 0.68, from 352 to 280 $m^2 \cdot g^{-1}$ and from 8.8×10^{-7} to 7.0×10^{-7} $m^3 \cdot g^{-1}$, respectively. As illustrated in Fig. V-11 to Fig. V-14, a slight reduction is observed for the network sizes 200×50 and 500×20. This is partly explained by the way the network is constructed. For the examples presented, inlet and outlet nodes are placed at the top and bottom of the periodic pore network (with respect to the y-axis) and to these nodes, we expressly remove all horizontal pores within the inlet and outlet nodes. This means that, as N_x increases (number of inlet or outlet nodes), a larger number of horizontal pores are removed.

When looking to the standard deviations calculated for the different textural properties and shown in Fig. V-11 to Fig. V-14, we observe that they remain globally constant.

Available data from 2D square networks (Z_{max}=4) can be found in Appendix V. A rather similar behaviour to that from 2D triangular networks is observed.

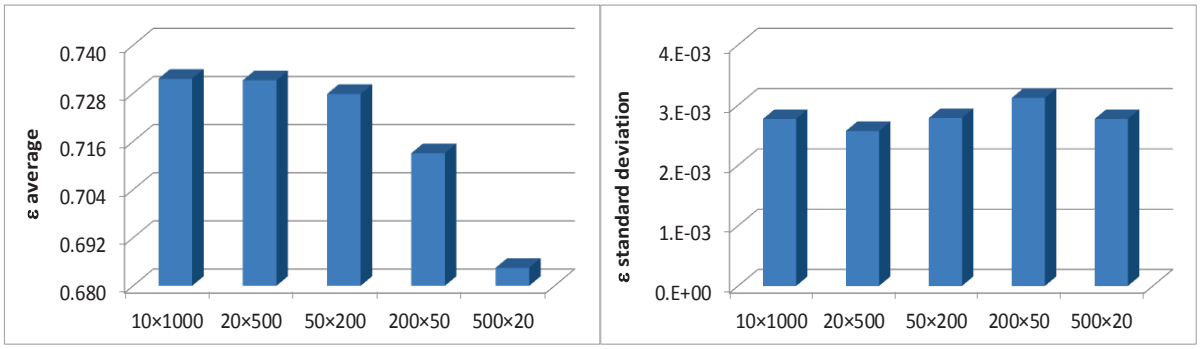


Fig. V-11. Porosity according to N_x/N_y. 2D networks, Z_{max} = 6, P = 0.7.

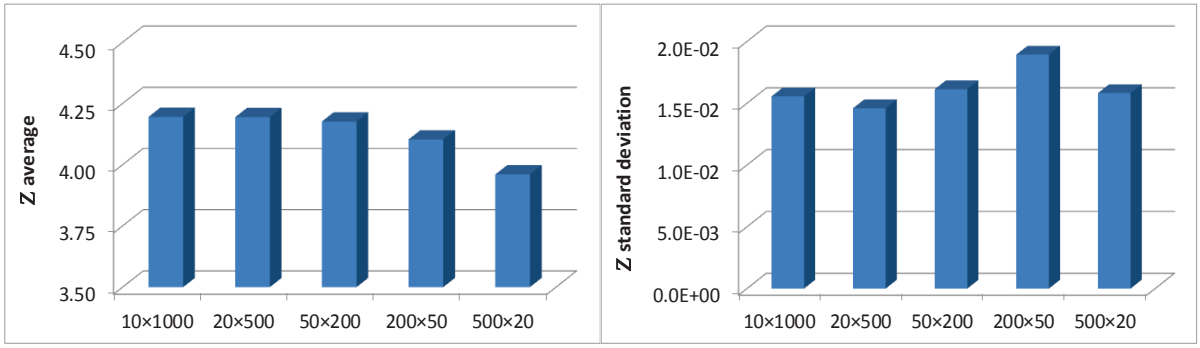


Fig. V-12. Connectivity according to N_x/N_y. 2D networks, Z_{max} = 6, P = 0.7.

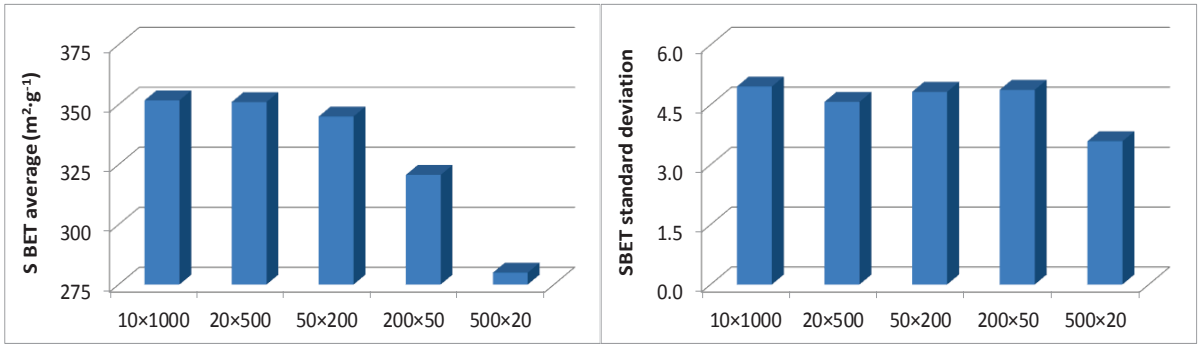


Fig. V-13. Specific surface area according to N_x/N_y. 2D networks, Z_{max} = 6, P = 0.7.

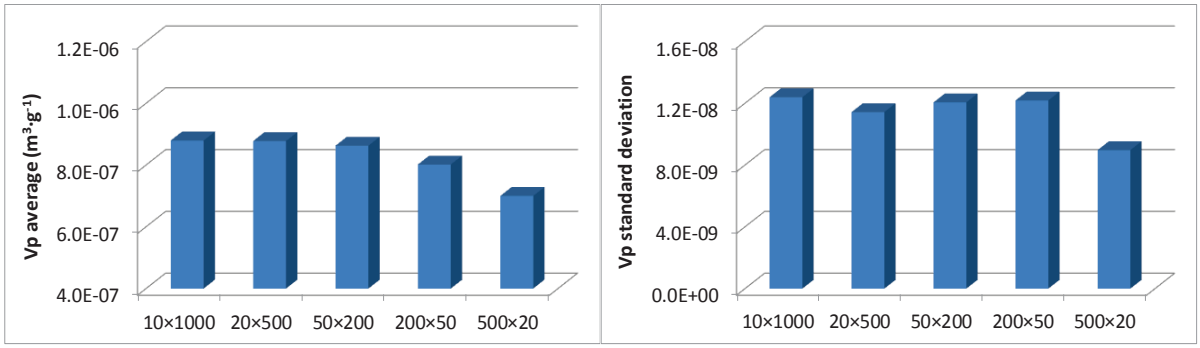


Fig. V-14. Pore volume according N_x/N_y. 2D networks, Z_{max} = 6, P = 0.7.

The effect of the aspect ratio N_x/N_y will especially be important when looking at the anisotropy observed on the mass transfer properties presented further on (cf. VI.3.1.).

V.4.2 INFLUENCE OF THE PORE EXISTENCE PROBABILITY: *P*

The results presented in Fig. V-15 to Fig. V-18 are averages over 30 pore networks at different pore existence probabilities. Two maximum network sizes are tested (50×50 and 100×100). Note that the 50×50 networks are only used to show the impact of the standard deviation since it has been shown in Table V-2 that 10,000 nodes are required to have a relative deviation lower than 5%.

In Appendix VI, we present the variation of the average, the variance, the standard deviation and the relative deviation of the different textural properties at different pore existence probabilities and as a function of the number of samples, ranging from 1 to 30.

From Fig. V-15 to Fig. V-18, one sees the textural properties (porosity, connectivity, particle specific surface area and pore volume) increasing with the pore existence probability. For the porosity and the mean connectivity, the effect of the pore existence probability is linear, while the increase in specific surface area and pore volume is more than linear with increasing pore existence probability. This behaviour is of course in agreement with the equations used to calculate the textural properties, which have been derived in section IV.2.1. The effect of the maximum connectivity Z_{max} will be strictly analogous to the effect of the pore existence probability. It is also important to note that the standard deviations take in general low values.

Moreover, a slight deviation of the textural properties is observed when comparing the values obtained from 50×50 to those from 100×100, the latter network size leading to slightly higher mean values and slightly lower standard deviations.

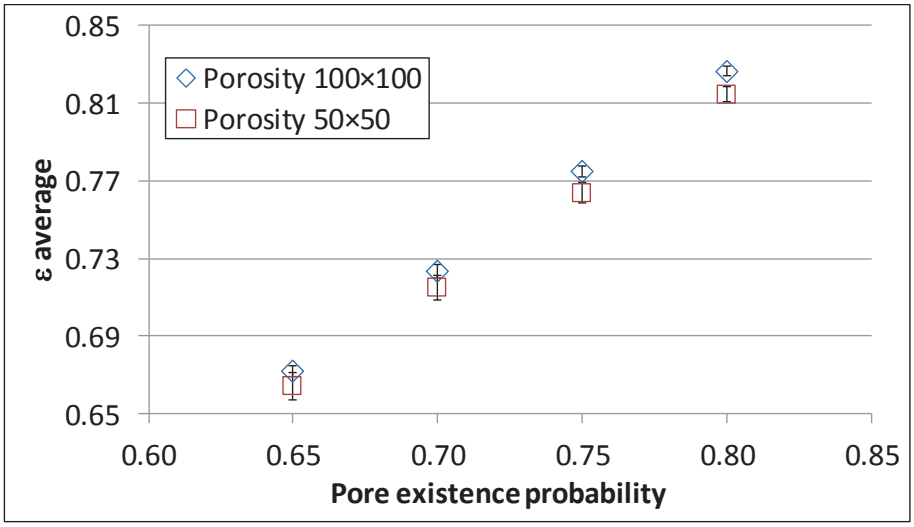


Fig. V-15. Mean porosity according to the pore existence probability, *P*. 2D networks, Z_{max} = 6.

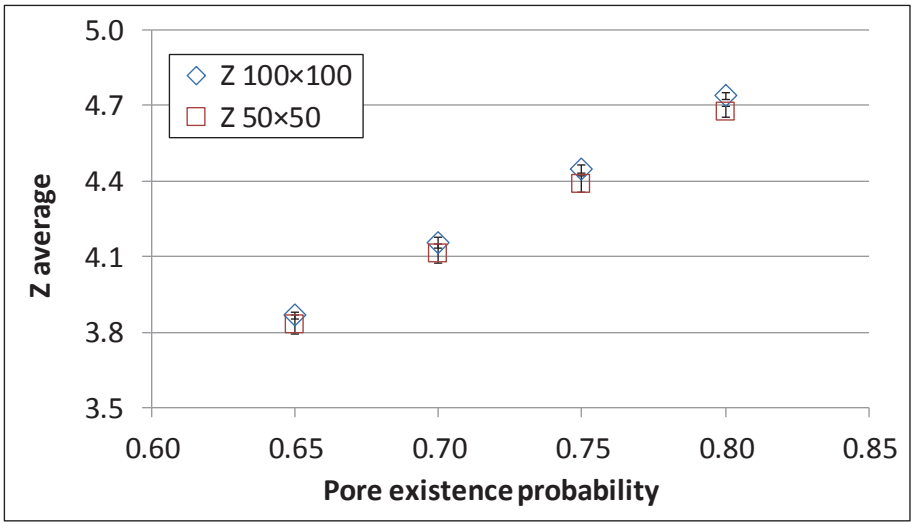


Fig. V-16. Mean connectivity according to the pore existence probability, *P*. 2D networks, Z_{max} = 6.

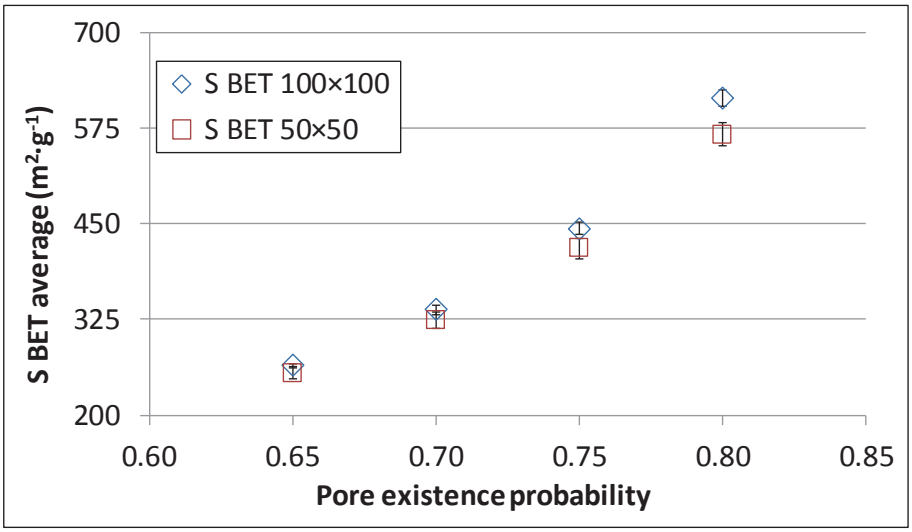


Fig. V-17. Mean s_{BET} according to the pore existence probability. 2D networks, Z_{max}=6.

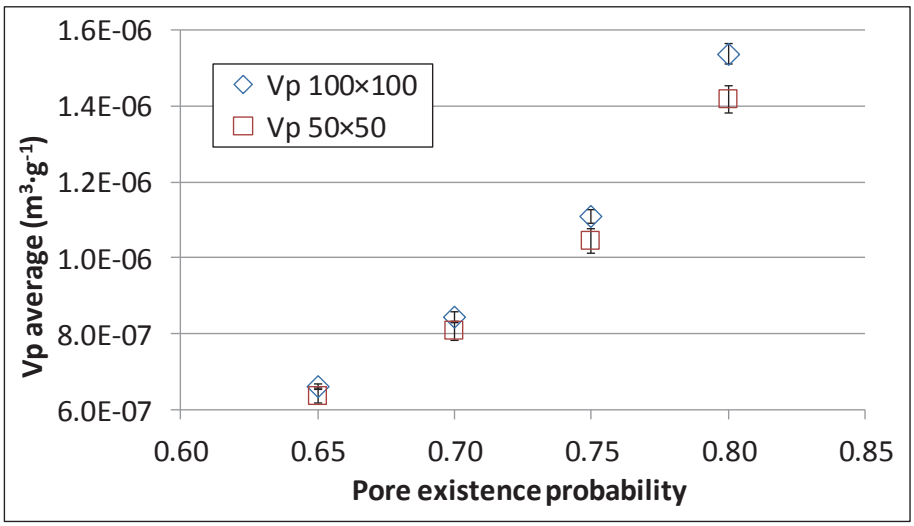


Fig. V-18. Pore volume according to the pore existence probability, *P*. 2D networks, Z_{max} = 6.

Extended data regarding 2D pore networks with a maximum connectivity of Z_{max}=4 is available in Appendix VI. The behaviour of the 2D square networks is similar to the one shown here for 2D triangular networks.

V.4.3 INFLUENCE OF THE PORE DIAMETER: D_P

In order to study the influence of the pore diameter on the textural properties, 30 pore networks were generated for two network maximum sizes 50×50 and 100×100. The corresponding mass transfer properties are presented further on, in section VI.3.3.

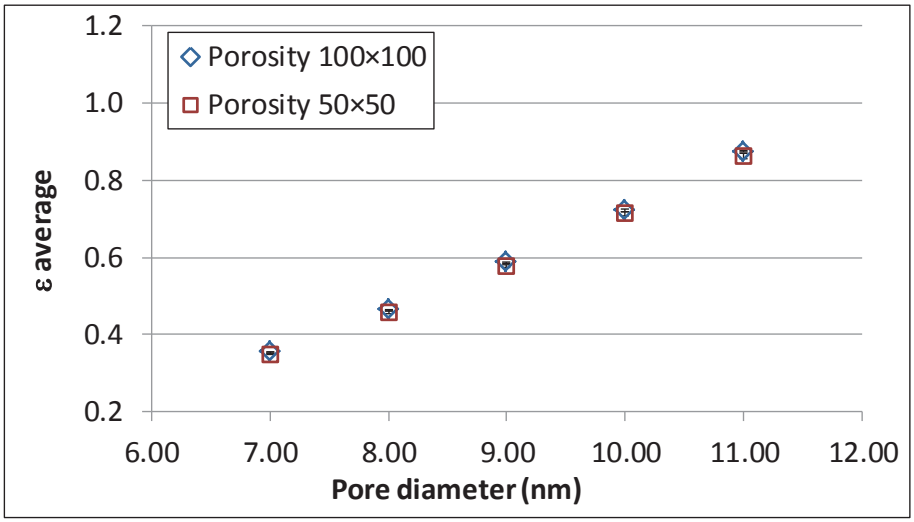


Fig. V-19. Porosity according to the pore diameter. 2D networks with Z_{max}=6 and P=0.7.

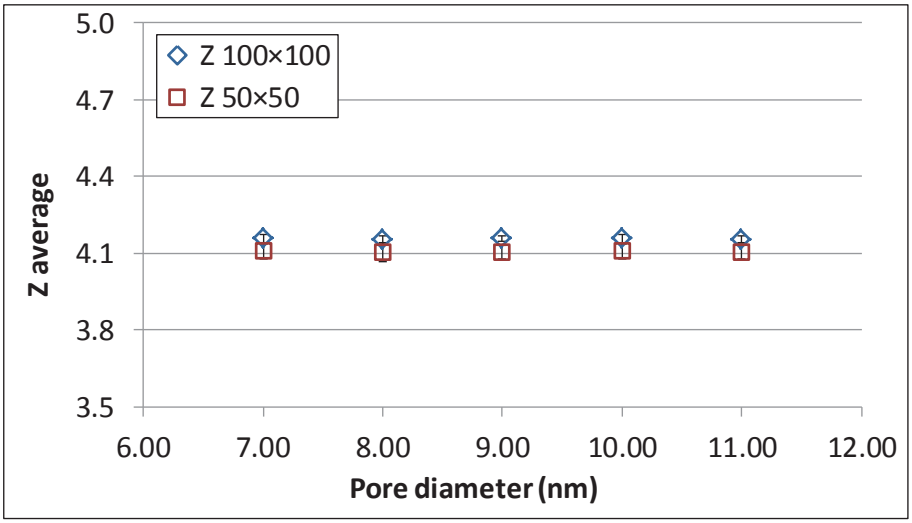


Fig. V-20. Connectivity according to the pore diameter. 2D networks with Z_{max}=6 and P=0.7.

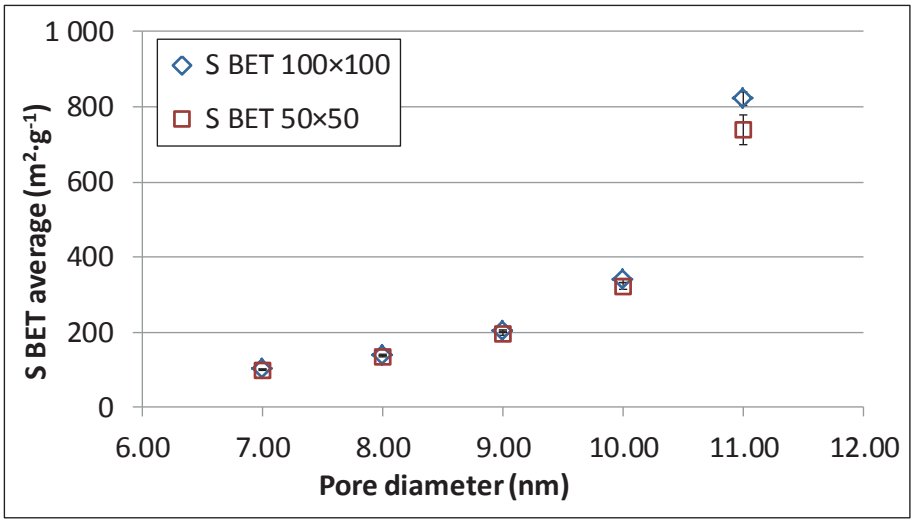


Fig. V-21. Specific surface area according to the pore diameter. 2D networks with Z_{max}=6 and P=0.7.

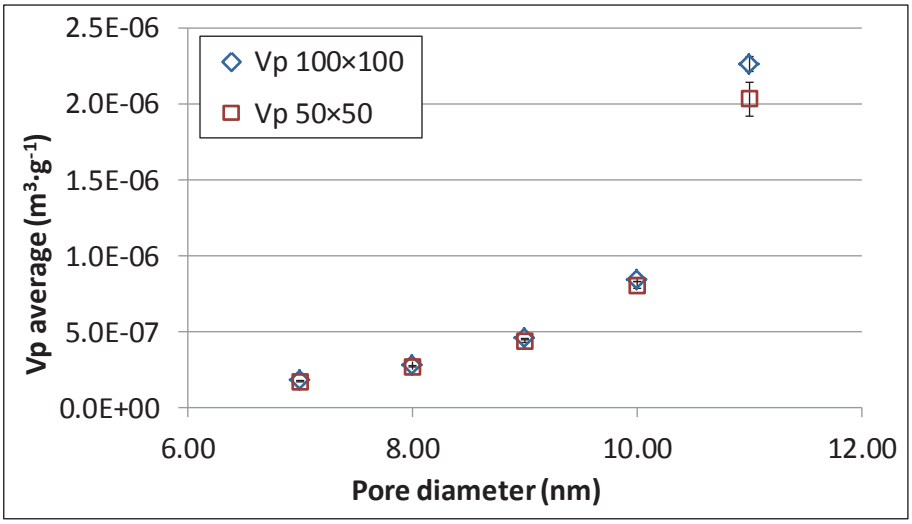


Fig. V-22. Pore volume according to the pore diameter. 2D networks with Z_{max}=6 and P=0.7.

Fig. V-19 to Fig. V-22 show that the mean textural properties increase with the increase in the pore diameter, except for the connectivity that remains constant, as expected. For the porosity, the effect of the pore diameter is quadratic, while the increase in the specific surface area is more than linear and the increase in pore volume is more than quadratic with increasing the pore diameter. This behaviour is in agreement with the equations used to calculate the textural properties (section IV.2.1). For both maximum network sizes (50×50 and 100×100), the standard deviations remain rather low.

V.4.4 INFLUENCE OF THE PORE LENGTH: L_P

The impact of the pore length on the textural properties was studied taking 30 pore networks for two network maximum sizes: 50×50 and 100×100 nodes. Available data on the mass transfer properties will be shown in section VI.3.4.

Fig. V-23 to Fig. V-26 show that as the pore length increases, the catalyst porosity, specific surface area and pore volume decrease while the average connectivity remains constant, as expected. The porosity can be represented by a hyperbolic function with respect to the square of the pore length, which is in agreement with the equations used to calculate the textural properties (section IV.2.1).

Comparing the results for the two maximum network sizes (50×50 and 100×100), similar values are obtained for the various textural properties, while the average connectivity increases slightly with the network size. Again, the calculated standard deviations remain rather low except for the average network connectivity.

Extended data regarding 2D pore networks with a maximum connectivity of Z_{max}=4 is available in Appendix VIII. The behaviour for these 2D square networks is similar to the one shown here for 2D triangular networks.

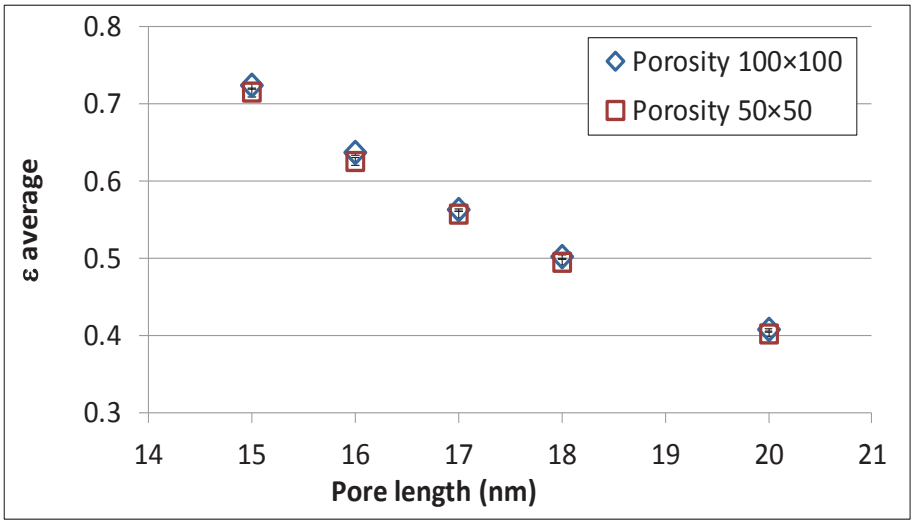


Fig. V-23. Porosity according to the pore length. 2D networks with Z_{max}=6 and P=0.7.

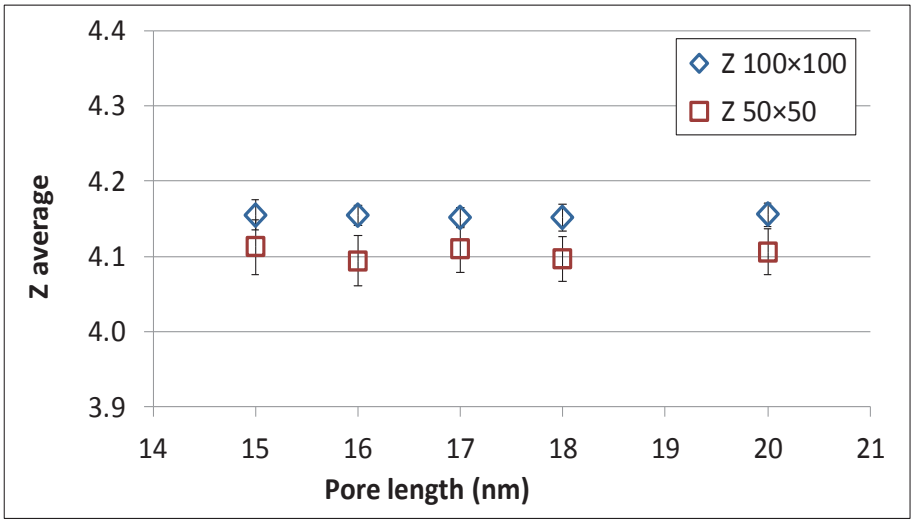


Fig. V-24. Connectivity according to the pore length. 2D networks with Z_{max}=6 and P=0.7.

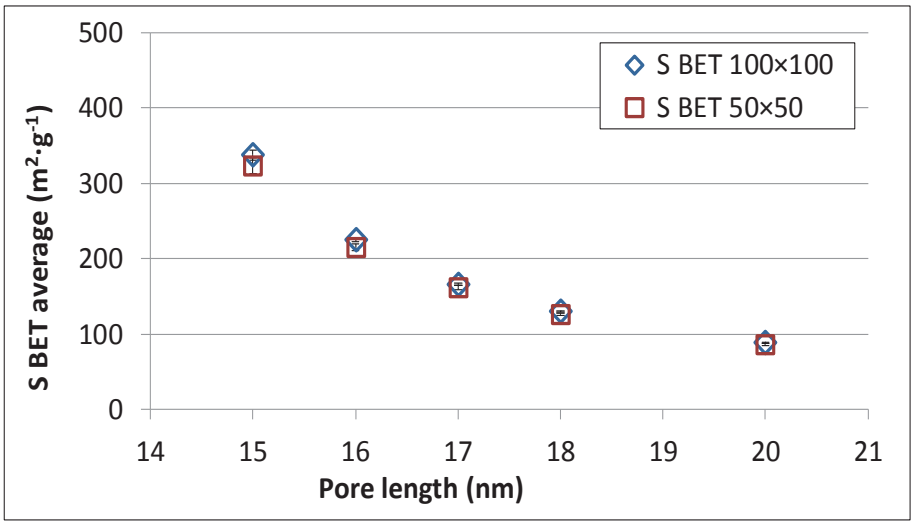


Fig. V-25. Specific surface area according to the pore length. 2D networks with Z_{max}=6 and P=0.7.

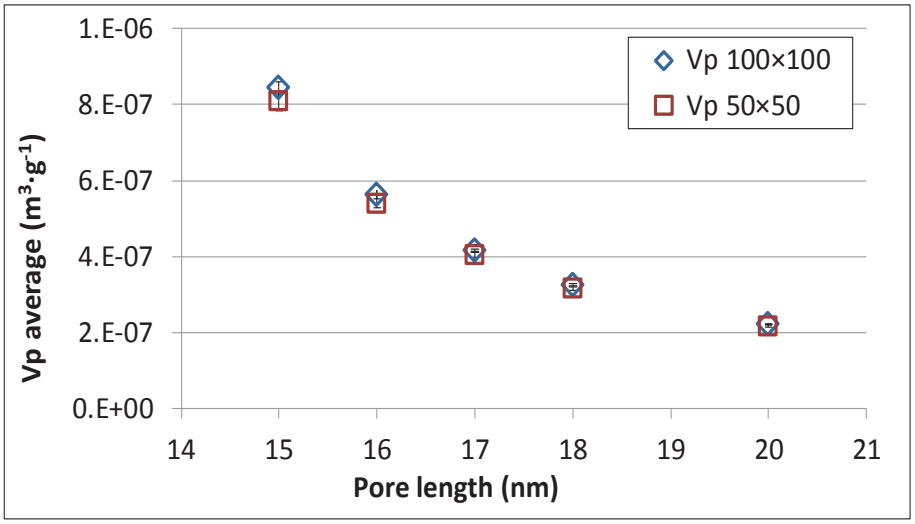


Fig. V-26. Pore volume according to the pore length. 2D networks with Z_{max}=6 and P=0.7.

V.4.5 RELATION BETWEEN THE AVERAGE CONNECTIVITY AND THE TEXTURAL PROPERTIES

The link between the network average connectivity, which is defined as the average of all the connectivities of the existing nodes within the pore networks, and the textural properties was studied taking 30 pore networks in 2D or 3D containing up to 10,000 nodes. We are here comparing two calculated properties of the model, the textural properties as a function of the average connectivity. Indeed, it is the variation of the pore existence probability that leads to the variation of the average connectivity. Different network configurations are used with maximum connectivities of Z_{max}=4 (2D square networks) and Z_{max}=6 (2D triangular and 3D cubic networks).

On Fig. V-27 to Fig. V-29 are gathered the textural properties as a function of the average connectivity with respect to the three network configurations: square (Z_{max}=4),

triangular (Z_{max}=6) and cubic (Z_{max}=6). On each type of network, different pore existence probabilities were used. For square networks, the probability inputs are: $P = \{0.80, 0.85, 0.90, 0.95, 0.98\}$, for triangular networks we used: $P = \{0.65, 0.70, 0.75, 0.8\}$ and finally, for cubic networks we have: $P = \{0.71, 0.77, 0.84, 0.90\}$.

As can be seen from Fig. V-27 to Fig. V-29, there is a unique behaviour of ε, s_{BET} and v_p as a function of the average connectivity, regardless the pore existence probability and the nature of the network: the three textural properties increase with the average connectivity. The porosity increases linearly with the average connectivity, while the increase in specific surface area and pore volume is faster than linear with increasing average connectivity. This behaviour is completely analogous to that of the pore existence probability and is in agreement with the equations used to calculate the textural properties, which have been derived in section IV.2.1.

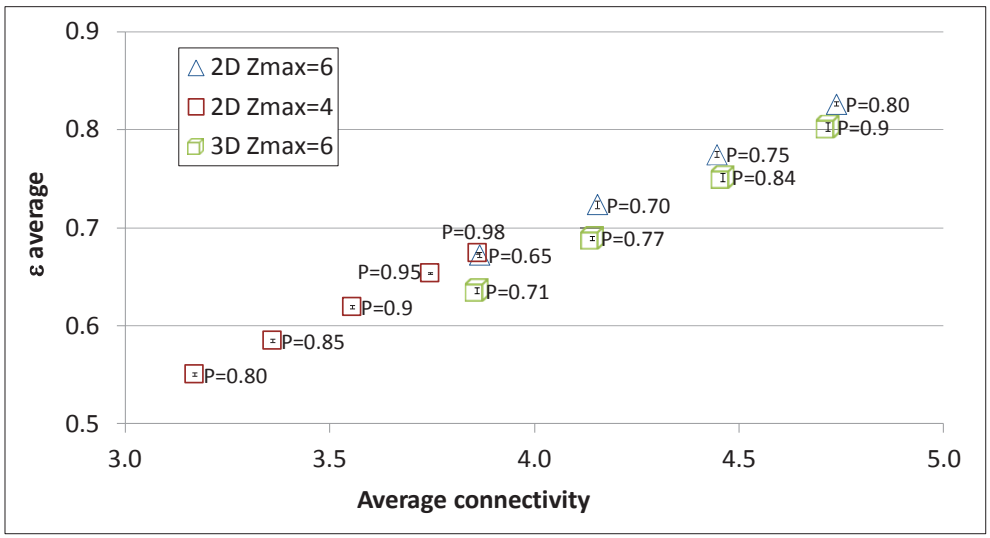


Fig. V-27. Catalyst porosity as a function of the average connectivity.

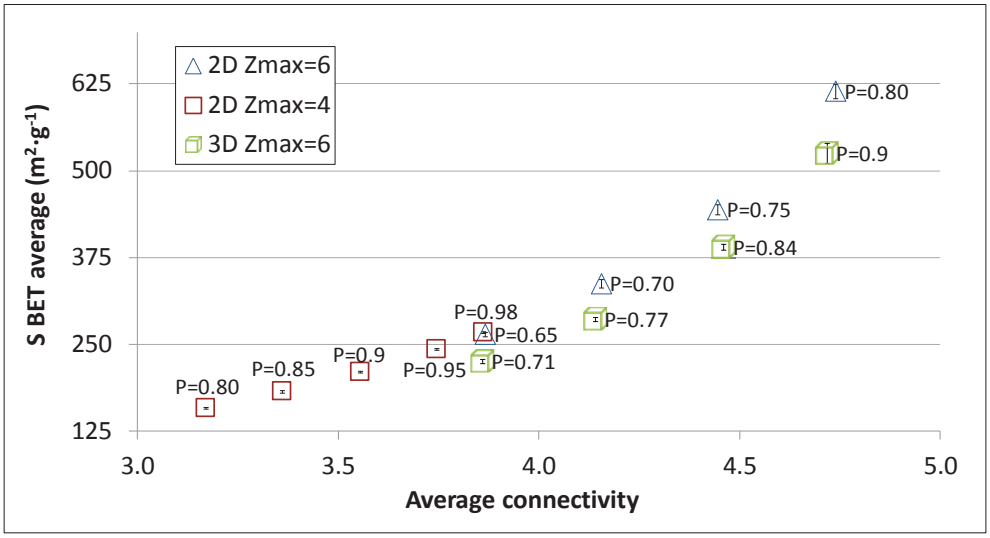


Fig. V-28. Specific surface area as a function of the average connectivity.

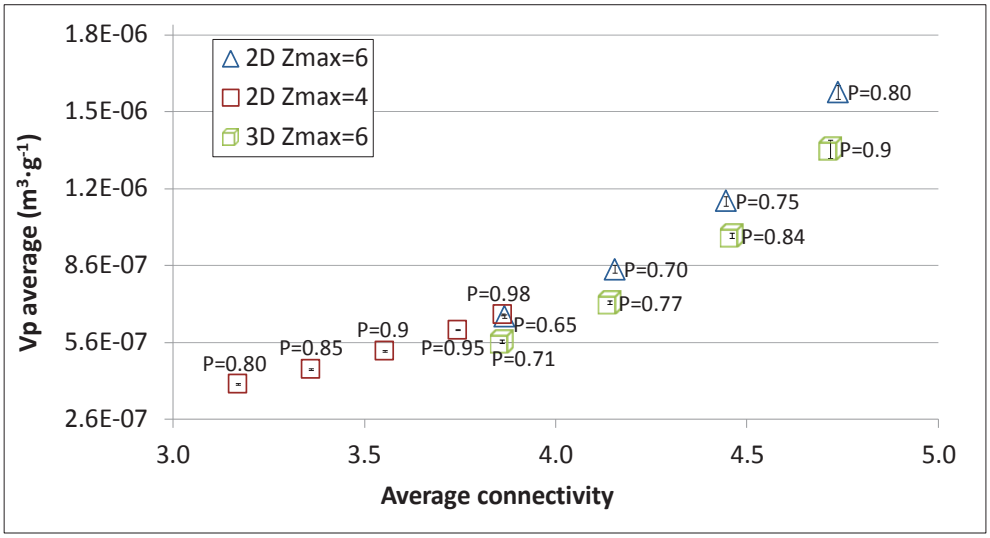


Fig. V-29. Particle pore volume as a function of the average connectivity.

If we compare the 2D Z_{max}=6 to the 3D Z_{max}=6 networks, Fig. V-27 to Fig. V-29 show that the 2D Z_{max}=6 has slightly higher values for the textural properties. Similarly, at an average connectivity of 3.86, where all three configurations cross, we can see that the 2D networks have somewhat higher values for the textural properties than the 3D Z_{max}=6 case, while similar textural properties are found for both the 2D Z_{max}=4 and the Z_{max}=6 configurations. Although this may seem in disagreement with the set of equations derived in section IV.2.1, we should recall that equations (IV-17) to (IV-19) are valid only for very large networks, because we neglected the fact that the nodes placed at the catalyst surface have lower connectivity (**Hypothesis 4**). Indeed, all pores directly connecting two inlet or outlet nodes are neglected. Hence, for a 3D network, the ratio of the number of surface nodes to the total number of nodes is larger than for a 2D network, resulting in a lower average connectivity for the same value of $Z_{max} \cdot P$. However, if larger networks are used, the differences between 2D and 3D networks decreases.

This case study also illustrates that we can generate pore network representations with widely varying properties: the catalyst porosity can go from 0.55 to 0.83, the specific surface area from 158 to 614 $m^2 \cdot g^{-1}$ and the pore volume from 3.95×10^{-7} to 1.54×10^{-6} $m^3 \cdot g^{-1}$.

As we have seen in this section, we are able to obtain similar textural properties using different geometrical configurations, the question that may be asked is: what are the mass transfer properties associated to these networks? Do they also have similar mass transfer properties?

V.5 CONCLUSIONS

From the Monte Carlo variability study, we have concluded that the initial or maximum network size (maximum number of nodes of the network) clearly impacts the textural properties of the networks. For different pore existence probabilities and for different network configurations, we have determined the required initial network size in order to reach constant textural properties. For instance, for a 2D Z_{max}=6 configuration and at a pore existence probability of 0.7 and at a maximum relative error of 5%, 10,000 nodes are required. We have also tested the influence of the number of samples on the calculated average values for the textural properties, and we showed that for the 2D Z_{max}=6 configuration and for P=0.7, 30 network samples are required to reach calculated values with a low standard deviation.

Concerning the sensitivity analyses, we may conclude that the increase on both the pore existence probability and the pore diameter, leads to an increase in the porosity, the specific surface area and the catalyst pore volume. We have also shown the positive correlation between these properties and the average connectivity of the network. Concerning the pore length, it has an opposite effect, the textural properties decrease when the pore length is increased. Regarding the separate study on the parallelepiped dimensions N_x and N_y, taking a 10,000 nodes network size, one observes rather constant standard deviations.

When looking at the values of the mean textural properties of the generated pore networks, we have shown that, by varying the input values, we can generate pore networks with widely varying properties: catalyst porosities ranging between 0.55 and 0.86, specific surface areas between 3.95×10^{-7} and 1.54×10^{-6} $m^3\cdot g^{-1}$ and pore volumes between 3.95×10^{-7} to 1.54×10^{-6} $m^3\cdot g^{-1}$. As these ranges comprise the values that are typical for commercial alumina supports, an optimization tool can be used to find the appropriate inputs in order to represent actual gamma alumina supports as characterized by their measured textural properties. A further chapter will be focusing on this part.

The next chapter will be dedicated to a sensitivity analysis of the Monte Carlo algorithm and of its parameters on the mass transfer properties for the studied pore networks presented in this chapter.

CHAPTER VI - MASS TRANSFER MODEL ANALYSIS

VI.1 INTRODUCTION

In order to test the mass transfer model, the analyses performed for the network generation algorithm, where the impact on the textural properties was observed (cf. Chapter V), is here applied to the continuum mass transfer properties, i.e. the effective diffusion coefficient or the diffusional tortuosity. Due to memory storage problems, the numerical solvers of the mass transfer model limit the sizes of the networks that can be simulated. Despite this, networks of 200×200 nodes containing up to 80,000 pores have been simulated. First, we will describe how to calculate the effective (macroscopic) mass transfer properties from the discrete (microscopic) 1D mass transfer simulation by diffusion through a periodic pore network.

VI.1.1 ESTIMATION OF THE EFFECTIVE DIFFUSION COEFFICIENT

In order to be able to compare data with some of the available theoretical and empirical correlations or with experimental data (Kolitcheff, 2017) relating the catalyst support tortuosity to its porosity, it is necessary to determine continuum mass transfer properties. To this end, we use the pore network mass transfer model as described in section IV.3.

As illustrated in Fig. VI-1, starting from an initial condition where the network has a concentration for species i equal to 0 everywhere, a concentration difference $\Delta c_i = c_{i1} - c_{i0} > 0$ of 1mol·m^{-3} is suddenly imposed at $t=t_0$ (step function) between the inlet and the outlet nodes of an infinite plate in the x direction. To satisfy the latter condition, a

periodic network in the *x* axis is built. For each pore belonging to the periodic network, mass transfer by diffusion is simulated using a molecular diffusion coefficient, D_{im}.

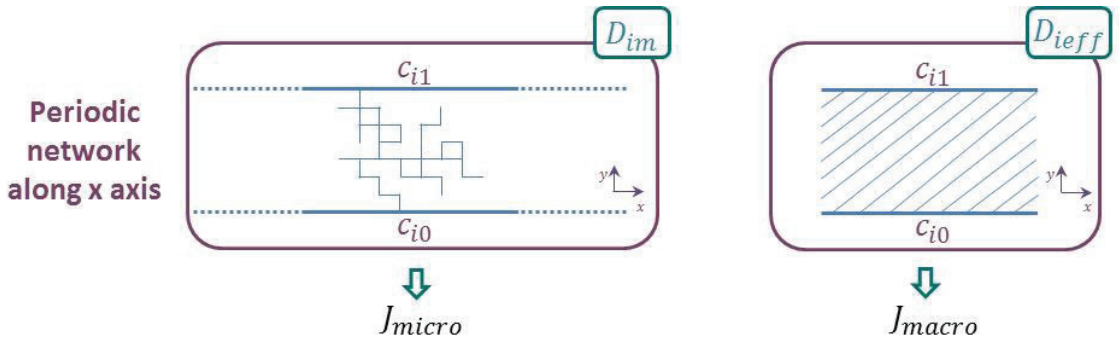


Fig. VI-1. Illustration comparing the discrete (microscopic) approach to a (macroscopic) continuum approach.

The outlet flux of species i is then calculated according to equation (VI-1) at the pore network level. In equation (VI-1), the sum is calculated over the pores placed at the outlet of the network.

$$J_i(mol \cdot m^{-2} \cdot s^{-1}) = \frac{\sum_p^{Np\ outlet} J_{ip} \cdot S_p}{\sum_t^{Np\ outlet} S_p} = \frac{\sum_p^{Np\ outlet} -D_{im} \cdot S_p \cdot \frac{\partial c_{ip}}{\partial l}}{\sum_p^{Np\ outlet} S_p} \quad \text{(VI-1)}$$

At the macroscopic level, the transfer process is assumed to occur only according to the *y* axis in a unique cylindrical straight fluid macropore. The effective diffusion coefficient is defined as follows (Ruthven, 1984):

$$J_i(mol \cdot m^{-2} \cdot s^{-1}) = -D_{i\,eff} \cdot \frac{\partial c_i}{\partial y} \quad \text{(VI-2)}$$

with D_{ieff} the effective diffusion coefficient and J_i the outlet flux in the periodic network. At the final steady state, the flux J_i is given by:

$$J_i(mol \cdot m^{-2} \cdot s^{-1}) = -D_{i\,eff} \cdot \frac{\Delta c_i}{L} \quad \text{(VI-3)}$$

with $L = (N_y - 1) \cdot L_p$ the thickness of the infinite plate. From this equation, the effective diffusion coefficient can be obtained as follows:

$$D_{i\,eff}(m^2 \cdot s^{-1}) = -J_i \cdot \frac{L}{\Delta c_i} \quad \text{(VI-4)}$$

As the molecular diffusion coefficient D_{im} used in the discrete simulations is known, the tortuosity can be calculated from equation (IV-5) (see Appendix I):

$$D_{i\,eff}(m^2 \cdot s^{-1}) = \frac{D_{im}}{\tau} \quad \text{(VI-5)}$$

In our simulations, we have taken for the molecular diffusion coefficient a value of D_{im}=$1 \times 10^{-10}\, m^2 \cdot s^{-1}$, which corresponds to the order of magnitude of a molecular diffusion coefficient in a liquid phase.

VI.2 MONTE CARLO ALGORITHM VARIABILITY

The 1D mass transfer simulation by diffusion was performed in order to investigate the sensitivity of continuum mass transfer properties to the algorithm, using the networks previously generated in Chapter V (only the required minimum network size influence from section V.3.1 is not here investigated in terms of mass transfer properties). The following sections show the results of this investigation.

VI.2.1 REQUIRED NUMBER OF SIMULATIONS

The estimation of the required number of simulations was performed using 1,000 2D networks of size 50×50 with a maximum connectivity of Z_{max}=6 and a pore existence probability of P=0.7.

The response of the effective diffusion coefficient is similar to that of the textural properties (see Fig. VI-2). The relative deviation decreases until reaching a constant value of 6.7%. Averaging over a sample of 1,000 simulations, the effective diffusion coefficient (D_{ieff}) amounts to 7.8×10^{-11} $m^2 \cdot s^{-1}$, while its standard deviation is 0.5×10^{-11} $m^2 \cdot s^{-1}$.

Again, for a sample with N values, the standard deviation of the mean is calculated as $s/\sqrt{n-1}$, while the confidence interval for the average is given by $\bar{X} \pm t_{0.95}(N-1) \cdot s/\sqrt{N-1}$. After dividing by the average value of the effective diffusion coefficient, the confidence interval can be expressed as a fraction of the average value. For a sample of 30 simulations, the confidence interval expressed as a relative deviation amounts to $2.042 \cdot 6.7\%/\sqrt{30-1} = 2.5\%$, which is considered to be sufficiently adequate.

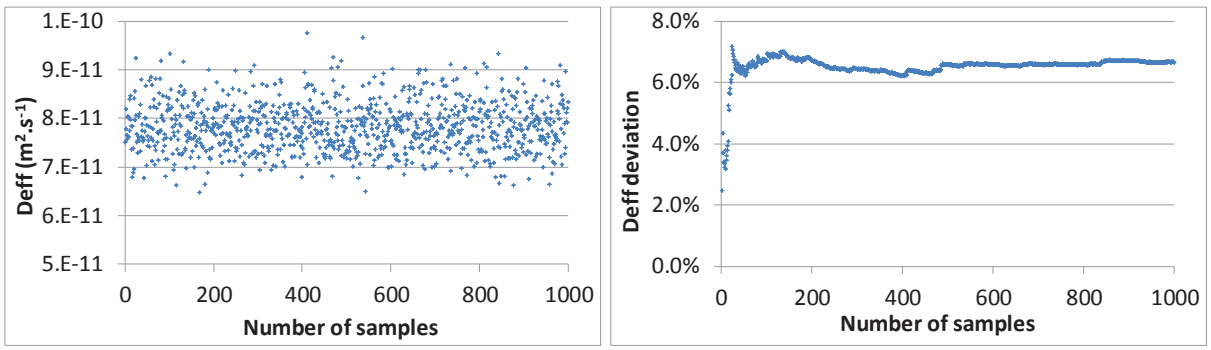


Fig. VI-2. Predicted effective diffusion coefficient of all 1000 2D networks of size 50×50 with Z_{max}=6 and P=0.7

We have gathered in the table below (Table VI-1) the relative deviations of each textural and mass transfer property for two different network sizes. One observes a considerable decrease in the relative deviation with the increase of the number of nodes of the network.

Table VI-1. Relative deviations from textural and mass transfer properties of 1000 generated pore networks.

Relative deviations	ε	Z_{avg}	S_{BET}	V_p	D_{ieff}
10×30	2.3%	2.2%	7.6%	7.6%	16.7%
50×50	0.8%	0.8%	2.7%	2.7%	6.7%

VI.3 INFLUENCE OF THE NETWORK GENERATION MODEL PARAMETERS

In this section are shown the continuum mass transfer properties regarding the sensitivity towards several network parameters, such as: the parallelepiped particle dimensions, the pore existence probability P, the pore diameter D_p and the pore length L_p. The relation between the textural properties and the average connectivity is also presented.

VI.3.1 INFLUENCE OF THE ASPECT RATIO N_X/N_Y WITH A CONSTANT MAXIMUM NUMBER OF NODES

The effective diffusion coefficients are here determined for the networks generated to study the influence on the particle dimensions N_x and N_y, N_z being equal to 1. The results for the textural properties have been shown in section V.4.1. This study was performed taking an identical maximum number of nodes of 10,000 nodes and testing the influence of the aspect ratio N_x/N_y. The pore networks are 2D triangular and periodic along the x-axis, therefore representing an infinite plate. In the mass transfer simulations, diffusion will occur along the direction of the y-axis.

For network sizes 10×1000, 20×500, 50×200, 200×50 and 500×20 containing an equal maximum number of nodes, the mean and standard deviations of the mass transfer properties are graphically represented on Fig. VI-3 and Fig. VI-4, while the textural properties have been discussed in section V.4.1.

Fig. VI-3 contains for each network size, the 30 pore networks previously presented that have been mass transfer simulated in order to obtain the corresponding tortuosity. As we

can see from this figure (Fig. VI-3), the dispersion of the results is very clear for lower N_x and this is confirmed in Fig. VI-4.

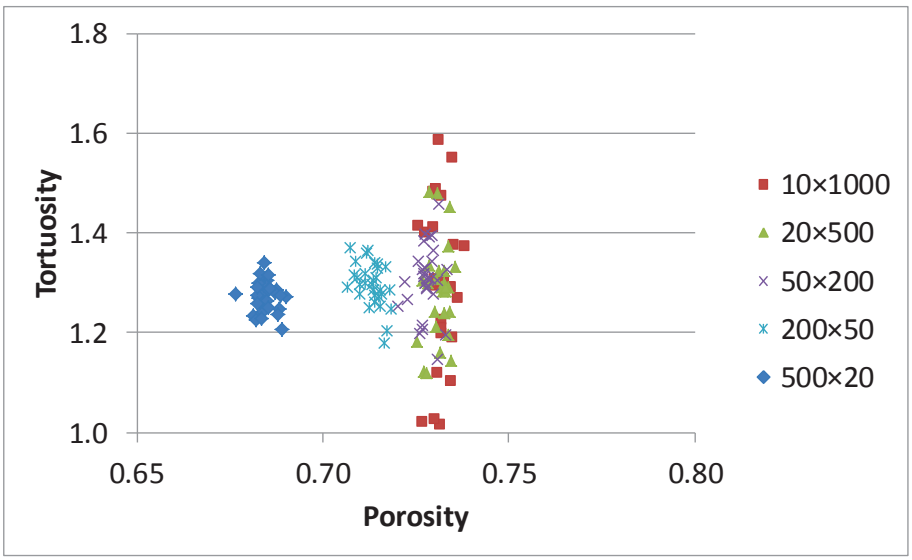


Fig. VI-3. Predicted tortuosity from mass transfer simulations as a function of the catalyst porosity for 5 different 2D Z_{max}=6 network sizes according to N_x/N_y.

Fig. VI-4 shows the average tortuosities for each network size varying between 1.26 and 1.31 for a porosity ranging from 0.68 to 0.73. The aspect ratio N_x/N_y of the pore network does not seem to have a significant impact on the average tortuosity. The overall average tortuosity amounts to 1.28 for an overall average porosity of 0.72.

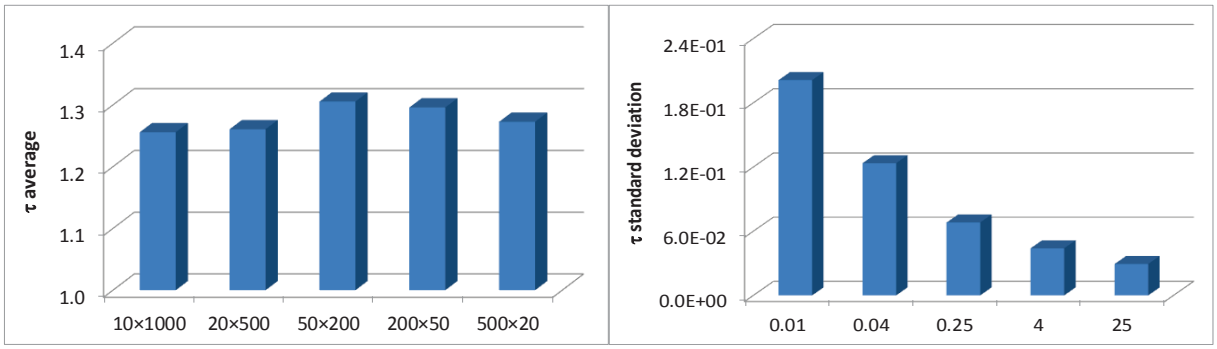


Fig. VI-4. Predicted tortuosity for 5 different 2D Z_{max}=6 network sizes as a function of the aspect ratio N_x/N_y.

When analysing the standard deviation of the tortuosity factor (Fig. VI-4), a lower standard deviation is observed for higher values of N_x, that is for lower values of N_y. This result may be explained as follows: for low values of N_x, a narrow (but thick) sample system is infinitely repeated along the x-axis, while for high values of N_x, a wide (but thin) sample system is infinitely repeated along the x-axis. This means that, for low values of N_x, there is a limited number of diverse pathways through the infinite plate, while, for high values of N_x, the number of diverse pathways through the infinite plate will be much higher. Hence, one can expect that for higher values of N_x, the impact of more "extreme" paths between the inlet and outlet nodes (either with τ=1 or with τ>>1) will be limited because it will be averaged out over a large number of tortuous pathways.

Moreover, if we increase the characteristic length of diffusion, that is if we increase N_y, the probability to find a given amount of bends along the y axis also increases and the dispersion of the results that is the standard deviation increases. Thus, as N_x increases and N_y decreases the standard deviation of the tortuosity will decrease, even though the average tortuosity does not significantly depend on the aspect ratio N_x/N_y.

We shall recall that N_x and N_y have a similar impact on the textural properties, while for the mass transfer properties and due to the fact that diffusion only occurs in the *y* direction for periodic networks along the *x*-axis, their impact differs.

This study on the impact of the aspect ratio N_x/N_y was also performed for square 2D pore networks (2D Z_{max}=4) and a similar behaviour was observed (cf. Appendix V).

VI.3.2 INFLUENCE OF THE PORE EXISTENCE PROBABILITY: *P*

The tortuosity (τ) obtained via the mass transfer simulation for the several networks presented in section V.4.2, is represented in Fig. VI-5 as a function of porosity and for several pore existence probabilities. Numerous theoretical correlations (Wakao and Smith, 1962; Tomadakis and Sotirchos, 1993; Beeckman, 1990) and empirical correlations (Weisz and Schwartz, 1962; Akanni and Evans, 1987) for porous catalysts are also available, and large variations can be observed depending on their hypotheses or origin.

From Fig. VI-5, we observe a decrease in the tortuosity factor with the catalyst porosity, which is an expected behaviour. If we reduce the pore existence probability, we remove a certain number of pores resulting in a lower porosity and creating a more tortuous path for the diffusing molecules. When comparing the simulated data, the lowest network size 50×50 has a larger standard deviation than the 100×100 network size, as expected, but the average tortuosities are similar for the two network sizes.

Concerning the theoretical and empirical correlations, the correlation from Tomadakis and Sotirchos (1993) has similar values to those simulated (1.16 to 1.40 ± 0.06). Indeed, this theoretical correlation is based on the simulation of random arrays of cylinders, quite similar to the pore networks that are being studied.

Additional data regarding 2D pore networks with a maximum connectivity of Z_{max}=4 is available in Appendix VI, where a similar trend for the relation of the tortuosity-porosity was observed for the 2D square networks. However, for a given porosity, the tortuosity values for the 2D square networks are different from the tortuosities obtained for 2D triangular networks (this is also observed in section VI.3.5). Contrary to what the correlations stick to, this observation leads us to the conclusion that the catalyst porosity

is not the only factor that comes into play in the tortuosity variation, but that the geometry of the porous structure is also critical.

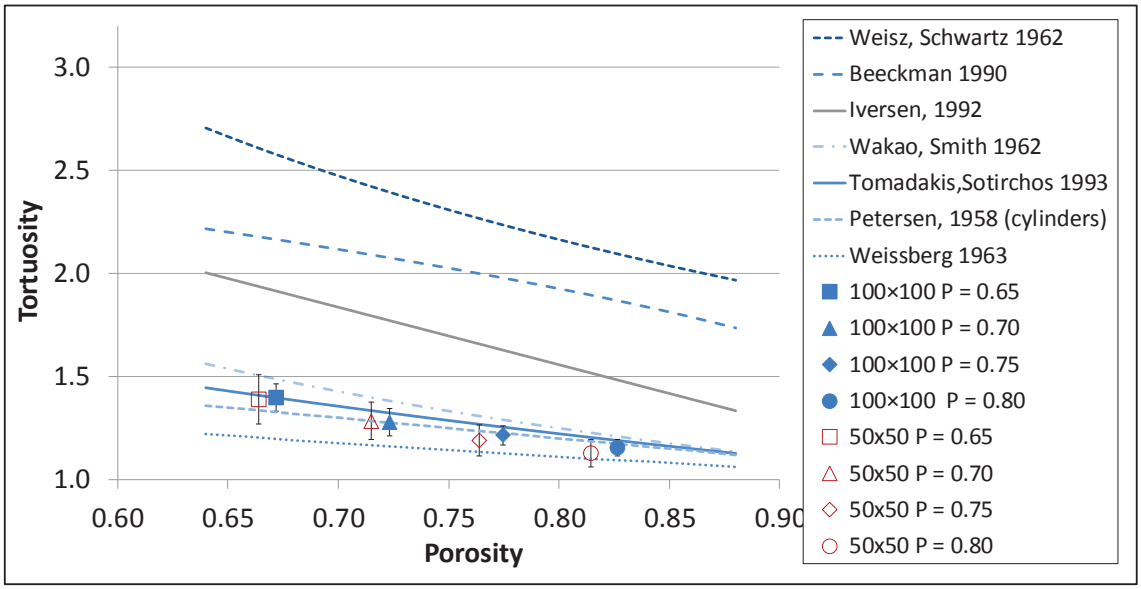


Fig. VI-5. Variation of the predicted tortuosities as a function of porosity for several pore existence probabilities. Correlations taken from Akanni and Evans (1987), Beeckman (1990), and Shen and Chen (2007).

VI.3.3 INFLUENCE OF THE PORE DIAMETER: D_P

In order to study the influence of the pore diameter on the mass transfer properties, mass transfer by diffusion was simulated within the 30 pore networks generated for each D_p from section V.4.3. Fig. VI-6 shows that the pore diameter does not influence the continuum mass transfer properties. Indeed, the simulated mass transfer is governed not by the diameter of the pore (Reyes *et al.*, 1989) but by its length, since our model is based on a 1D diffusion simulation.

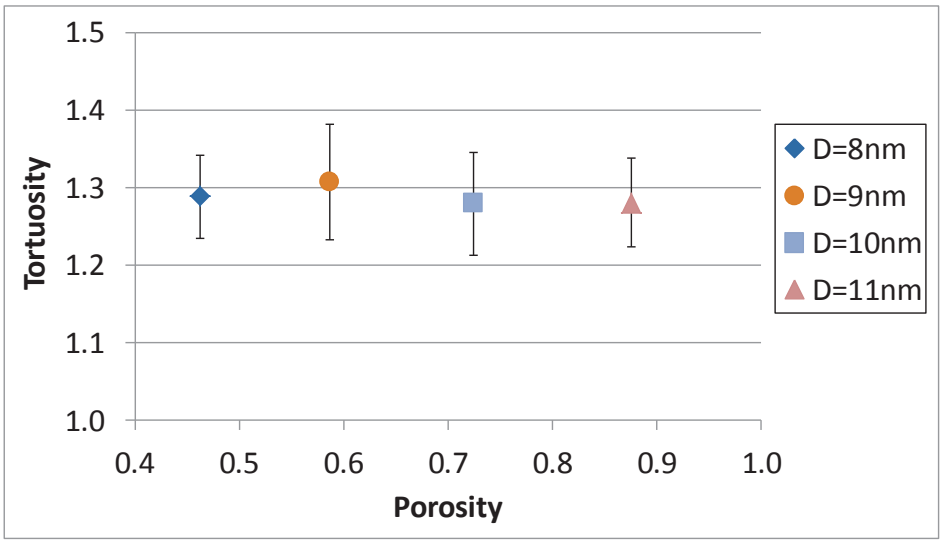


Fig. VI-6. Variation of the average predicted tortuosities as a function of porosity for several pore diameters. 2D networks with Z_{max}=6 and P=0.7 and a network size of 100×100.

Further data obtained for 2D square pore networks with maximum connectivity Z_{max}=4 and a pore existence probability of P=0.97 is available in Appendix VII. The same behaviour is found comparing the 2D square networks.

VI.3.4 INFLUENCE OF THE PORE LENGTH: L_P

The impact of the pore length on the mass transfer properties was studied simulating the diffusion process on the 30 pore networks studied for each L_p on section V.4.4. For each generated network, mass transfer by diffusion within an infinite plate was simulated in order to calculate the average tortuosity.

The diffusive data presented in Fig. VI-7 shows that the tortuosity factor keeps a constant value when varying the pore length. This may seem surprising because the pore length governs the mass transfer process by diffusion, as mentioned in the previous section (VI.3.3). However, in our pore networks $N_y=E_y/L_p$ (see section IV.2) and as we increase the pore length L_p, we also increase E_y with constant N_y (fixed network size). This means that the increase in the pore length generates an increase in the characteristic continuum length of diffusion (plate thickness), therefore showing no impact on the mass transfer properties although the porosity decreases. The mean tortuosity found takes a value of 1.29±0.06 for average porosities varying from 0.40 to 0.72.

Additional data regarding 2D pore networks with a maximum connectivity of Z_{max}=4 is available in Appendix VIII. The same behaviour was observed for the 2D square networks.

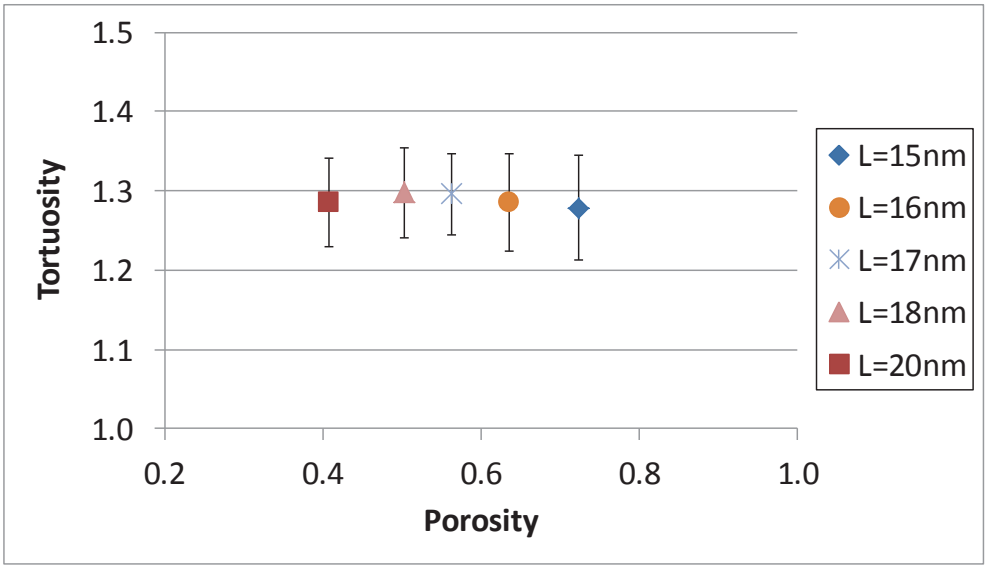


Fig. VI-7. Variation of the average predicted tortuosities as a function of porosity for several pore lengths and taking 2D pore networks with Z_{max}=6 and P=0.7.

VI.3.5 RELATION BETWEEN THE AVERAGE CONNECTIVITY AND THE MASS TRANSFER PROPERTIES

The impact of the network connectivity on the mass transfer properties was studied taking the 30 pore networks in 2D or 3D containing up to 10,000 nodes with different configurations, as shown in section V.4.5, where the textural properties were discussed. It is also recalled that the average connectivity was varied by modifying the maximum connectivity and by modifying the pore existence probability.

Fig. VI-8 shows a clear correlation between the network average connectivity Z_{avg} and the tortuosity: for a given network configuration the tortuosity decreases with increasing Z_{avg} as expected.

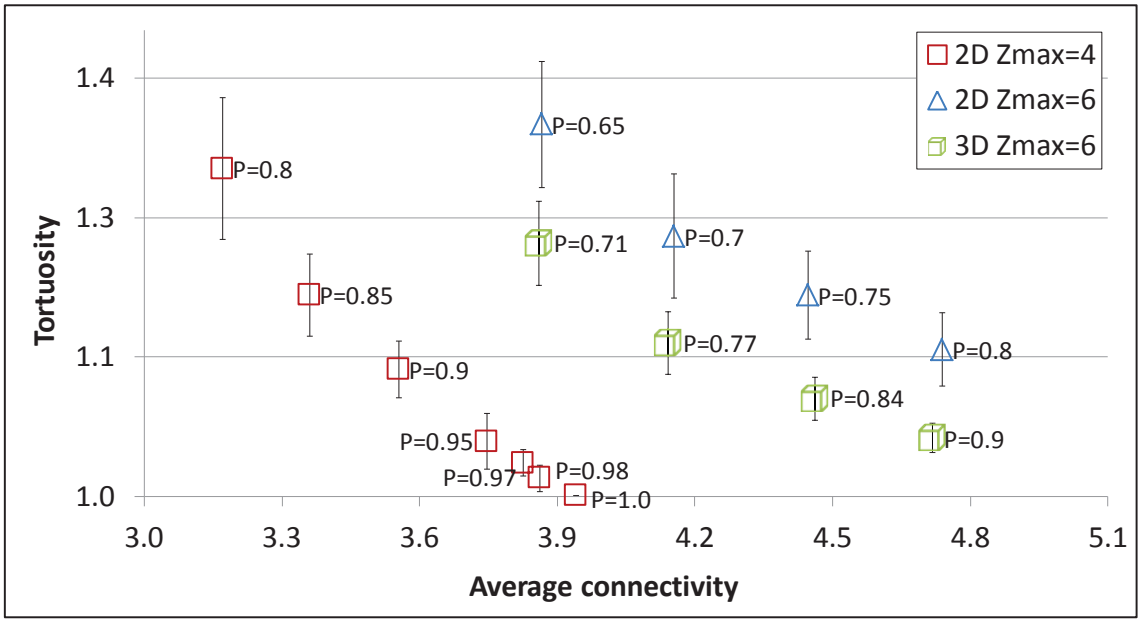


Fig. VI-8. Variation of the predicted tortuosities as a function of the average connectivity, having varied the pore existence probability. 3 sets of data are available: 2D Z_{max} =4, 6 and 3D Z_{max}=6.

Comparing the 2D square (P=0.98) with 2D triangular (P=0.65) and 3D cubic networks (P=0.71), for a given average connectivity, the tortuosity increases with the maximum connectivity Z_{max} and is greater in a 2D network than in a 3D network, for the same Z_{max}. This is probably due to the lower pore existence probability that is used for 2D triangular networks than for 3D cubic networks and subsequently, for 2D square networks.

We may recall that at equal average connectivities, we have observed in section V.4.5 that the textural properties of the three different configurations have similar values. So, this leads us to conclude that at equal average connectivities and similar catalyst porosities (cf. section V.4.5, Fig. V-27), it is the non-isotropy of the system (different pore existence probabilities for the three configurations) that will make a difference on

the tortuosity factor, regardless of the initial configuration of the network. This also means that the porosity is not necessarily the key-parameter but could rather be the "surface porosity" defined as the ratio of the pores surface with a projection in the diffusion direction and the total surface of pores.

VI.3.6 COMPARISON OF THE PREDICTED TORTUOSITIES WITH THE EFFECTIVE MEDIUM THEORY FOR CONSTANT PORE DIAMETERS

We have also compared, the relation of the tortuosity with the average connectivity to the apparent tortuosity obtained via the effective medium theory (EMT), see section III.2.1.2 and equation (III-23). The results obtained in Fig. VI-9 are averages from 30 pore networks for each pore existence probability. From this figure, it is clear that for all configurations the EMT tortuosities are very high compared to the predicted tortuosities. Taking the EMT tortuosities, at equal average connectivity, the different network configurations give an identical tortuosity whereas the simulated tortuosities differ.

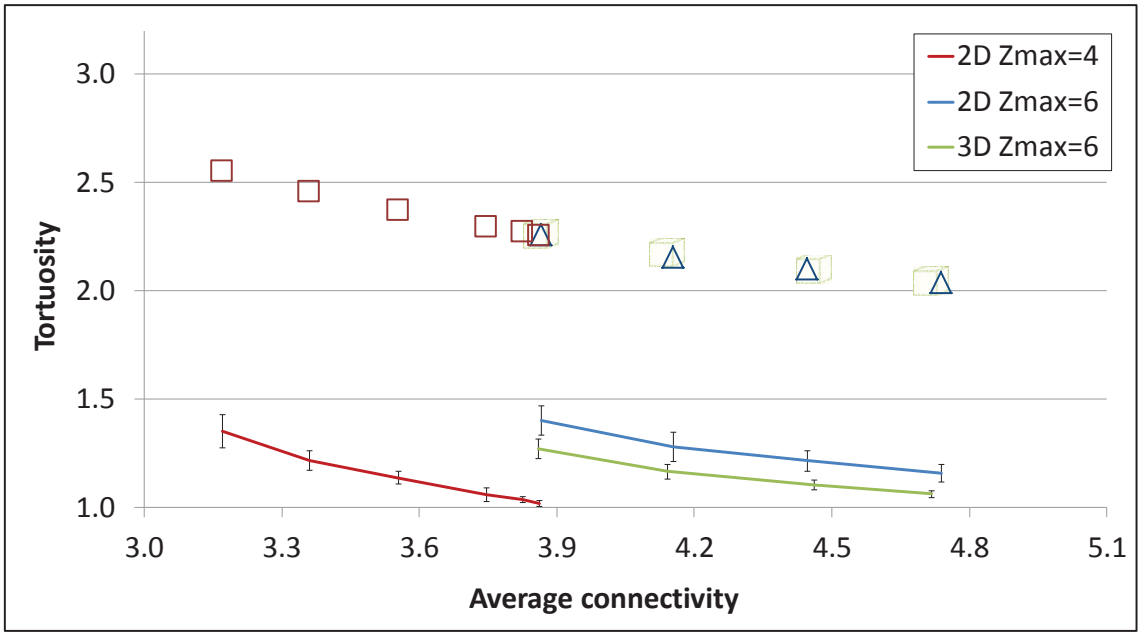


Fig. VI-9. Comparison of the predicted tortuosities (curved lines) as a function of the average connectivity to the apparent tortuosities obtained via the EMT (dotted plots), having varied the pore existence probability. Taking 2D networks with constant pore diameter and length.

Even though it has not been represented on Fig. VI-9, we have also observed that for both 2D configurations and at a pore existence probability of P=1.0, the value of the apparent tortuosity obtained from the EMT abruptly decreases to a value of 1.62 for 2D Z_{max}=4 with Z_{avg}=3.94 and to a value of 1.87 for 2D Z_{max}=6 with Z_{avg}=5.92. If we look at the predicted tortuosities obtained via our model, for networks having P=1.0, the tortuosity factor takes simply the value of τ=1.0.

VI.3.7 COMPARISON OF THE PREDICTED TORTUOSITIES WITH THE EFFECTIVE MEDIUM THEORY FOR PORE DIAMETER DISTRIBUTED NETWORKS

In the previous section VI.3.6, the comparison of the simulated tortuosities to the tortuosities obtained from the application of the effective medium theory was performed for networks with a constant pore diameter and a constant length. In this section, we intend to compare both approaches for networks with a pore diameter distribution, while keeping a constant length.

To this aim, we have generated, for each tested probability, thirty 2D triangular networks (Z_{max}=6) with a similar pore number distribution with a left skewed shape, as illustrated in Fig. VI-10.

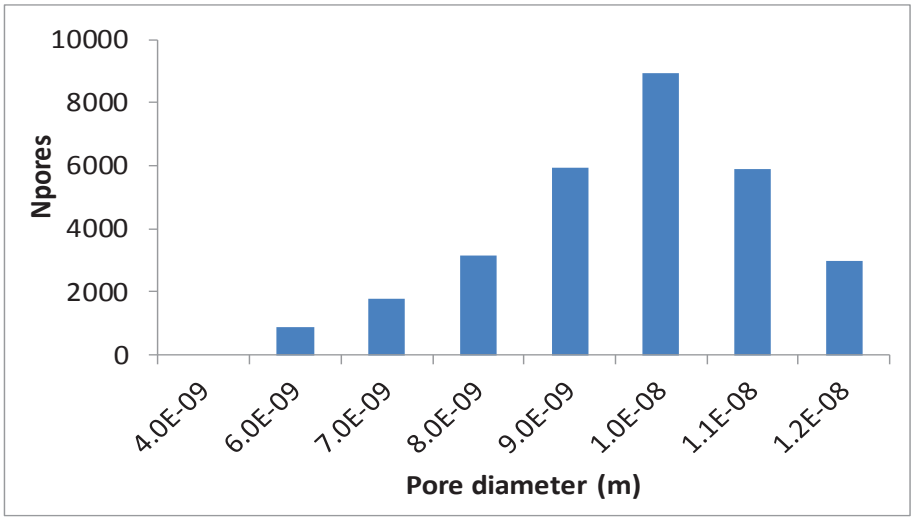


Fig. VI-10. Illustrative pore diameter distribution taken from a 2D triangular network with P=1.0 used in the comparison of the predicted tortuosities with the EMT.

We have gathered in Fig. VI-11, for several pore existence probabilities: $P = \{ 0.7, 0.8, 0.9, 1.0 \}$, the simulated and calculated EMT tortuosities.

As we can see from Fig. VI-11, both approaches present a similar behaviour, i.e. the tortuosity decreases with the increase in average connectivity. We also observe that the effective medium theory keeps overestimating the tortuosity values, as already shown for networks with constant diameter and pore length.

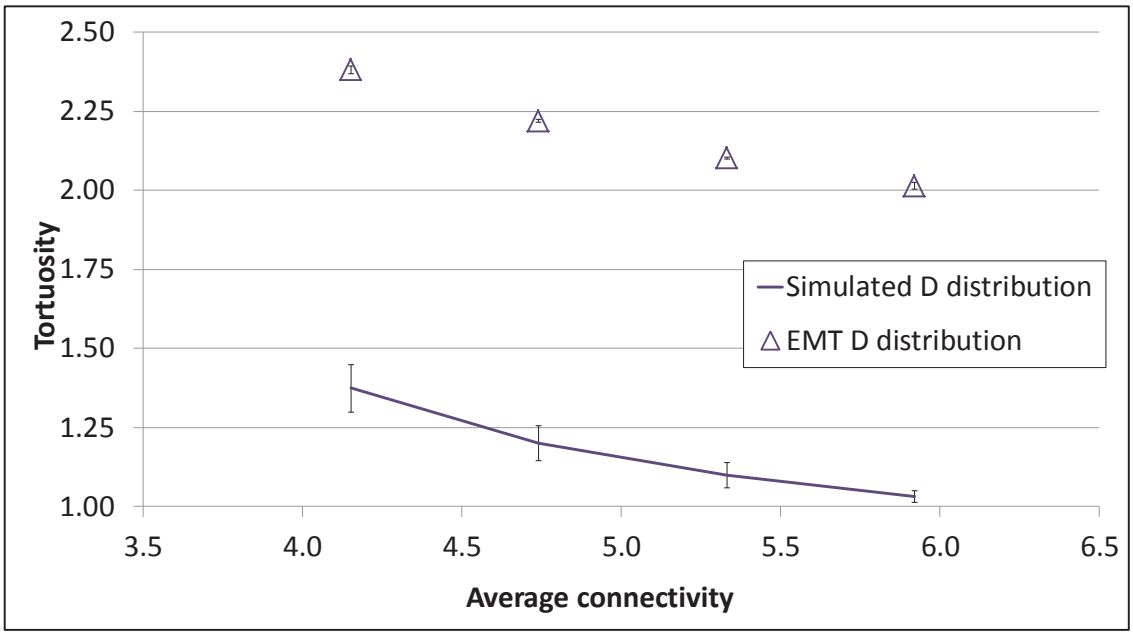


Fig. VI-11. Comparison of the predicted tortuosities as a function of the average connectivity to the apparent tortuosities obtained via the EMT, having varied the pore existence probability. Taking 2D networks with Z_{max}=6 and a pore diameter distribution.

VI.4 CONCLUSIONS

From the Monte Carlo variability study, we have concluded that after simulating 1000 pore networks with 2D Z_{max}=6 and P=0.7, the relative deviation (= standard deviation / mean value) of the effective diffusion coefficient levels off at a value of 6.7%. For a sample of 30 simulations, a standard error on the mean effective diffusion coefficient represents a relative error of 1.3%.

Concerning the various sensitivity analyses performed, we can conclude that the variation of the pore diameter does not influence the mass transfer properties as a consequence of the main hypothesis of our model of 1D diffusion at the microscopic scale. The pore length on the other hand completely governs the mass transfer simulation at the microscopic scale. However, at the macroscopic scale, we have actually obtained constant tortuosity factors when the pores length was varied yet, this is merely due to the fact that when we increased the pore length, the thickness of the periodic plate was also increased, as the number of nodes was kept constant at $N_y=E_y/L_p$.

The sensitivity analysis performed on the pore existence probability, where we have put in evidence a graphical representation of the tortuosity as a function of the catalyst porosity, infers that the increase in the pore existence probability reduces the tortuosity factor. This was an expected result since reducing the probability leads to a removal of more pores thereby creating more tortuous pathways, hence increasing the tortuosity factor. The comparison of the correlated tortuosity data with the simulated tortuosities is

in agreement with the Tomadakis and Sotirchos (1993) correlation. This is also consistent since this specific correlation is based on the simulation of random arrays of cylinders very similar to those we generate.

From the relation between the tortuosity with the average connectivity, a unique behaviour is exhibited, whatever the pore existence probability and the nature of the network. At identical average connectivities, we observed that all 3 configurations led to rather similar porosities (cf. section V.4.5, Fig. V-27). So, for constant average connectivity and at iso-porosity, we could say that regardless the initial network configuration (Z_{max}), it is the non-isotropy of the system that comes into play i.e. the decrease in pore existence probability. For the highest tortuosity obtained, the lower the pore existence probability is used amplifying the anisotropy of the system.

Regarding the parallelepiped dimensions N_x and N_y, the increase in the aspect ratio N_x/N_y at equal initial network sizes shows a reduction on the standard deviation of $D_{i,eff}$. As the number of diffusive pathways increases with increasing aspect ratio, the dispersion in the tortuosity results is decreased.

The comparison of the simulated tortuosities as a function of Z_{avg} with the effective medium theory (EMT) shows that this theory overestimates the simulated tortuosity values.

We have observed in this chapter that the tortuosity factors obtained via the simulation of our 2D and 3D networks are rather low ($\tau<1.5$) when compared to the experimental data that yields values ranging from 2 to 3.

DYNAMIC STUDY

CHAPTER VII - DYNAMIC BEHAVIOUR OF THE SYSTEM

In this section, we intend to compare the transient behaviour of both the discrete and the pseudo-homogeneous continuum models, once the tortuosity is determined from the steady state behaviour, as described in section VI.1.1. This study can be very important to validate the continuum representation and it could also be a future tool to the comparison with experimental transient data obtained via inverse chromatography, as we have been comparing the simulated tortuosity factors to experimental tortuosities estimated by this technique.

First, we will show some introductory and very simple case studies regarding the discrete dynamic response only in order to understand the effects of dead volumes, and of the network volume.

A preliminary example is then studied where the transient mass transfer responses of the discrete and the pseudo-homogeneous models are compared using a 2D triangular network with P=1.0. We may recall that the discrete model makes use of a molecular diffusion coefficient and the continuum model uses an effective diffusion coefficient in a single pore with a macroscopic pore length that is equal to the plate thickness of the pore network (discrete model). The comparison of the two models is based on the outlet flux.

Subsequently, we pursued the study by comparing, for simple cases, the dynamic responses of the discrete model and the pseudo-homogeneous model. Finally, the development towards our general 2D networks is presented.

VII.1 INTRODUCTORY CASE STUDIES FOR THE DISCRETE MODEL

In this section, the dynamic response of the discrete model is studied. The effects of the network volume, the presence of a dead volume and also of the initial conditions are

considered, the latter being available in Appendix IX. In the simulations performed, we have used constant pore diameter of 10×10^{-9} m and a constant pore length of 15×10^{-9} m.

VII.1.1 EFFECT OF THE NETWORK VOLUME

In order to understand the effect of the pore volume on the dynamic response of a pore network, we have simulated the dynamic response for CS 1. This is simply a discrete model with three pores in series. In the simulations, three different diameters for the horizontal pore, D_2 (2nd pore, cf. Fig. VII-1) were used. The chosen diameters for this 2nd pore are given in Table VII-1.

Table VII-1. Effect of the network volume on the dynamic responses. Variation of the 2nd pore diameter.

CS	Diameter, m	Volume of the 2nd pore (V_2), m^3	Network pore volume (V_{pores}), m^3
1a	$D_2 = D = 10 \times 10^{-9}$	V	1.77×10^{-24}
1b	$D_2 = \sqrt{2} \cdot D$	$2 \cdot V$	2.26×10^{-24}
1c	$D_2 = \sqrt{3} \cdot D$	$3 \cdot V$	2.95×10^{-24}

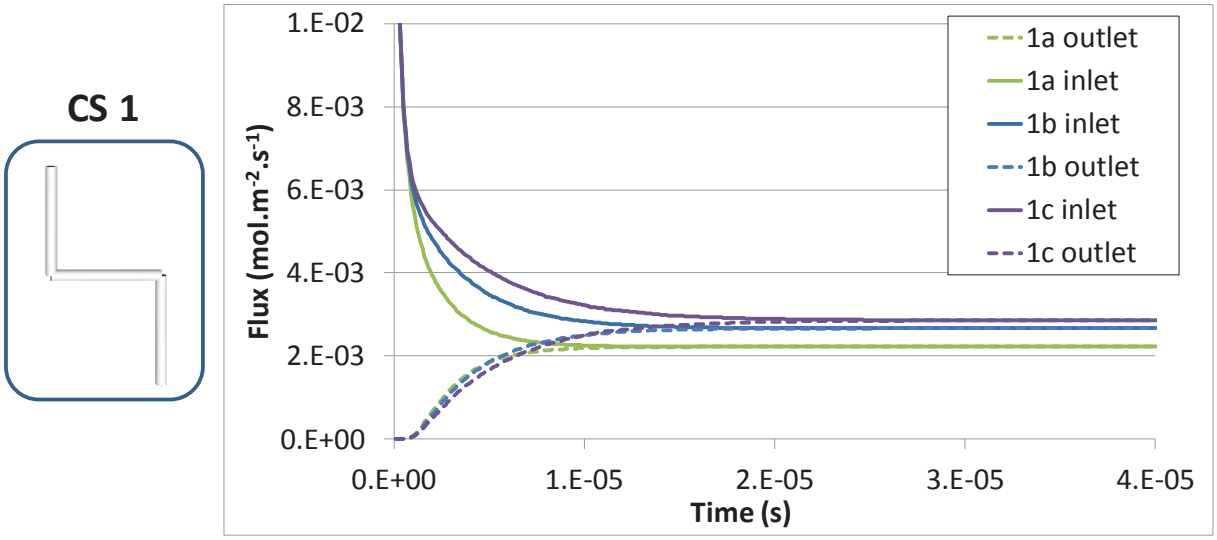


Fig. VII-1. Dynamic responses of the inlet and outlet flux for CS 1, having varied the diameter of the horizontal pore.

For these three different diameters, the dynamic responses in terms of inlet and outlet flux are represented graphically in Fig. VII-1. A binary mixture is used with species *A* diffusing from the inlet node at the top of the network to the outlet node that is positioned at the bottom. The initial condition with respect to species *A* is $c_A(l, t = 0) =$

$0\ mol \cdot m^{-3}$ and the boundary conditions at the inlet and outlet nodes are: $c_{A\ inlet} = 1$ and $c_{A\ outlet} = 0\ mol \cdot m^{-3}$.

When the diameter of the horizontal pore is increased, the pore volume is increased and the mass transfer resistance of the network decreases. Indeed, the resistance for each pore is given by the following equation:

$$R_i = L_p / \left(\pi \cdot R_p^2 \cdot D_{im} \right)$$

The global resistance of the network that is the sum of all resistances, for cases 1b and 1c is smaller, yielding higher flows and also higher fluxes at the outlet since, the diameter of the outlet pore is kept constant (see Fig. VII-1).

When looking to the dynamic responses and taking the fact that the capacitive volume increases, we expect to obtain different dynamic responses. The sequence of delays we expect to find is D, $\sqrt{2} \cdot D$ and, $\sqrt{3} \cdot D$, which is in good agreement with Fig. VII-1.

To confirm the exactness of the numerical tools, we have calculated the surface area between the inlet and outlet flux by integrating along the time step as follows:

$$I(mol) = \left[\left(\sum_{t=t_0}^{t_f} J_{inlet} - J_{outlet} \right) \times t_{step} \right] \times S_p \qquad \text{(VII-1)}$$

with $J_{inlet/outlet}$ the inlet and outlet flux, t_{step} the time step used in the integration method to calculate the number of moles and S_p, the surface of a pore at the inlet or outlet, which are identical in case study 1. The calculated integral is compared to the variation of the number of moles in the network:

$$n(mol) = V_{pores} \times \bar{c}$$

$$n(mol) = V_{pores} \times \frac{\int_0^{V_{pores}} c(V) dV}{\int_0^{V_{pores}} dV} \qquad \text{(VII-2)}$$

with the average concentration within the network equal to $0.5\ mol \cdot m^{-3}$.

Table VII-2. Estimated number of moles obtained from the inlet and outlet flux. Effect of the network volume.

Diameter, m	Theoretical n, mol	Estimated n, mol $t_{step}=1\times10^{-7}s$	Estimated n, mol $t_{step}=5\times10^{-9}s$	Relative error $1\times10^{-7}s$	Relative error $5\times10^{-9}s$
D	1.77×10^{-24}	1.54×10^{-24}	1.70×10^{-24}	13%	4%
$\sqrt{2} \cdot D$	2.26×10^{-24}	2.13×10^{-24}	2.28×10^{-24}	10%	3%
$\sqrt{3} \cdot D$	2.95×10^{-24}	2.71×10^{-24}	2.86×10^{-24}	8%	3%

The estimated number of moles for a time step of 5×10^{-9}s is very similar to the theoretical number of moles with an error of 3 to 4%. For higher time steps, the relative errors increase as we can see from Table VII-2.

VII.1.2 EFFECT OF A DEAD VOLUME

In order to understand the effect of adding a dead volume to a given pore network CS 1, CS 11 and CS 11b are used (Fig. VII-2). The general definition of a dead volume is a volume in which there is a zero flux during the steady state regime. To CS 1 we have added a dead volume, resulting in CS 11 and CS 11b that differ only in where the dead volume is placed.

In order to explain the effect of the network volume, the concept of percolating volume and capacitive volume must first be defined. If we are under a steady state regime, the percolating volume is the volume where the diffusion process takes place, whereas the capacitive volume corresponds to the volume of the network including for instance, dead volumes that do not participate in the steady-state diffusion process ($F_{dead\text{-}end}$=0 during the steady state). And as we quote from Reyes *et al.* (1989), the dead-end porosity does not contribute to the net transport, and should not be included in the calculation of the net pore volume available for diffusion.

In Fig. VII-2, the dynamic responses in terms of the inlet and the outlet flux are displayed. The initial and boundary conditions taken in the previous section are used.

Cases CS 1, CS 11 and CS 11b have an equal percolating volume but the capacitive volumes of cases CS 11 and CS 11b are larger than their percolating volumes, due to the presence of the dead volume. Also, $V_{capacitive\ CS\ 11} = V_{capacitive\ CS\ 11b}$. Since all these networks have an identical percolating volume, an identical steady state is expected for CS 1, CS 11 and CS 11b, which is verified in Fig. VII-2.

Concerning the dynamic responses and as we can see from the inlet fluxes in Fig. VII-2, CS 11b and CS 11 are delayed compared to CS 1. This is due to the fact that CS 11 and CS 11b have a larger capacitive volume than CS 1. Also, CS 11b has an extra delay with respect to CS 11 that is explained by the number of moles that is retained in the dead volume on each CS (11 or 11b). Since, the dead volume from CS 11b is closer to the inlet node that has a boundary condition of $c_{A\ inlet} = 1\ mol \cdot m^{-3}$, its concentration at steady state is necessarily larger than that from the dead volume in CS 11, placed near the outlet node with $c_{A\ outlet} = 0\ mol \cdot m^{-3}$.

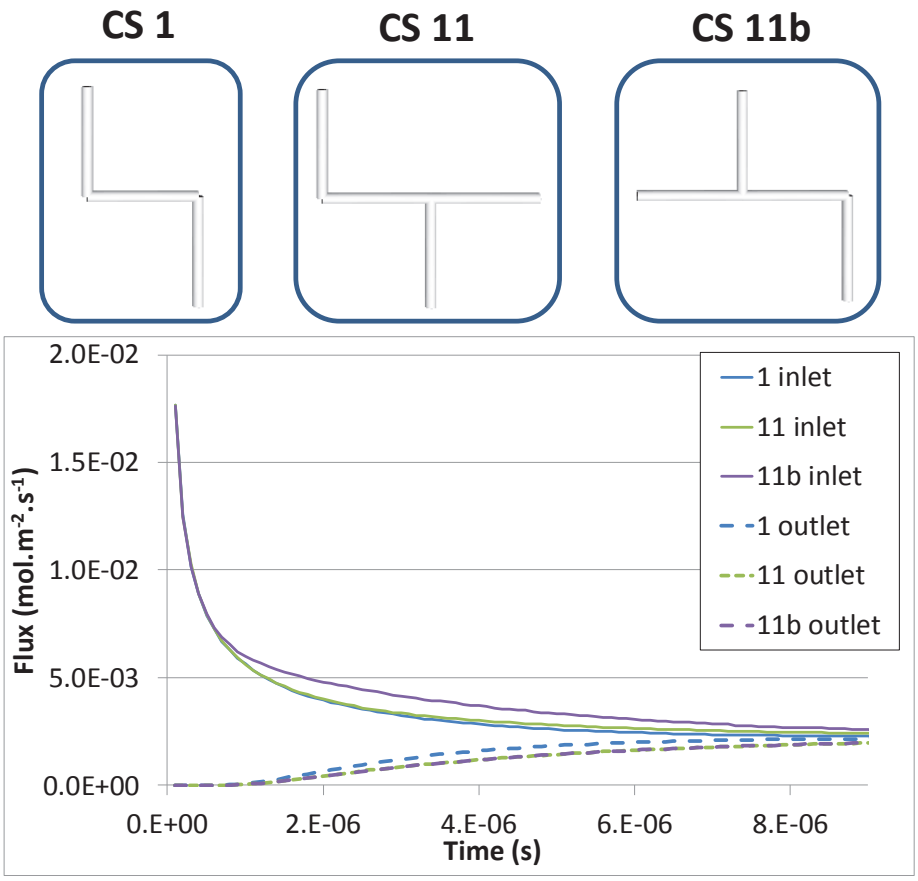


Fig. VII-2. Dynamic responses of CS 1, 11 and 11b, observation of the dead volume effect.

Let us remark as well that, as is visible in Fig. VII-2, the outlet fluxes from CS 11 and CS 11b are identical. The difference between these two networks is indeed only sensitive to their inlet nodes. If instead of filling process, we simulate a purging process we would have a flux sensitive to the outlet nodes, as shown in Appendix IX, when testing different initial conditions.

We have also studied the dynamic response for larger discrete pore networks with an increased diffusion path, by means of CS 30, illustrated in Fig. VII-3. To this network, we have added a dead volume placed at different positions of the network, resulting in CS 31, CS 32 and CS 33. Within these case studies we created pore networks with dead volumes placed either close to an inlet node or near an outlet node. The same initial and boundary conditions are used as in the previous study $(c_A(l, t=0)=0, c_A(l=0, t)=1, c_A(l=L, t)=0\, mol\cdot m^{-3})$. The addition of the dead volumes to CS 30 does not influence the steady state regime, since all cases have identical percolation volumes and, the diffusional tortuosity is simply τ=1.96.

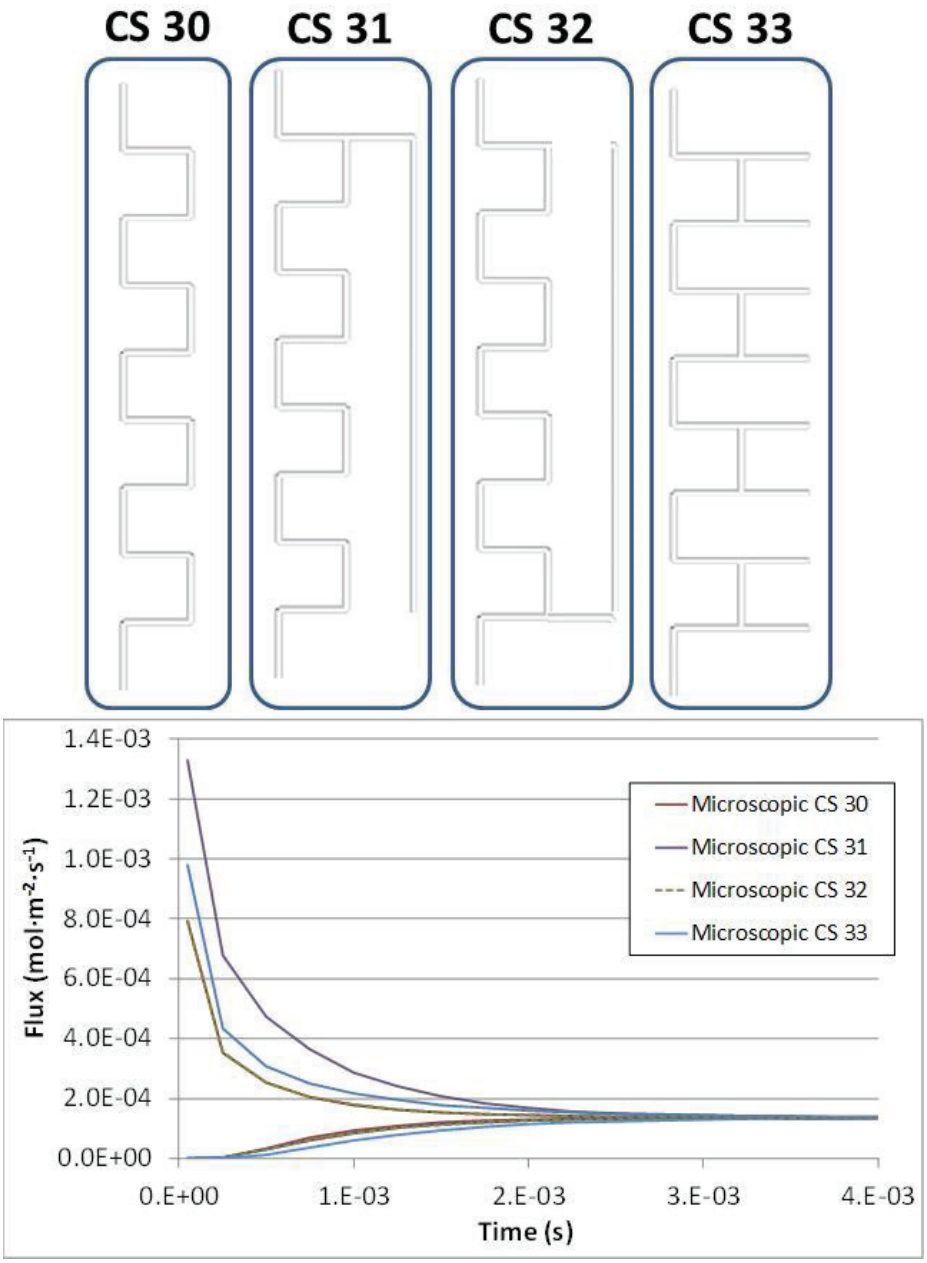


Fig. VII-3. Dynamic response in terms of the inlet and outlet flux for the discrete (microscopic) approach of case studies 30, 31, 32 and 33. Illustration of the pore network for the different case studies.

If we look at the outlet transient responses in Fig. VII-3, we have practically a match for all case studies with dead volumes, since the perturbation created by the dead volumes is only reflected on the inlet flux. Logically, the sequence by which the molecules would leave the different networks is CS 30, 32, 33 and finally, 31. This means that CS 30 has a lower characteristic time than CS 32 and so on, which is confirmed with Fig. VII-3. This sequence of delay is mainly due to the fact that CS 30 does not have any dead volume and to the disposition of the dead volumes in the different CS.

In CS 31, the number of molecules delayed in the dead volumes is greater than any other case study. As we may recall, the concentration gradient imposed by the boundary

conditions is 1 mol·m^{-3}, since we have a concentration of 1 and 0 mol·m^{-3}, for the inlet nodes and the outlet nodes, respectively. That means that for CS 31, the steady state concentration in the dead volume is uniform and close to 1.0, since the dead volume is placed near the inlet node. For CS 33, the concentration of the dead volumes is going to vary from 1 to 0 mol·m^{-3}. Finally, due to the fact the dead volume is placed close to the outlet node for CS 32, the steady state concentration in the dead volume is close to 0, so a reduced amount of molecules is delayed. Case studies 1, 11 and 11b have already clarified this point.

The following section is dedicated to the comparison of the dynamic response of the discrete model and the pseudo-homogeneous continuum model for simple cases.

VII.2 COMPARISON OF THE TRANSIENT RESPONSES FOR THE DISCRETE MODEL AND THE CONTINUUM MODEL

In order to compare the transient response of our discrete model with that of the pseudo-homogeneous continuum model, as illustrated in Fig. VI-1 from section VI.1.1, we have simulated the mass transfer by diffusion along a 50×50 pore network of maximum connectivity Z_{max}=6 and a pore existence probability of P=1.0, meaning that all pores from the initial grid exist. In total, 7,500 partial differential equations are simulated within this network.

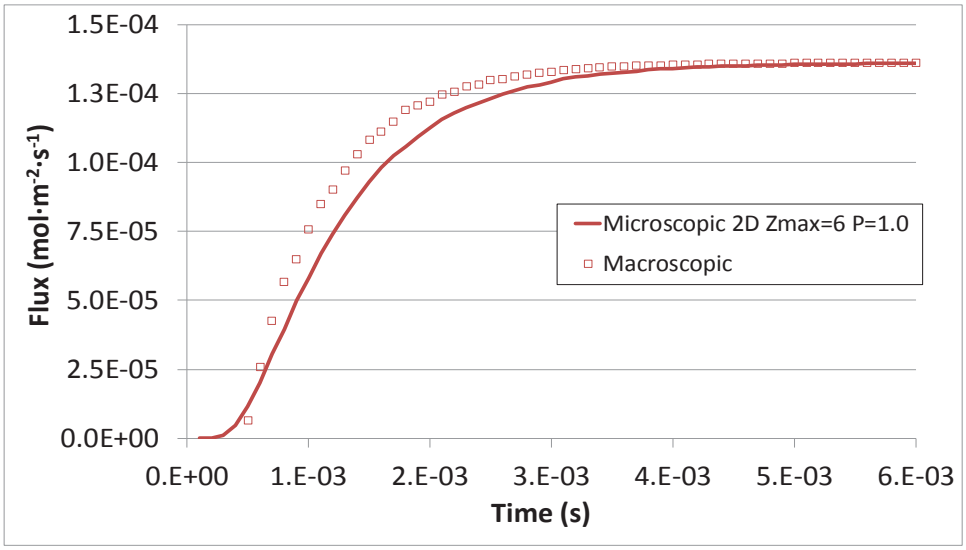


Fig. VII-4. Outlet flux given by the discrete (microscopic) and continuum (macroscopic) models. 2D network with Z_{max}=6 and P=1.0.

Fig. VII-4 shows that both approaches lead to identical steady state outlet fluxes since the effective diffusion coefficient has been obtained to satisfy these conditions, with a diffusional tortuosity of 1.0. On the contrary, the dynamic behaviour of the two models is different: the continuum (macroscopic) model response is faster than that of the discrete

(microscopic) model, which means that the molecules in the discrete pore network are retained longer.

To understand this difference in time delay, several hypotheses can be considered. The 1st hypothesis (**Hypothesis 5**) is related to a possible difference between the pore volume fraction and the pore surface fraction. For a given surface element of a given pore network, the pore surface fraction can be translated into the ratio of all pore surfaces intersecting the surface element divided by the percolating pores surface, i.e. the surface ratio of the total number of pores divided by the pores with a projection of the diffusion path in the *y*-axis in the surface element. As an example, for a 2D triangular network of size 50×50 and a pore existence probability of 1.0 an average surface porosity of 0.67 was found whereas the catalyst porosity takes a value of 1.0. A 2nd hypothesis (**Hypothesis 6**) is linked to the possibility of having different capacitive volumes for the two models, i.e. the presence of dead volumes in the discrete pore network.

As far as the 1st hypothesis is concerned, let us consider the mass balance of species *i* in a continuum model with a different surface fraction from the ordinary volumetric porous fraction (porosity):

$$\varepsilon \cdot \frac{\partial c_i}{\partial t} = \sigma \cdot D_{ieff} \cdot \frac{\partial^2 c_i}{\partial y^2} \tag{VII-3}$$

At a constant correction factor $CF = \frac{\varepsilon}{\sigma}$ to the classical continuum mass balance where ε and σ are implicitly considered to be equal, the mass balance is then defined as follows:

$$CF \cdot \frac{\partial c_i}{\partial t} = D_{ieff} \cdot \frac{\partial^2 c_i}{\partial y^2} \tag{VII-4}$$

Considering a pore network that is sufficiently large, the surface fraction can be translated into a volume. Hence, the correction factor is simply the available/capacitive pore volume of the discrete network divided by the pore volume of the network that would participate in the diffusion process given a continuum model (i.e. those who have a diffusion projection in the *y*-axis):

$$CF = \frac{V_{pores}}{V_{pores\ diffusion}} \tag{VII-5}$$

In the next sections, we try to clarify the origin of the time delay observed between the responses of the discrete network and the continuum model observed in Fig. VII-4. We will first start by comparing the responses of the discrete model to those of the continuum model for simple case studies. Then, to each of them, a dead volume is added and the model's responses are compared. Finally, networks having a larger thickness will

be tested and the overall results will lead us to the final conclusions on our 2D pore networks.

VII.2.1 SIMPLE CASE STUDIES FOR THE COMPARISON OF THE TRANSIENT RESPONSES OF THE DISCRETE MODEL AND THE CONTINUUM MODEL

In Fig. VII-5 are represented two simple networks under consideration and the simulated dynamic responses obtained during a filling process. The green and purple solid lines correspond to the outlet fluxes obtained via the discrete (microscopic) approach, respectively for the first and second case studies (CS 1 and CS 2), whereas the dashed plots correspond to the fluxes obtained via a continuum (macroscopic) approach. The responses of the continuum model have been obtained with and without the correction factor applied to the accumulation term, see eq. (VII-4) and (VII-5).

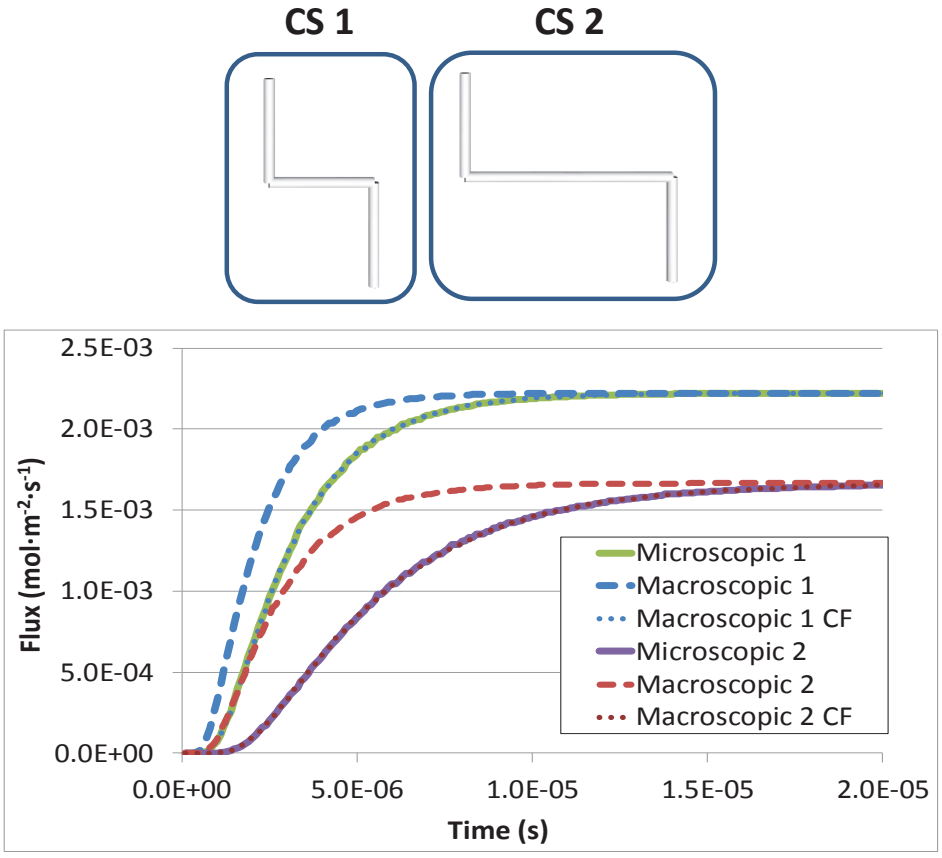


Fig. VII-5. Comparison of the predicted outlet flux in transient regime by discrete (microscopic) and continuum (macroscopic) models for case study 1 and 2.

The first observation that we may take from Fig. VII-5 is related to the steady state regimes. For each case study, the same steady state is obtained for the two models. This is expected since the effective diffusion coefficient is determined to satisfy this constraint. Moreover, CS 1 and CS2 exhibit different steady state regimes due to the fact that CS 2 has a larger percolating volume.

The steady state fluxes obtained take the following values: $F_{CS\,1}(mol \cdot m^{-2} \cdot s^{-1}) = 2.22 \times 10^{-3}$ and $F_{CS\,2}(mol \cdot m^{-2} \cdot s^{-1}) = 1.67 \times 10^{-3}$. The effective diffusion coefficient of species *A* is then $D_{eff\,CS\,1}(m^2 \cdot s^{-1}) = 6.67 \times 10^{-11}$ and $D_{eff\,CS\,2}(m^2 \cdot s^{-1}) = 5.00 \times 10^{-11}$. A geometric tortuosity was also calculated and compared to the diffusional tortuosity. As all pores have the same length and diameter (we have used equal D_p and L_p for all pores), the geometric tortuosity is simply calculated as the number of pores through which the molecules diffuse within the discrete pore network divided by the number of pores that correspond to the thickness of the plate. For CS 1, we find that $\tau_{geom_1} = 3/2$. For both models, an identical value for each case study is found. The estimated diffusional and geometric tortuosities are: $\tau_{\mathrm{CS}\,1} = 1.5$ and $\tau_{\mathrm{CS}\,2} = 2.0$.

As far as the transient behaviour is concerned, it can be seen in Fig. VII-5 that the transient responses of the discrete pore network and those of the continuum model differ significantly. However, when a correction factor of *CF* of 3/2 = 1.5 for CS 1 and *CF*=4/2=2.0 for CS 2 are applied to the dynamic response of the continuum model, a good agreement is found. For these simple case studies, the correction factor can be simply imagined as the volume of pores in the discrete representation divided by the volume of the continuum representation. We can define *CF* by the number of pores instead of taking the volume of pores since we have a constant pore diameter and a constant pore length. The remaining case studies can be found in Appendix IX and section IX.2.

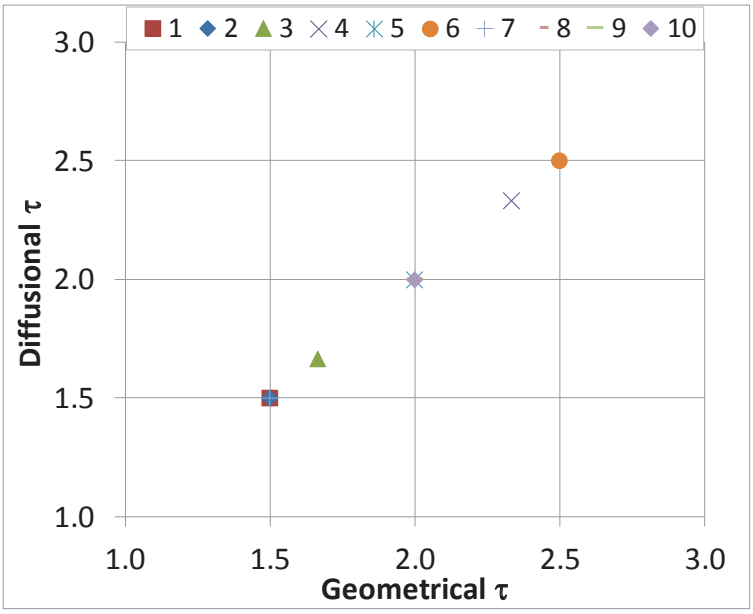


Fig. VII-6. Diffusional tortuosity as a function of the geometric tortuosity from case studies 1 to 10.

Fig. VII-6 compares the diffusional and geometric tortuosities for all case studies from 1 to 10 (extra data is available in Appendix IX). For each case study, the diffusional tortuosity is identical to the geometric tortuosity.

Also, it is visible that the tortuosity factors generally increase from the first case study to the latter. This is due to the fact that from case study 1 to 10 the pathway of the network is generally increased and so the percolating volume increases, as well. And of course, knowing that, we have maintained the same molecular diffusion coefficient and the same concentration gradient Δc.

VII.2.2 SIMPLE CASE STUDIES WITH DEAD VOLUMES FOR THE COMPARISON OF THE TRANSIENT RESPONSES OF THE DISCRETE MODEL AND THE CONTINUUM MODEL

In order to check for their influence, dead volumes have been added to the networks CS 1 to 10, resulting in CS 11 to 20, respectively.

In Fig. VII-7 are compared the outlet fluxes obtained for case study CS 1, CS 11 and CS 11b. A dead volume has been added to CS 1 to get CS 11 and CS 11b. The last two differ only by the position of the dead volume.

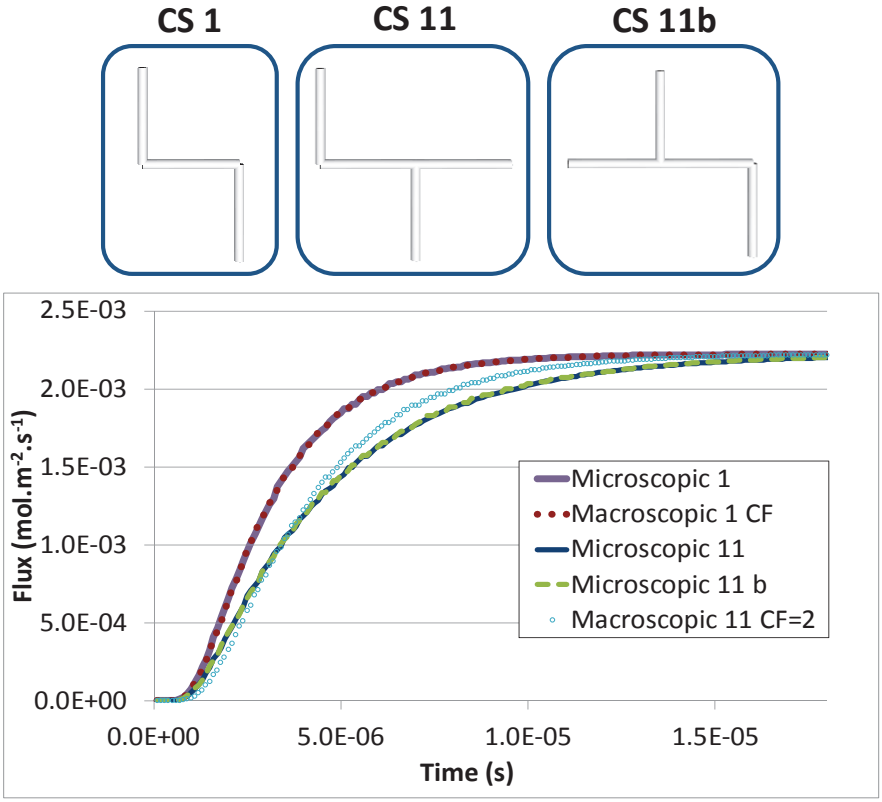


Fig. VII-7. Comparison of the transient responses for the discrete (microscopic) model and continuum (macroscopic) model for CS 1, 11 and 11b.

All three networks present the same steady state behaviour since their percolating volumes are the same. The steady states are in good agreement whatever the model and the CS, which is an expected result since a dead volume does not interfere on the steady state of the diffusion process. Indeed, the presence of a dead volume does not interfere with the system steady state that exhibits equal percolating volumes. The geometric and diffusional tortuosities from CS 11 take a value of $\tau_{CS\,11} = 1.5$, which is equal to $\tau_{CS\,1}$.

Looking at the transient responses, case study 11 and case study 11b have curiously the same dynamic. This is merely due to the fact that we are in the filling process and that the delay for CS 11b is only observed on the inlet flux (cf. Fig. VII-2). Comparing the transient responses of the discrete model for case study 1 with case studies 11/11b, we observe that they exhibit a different behaviour due to the dead volume.

Moreover, if one applies the correction factor of CF=4/2 to both continuum models of CS 11 and CS 11b, the corrected dynamic response of the continuum model does not match the dynamic response of the discrete model. This can be explained by the fact that the discrete pore network contains a dead volume that needs to be taken into account in the pseudo-homogeneous representation. A good representation for the continuum model when we are in the presence of dead volumes would be to have a correction factor CF that accounts only for the diffusive pores and to add a dead volume in the continuum representation.

The remaining case studies (CS 11-20), where a dead volume is added to case study 1-10 respectively, can be found on Appendix IX.

VII.2.3 SIMPLE CASE STUDIES WITH AN INCREASED POROUS MEDIA LENGTH ΔL FOR THE COMPARISON OF THE TRANSIENT RESPONSES OF THE DISCRETE MODEL AND THE CONTINUUM MODEL

In this section, we have extended the comparison of the dynamic responses of the discrete and continuum models towards the understanding of larger network sizes. The connectivity and the dead volume effects are tested.

We started by the pore network illustrated in Fig. VII-8 and corresponding to case study 30. It has a diffusional tortuosity of 1.96, which is equal to the geometric tortuosity. The dynamic response of both discrete and continuum models is also shown in Fig. VII-8.

Logically, the dynamic response of the continuum model is much faster than the dynamic response of the discrete model. We have therefore corrected the response of the continuum model, as we did before for simple networks and in order to account for the adequate capacitive volume. We remind that the correction factor CF is equal to the ratio of the volume of pores in the discrete representation divided by the volume of the continuum representation. For this specific case (CS 30), the correction factor required takes a value of CF=49/25=1.96, as there is a total amount of 49 pores and 25 diffusing pores along the y axis. By applying this correction factor to the dynamic response of the continuum model, this response gets in line with the dynamic response of the discrete model (see Fig. VII-8).

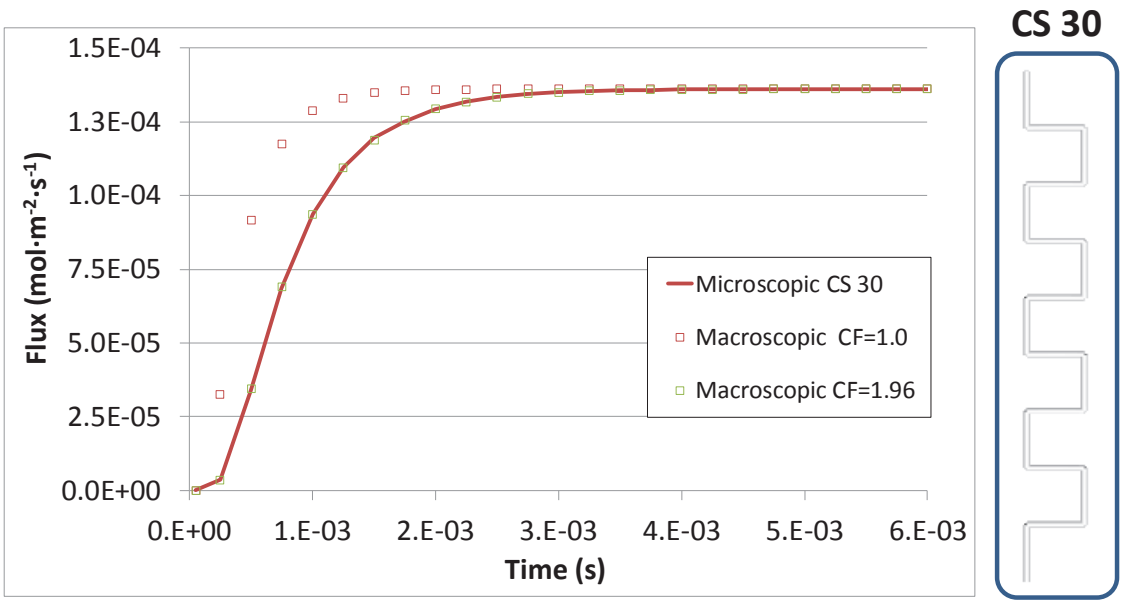


Fig. VII-8. Dynamic response of both discrete (microscopic) and continuum (macroscopic) models for case study 30. Illustration of the pore network respective to the considered case study.

The case "CS 30 triangle" is generated by increasing the connectivity of CS 30, as illustrated in Fig. VII-9. A diffusional tortuosity of 1.03 is obtained. Regarding the geometric tortuosity, we can no longer calculate this value, as we have been commonly calculating for simple networks. Here, the geometric tortuosity could be calculated for instance, based on random walk theories (Bhatia, 1985).

Until now, the correction factor was simply the total pore volume divided by the diffusing pores, i.e. pores that exhibit a projection of the diffusing vector on the *y* axis (from now on designated by CF_{global}). This gave identical values of *CF* as for a *CF* defined by the ratio of the volume of the discrete representation divided by the volume of the continuum representation. Yet, for "CS 30 triangle", these two ratios do not give the same value. Indeed, the first one gives $CF_{global}=72/48=1.5$ and the second one gives $CF=V_{pores}/V_{macropore}=72/25=2.88$. A good agreement was found taking $CF=2.88$, as illustrated in Fig. VII-9.

The dynamic responses obtained from the two proposed corrections for the continuum model are graphically represented in Fig. VII-9, for CS "30 triangle".

As we have concluded before from Fig. VII-9, the dynamic response of the continuum model from "CS 30 triangle" that fits better is that from a correction factor *CF* given by the ratio of the pore volume of the discrete representation divided by the volume taken by the continuum representation.

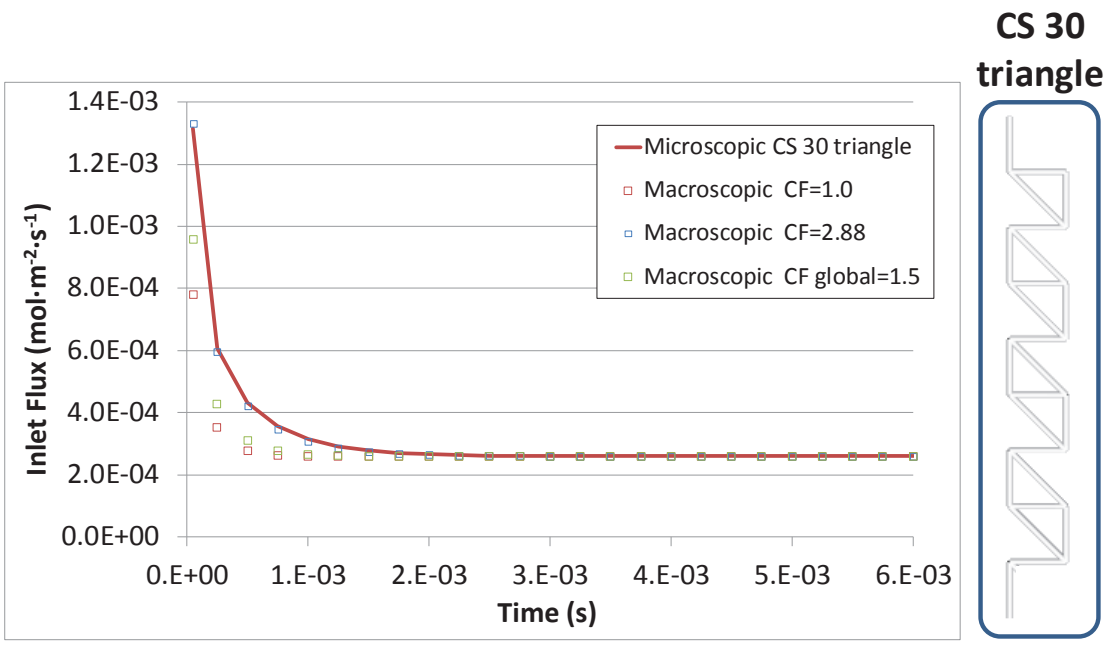


Fig. VII-9. Dynamic response of both discrete (microscopic) and continuum (macroscopic) models for CS 30 triangle. Illustration of the pore network respective to the considered case study.

The two correction factors that have been proposed in this section are going to be tested in the correction of the dynamic response of our 2D networks. With all the information collected, we are finally able to understand the dynamic responses of our pore networks.

VII.2.4 PERIODIC 2D NETWORKS FOR THE COMPARISON OF THE TRANSIENT RESPONSES OF THE DISCRETE MODEL AND THE CONTINUUM MODEL

After having analysed several simple case studies on the comparison of the transient response for the discrete and continuum models, we have concluded our study with some examples on the dynamic response of 2D networks.

The dynamic responses of both discrete and continuum models for periodic networks along the *x*-axis of size 50×50 with Z_{max}=6, *P*=1.0 and constant pore diameter (10 nm) and length and (15nm) are displayed in Fig. VII-10. The diffusional tortuosity for a pore network of *P*=1.0 is τ=1.0. Regarding the dynamic responses of the pseudo-homogeneous model, for *CF*=1.0, we observe of course a time delay when comparing to the response of the discrete model. *CF*=1.0 means that no correction is applied. Using the two correction factors defined in section VII.2.3, similar values of *CF* are obtained and the dynamic responses of the continuum models are able to correctly describe the dynamic response of the discrete model.

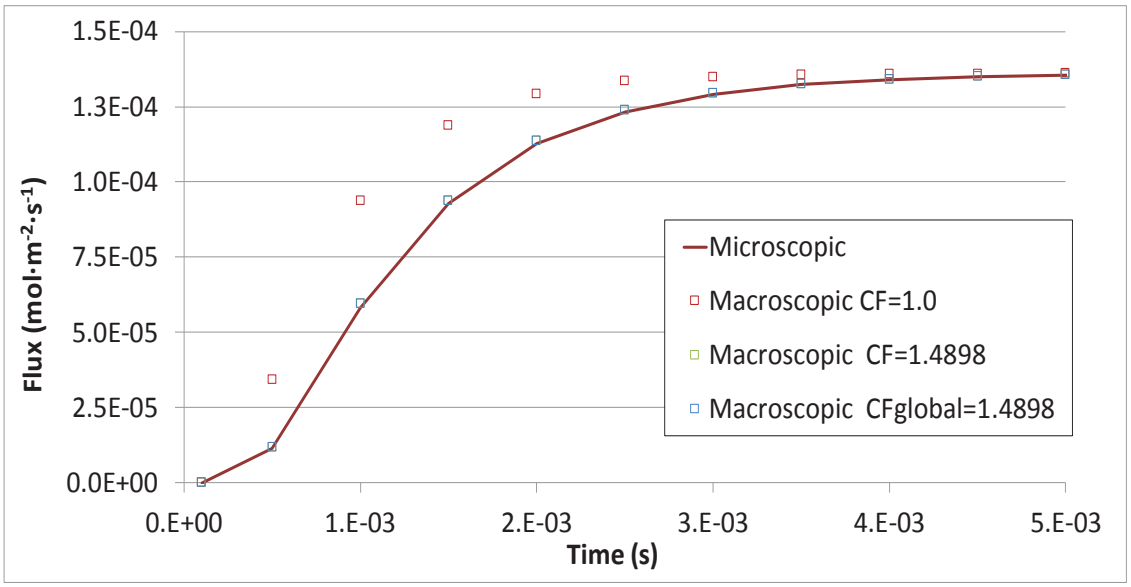


Fig. VII-10. Dynamic responses from the discrete (microscopic) and continuum (macroscopic) models for a 2D periodic network with Z_{max}=6 and of size 50×50 and at a P=1.0.

We pursued our study by decreasing the pore existence probability, in order to check whether the correction factors are still capable of correctly describing the dynamic response of the discrete model. Two periodic networks with a P=0.7 and P=0.6 were generated and their dynamic responses are shown in Fig. VII-11 and Fig. VII-12, respectively, with the diffusional tortuosities of 1.29 and 1.37.

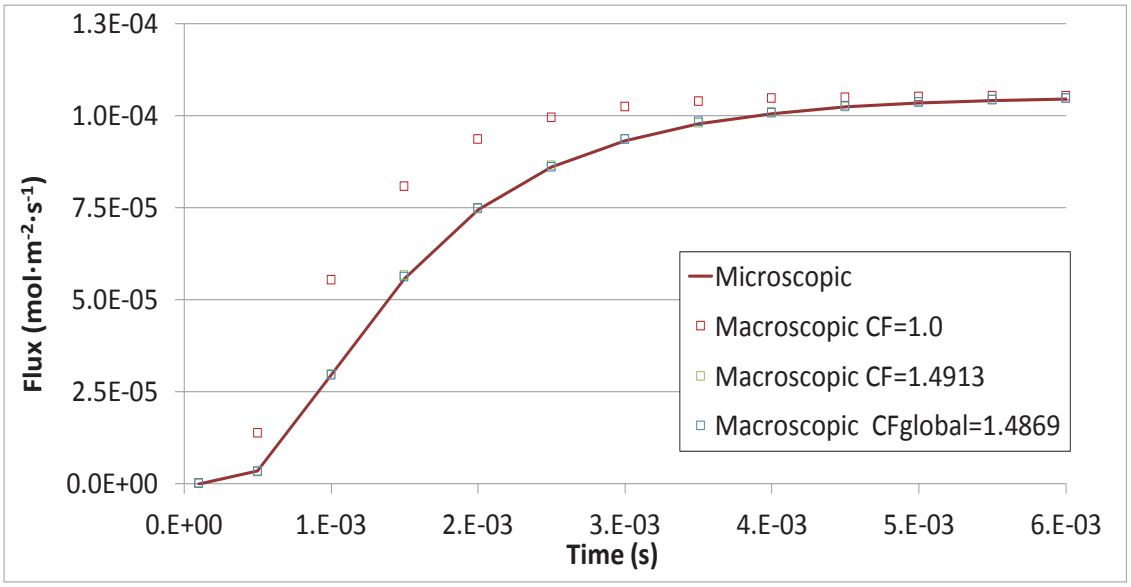


Fig. VII-11. Dynamic responses from the discrete (microscopic) and continuum (macroscopic) models for a 2D periodic network with Z_{max}=6 and of size 50×50 and at a P=0.7.

As the pore existence probability decreases, only the correction factor defined by the ratio of the pore volume of the discrete representation to the volume of the macropore agrees. The corrected dynamic response of the continuum model using CF_{global} starts to shift from the dynamic response of the discrete model. In summary, we could say that an

approximated and fair representation of the continuum model to the dynamic description is obtained for $CF = V_{pores}/V_{macropore}$.

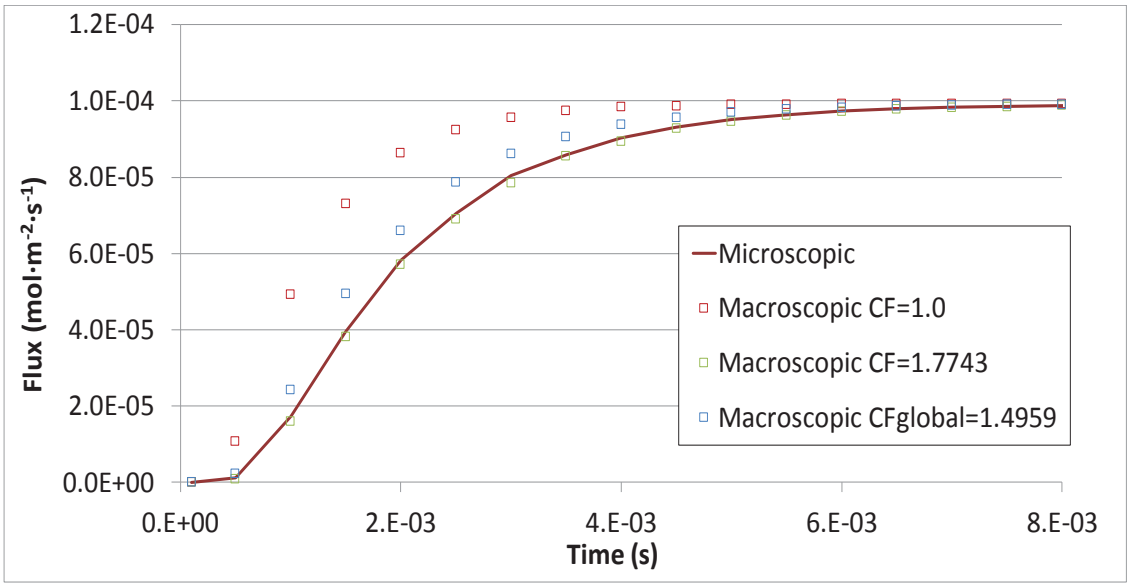


Fig. VII-12. Dynamic responses from the dicsrete (microscopic) and continuum (macroscopic) models for a 2D periodic network with Z_{max}=6 and of size 50×50 and at a P=0.6.

We have also simulated 2D pore networks with Z_{max}=4 and with a network size of 50×50 and at different pore existence probabilities: $P = \{1.0,\ 0.95,\ 0.9\}$ leading to the following diffusional tortuosities $\tau = \{1.0, 1.1, 1.18\}$. The dynamic responses from both discrete and continuum models are represented graphically in Fig. VII-13, Fig. VII-14 and Fig. VII-15.

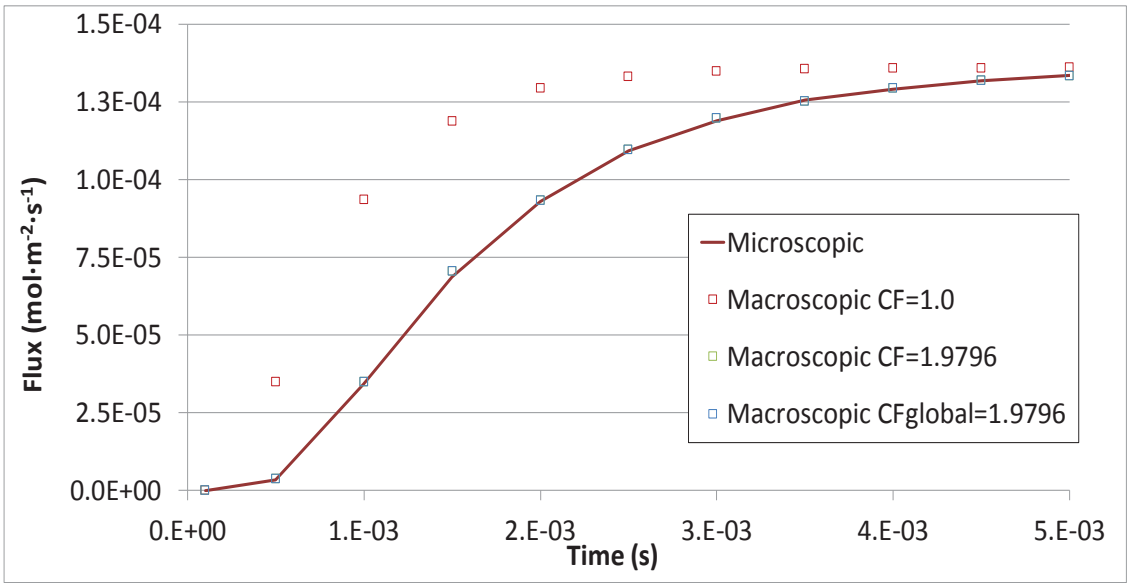


Fig. VII-13. Dynamic responses from the discrete (microscopic) and continuum (macroscopic) models for a 2D periodic network with Z_{max}=4 and of size 50×50 and at a P=1.0.

A similar behaviour to that from Z_{max}=6 networks is found for networks with a reduced connectivity of Z_{max}=4. At a pore existence probability of P=1.0, the dynamic response

can easily be corrected. But as we decrease the pore existence probability, only $CF = V_{pores}/V_{macropore}$ is capable to give a good agreement for the dynamic response.

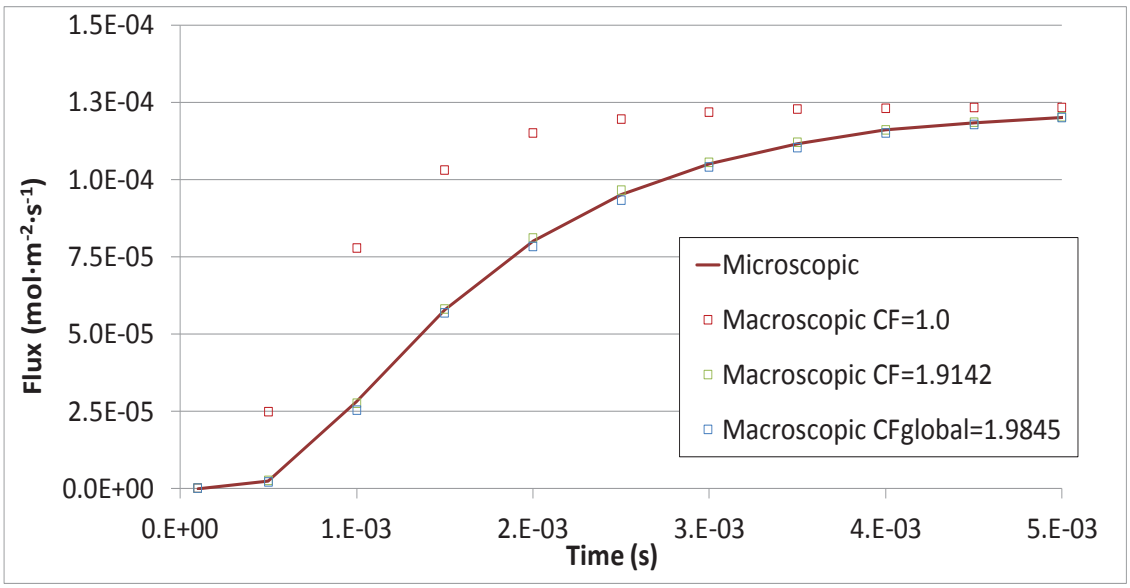


Fig. VII-14. Dynamic responses from the discrete (microscopic) and continuum (macroscopic) models for a 2D periodic network with Z_{max}=4 and of size 50×50 and at a P=0.95.

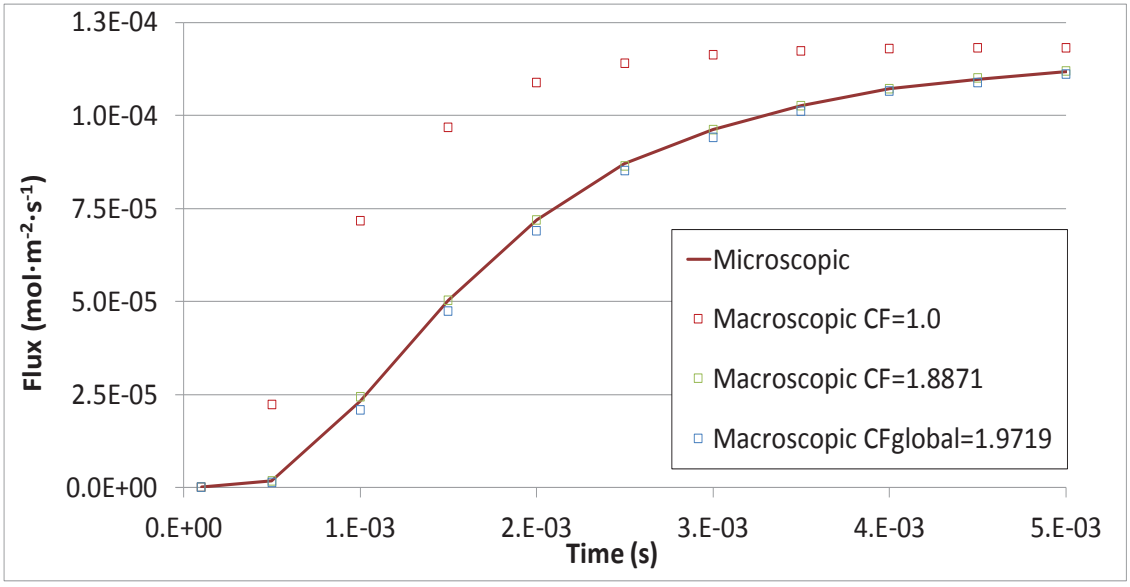


Fig. VII-15. Dynamic responses from the discrete (microscopic) and continuum (macroscopic) models for a 2D periodic network with Z_{max}=4 and of size 50×50 and at a P=0.9.

VII.3 CONCLUSIONS

The general concept of percolating and capacitive volumes is here considered. Different percolating volumes lead to different steady states. And different capacitive volumes lead to different dynamic responses.

Regarding the 1st hypothesis mentioned in section VII.2 (**Hypothesis 5**), for 2D periodic networks the dynamic response from the continuum model match the response of the discrete model, by using a correction factor associated to the accumulation term. Two correction factors were tested but the most appropriate is the ratio of the pore volume used in the discrete representation to the volume used in the continuum representation. Nevertheless, the reader should keep in mind that this corrected pseudo-homogeneous model is merely an approximate model. When it comes to simple pore networks with dead volumes, the corrected continuum model is not capable of correctly predicting the dynamic response of the discrete model.

As far as the 2nd hypothesis (**Hypothesis 6** from section VII.2) is concerned, for 2D periodic networks, since the capacitive volume is larger than the percolating volume, to correctly describe the dynamic response of the pseudo-homogeneous model, the extra volume from the capacitive volume must be taken into account, i.e. by the use of dead volumes.

For our actual pore networks and whatever their configuration, either 2D Z_{max}=6 or 2D Z_{max}=4, and taking a fully completed pore network with P=1.0 or for lower pore existence probabilities, we still observe a good agreement when describing the dynamic response of the continuum model according to **Hypothesis 5**.

The next chapter will focus on the representativeness of the generated pore networks in terms of the textural properties and for the mass transfer properties by comparing them to actual aluminas.

COMPARISON TO ACTUAL ALUMINAS

CHAPTER VIII - REPRESENTATIVENESS OF 2D NETWORKS

VIII.1 INTRODUCTION

In this chapter, we intend to compare both the textural and mass transfer properties from our pore networks with experimental data obtained respectively via physisorption and inverse liquid chromatography techniques. Table VIII-1 contains the available textural and mass transfer properties on the aluminas studied experimentally at IFP Energies Nouvelles (Kolitcheff, 2017).

Table VIII-1. Textural and mass transfer properties obtained for 5 samples of actual porous aluminas (Kolitcheff *et al.*, 2017).

Alumina	D_{avg} (nm)	s_{BET} $(m^2 \cdot g^{-1})$	$v_p \times 10^6$ $(m^3 \cdot g^{-1})$	**ε**	τ
A	7.1	340	0.71	0.72	3.0
B	8.0	300	0.72	0.70	2.8
C	9.0	290	0.78	0.72	2.4
D	9.6	270	0.74	0.71	2.5
E	17.6	160	0.77	0.73	2.0

Fig. VIII-1 contains the pore size distributions obtained for the various aluminas (Kolitcheff *et al.*, 2017). As we can see from Fig. VIII-1 and from Table VIII-1, all studied aluminas are strictly mesoporous and have a similar porosity and pore volume but different tortuosities. Only the BET surface area s_{BET} that essentially depends on the smallest pores, varies significantly as do the pore size distributions.

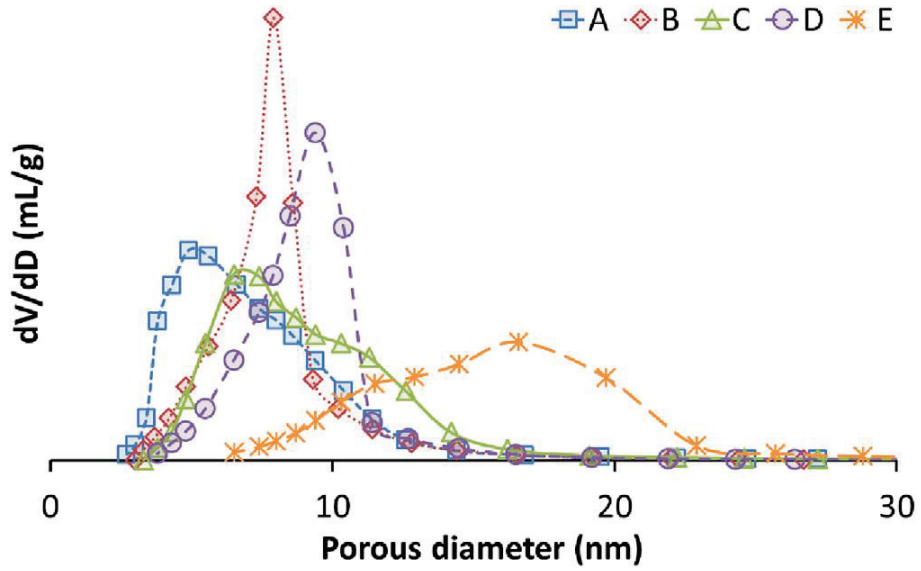


Fig. VIII-1. Alumina supports pore size distribution experimentally estimated by the BJH method taking the desorption branch (Kolitcheff *et al.*, 2017).

From the sensitivity analyses performed on the model parameters and presented in Chapter V, we have seen that the model is capable of generating pore networks with textural properties within the same order of magnitude of actual porous aluminas.

On the other hand, from Chapter VI, we have observed that the tortuosity values remain rather low, not exceeding values of 1.5, while the experimental tortuosities are in the range of 2 to 3. Fig. VIII-2 compares the simulated to experimental tortuosities.

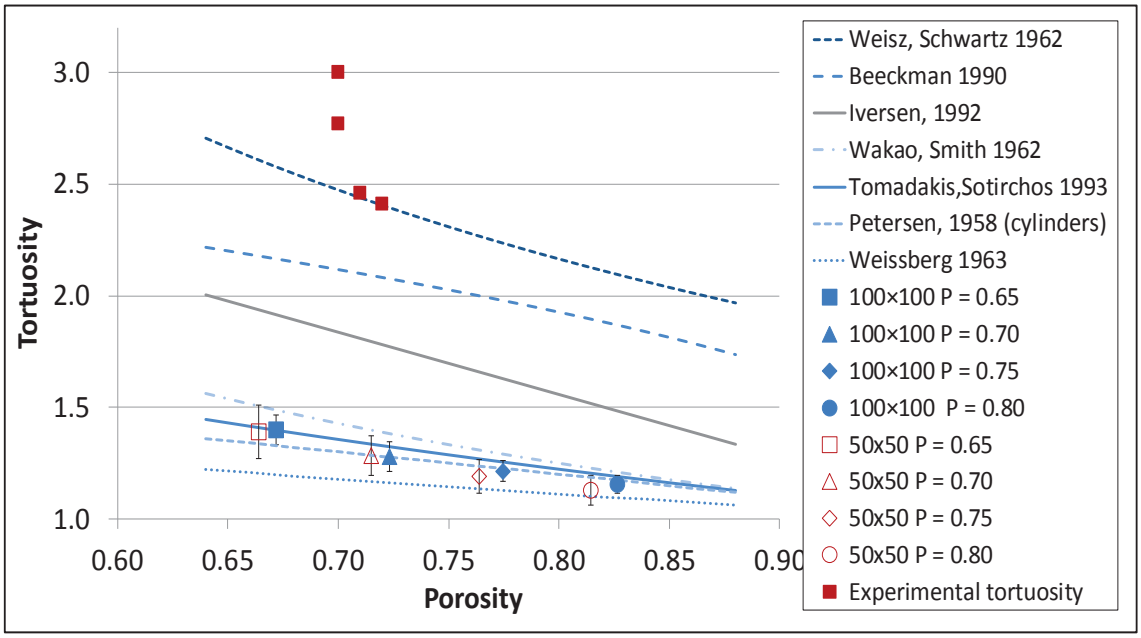


Fig. VIII-2. Variation of the predicted tortuosities as a function of the catalyst porosity for several pore existence probabilities. Correlations taken from Akanni and Evans (1987), Beeckman (1990), and Shen and Chen (2007).

The conclusion given in Kolitcheff *et al.* (2017) that we quote here is: "behind the textural properties, the organization of the pore network may play an important role in the diffusion behaviour inside the solids. (…) With an overall porosity around 0.7, the measured tortuosity values of the solids are much higher (2 to 3) than the tortuosity values predicted by the correlations (1.2 to 1.4) suggesting that only part of the porosity of the alumina support actively contributes to the mass transfer" (Kolitcheff *et al.*, 2017). It is therefore assumed that the pore network is hierarchically organized into two different levels, as already suggested in recent studies (Forman *et al.*, 2016) and also on the presented works of Morin (2014) and Weiland (2015) (cf. section I.2).

Therefore, in this chapter, we first intend to describe the generation of a two-level pore network and what it looks like. Secondly, we will optimize the model parameters in order to construct pore networks with textural properties that are similar to those of actual aluminas. Afterwards, the mass transfer properties of these two-level pore networks are compared to the experimental data.

VIII.2 CONSTRUCTION OF TWO-LEVEL PORE NETWORKS

We have proposed a two-level network constituted by different regions of interconnected pores of small size. These regions are surrounded by the second level of porosity that is simply constituted by pores of larger pore diameter. Fig. VIII-3 schematically illustrates such a two-level network.

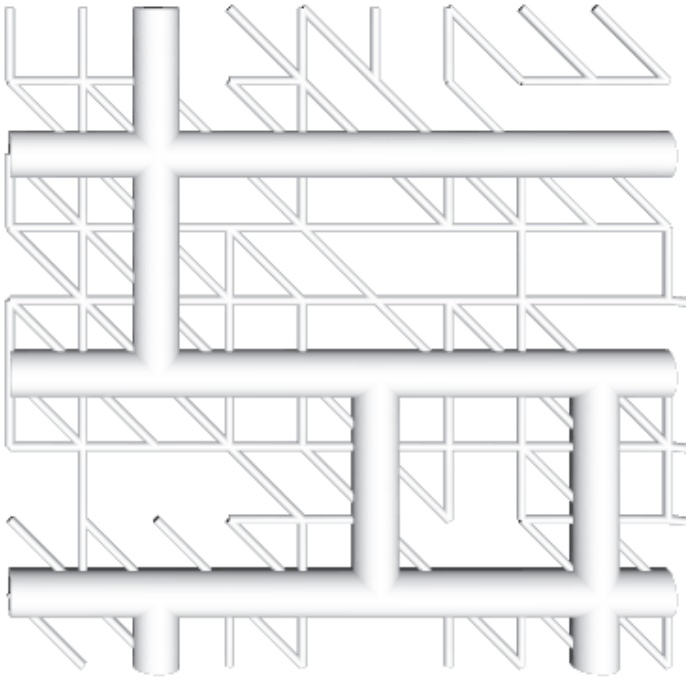


Fig. VIII-3. Illustration of a two-level network.

For the construction of a two-level pore network, we have used the same model parameters as before. In this case, however, two pore diameters are admitted, as well as

two pore lengths and two pore existence probabilities, one for each level of porosity. We have also added (see Fig. VIII-3) a spacing parameter that defines where the larger pores are inserted. The diagram presented in Fig. VIII-4 represents the flowchart for the construction of a two-level network. The difference with the previous tool is the fact that the pore diameter depends on the porosity level.

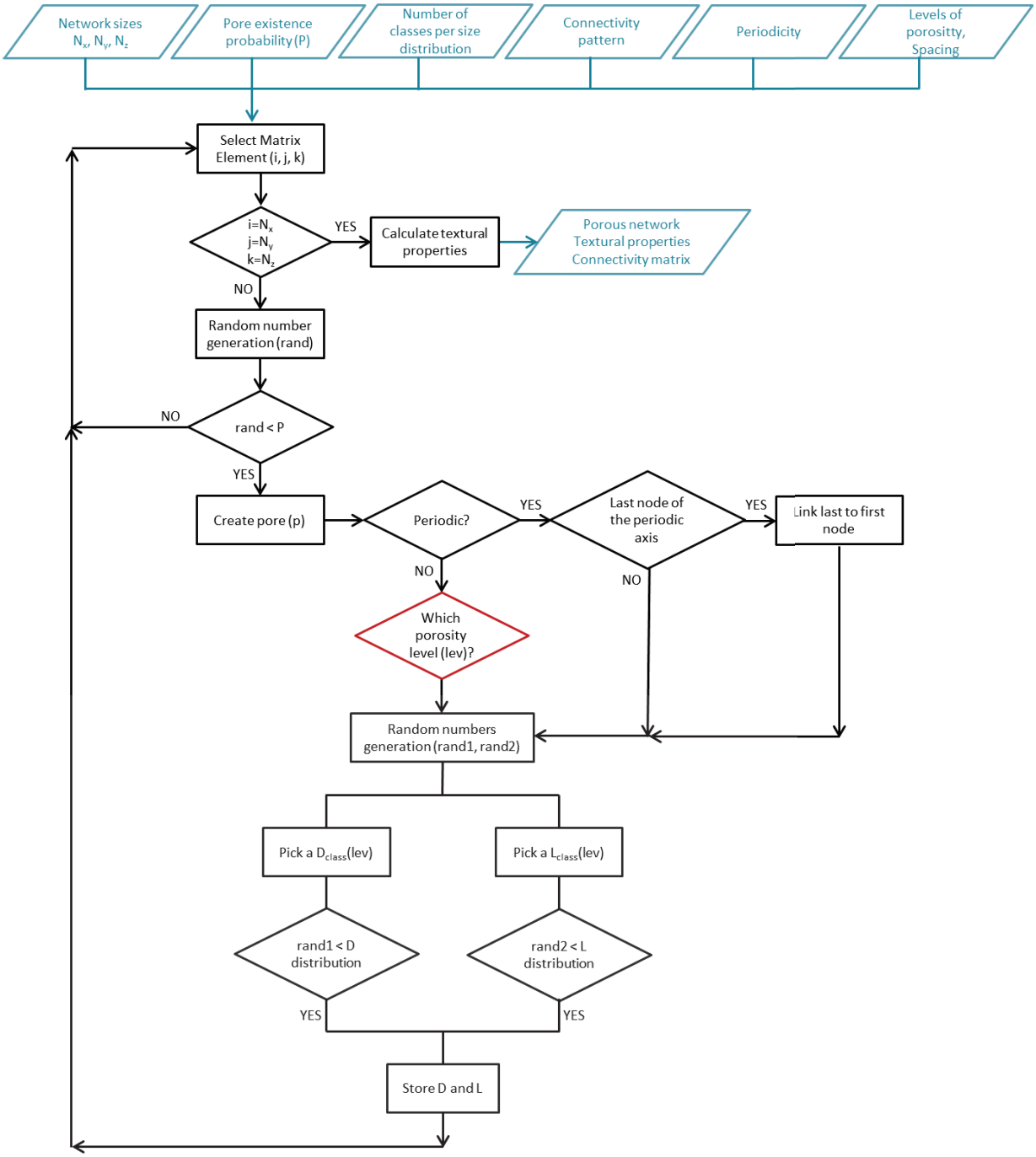


Fig. VIII-4. Flowchart describing briefly the construction of a two-level pore network generation.

The step added in the flowchart ensures the definition of the porosity level for a given pore, either belonging to the 1st level of porosity (smaller pores) or to the 2nd one (larger pores). Moreover, if we take a spacing of 3 and a pore length of 15nm, then the first

level has L_1=15nm and the second level of porosity has in fact L_2=45nm. An important aspect to be mentioned is that the dimensions E_x, E_y and E_z of the parallelepiped particle depend on the pore length L_1 for the smallest pores.

The elimination of the inaccessible pore volume and the mass transfer models are not submitted to modifications caused by the implementation of the two-level pore networks.

In order to optimize the model parameters so that we may simultaneously represent both the textural and the mass transfer properties of actual aluminas, we have decided to study the influence of each model parameter from each porosity level on these features. The next section is dedicated to these sensitivity analyses.

VIII.3 SENSITIVITY ANALYSES ON TWO-LEVEL PORE NETWORKS

The new configuration of networks in two levels of porosity is here submitted to a sensitivity analyses on the different model parameters, such as the pore existence probability, pore diameter and pore length. As we did previously during the sensitivity analyses shown in Chapter V and Chapter VI, for each set of model parameters, we have generated thirty periodic pore networks of size 50×50 and Z_{max}=6. For each of these, we have calculated the textural and mass transfer simulated diffusion. An average over the thirty pore networks is then calculated.

VIII.3.1 INFLUENCE OF THE PORE EXISTENCE PROBABILITY

In order to test the influence of the pore existence probability, we have varied separately P_1 and P_2 corresponding to the pore existence probability for the first level of porosity and for the second level of porosity. The remaining model parameters take the following values: D_1=5nm, D_2=20nm, L_1=15nm with a spacing of 3. When P_1 is varied, P_2 = 0.7 and when P_2 is varied, P_1 = 0.7.

We have gathered in Fig. VIII-5 and Fig. VIII-6 the evolution of the specific pore volume and surface area as a function of the pore existence probability P_1 or P_2. For the variation of P_1, the averages on the specific pore volume range from 1.0 to 1.4×10^{-6} $m^3 \cdot g^{-1}$, the specific surface area from 317.3 to 455.7 $m^2 \cdot g^{-1}$, the catalyst porosity between 0.76 to 0.81 and finally, the average connectivity from 4.1 to 5.1. For the variation of P_2, the averages range from 1.0 to 4.9×10^{-6} $m^3 \cdot g^{-1}$, from 317.3 to 1425.5 $m^2 \cdot g^{-1}$, from 0.76 to 0.94 and from 4.1 to 4.4 respectively for the specific pore volume, surface area, porosity and connectivity. Additional data regarding the evolution of the catalyst porosity and the connectivity as a function of the pore existence probabilities can be found in Appendix X.

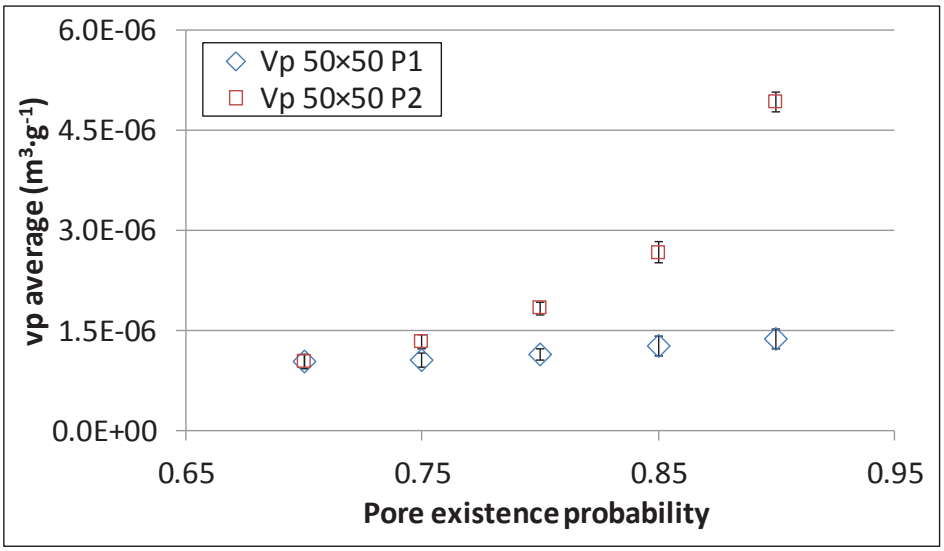


Fig. VIII-5. Influence of the pore existence probabilities P_1 (dotted blue plot) and P_2 (dotted red plot) on the specific pore volume for a two-level network taking the 1st configuration.

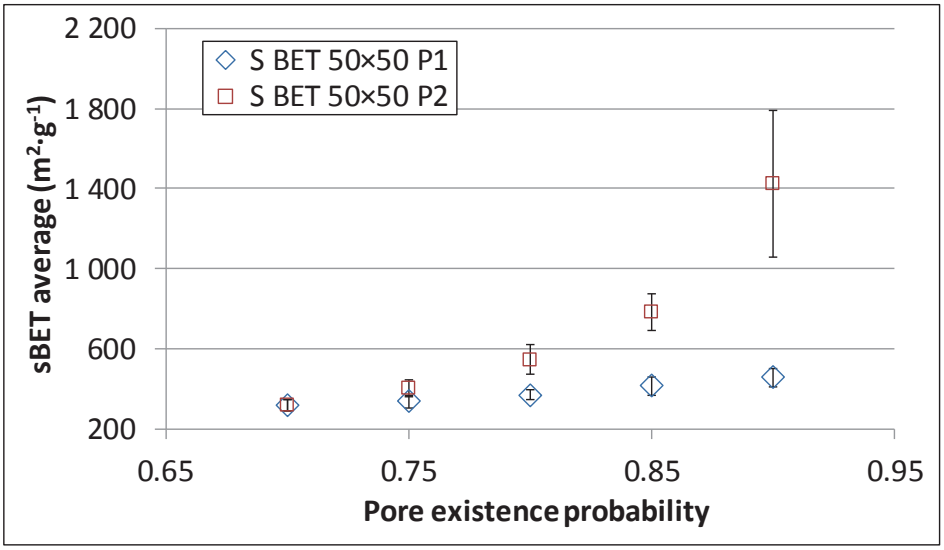


Fig. VIII-6. Influence of the pore existence probabilities P_1 (dotted blue plot) and P_2 (dotted red plot) on the specific surface area for a two-level network taking the 1st configuration.

We have observed that for pore networks generated at $P_1=P_2$ = 0.7, the pore volume ratio between the larger and smaller pores V_2 / V_1 is around 4.5. Even though the number of small pores is quite significant compared to the number of large pores, the high pore diameter ratio D_2/D_1=20/5=4 is preponderant and hence, the variation of the pore existence probability P_2 for the 2nd level of porosity has a much larger impact on the textural properties than the pore existence probability P_1 (see Fig. VIII-5 and Fig. VIII-6).

Regarding the mass transfer properties, the tortuosity factor is represented in Fig. VIII-7 as a function of the catalyst porosity. Again, it is observed that P_2 is preponderant against P_1.

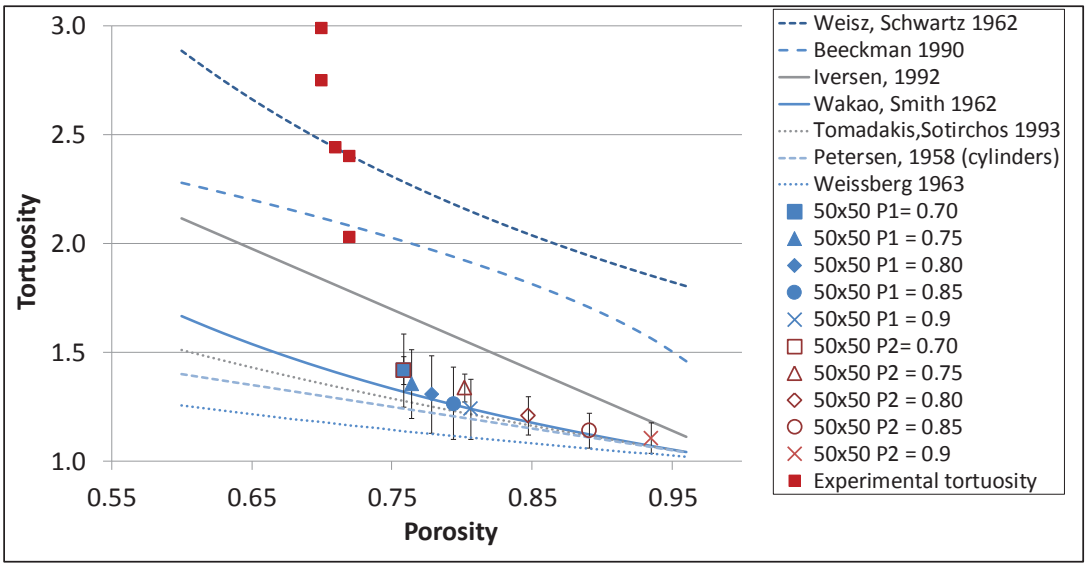


Fig. VIII-7. Influence of the pore existence probabilities P_1 (dotted blue plot) and P_2 (dotted red plot) on the tortuosity for a two-level network taking the 1st configuration.

The plausible explanation for that to happen is once more related to the pore volume ratio or herein, to the pore surface ratio between the two levels of porosity ($S_2/S_1 \approx 4.0$ for $P_1=P_2=0.7$). For the variation of P_1, the average tortuosity ranges from 1.42 to 1.24 for an average porosity of 0.76 to 0.81 and when P_2 is varied, we have τ =[1.42, 1.10] and ε=[0.76, 0.94]. It can be seen in Fig. VIII-7 that the tortuosities remain rather low compared to the experimental data. In order to increase τ, we thought of another way of constructing a two-level pore network that does not oblige the larger pores to fill the spacing range and, where L_2 can be lower than D_2, as illustrated in Fig. VIII-8:

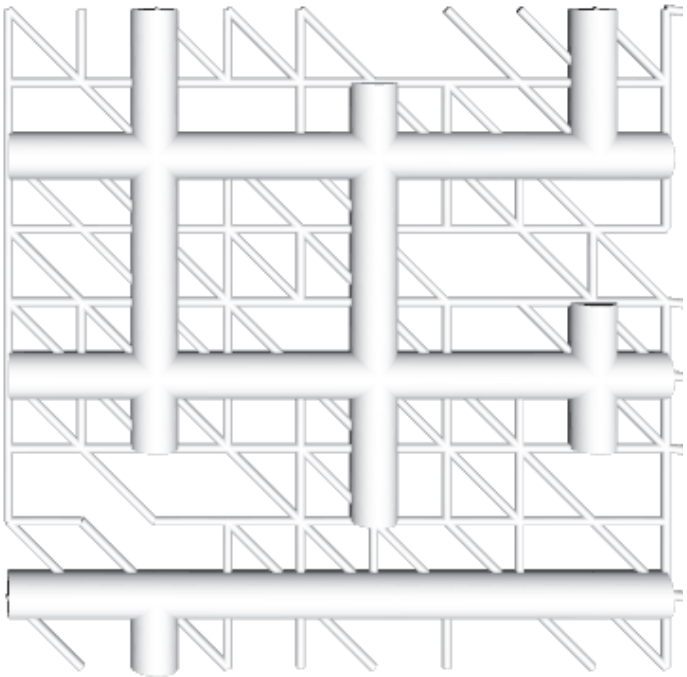


Fig. VIII-8. Illustration of a two-level network with a second configuration where L_2 can be lower than D_2.

With this kind of network configuration, the same sensitivity analysis was performed and we are able to expand the tortuosity values, as can be seen in Fig. VIII-9. Additional data regarding the textural properties can be found in Appendix X.

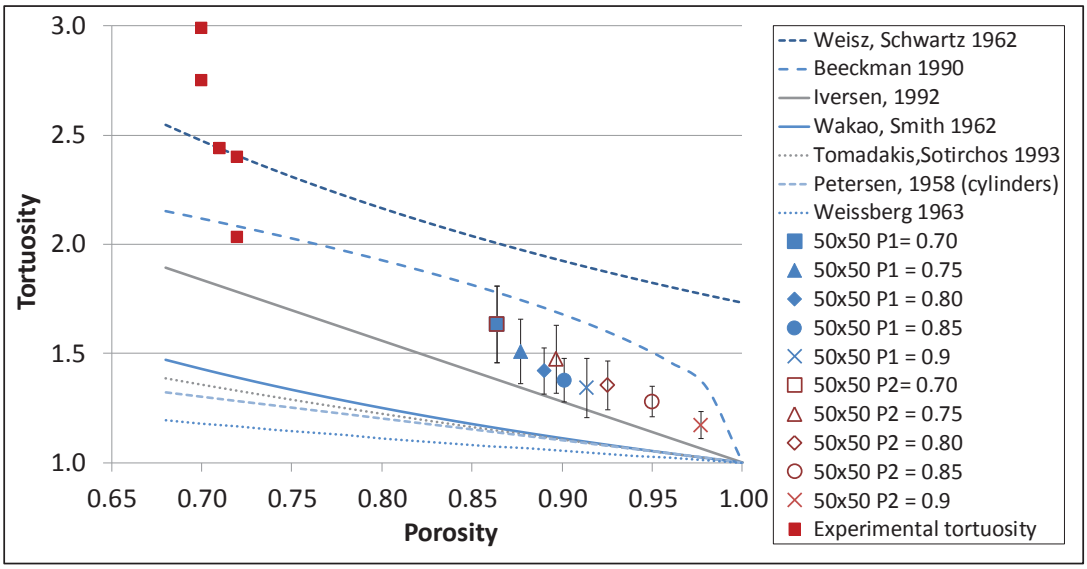


Fig. VIII-9. Influence of the pore existence probabilities P_1 (dotted blue plot) and P_2 (dotted red plot) on the tortuosity for a two-level network taking the 2nd configuration.

VIII.3.2 INFLUENCE OF THE PORE DIAMETER

To perform a sensitivity analyses on the pore diameter, we have varied separately D_1 and D_2 that are respectively the pore diameter for the first level of porosity and for the second level of porosity. For these simulations, we have used P_1=P_2=0.7, L=15 nm and a spacing of 3. When D_1 is varied from 3 to 6 nm, D_2=20 nm and when D_2 is varied from 18 to 21 nm, D_1 = 5 nm.

Table VIII-2 gathers the information relative to the calculated average textural properties when studying the influence of the average pore diameters.

Table VIII-2. Influence of the pore diameter on the average textural properties for two-level networks taking the 1st configuration of a two-level network.

Average textural properties	D_1	D_2
D_{avg} **(nm)**	6.7 - 9.23	7.8 - 8.5
$v_p \times 10^7$ **(m^3·g^{-1})**	6.6 – 15.6	5.8 – 14.5
s_{BET} **(m^2·g^{-1})**	188.4 – 489.8	200.7 – 427.4
ε	0.67 – 0.83	0.64 – 0.82
Z	≈4.11	≈4.11

Fig. VIII-10 shows the average pore diameter D_{avg} when varying the pore diameter from the first level of porosity D_1 and when varying the pore diameter from the second level D_2. Since the number of small pores is much larger than the number of large pores, D_{avg} is more sensitive to the variation of D_1, as shown in Fig. VIII-10. Indeed, starting from the simulations where D_1=5nm and D_2=20nm, if we increase D_2 from 20 to 21 nm, the D_2 relative variation of $\Delta D_2 = 1/20$ and the average pore diameter only varies slightly, while increasing D_1 from 5 to 6nm represents a relative change ΔD_1=1/5 that is much larger, thereby strongly impacting the average pore diameter.

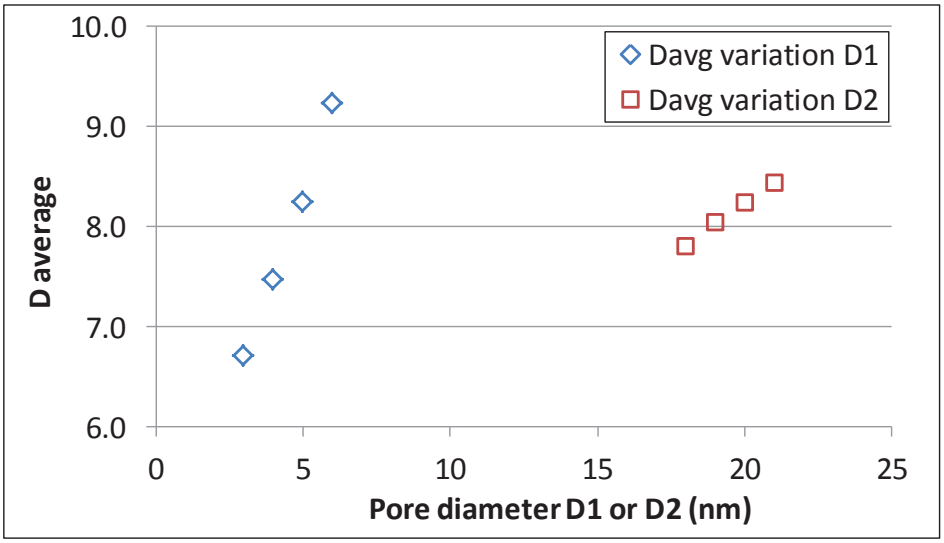


Fig. VIII-10. Influence of the pore diameters D_1 (dotted blue plot) and D_2 (dotted red plot) on the average pore diameter for a two-level network taking the 1st configuration.

Fig. VIII-11 and Fig. VIII-12 show the variation of the specific pore volume and surface area as a function of the pore diameter D_1 or D_2.

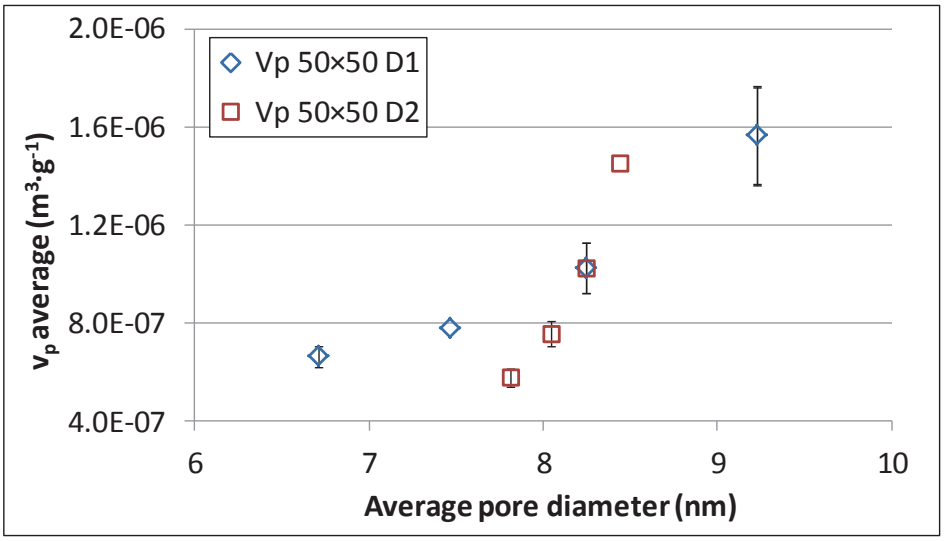


Fig. VIII-11. Influence of the pore diameters D_1 (dotted blue plot) and D_2 (dotted red plot) on the specific pore volume for a two-level network taking the 1st configuration.

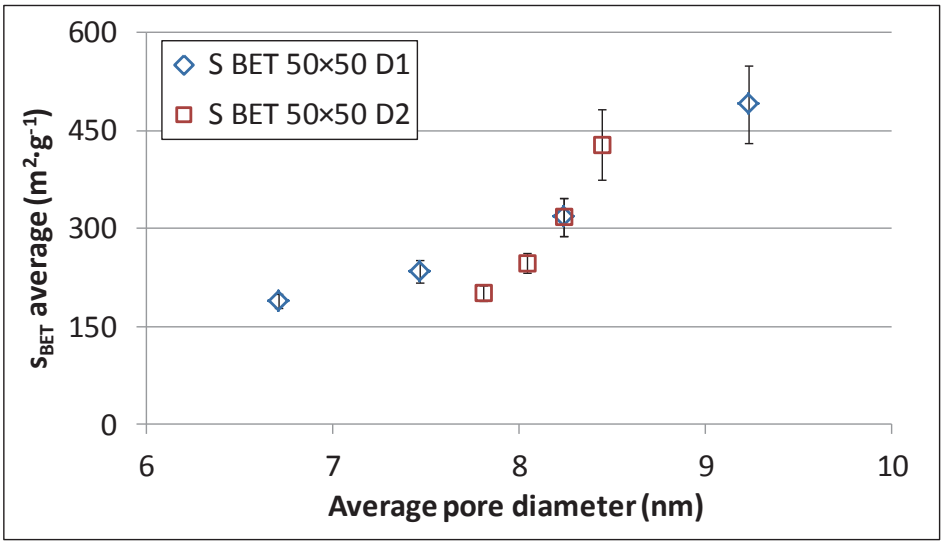


Fig. VIII-12. Influence of the pore diameters D_1 (dotted blue plot) and D_2 (dotted red plot) on the specific surface area for a two-level network taking the 1st configuration.

From the evolution of the specific pore volume and surface area, we can see that there is not much difference in the ranges obtained. As explained above, the effect of the variation of D_1 on the average pore diameter is more significant than D_2, but this is counterbalanced by the effect of the pore volume ratio within a pore network, which is, as we know more significant for larger pores.

For the variation of D_1 (ΔD_1), the average tortuosity ranges from 1.54 to 1.27 for an average porosity of 0.67 to 0.83 and when D_2 is varied (ΔD_2), we have τ = [1.37, 1.49] and ε = [0.64, 0.82], as shown in Table VIII-3, which also lists the outlet pore surface of the infinite plate, the total outlet flow and flux.

Table VIII-3. Mass transfer properties obtained at the outlet surface of the infinite plate and taking the variation of D_1 and D_2 on a two-level pore network taking the 1st configuration of a two-level network.

	$\boldsymbol{D_1(nm) = [3, 4, 5, 6]}$	$\boldsymbol{D_2(nm) = [18, 19, 20, 21]}$
Total outlet flow ×10^{19} (mol·s^{-1})	[3.6, 4.1, 4.7, 5.5]	[4.1, 4.5, 4.7, 4.9]
Total outlet flux ×10^{5} (mol·m^{-2}·s^{-1})	[9.0, 9.5, 9.7, 10.8]	[10.1, 10.3, 9.7, 9.4]
Outlet pore surface ×10^{15} (m^{-2})	[4.0, 4.3, 4.8, 5.1]	[4.1, 4.3, 4.8, 5.3]
Tortuosity, τ	[1.54, 1.47, 1.42, 1.27]	[1.37, 1.36, 1.42, 1.49]

Looking at Fig. VIII-13, the first conclusion is that for two-level pore networks, the pore diameters have an impact on the simulated tortuosities. This is contrary to the effect obtained for the one-level pore networks. Indeed, for one-level pore networks, when the

pore diameter is varied, it changes the diameter of all pores within the network. For two-level pore networks, only some of them are changed, thereby impacting the tortuosity.

The second conclusion that can be taken from Table VIII-3 and Fig. VIII-13 is related to effects of the two diameters. When diameter D_1 is increased, the tortuosity is reduced, while for diameter D_2, the tortuosity remains rather constant. Whether increasing D_1 or D_2 the total outlet flow increases in both cases, but the impact is more important for D_1. This is especially due to the fact that $\Delta D_1 >> \Delta D_2$. Moreover, the variation of the outlet pore surface area is increased in a similar manner for D_2 and D_1, since for a given pore network $S_2/S_1>>1$. Hence, for the variation of D_2, as both the total outlet flow and pore surface area increase simultaneously, we obtain a rather constant tortuosity. But for D_1, the variation of the total outlet flow is preponderant against the variation of the outlet surface area and hence, the total outlet flux increases and the tortuosity are reduced.

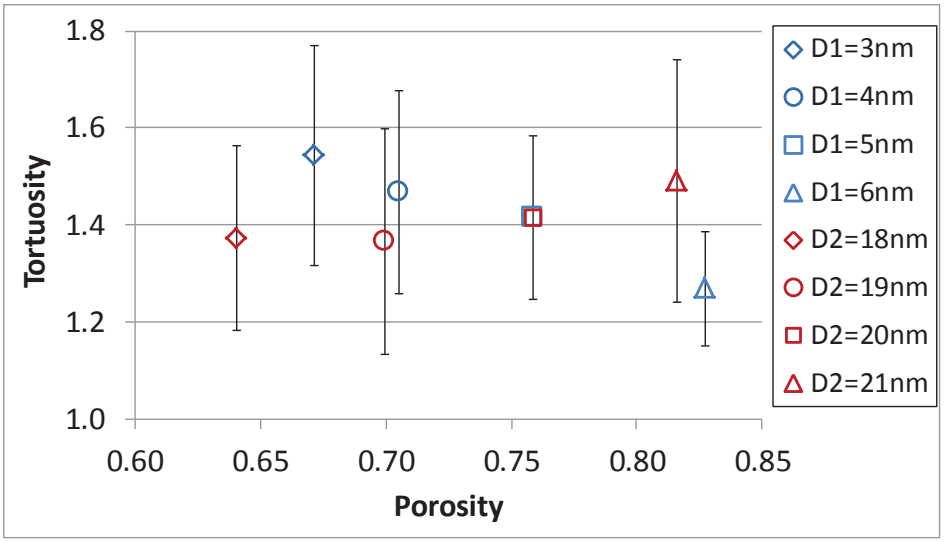


Fig. VIII-13. Influence of the pore diameters D_1 (dotted blue plot) and D_2 (dotted red plot) on the tortuosity for a two-level network taking the 1st configuration.

We have also simulated the second configuration of the two-level pore networks and, as we can see in Fig. VIII-14, the tortuosity values decrease with increasing D_1, but remain constant when D_2 is varied. For this kind of configuration, the behaviour of the textural properties as a function of the pore diameters is collected in Appendix X.

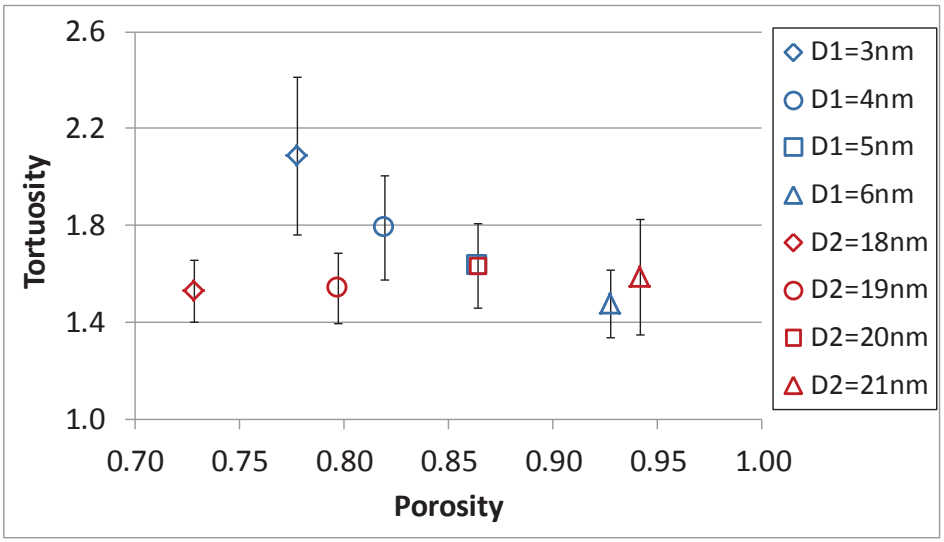


Fig. VIII-14. Influence of the pore diameters D_1 (dotted blue plot) and D_2 (dotted red plot) on the tortuosity for a two-level network taking the 2nd configuration.

VIII.3.3 INFLUENCE OF THE PORE LENGTH

A sensitivity analysis on the influence of the pore lengths will be described in this section. We have varied separately L_1 and L_2, which correspond respectively to the pore length attributed to the first level of porosity and to the pore length for the second level of porosity. For these simulations, P_1=P_2=0.7, D_1=5nm, D_2=20nm and a spacing of 3 are used. When L_1 or L_2 are varied from 15 to 18 nm, L_2=15nm and L_1=15nm, respectively. An important aspect to be mentioned is that the dimensions E_x, E_y and E_z of the parallelepiped particle depend on the pore length L_1 for the smallest pores. Table VIII-4 gathers the information relative to the calculated average textural properties when studying the influence of the pore lengths L_1 and L_2. Fig. VIII-15 and Fig. VIII-16 show the variation of the specific pore volume and surface area as a function of the pore length L_1 or L_2.

Table VIII-4. Influence of the pore length on the average textural properties for two-level networks taking the 1st configuration of a two-level network.

Average textural properties	L_1	L_2
$v_p \times 10^7$ ($m^3 \cdot g^{-1}$)	10.2 – 3.4	10.2 – 11.0
s_{BET} ($m^2 \cdot g^{-1}$)	317.3 – 110.1	317.3 – 325.8
ε	0.76 – 0.51	0.76 – 0.77
Z	≈4.11	≈4.11

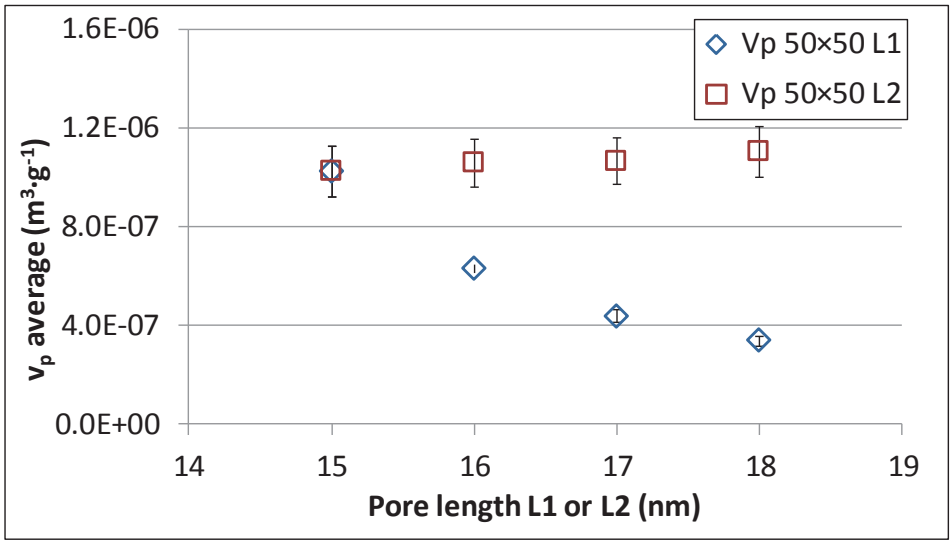


Fig. VIII-15. Influence of the pore lengths L_1 (dotted blue plot) and L_2 (dotted red plot) on the specific pore volume for a two-level network taking the 1st configuration.

Looking at Fig. VIII-15, we expected that the pore volume would be further increased with L_2 due to the fact that the pore volume ratio is greater for larger pores. As we saw in the equations derived in section IV.2.1 for the specific pore volume, the denominator depends on L^2. As mentioned before, the pore length used for the two-level pore networks corresponds to L_1, the pore length of the smallest pores. Hence, increasing pore length L_1 will also increase the size of the parallelepiped particle, thereby reducing the specific pore volume, while the specific pore volume will slightly increase when increasing L_2 at constant values of L_1, i.e. at a constant particle size. Analogously to the evolution of the specific pore volume, the behaviour of the specific surface area as a function of the pore lengths L_1 or L_2 is very similar Fig. VIII-16.

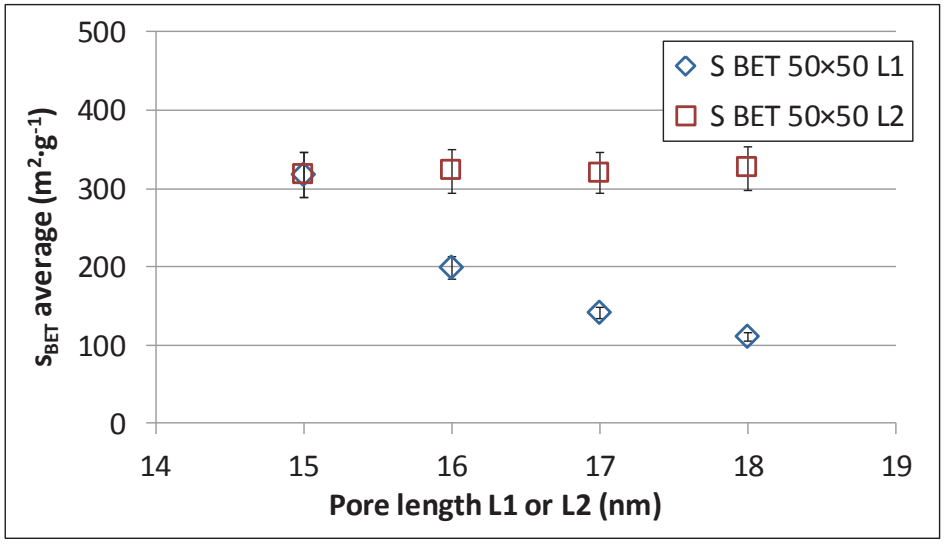


Fig. VIII-16. Influence of the pore lengths L_1 (dotted blue plot) and L_2 (dotted red plot) on the specific surface area for a two-level network taking the 1st configuration.

For the variation of L_1, the average tortuosity ranges from 1.42 to 1.24 for an average porosity of 0.76 to 0.51 and when L_2 is varied, τ = [1.42, 1.60] and ε = [0.76, 0.77]. Fig. VIII-17 shows the average tortuosity increasing with the reduction in L_1 and, with the increase in L_2.

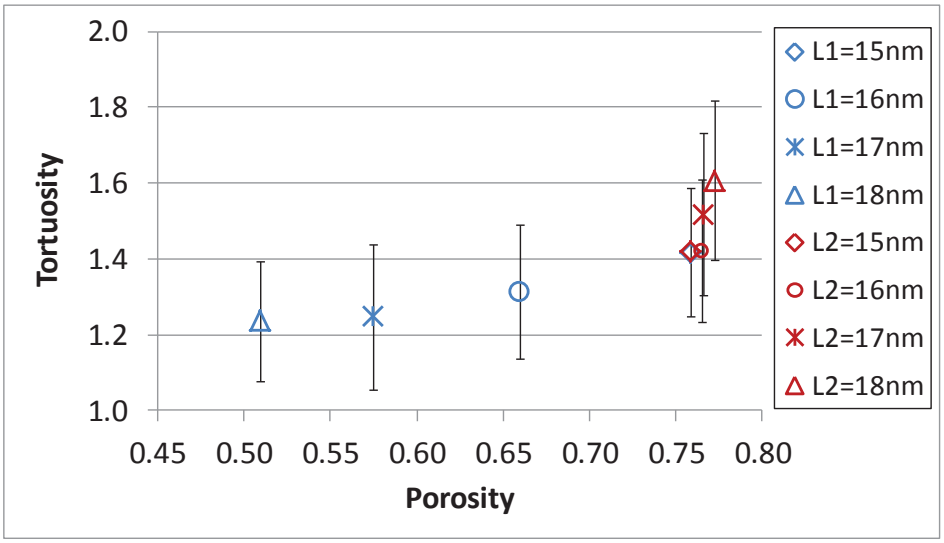


Fig. VIII-17. Influence of the pore lengths L_1 and L_2 on the tortuosity for a two-level network taking the 1st configuration of a two-level network.

Looking at Fig. VIII-17 and the available data in Table VIII-5, when increasing L_2, we observe the total outlet flow is reduced, whereas for L_1, it remains relatively constant. Indeed, the total outlet flow rate gets more affected by the variation of L_2 since, within a given pore network the pore surface ratio is significantly greater than 1, $S_2/S_1>>1$.

To calculate the total outlet flux, the total outlet flow rate is divided by the outlet pore surface area, which remains, of course, constant with the variation of L_1 or L_2. Hence, the total outlet flux shows the same behaviour as the total outlet flow rate.

Table VIII-5. Mass transfer properties obtained on the influence of L_1 and L_2 on a two-level pore network taking the 1st configuration of a two-level network.

	$L_1(nm) = [\,15, 16, 17, 18\,]$	$L_2(nm) = [\,15, 16, 17, 18\,]$
Total outlet flow $\times 10^{19}$ (mol·s^{-1})	$[\,4.7, 4.6, 4.5, 4.5\,]$	$[\,4.7, 4.4, 4.3, 4.1\,]$
Total outlet flux $\times 10^{5}$ (mol·m^{-2}·s^{-1})	$[\,9.7, 9.9, 9.9, 9.4\,]$	$[\,9.7, 9.7, 9.2, 8.6\,]$
Tortuosity, τ	$[\,1.42, 1.31, 1.25, 1.24\,]$	$[\,1.42, 1.42, 1.52, 1.60\,]$

Once again, we remind that we have defined the plate thickness based on L_1 and hence, if L_2 is increased the plate thickness remains the same. This implies that, when L_2

becomes larger than L_1, the large pores are no longer straight cylindrical pores, but they become slightly bent (i.e. tortuous) to connect to nodes that are a distance L_1 apart. Hence, when it comes to the calculation of the effective diffusion coefficient, the increase in L_1 increases D_{ieff} and reduces the tortuosity factor. On the other hand, with the increase in L_2, the plate thickness is not affected and hence, D_{ieff} decreases like the outlet flux and the tortuosity increases.

For the 2nd configuration, we have obtained a similar behaviour that is presented in Fig. VIII-18, but in addition, we obtain larger tortuosity values. This is due to the fact that the larger pores are more frequently connected to smaller pores. The corresponding textural properties can be found in Appendix X.

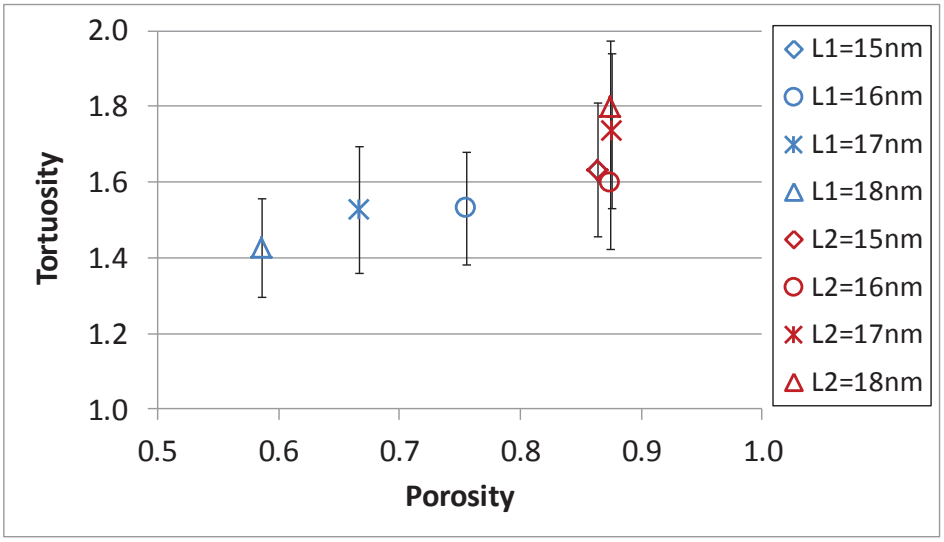


Fig. VIII-18. Influence of the pore lengths L_1 and L_2 on the tortuosity for a two-level network taking the 2nd configuration of a two-level network.

VIII.4 GENERATION OF A TWO-LEVEL NETWORK FOR ALUMINA C

In order to find the model parameters capable of generating pore networks with textural properties that are similar to those of actual aluminas, an optimization tool was developed and is described in this section. As an example, it is applied to alumina C.

As we have seen before, the textural properties can be easily correlated with the pore existence probabilities from the two porosity levels, P_1 and P_2, with a finite range [0,1] Hence, the developed optimization methodology is a simple iterative tool based on dichotomy. We have simplified the optimization tool by keeping constant the pore diameters, lengths and spacing, although one could optimize all these parameters simultaneously. As targets for the optimization, we only have two independent experimental textural properties, the experimental catalyst porosity and the specific surface area.

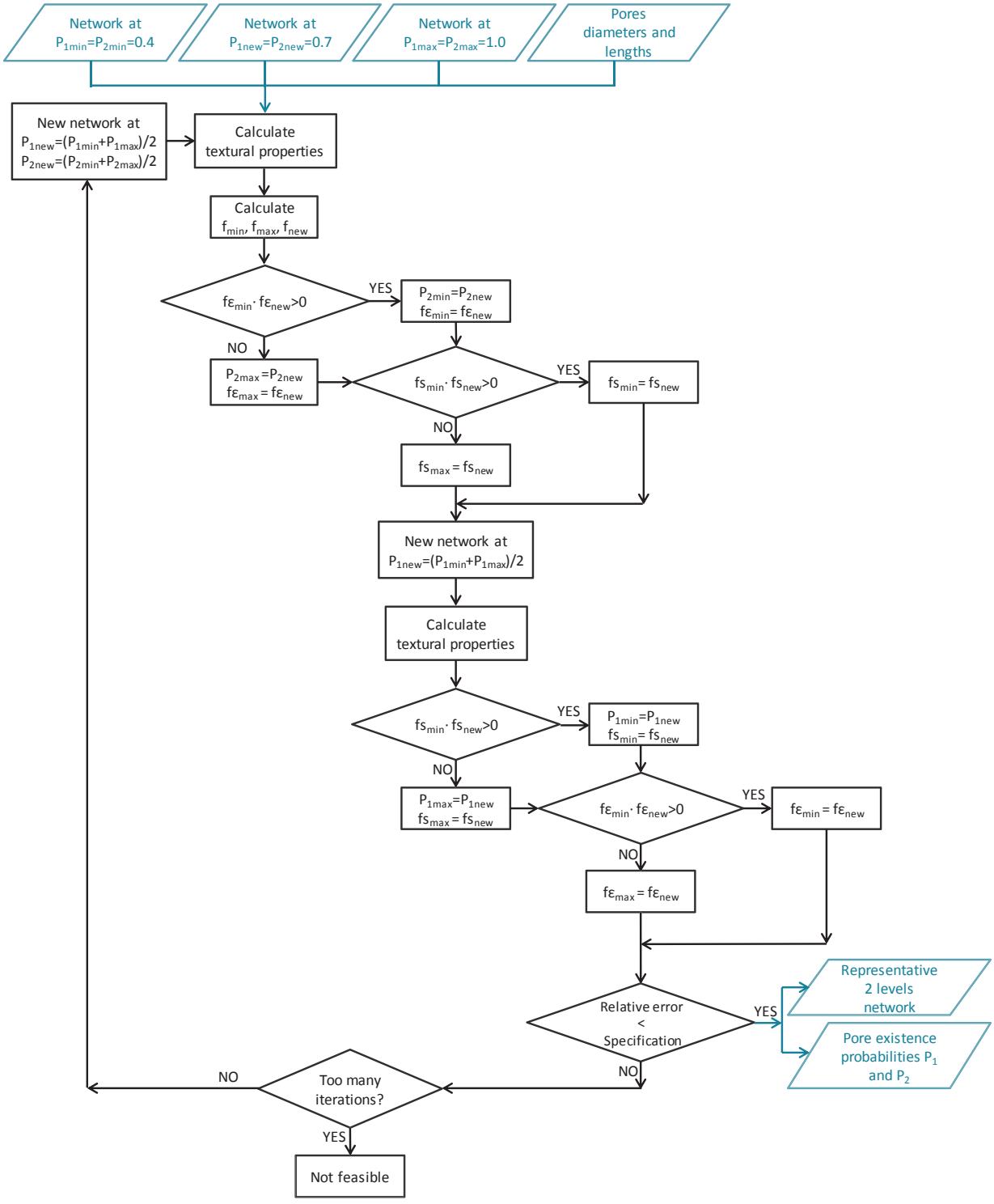


Fig. VIII-19. Flow sheet diagram describing the optimisation of the textural properties, optimizing P_1 and P_2 to obtain respectively, a specific surface area and porosity similar to those from actual aluminas.

The diagram in Fig. VIII-19 describes in summary, the optimization tool used to search for the pore existence probabilities, P_1 and P_2, that are able to generate representative pore networks in terms of the specific surface area and catalyst porosity. The two simulated textural properties are calculated as an average over 30 simulations.

The choice of the parameter, P_1 or P_2, that optimizes either the catalyst porosity or the specific surface area is taken based on the sensitivity analyses shown in the previous section (VIII.3). Taking the first configuration for two-level pore networks, having Z_{max}=6, D_1=5nm, D_2=18nm and L_1=L_2=15nm, we have generated thirty pore networks at a low pore existence probability (P_1=P_2=0.4) and at the maximum pore existence probability (P_1=P_2=1.0). As mentioned before, for both extremes, the average catalyst porosity and specific surface area are calculated over thirty pore networks. These features are then confronted to the experimental values to check if, in between the considered probability range, it is possible to find the target and which new range must be chosen to continue the iteration until the target is reached.

Fig. VIII-20 and Fig. VIII-21 show the behaviour of the absolute error calculated from the textural properties, considering a separate variation of the pore existence probabilities, P_1 and P_2.

As we can see from Fig. VIII-20 and Fig. VIII-21, the absolute errors obtained for the catalyst porosity and specific surface area reach a value of 0, for values of P_1 or P_2 that fall within the range [0,1] Hence, it is possible to find a two-level pore network with textural properties that are similar to those of actual aluminas.

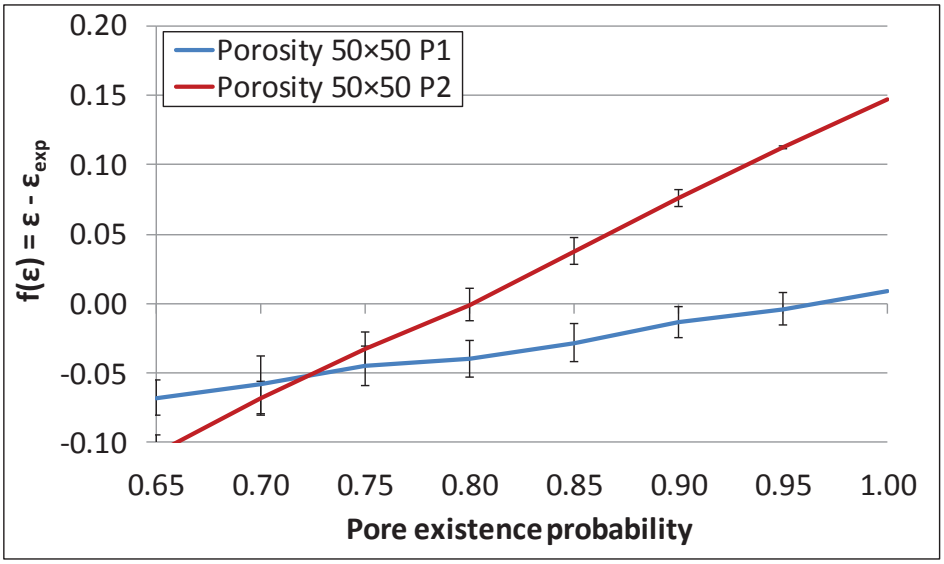


Fig. VIII-20. Absolute error obtained for the porosity having varied either P_1 or P_2.

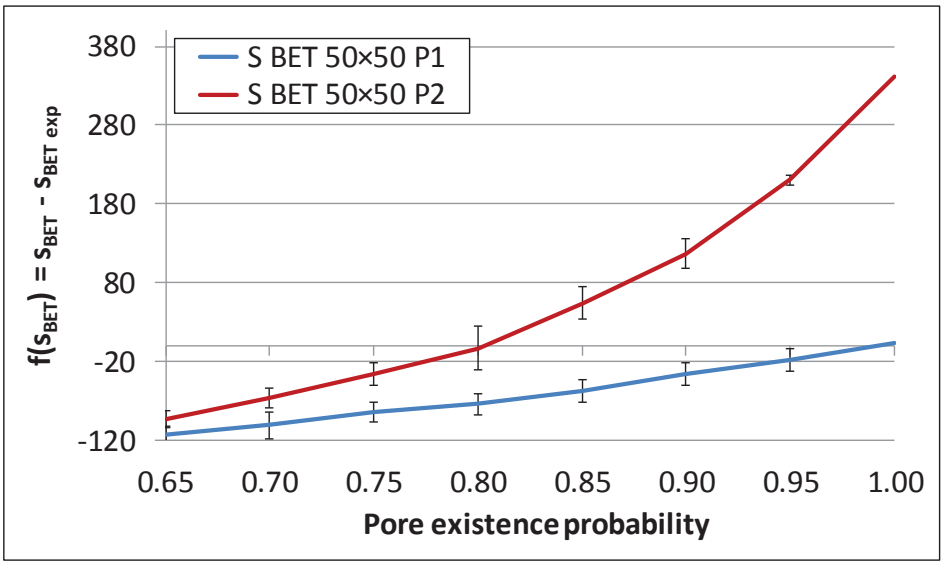


Fig. VIII-21. Absolute error obtained for the specific surface area having varied either P_1 or P_2.

Taking the 2nd configuration of two-level pore networks (Fig. VIII-8) and a network size of 100×100, we have optimised the pore existence probabilities for different sets of models parameters (L_1, D_2 and D_1) in order to represent alumina C (cf. Table VIII-1). The available textural properties are gathered in Fig. VIII-22 to Fig. VIII-24. The different sets of model parameters are assembled in groups of given pore length L_1 and pore diameter D_2. For each group, several pore diameters D_1 have been tested.

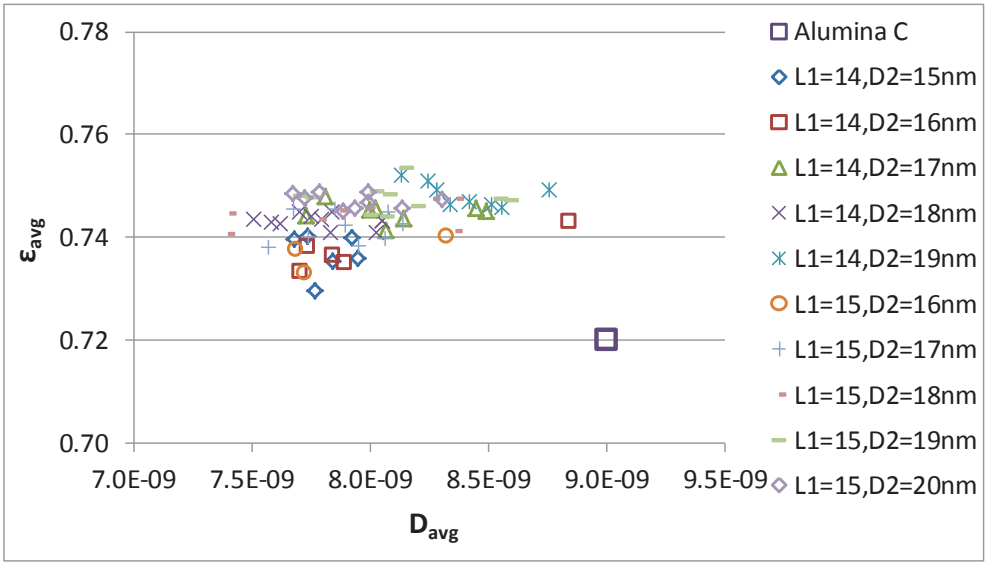


Fig. VIII-22. Catalyst porosity as a function of the average pore diameter obtained for two-level pore networks representing alumina C. Taking in consideration the diagram from Fig. VIII-19.

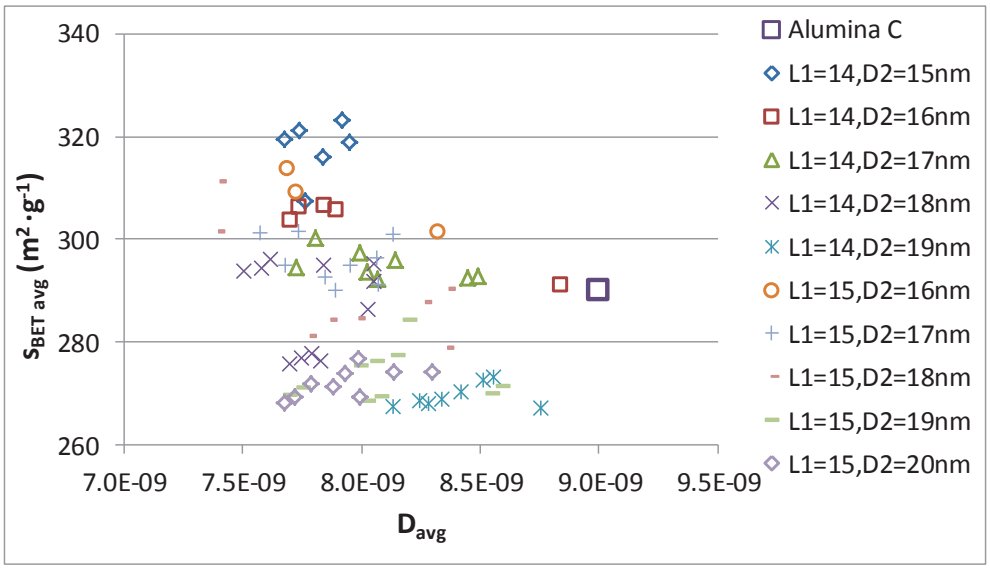


Fig. VIII-23. Specific surface area as a function of the average pore diameter obtained for two-level pore networks representing alumina C. Taking in consideration the diagram from Fig. VIII-19.

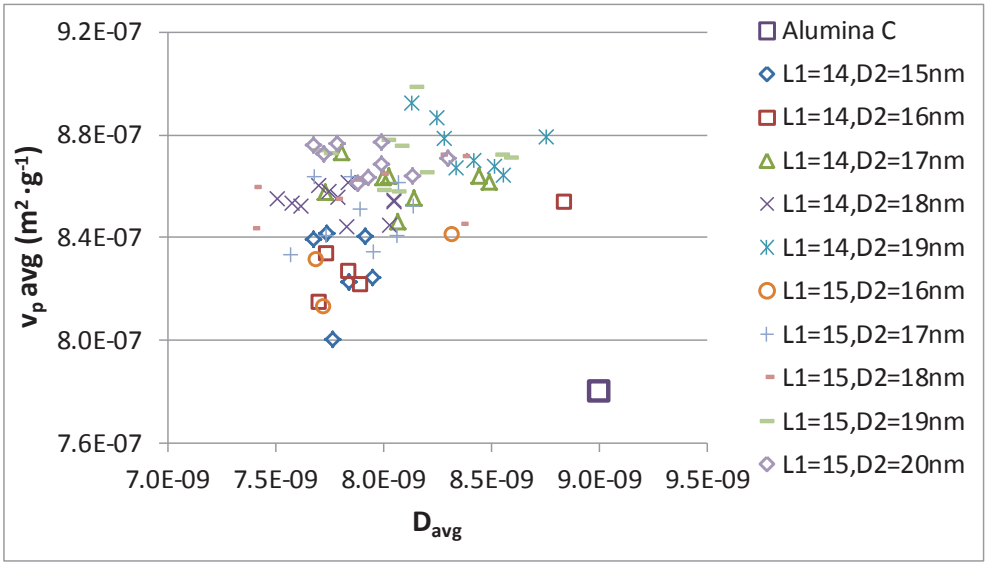


Fig. VIII-24. Specific pore volume as a function of the average pore diameter obtained for two-level pore networks representing Alumina C. Taking in consideration the diagram from Fig. VIII-19.

As we can see from these figures, several sets of model parameters allow to obtain similar textural properties. Moreover, the textural properties are relatively close to those of alumina C, even if the average diameter remains somewhat underestimated. This also shows that the two-level pore networks are overdetermined, as different combinations of model parameters lead to similar properties. To find a unique set of model parameters that fulfils the structural characteristics of alumina C, it will be necessary to include additional data, for instance based on the simulation of physisorption within these networks.

Starting from this first set of simulations, we selected some of the model parameter sets (diameters and lengths) and their corresponding optimised pore existence probabilities.

For a selected number of cases, the two-level pore networks were generated and their mass transfer properties were calculated. The values obtained with this second set of simulations were then compared to those of alumina C, as shown in Fig. VIII-25 to Fig. VIII-27. As can be seen, the textural properties are quite well represented by these two-level pore networks.

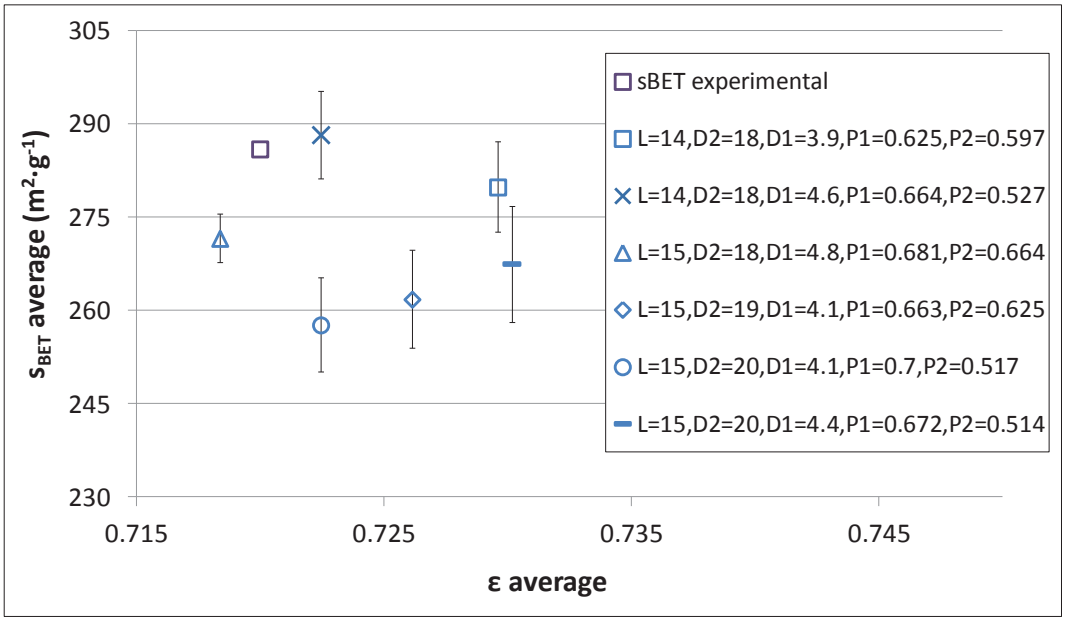


Fig. VIII-25. Specific surface area according to catalyst porosity obtained from optimised two-level pore networks (100×100) representing alumina C.

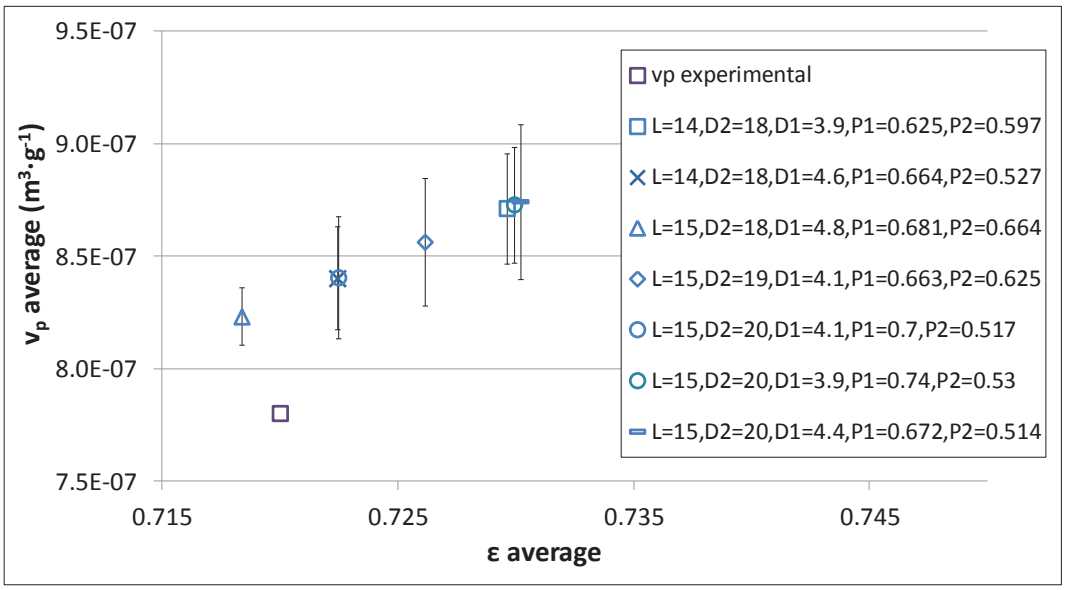


Fig. VIII-26. Specific pore volume according to the catalyst porosity obtained from optimised two-level pore networks (100×100) representing alumina C.

The corresponding mass transfer properties are presented in Fig. VIII-27, showing the average tortuosity as a function of the average catalyst porosity. As can be observed

from Fig. VIII-25 to Fig. VIII-27, the use of a two-level pore network allows us to reproduce both textural and mass transfer properties of alumina C networks.

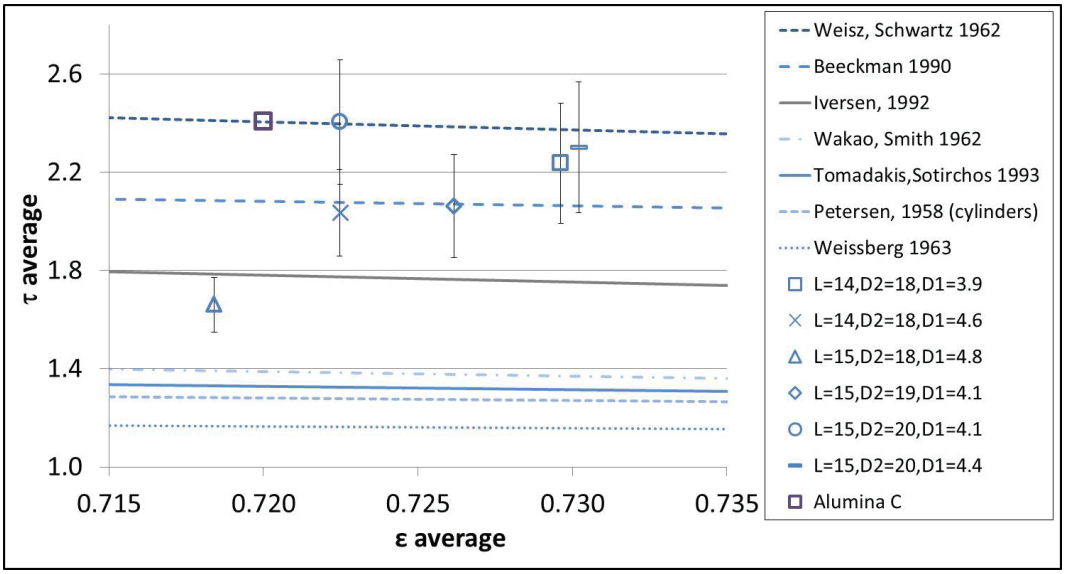


Fig. VIII-27. Tortuosity according to porosity obtained from optimised two-level pore networks (100×100) representing alumina C. Correlations taken from Akanni and Evans (1987), Beeckman (1990), and Shen and Chen (2007), and experimental data for different aluminas from Kolitcheff (2017).

We have decided to go a little further on this study by taking the set of parameters L=15, D_2=20, D_1=4.1 nm and, the pore existence probabilities of P_1=0.7 and P_2=0.517. As we can see from Fig. VIII-27, with this set of parameters, we obtain a tortuosity that is similar to that for alumina C. We therefore decided to test another set of parameters with D_1=3.9nm (green dot) and, a second one with P_1=0.72 (dark red).

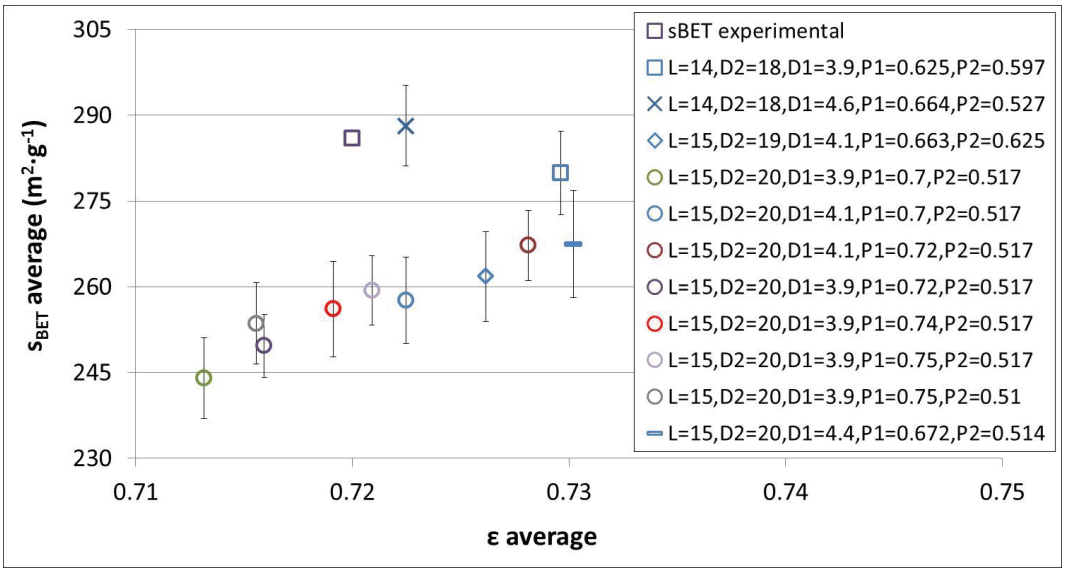


Fig. VIII-28. Specific surface area according to the catalyst porosity obtained from two-level pore networks (100×100) representing alumina C.

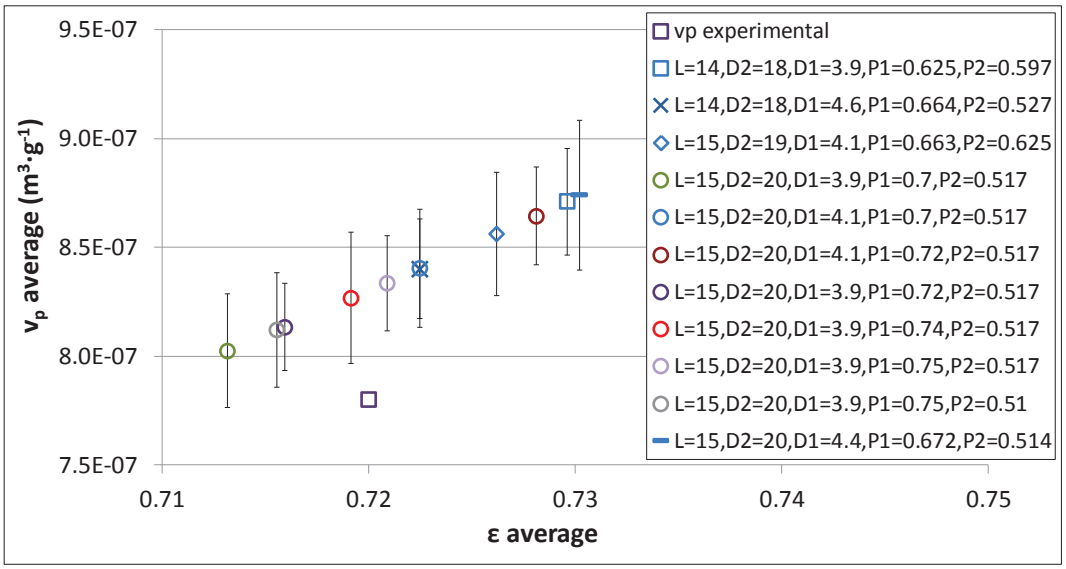


Fig. VIII-29. Specific pore volume according to the catalyst porosity obtained from optimised two-level pore networks (100×100) representing alumina C.

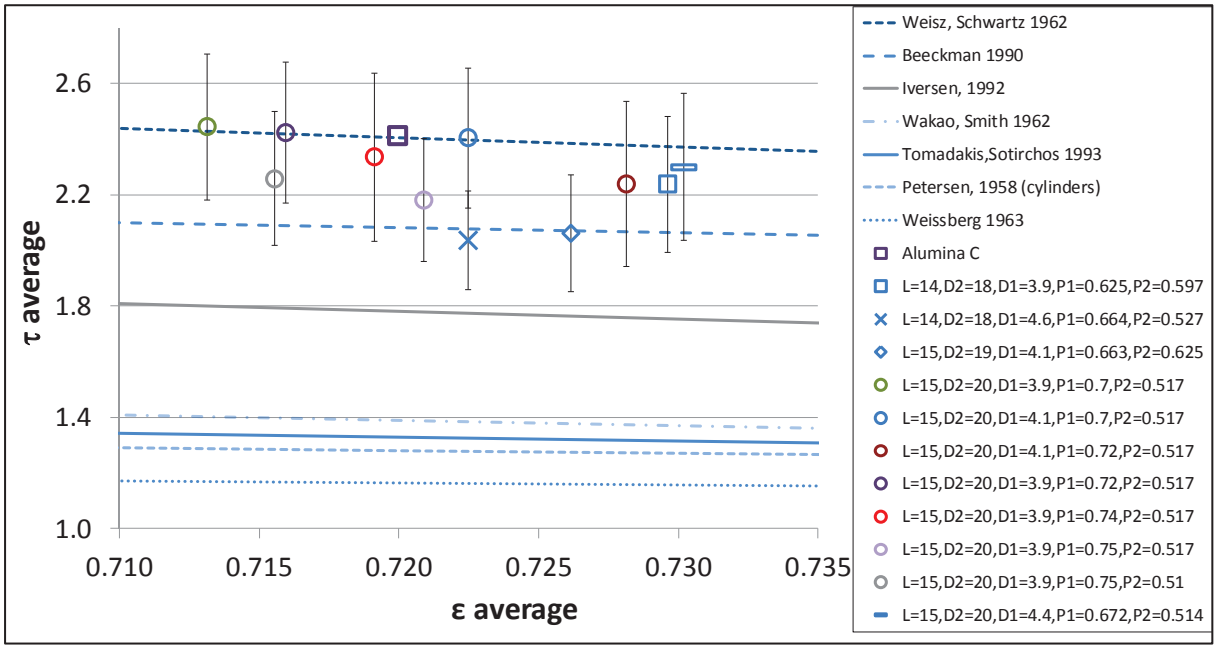


Fig. VIII-30. Tortuosity according to the porosity obtained from two-level pore networks (100×100) representing alumina C. Correlations taken from Akanni and Evans (1987), Beeckman (1990), and Shen and Chen (2007), and experimental data for different aluminas from Kolitcheff (2017).

With the decrease in the diameter D_1, we increase the tortuosity and reduce v_p approaching the actual data. Yet, the s_{BET} is reduced, as well as ε deviating once more from the experimental data. With the increase of P_1, the tortuosity, ε and v_p are not favoured but the s_{BET} gets closer. The combined effect of decreasing D_1 and increasing P_1 (L=15, D_2=20, D_1=3.9nm, P_1=0.72 and P_2=0.517 - dark purple dot), gives rather similar values to those from alumina C in terms of τ, v_p and ε whereas, the s_{BET} is rather low compared to the experimental value.

Taking then this set of model parameters where L=15, D_2=20, D_1=3.9nm, P_1=0.72 and P_2=0.517, we pursued the study by increasing the pore existence probability P_1 to 0.74 (red dot) and then to 0.75 (light purple). As can be observed, the parameters set L=15nm, D_2=20nm, D_1=3.9nm, P_1=0.74, P_2=0.517 agrees in terms of the diffusional properties. Also, the relative errors obtained respectively, for the specific pore volume and surface area are of 10.5 and 6%.

VIII.5 CONCLUSIONS

Using one-level pore networks, we have seen in Chapter V that the textural properties from these networks are in accordance with the orders of magnitude for actual aluminas. On the other hand, when confronting the simulated tortuosities (<1.5) with experimental data (2 to 3, cf. Fig. VIII-2), a large discrepancy is observed. Moreover, during the experimental study of actual aluminas (Kolitcheff *et al.*, 2017) via inverse liquid chromatography, a different organization of the aluminas structure was proposed, suggesting an organization in two porosity levels. This proposal was reproduced in our model that was imagined to be constituted by several regions containing small pores (1st level of porosity), which are surrounded by slightly larger pores (2nd level of porosity). The developed two-level pore networks therefore contain two different pore diameters, pore lengths and pore existence probabilities.

A sensitivity analysis was performed to the model parameters in order to understand which parameters should be optimised in order to reproduce the experimental textural properties, specifically the catalyst porosity and specific surface area. The chosen parameters are P_1 and P_2, used respectively to reproduce the specific surface area and the porosity.

With the developed optimisation tool, several sets of model parameters (L, D_2 and D_1) were considered and fixed in order to determine P_1 and P_2. For each set, thirty 2D triangular pore networks of size 100×100 were generated, and the average properties over these thirty networks were used to select P_1 and P_2. Taking some of the sets and their corresponding pore existence probabilities obtained via the optimisation tool, we have once more generated thirty 2D triangular networks of size 100×100 to calculate both, the textural and the mass transfer properties and compare them to the experimental data of alumina C. It was shown that, for some of these parameter sets, the two-level pore networks could reproduce the textural properties and the tortuosity value of alumina C. For this alumina, the selected final model parameters are: L=15nm, D_2=20nm, D_1=3.9nm, P_1=0.74 and P_2=0.517.

THESIS CONCLUSIONS

We have dedicated this project to a better understanding of the mass transfer description within porous catalysts, specifically on gamma-alumina supports, which are highly complex porous systems. These catalyst supports are widely used in the refining industry, and a correct understanding of their impact is essential. Since the catalyst performance directly depends on the porous structure, dispersion of the active sites, the diffusing molecules and the diffusion regime, the need to correctly represent both the porous structure and mass transfer seems clear.

As cited in the literature review, Keil (1999) considered that the preferred model to investigate the influence of the porous structure on the mass transfer description is a discrete representation. Several models can be found in the open literature, yet, to our knowledge, none of these models tried to simultaneously recreate both textural and mass transfer features of actual gamma-alumina supports.

In order to correctly represent the porous structure of actual aluminas, it is necessary to rely on experimental characterization. Some textural properties can be measured via physisorption techniques. The main features that can be obtained are essentially the pore volume, the specific surface area, as well as the pore size distribution and the connectivity. In a parallel PhD thesis carried out by Svetan Kolitcheff, the nitrogen sorption technique was used to obtain, for five different aluminas, their main textural properties.

Moreover, it is also important to rely on the experimental study of mass transfer within actual aluminas. An Inverse Chromatography setup was used in the framework of

Kolitcheff's Ph.D. resulting in the estimation of diffusional tortuosities obtained for the studied aluminas.

We have developed a simulation tool that is based on a discrete representation and that is capable of generating random pore networks and simulate mass transfer by diffusion within each pore.

The pore network generation model was validated in terms of its Monte Carlo variability and it was concluded that, for a 2D pore network of maximum connectivity 6 and with a pore existence probability of 0.7, the minimum network size required is of 10,000 nodes. Also, averaging the simulation results over 30 pore networks allows obtaining sufficiently high and repeatable model precision. The model was also tested in terms of the network aspect ratio N_x/N_y, .i.e. the ratio of its size in the x and y direction when $N_x \neq N_y$, and it was concluded that a rather high ratio of N_x/N_y is preferred.

The sensitivity analysis performed on the algorithm showed that the textural properties increase with the model parameters, such as the pore existence probability, pore diameter and length. We have obtained a satisfactory to good agreement between the textural properties of the discrete representation and the values for the actual gamma-aluminas.

Regarding the results on the mass transfer properties obtained through sensitivity analyses, for the variation of the pore existence probability, a relation of the tortuosity with the catalyst porosity was put in evidence. We observed that the tortuosity decreases with increasing catalyst porosity. A comparison with theoretical correlations showed a similar trend between data, and our tortuosity values were rather similar to those obtained by Tomadakis and Sotirchos (1993). However, the simulated tortuosities showed rather low values when compared to the experimental results obtained via Inverse Chromatography. We also observed that the tortuosity was not affected by the variation of the pore diameters and pore lengths. Hence, we concluded that this is due to the underlying hypotheses of the model respectively, 1D diffusion and the fact that when we increase the pore length, the network expands as well.

The dynamic mass transfer study compared our discrete representation with a pseudo-homogeneous continuum model, and showed that a correcting factor is required between the two models. It was concluded that this correcting factor should be applied to the accumulation term, when simulating mass transfer with the pseudo-homogeneous continuum representation. This correction factor is simply the volume ratio of the continuum to discrete representation. This correction is required due to the fact that we have used the outlet pore surface of the periodic network (discrete representation) as the outlet surface of the macro-pore (continuum representation), and also that the infinite

plate thickness defined the macro-pore length. Hence, the total accessible volume from the two representations is different. However, it is important to mention that a good representation of the dynamic response of the continuum model using the correction factor is only valid when it comes to sufficiently large pore networks, and that the effect of dead volumes must be accounted otherwise.

At this point, we focused on the experimental mass transfer characterization in order to understand how to reproduce the mass transfer properties of actual aluminas. Kolitcheff stated that the porous structure of actual aluminas was probably organized in several porosity levels. We have therefore tried to reproduce random pore networks with this main characteristic, by creating regions, where small pores are interconnected, that are surrounded by larger pores.

With this new representation of pore networks with two-levels of porosity, we observed an increase in the tortuosity values. After implementing an optimization tool to determine the pore existence probabilities from the textural properties, we have been able to reproduce both the textural and mass transfer properties, as was illustrated for alumina C. Taking a 2D periodic network of size 100×100, a good agreement was found between the simulated and experimental data, having obtained a tortuosity of 2.34 against 2.40, while the deviations for the textural properties are rather low, and more specifically, relative errors of 0.12%, 10%, and 6% were found for the catalyst porosity, the specific pore volume and specific surface area, respectively.

PERSPECTIVES

As shown above, an optimization tool was implemented in order to identify the set of model parameters that are able to represent the alumina studied – alumina C. From this study available in Chapter VIII, we have concluded that several sets of model parameters are able to fulfil this task. We believe that extra comparative data would allow to discard some of these sets. To this aim, one could rely on the simulation of nitrogen adsorption/desorption within our random pore networks.

We have started by implementing a simple tool capable of conducting the nitrogen adsorption/desorption phenomena within the periodic pore networks. This algorithm, that was in part developed by Monsur Uddin during his supervised internship, is divided in two main parts: the nitrogen adsorption simulation and the nitrogen desorption simulation.

At each relative pressure, the Kelvin or critical radius r_K is calculated, attending to factor *f* that takes a value of 1 during adsorption and of 2 during desorption. This factor takes into account the shape of the liquid-vapour interface, a cylindrical interface for adsorption and a hemispherical during desorption. The adsorbed layer thickness t is calculated as well. Two correlations are tested in this model: the De Boer's and the Halsey equations, retrieved from Hammond and Conner (2013).

In order to simulate the adsorption process, we calculate the adsorbed volume at each incremented relative pressure and for each pore of the network making use of the Kelvin and thickness equations. The Kelvin radius is going to dictate which pores of the network are going to be completely filled with adsorbed nitrogen where $(R_p - t) \leq r_K$ and those that will keep filling layer by layer and therefore having $(R_p - t) > r_K$. The diagram that

follows (Figure 1) gives a global flow diagram of the algorithm used to simulate the adsorption process.

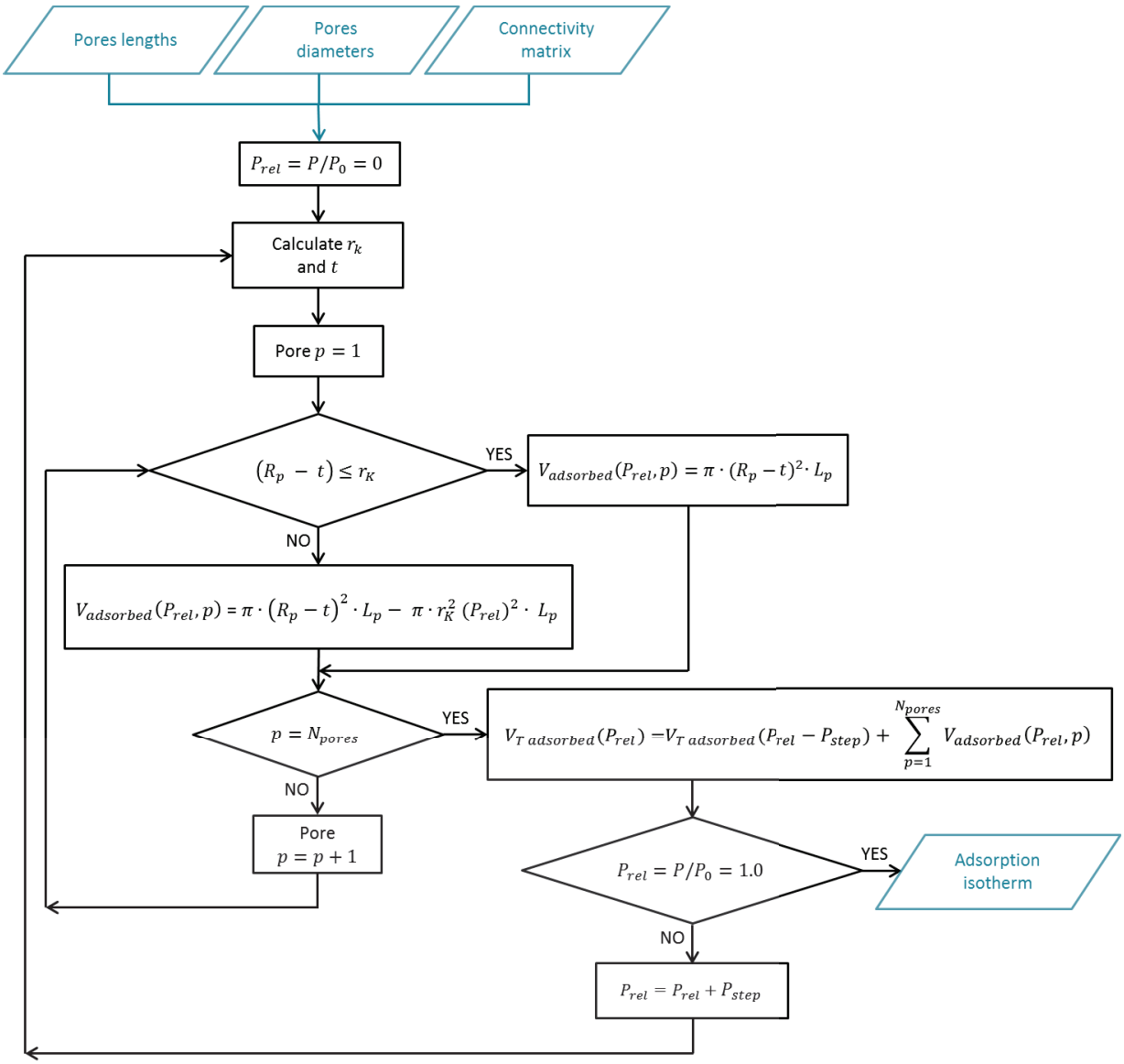


Figure 1. Conduction of the adsorption algorithm.

For the desorption process, the algorithm developed calculates the desorbed volume accounting for the percolation phenomenon caused by the network connectivity. This reproduces the hysteresis on the adsorption/desorption isotherm, as we have seen from the Seaton model (Seaton, 1991). In order to take into account for the network connectivity, the definition of an equivalent diameter is used.

The equivalent diameter of a given pore is the actual pore diameter at which the nitrogen is going to desorb due to the network connectivity. Hence, the equivalent diameter D_{eq} is not necessarily given by the pore diameter itself D_p, but can possibly be imposed by the diameter of an adjacent pore. The algorithm implemented is briefly described in the following diagram (Figure 2).

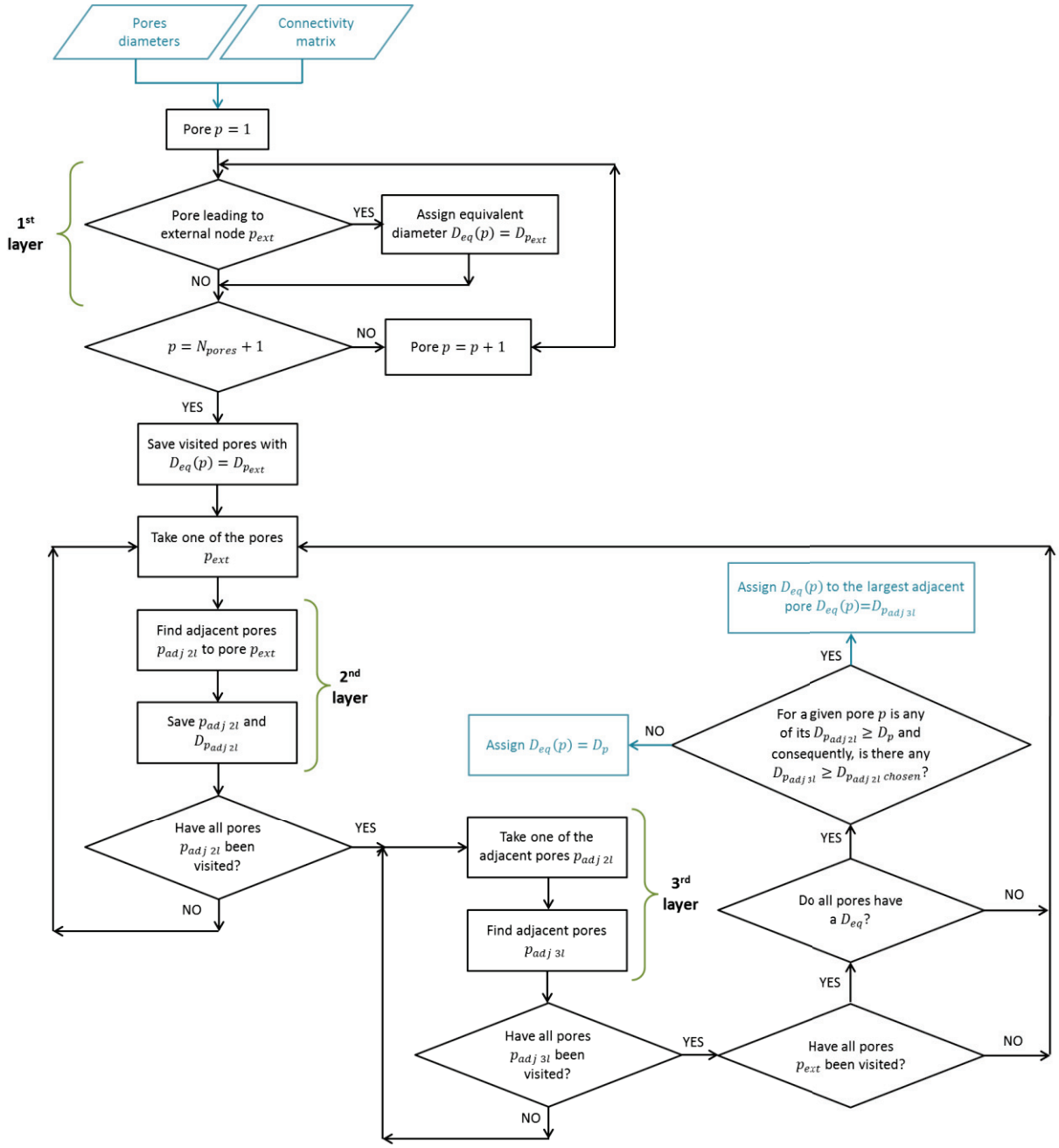


Figure 2. Definition of the equivalent diameter in order to simulate desorption taking into account the connectivity effect.

We first assign to each pore connected to an external node their equivalent diameter D_{eq}. Due to the fact that these pores are directly connected to the external surface, their equivalent diameter is simply their own diameter D_p. Then, taking these external pores, we cover their adjacent pores (representing the 2nd layer) and their pore diameters are saved. We pursue with another layer of adjacent pores (representing the 3rd layer).

After assigning the equivalent diameter to each pore of the network, one may simulate desorption using the Kelvin radius and comparing to the equivalent radius. The algorithm

for the desorption simulation becomes very similar to that from the adsorption, as shown in the following Figure 3.

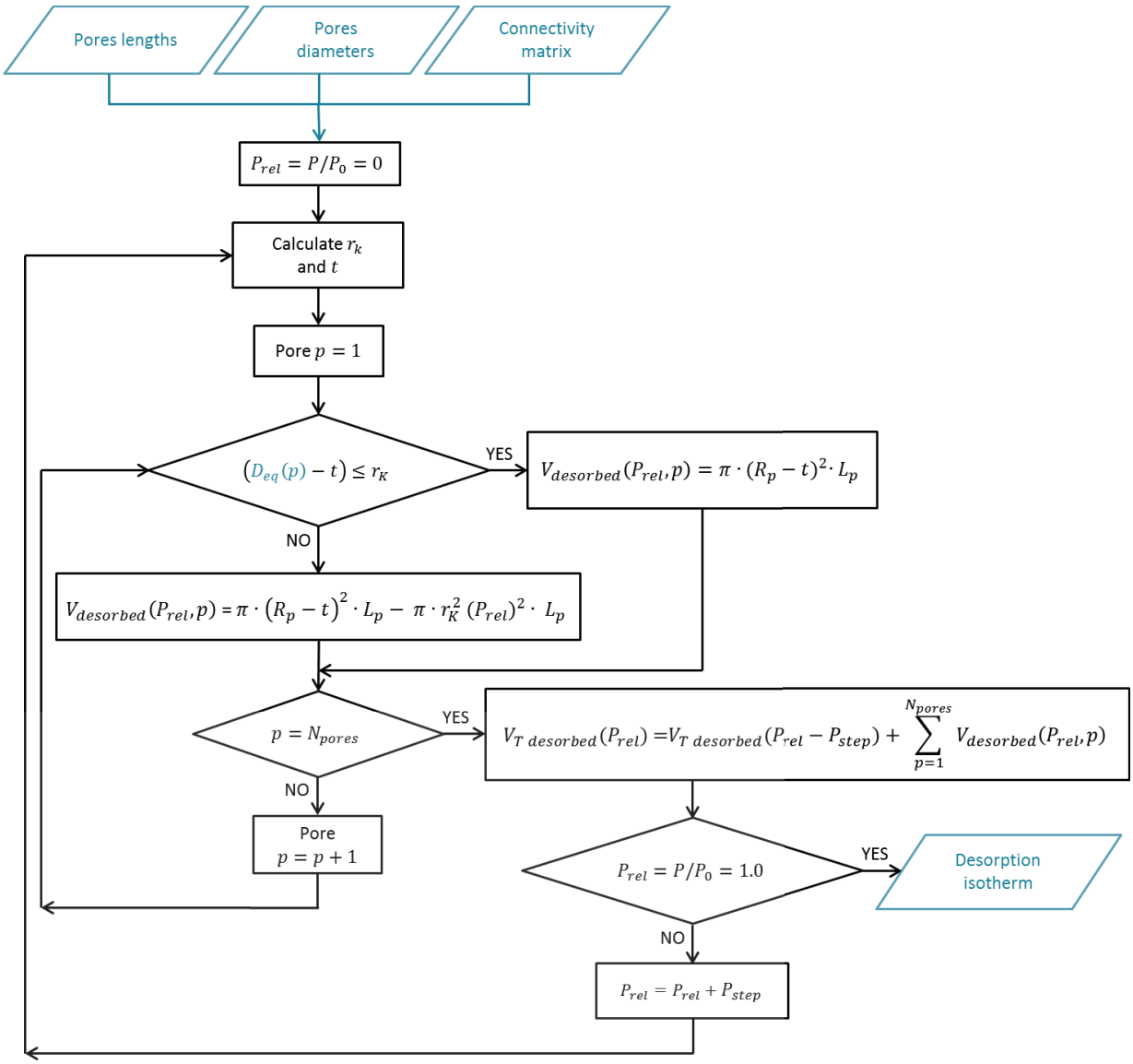


Figure 3. Desorption simulation using the equivalent diameter previously defined.

In order to test the algorithm, a sensitivity analysis was performed taking several pore size distributions (*PSD*). The sensitivity analyses are performed to study qualitatively the effect of different *PSDs* on the adsorption/desorption isotherms. For instance, in Figure 4 to Figure 6, the effect of the *PSD* spread on the isotherm is considered. For narrower pore size distributions, if we take a look at the desorption branch, we observe the adsorbed volume being reduced more abruptly. Now, comparing the effect of having a greater amount of smaller pores to a greater amount of larger pores, Figure 7 and Figure 8 respectively, show that for a greater amount of smaller pores, the desorption delay is increased.

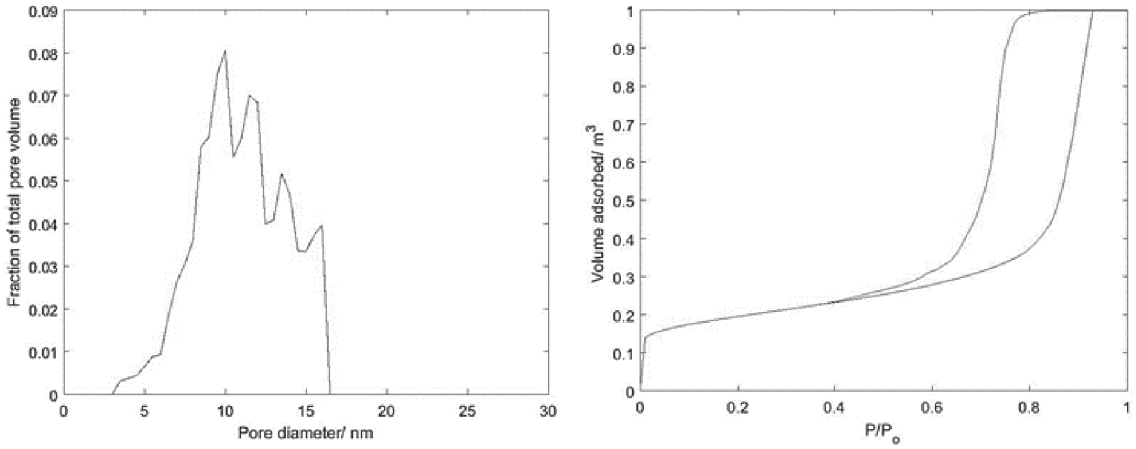


Figure 4. Wide spread pore size distribution (on the left) with the corresponding adsorption/desorption simulation (on the right).

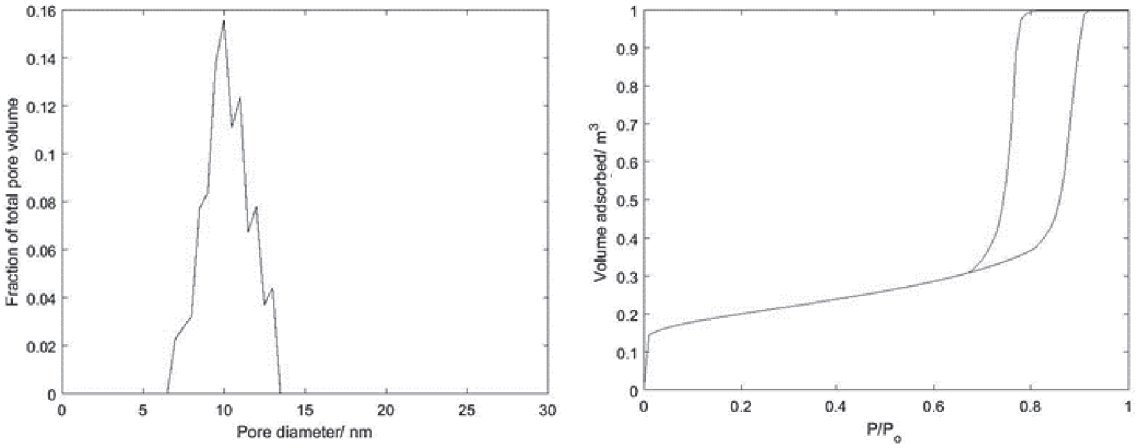


Figure 5. Medium spread pore size distribution (on the left) with the corresponding adsorption/desorption simulation (on the right).

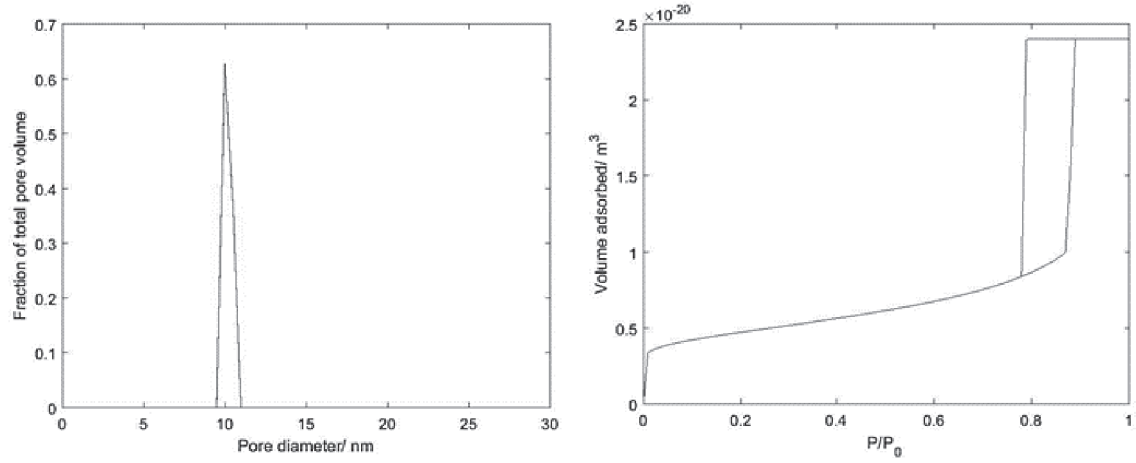


Figure 6. Narrow spread pore size distribution (on the left) with the corresponding adsorption/desorption simulation (on the right).

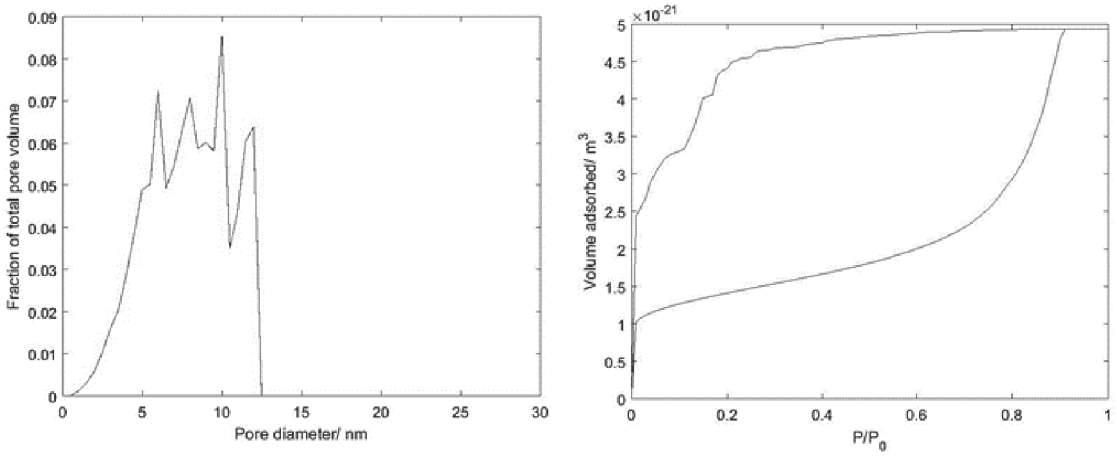


Figure 7. Positive skew pore size distribution (on the left) with the corresponding adsorption/desorption simulation (on the right).

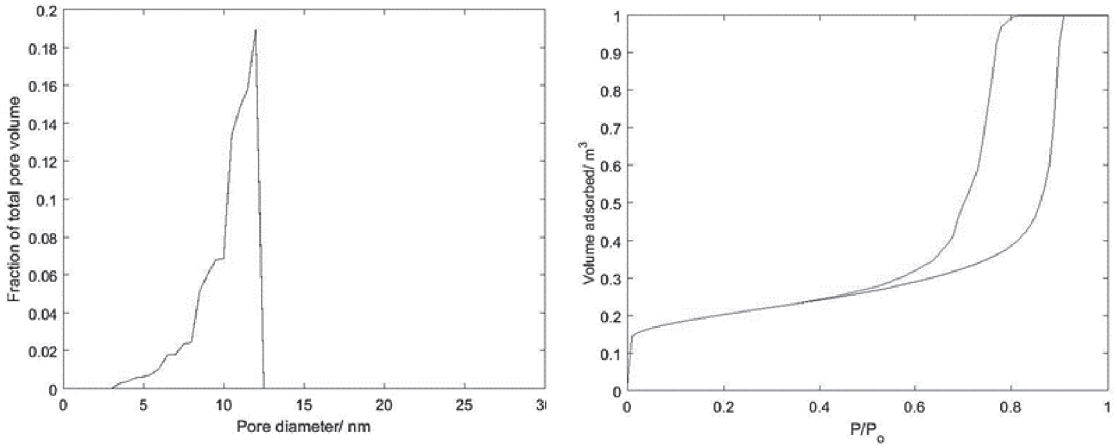


Figure 8. Negative skew pore size distribution (on the left) with the corresponding adsorption/desorption simulation (on the right).

As mentioned before, the simulation of the adsorption/desorption phenomena within our random pore networks could be an asset to define the set of model parameters capable of reproducing actual aluminas. The developed algorithm could be used to go further on this subject.

During this PhD thesis, we have mainly focused on calculated textural and mass transfer properties obtained for pore networks with constant pore diameter. The effect of pore size distributions on the textural and mass transfer features should also be investigated and may get us closer to the real system. Moreover, the simulation of physisorption within the generated two-level pore networks could probably allow a better reproduction of the textural properties and the pore size distribution of actual aluminas.

Concerning the mass transfer simulations, the continuum representation was used to determine the calculated tortuosity from the steady state flux at the outlet of the discrete simulation. The dynamic simulations could also be directly compared to the experimental

transient data obtained via inverse chromatography, instead of extracting “experimental” tortuosities from the data.

In order to utilize our discrete model for actual applications, it would be interesting to study non-linear systems, by accounting for adsorption and for catalytic reactions, and also test the the use of multicomponent mixtures. The effect of the organization of the alumina support on the catalytic performances could then be studied by using representations of several existing aluminas in such diffusion-reaction systems. Additionally, to validate these simulations, one could then prepare different catalysts by impregnating the same active phase on different alumina supports and perform the corresponding experiments.

Ultimately, these tools may be used to generate the “optimal” alumina support for a given reaction system by creating various alumina supports and simulating the coupled diffusion-reaction for each of these supports with a given active phase.

BIBLIOGRAPHIC REFERENCES

Akanni, K.A.; Evans, J.W. (1987) "Effective transport coefficients in heterogeneous media". Chemical Engineering Science, vol. 42, n° 8, p. 1945–1954. En ligne : http://www.sciencedirect.com/science/article/pii/0009250987801410.

Androutsopoulos, G.P.; Salmas, C.E. (2000) "A New Model for Capillary Condensation-Evaporation Hysteresis Based on a Random Corrugated Pore Structure Concept. Prediction of Intrinsic Pore Size Distributions. 1. Model Formulation". Industrial & Engineering Chemistry Research, vol. 39, p. 3747–3763.

Balakrishnan, K.; Gonzalez, R.D. (1993) "Preparation of Pt/Alumina Catalysts by the Sol-Gel Method". Journal of Catalysis, vol. 144, 1993. En ligne : http://www.sciencedirect.com/science/article/pii/S0021951783713412

Barrande, M.; Bouchet, R.; Denoyel, R. (2007) "Tortuosity of Porous Particles". Analytical Chemistry, vol. 79, n° 23, p. 9115–9121. DOI: 10.1021/ac071377r.

Barrett, E.P.; Joyner, L.G.; Halenda, P.P. (1951) "The Determination of Pore Volume and Area Distributions in Porous Substances. I. Computations from Nitrogen Isotherms". Journal of the American Chemical Society, vol. 73, n° 1, p. 373–380. DOI: 10.1021/ja01145a126.

Becker, E.R.; Pereira, C.J. (1993) "Computer-aided design of catalysts". New York : M. Dekker (Chemical industries, 51).

Beeckman, J.W. (1990) "Mathematical description of heterogeneous materials". Chemical Engineering Science, vol. 45, n° 8, p. 2603–2610. En ligne : http://www.sciencedirect.com/science/article/pii/0009250990801488.

Beeckman, J.W.; Froment, G.F. (1980) "Catalyst deactivation by site coverage and pore blockage". Chemical Engineering Science, vol. 35, 1980, p. 805–815. En ligne : http://www.sciencedirect.com/science/article/pii/0009250980850640.

Bhatia, S.K. (1985) "Directional Autocorrelation and the Diffusional Tortuosity of Capillary Porous Media". Journal of Catalysis, vol. 196, p. 192–196.

Bird, R.B.; Stewart, W.E.; Lightfoot, E.N. (2007) "Transport phenomena". Rev. 2nd ed. New York : J. Wiley.

Bobin, C. (2010) "État de l'art sur les méthodes développées en porosimétrie mercure et en physisorption d'azote pour une meilleure caractérisation texturale des solides poreux ou divisés". Ph.D. thesis, Université Claude Bernard Lyon-I.

Boudreau, B.P. (1996) "The diffusive tortuosity of fine-grained unlithified sediments". Geochimica et Cosmochimica Acta, vol. 60, 1996, n° 16, p. 3139–3142.

Brenan, K.E.; Campbell, L.R. (1996) "Numerical Solution of Initial-Value Problems in Algebraic Equations". En ligne : https://books.google.fr/books?id=o_bd8PBZMkkC&pg=PA221&lpg=PA221&dq=daspk+solver+differential+algebraic+systems+Newton+iteration+and+direct+method+for+linear+system+solution&source=bl&ots=WULpmxNc7y&sig=_lI81PgP08OP0EGVbytXK1NAXEI&hl=fr&sa=X&ved=0ahUKEwj685qBrqnKAhWLPhQKHbYJAg8Q6AEIdDAJ#v=onepage&q=daspk%20solver%20differential%20algebraic%20systems%20Newton%20iteration%20and%20direct%20method%20for%20linear%20system%20solution&f=false.

Brunauer, S.; Emmet, P.H.; Teller, E. "Adsorption of gases in multimolecular layers", Journal of the American Chemical Society, vol 60(2), pages 309-319 (1938)

Brunauer, S.; Deming, L.S.; Deming, W.E.; Teller, E. (1940) "On a Theory of the van der Waals Adsorption of Gases". Journal of the American Chemical Society, vol. 62, n° 7, p. 1723–1732. DOI: 10.1021/ja01864a025.

Carniglia, S.C. (1986) "Construction of the tortuosity factor from porosimetry". Journal of Catalysis, vol. 102, n° 2, p. 401–418. DOI: 10.1016/0021-9517(86)90176-4.

Chang, P.; Wilke, C.R. (1955) "Some measurements of diffusion in liquids". Journal of Physical Chemistry, vol. 59, n° 1, p. 592–596.

Coppens, M.O.; Bhatt, J.B. (2017) "Models representing porous media". Department of Chemical Engineering, University College London, Torrington Place, consulté le 19 octobre 2017.

Direction Physique et Analyse - Groupe de travail texture et Polissage Ionique (2014) "MEB polissage ionique. Images de la macroporosité dans les alumines mésoporeuses". Solaize : IFPEN.

Dykhuizen, R.C.; Casey, W.H. (1989) "An analysis of solute diffusion in rocks". Geochimica and Cosmochimica Acta, vol. 53, n° 1, p. 2797–2805.

Emmett, P.H.; Brunauer, S. (1938) "The Use of Low Temperature van der Waals Adsorption Isotherms in Determining the Surface Area of Iron Synthetic Ammonia Catalysts". Journal of the American Chemical Society, vol. 1754, n° 428, p. 1553.

Feng, C.; Stewart, W.E. (1973) "Practical Models for Isothermal Diffusion and Flow of Gases in Porous Solids". Industrial & Engineering Chemistry Fundamentals, vol. 12, n° 2, p. 143–147. DOI: 10.1021/i160046a001.

Forman, E.M.; Trujillo, M.A.; Ziegler, K.J.; Bradley, S.A.; Wang, H.; Prabhakar, S.; Vasenkov, S. (2016) "Self-diffusion of heptane inside aggregates of porous alumina particles by pulsed field gradient NMR". Microporous and Mesoporous Materials, vol. 229, p. 117–123. DOI: 10.1016/j.micromeso.2016.04.027.

Friedman, S.P.; Seaton, N.A. (1995) "A corrected tortuosity factor for the network calculation of diffusion coefficients". Chemical Engineering Science, vol. 50, 1995.

Gao, X.; Diniz da Costa, J.C.; Bhatia, S.K. (2014) "Understanding the diffusional tortuosity of porous materials. An effective medium theory perspective". Chemical Engineering Science, vol. 110, p. 55–71. DOI: 10.1016/j.ces.2013.09.050.

Gaulier, F. (2014) "Rapport mi-thèse: Étude de la diffusion des charges lourdes en conditions réelles dans les catalyseurs d'hydrotraitement". Solaize.

Halsey, G. (1948) "Physical Adsorption on Non-Uniform Surfaces". The Journal of Chemical Physics, vol. 16, n° 10, p. 931–937. DOI: 10.1063/1.1746689.

Hammond, K.D.; Conner, W.C.Jr. (2013) "Analysis of Catalyst Surface Structure by Physical Sorption". Advances in Catalysis. vol. 56, p. 1-102.

Haq, N.; Ruthven, D.M. (1986) "A Chromatographic Study of Sorption and Diffusion in 5A Zeolite". Journal of Colloid and Interface Science, vol. 112, n° 1, p. 164–169. DOI: 10.1016/0021-9797(86)90078-0.

Haynes, H.W.; Sarma, P.N. (1973) "A Model for the Application of Gas Chromatography to Measurements of Diffusion in Bidisperse Structured Catalysts". Journal of the American Institute of Chemical Engineering, vol. 19, n° 5.

Iversen, N.; Jorgensen, B.B. (1993) "Diffusion coefficients of sulfate and methane in marine sediments: Influence of porosity". Geochimica et Cosmochimica Acta, vol. 57, n° 5, p. 571–578. DOI: 10.1016/0016-7037(93)90368-7.

Jarzbeski, A.B.; Lorenc, J. (1995) "Pore network connectivity and effective diffusivity of silica aerogels". Chemical Engineering Science, vol. 50, n° 2, p. 357–360.

Johnson, A.; Roy, I.M.; Matthews, G.P.; Patel, D. (2003) "An improved simulation of void structure, water retention and hydraulic conductivity in soil with the Pore-Cor three-dimensional network". European Journal of Soil Science, vol. 54, p. 477–489.

Johnson, M.F.L.; Stewart, W.E. (1965) "Pore Structure and Gaseous Diffusion in Solid Catalysts". Journal of Catalysis, vol. 4, 1965, p. 248–252.

Keil, F.J. (1999) "Diffusion and reaction in porous networks". Catalysis Today, vol. 53, n° 2, p. 245–258. DOI: 10.1016/S0920-5861(99)00119-4.

Kirkpatrick, S. (1973) "Percolation and Conduction". Review of Modern Physics, vol. 45, p. 574.

Klobes, P.; Meyer, K.; Munro, R.G. (2006) "Porosity and Specific Surface Area Measurements for Solid Materials". Washington.

Köhler, K. (2006) "Modern Methods in Heterogeneous Catalysis Research". Berlin.

Kolitcheff, S. (2015) "Rapport mi thèse. Approche multi technique des phénomènes de diffusion en hydrotraitement de distillat". Solaize.

Kolitcheff, S. (2017) "Approche multitechnique des phénomènes de diffusion en hydrotraitement de distillats". Ph.D. Thesis, Université Claude Bernard - Lyon 1, École Doctorale de Chimie de Lyon, Lyon.

Kolitcheff, S.; Jolimaitre, E.; Hugon, A.; Verstraete, J.; Carrette, P.-L.; Tayakout-Fayolle, M. (2017) "Tortuosity of mesoporous alumina catalyst supports. Influence of the pore network organization". Microporous and Mesoporous Materials, vol. 248, p. 91–98. DOI: 10.1016/j.micromeso.2017.04.010.

Kortunov, P.; Vasenkov, S.; Kärger, J.; Fé Elía, M.; Perez, M.; Stöcker, M. (2005) "Pulsed-field gradient nuclear magnetic resonance study of transport properties of fluid catalytic cracking catalysts". Magnetic resonance imaging, vol. 23, n° 2, p. 233–237. DOI: 10.1016/j.mri.2004.11.016.

Krishna, R.; Wesseling, J.A. (1997) "Maxwell-Stefan approach to mass transfer". Chemical Engineering Science, vol. 52, n° 6, p. 861–911.

Kuchta, B. (2010) "Adsorption: Modelling of physisorption in porous materials". Laboratoire Madirel, Université Aix-Marseille. En ligne : https://www.google.fr/search?ie=UTF-8&oe=utf-8&q=kuchta&safe=strict&gws_rd=cr,ssl&ei=RoeTVqmQGoqNap2ej_AB#safe=strict&q=kuchta+Adsorption:+Modelling+of+physisorption+in+porous+materials, consulté le 11 décembre 2015.

Laudone, G.M.; Matthews, G.P.; Gane, P.a.C. (2008) "Modelling diffusion from simulated porous structures". Chemical Engineering Science, vol. 63, n° 7, p. 1987–1996. DOI: 10.1016/j.ces.2007.12.031.

Laudone, G.M.; Matthews, G.P.; Gane, P.A.C.; Matthews, A.G.; Ridgway, C.J.; Schoelkopf, J.; Huggett, S.A. (2007) "Estimation of structural element sizes in sand and compacted blocks of ground calcium carbonate using a void network model". Transport in Porous Media, vol. 66, p. 403–419. DOI: 10.1007/s11242-006-0031-y.

Laudone, G.M.; Matthews, G.P.; Gane, P.A.C.; Ridgway, C.J.; Schoelkopf, J. (2005) "Estimation of the effective particle sizes within a paper coating layer using a void network model". Chemical Engineering Science, vol. 60, n° 23, p. 6795–6802. DOI: 10.1016/j.ces.2005.06.002.

Leprince, P. (1998) "Raffinage du Pétrole. Procédés de transformation". Institut Français du Pétrole, p. 104–173.

Liu, H.; Seaton, N.A. (1994) "Determination of the connectivity of porous solids from nitrogen sorption measurements - III. Solids containing large mesopores". Chemical Engineering Science, vol. 49, n° 11, p. 1869–1878.

Liu, H.; Zhang, L.; Seaton, N.A. (1992) "Determination of the connectivity of porous solids from nitrogen sorption measurements - II. Generalisation". Chemical Engineering Science, vol. 47, n° 17/18, p. 4393–4404. DOI: 10.1016/0009-2509(92)85117-T.

Mantle, M.D. (2010) "Diffusion and Effective Diffusivity in Porous Media". Cambridge University.

Morin, C. (2014) "Préparation d'alumine à porosité contrôlée. Etude de l'interaction de la boehmite dans des solvants et des propriétés fonctionnelles des matériaux resultants". Ph.D. Thesis Université Pierre et Marie Curie, Paris.

Petersen, E.E. (1958) "Diffusion in a Pore of Varying Cross Section". American Institute of Chemical Engineers Journal, vol. 4, p. 343–345.

Petzold, L. (1982) "Numerical Solution of Differential-Algebraic Equations". Department of Computer Science, University of Minnesota, Minneapolis.

Poncelet, G.; Grange, P. (1983) "Preparation of Catalysts III Scientific Bases for the Preparation of Heterogeneous Catalysts". Elsevier. P. A. Jacobs, éd. En ligne : https://books.google.fr/books?id=aaMWw_9qOMoC&pg=PA306&lpg=PA306&dq=gamma+alumina+support+precipitation&source=bl&ots=WfHYMZkref&sig=iASfxPAunm-XX72KBf4Kdo--Rnc&hl=fr&sa=X&ei=ghTbVI_mIMrpasjfgOAM&ved=0CC0Q6AEwAQ#v=onepage&q=support&f=false.

Rao, S.M.; Coppens, M.-O. (2012) "Increasing robustness against deactivation of nanoporous catalysts by introducing an optimized hierarchical pore network—Application to hydrodemetalation". Chemical Engineering Science, vol. 83, p. 66–76. DOI: 10.1016/j.ces.2011.11.044.

Reyes, S.; Iglesia, E.; Jensen, K.F. (1989) "Application of percolation theory concepts to the analysis of gas-solid reactions". Solid State Ionics, 1989, p. 833–842.

Reyes, S.; Jensen, K.F. (1985) "Estimation of effective transport coefficients in porous solids based on percolation concepts". Chemical Engineering Science, vol. 40, 1985, p. 1723–1734.

Rieckmann, C.; Keil, F.J. (1997) "Multicomponent Diffusion and Reaction in Three-Dimensional Networks: General Kinetics". Industrial & Engineering Chemistry Research, vol. 36, n° 8, p. 3275–3281.

Rieckmann, C.; Keil, F.J. (1999) "Simulation and experiment of multicomponent diffusion and reaction in three-dimensional networks". Chemical Engineering Science, vol. 54, p. 3485–3493.

Rouquerol, J.; Everett, D.H.; Avnir, D.; Fairbridge, C.W.; Haynes, J.H.; Pernicone, N. (1994) "Recommendations for the characterisation of porous solids". Pure and Applied Chemistry, vol. 66, n° 8, p. 1739–1758.

Rouquerol, J.; Rouquerol, F.; Llewellyn, P.; Maurin, G.; Sing, K.S.W. (2014) "Adsorption by Powders and Porous Solids". Elsevier, Academic Press, Marseille, Montpellier. En ligne : http://www.sciencedirect.com/science/book/9780080970356.

Rouquerol, J.; Rouquerol, F.; Sing, K.S.W. (1999) "Adsorption by Powders and Porous Solids". 1st edition. San Diego.

Ruthven, D.M. (1984) "Principles of Adsorption and Adsorption Processes". Wiley-Blackwell.

Salmas, C.E.; Ladavos, A.K.; Skaribas, S.P.; Pomonis, P.J.; Androutsopoulos, G.P. (2003) "Evaluation of Microporosity, Pore Tortuosity, and Connectivity of Montmorillonite Solids Pillared with LaNiOx Binary Oxide. A Combined Application of the CPSM Model, the Plot method and a Pore Percolation - Connectivity Model". Langmuir, vol. 19, n° 9, p. 8777–8786.

Seaton, N.A. (1991) "Determination of the connectivity of porous solids from nitrogen sorption measurements—III. Solids containing large mesopores". Chemical Engineering Science, vol. 46, n° 8, p. 1895–1909. DOI: 10.1016/0009-2509(94)80071-5.

Shen, L.; Chen, Z. (2007) "Critical review of the impact of tortuosity on diffusion". Chemical Engineering Science, vol. 62, n° 14, p. 3748–3755. DOI: 10.1016/j.ces.2007.03.041.

Sing, K.S.W.; Everett, D.H.; Haul, R.; Moscou, L.; Pierotti, R.A.; Rouquerol, J.; Siemieniewska, T. (1984) "Reporting Physisorption Data For Gas Solid Systems with Special Reference to the Determination of Surface Area and Porosity". Pure and Applied Chemistry, vol. 57, n° 4, p. 603–619.

Soliman, M.; Al-Zeghayer, Y.; Ajbar, A. (2014) "A modified orthogonal collocation method for reaction diffusion problems". Brazilian Journal of Chemical Engineering, vol. 31, n° 4, p. 967–975. DOI: 10.1590/0104-6632.20140314s00002692.

Spearing, M.C.; Matthews, G.P. (1991) "Modelling Characteristic Properties of Sandstones". Transport in Porous Media, vol. 6, n° 1991, p. 71–90.

Stauffer, D.; Aharony, A. (1985) "Introduction to Percolation Theory". Revised 2nd Edition. London: Taylor and Francis, London. En ligne : http://books.google.fr/books?hl=fr&lr=&id=v66plleij5QC&oi=fnd&pg=PP1&dq=Stauffer+Introduction+to+percolation+theory+1985&ots=22LMa9tbac&sig=ceiqFEPDSG7PqyTPRmA8akzP7c4#v=onepage&q=Stauffer Introduction to percolation theory 1985&f=false.

Surjanhata, H. (1993) "An orthogonal collocation sollutions of partial differential equations". Institute of Technology. Faculty of New Jersey, New Jersey. En ligne : http://www.google.fr/url?sa=t&rct=j&q=&esrc=s&source=web&cd=2&cad=rja&uact=8&ved=0ahUKEwjk7bWTqavKAhVCUhoKHfHWAIkQFggnMAE&url=http%3A%2F%2Farchives.njit.edu%2Fvol01%2Fetd%2F1990s%2F1993%2Fnjit-etd1993-022%2Fnjit-etd1993-022.pdf&usg=AFQjCNECyREM8cY3nr39xd7a8gRG0PBorQ, consulté le 15th January.

Tomadakis, M.M.; Sotirchos, S.V. (1993) "Transport properties of random arrays of freely overlapping cylinders with various orientation distributions". The Journal of Chemical Physics, vol. 98, n° 1, p. 616–626. DOI: 10.1063/1.464604.

Toulhoat, H.; Hudebine, D.; Raybaud, P.; Guillaume, D.; Kressmann, S. (2005) "THERMIDOR: A new model for combined simulation of operations and optimization of

catalysts in residues hydroprocessing units". Catalysis Today, vol. 109, n° 1-4, p. 135–153. DOI: 10.1016/j.cattod.2005.08.023.

Uzio, D. (1997) "Note technique: Détermination de la connectivité d'un réseau poreux à partir des isothermes d'adsorption d'azote - Application à l'étude de catalyseurs industriels". Solaize.

Uzio, D.; Euzen, P. (2000) "Note technique: Caractérisation de supports de catalyseur par adsorption d'azote. Influence des opérations unitaires de préparation sur les propriétés texturales". Solaize.

Van Eekelen, H.A.M. (1973) "The random-spheres model for porous materials". Journal of Catalysis, vol. 29, n° 1, p. 75–82. DOI: 10.1016/0021-9517(73)90204-2.

Villadsen J.; Michelsen M.L. (1978) "Solution of Differential Equation Models by Polynomial Approximation" Prentice-Hall, Englewood Cliffs, NJ.

Villadsen J.; Stewart, W.E. (1967) "Solution of boundary-value problems by orthogonal collocation". Chemical Engineering Science, vol. 22, November 1967. En ligne : http://www.sciencedirect.com/science/article/pii/0009250967800745, consulté le 15th January.

Wakao, N.; Smith, J.M. (1962) "Diffusion in catalyst pellets". Chemical Engineering Science, vol. 17, p. 825–834. DOI: 10.1016/0009-2509(62)87015-8.

Weiland, E. (2015) "Caractérisation des propriétés texturales et de transport de supports de catalyseurs. Apport de la RMN du 129Xe".

Weissberg, H.L. (1963) "Effective Diffusion Coefficient in Porous Media". Journal of Applied Physics, vol. 34, 1963.

Weisz, P.B.; Schwartz, A.B. (1962) "Diffusivity of Porous-Oxide-Gel-Derived Catalyst Particles". Journal of Catalysis, vol. 406, p. 399–406. DOI: 10.1016/0021-9517(62)90090-8.

Ye, G.; Sun, Y.; Zhou, X.; Zhu, K.; Zhou, J.; Coppens, M.-O. (2017) "Method for generating pore networks in porous particles of arbitrary shape, and its application to catalytic hydrogenation of benzene". Chemical Engineering Journal, vol. 329, n° 1, p. 56-65.

APPENDICES

APPENDIX I

In what follows, we assume a spherical shape for the particle. Let us first consider the case where c_i is defined as the molar concentration within the pores at the macroscopic scale. The flux continuity in the fluid phase with respect to the film theory at the interface is as follows:

$$k_{if} \cdot \left(c_{i\ bulk} - c_i|_{r=R_{particle}}\right) = \frac{D_{im}}{\tau}\frac{\partial c_i}{\partial r}\bigg|_{r=R_{particle}} \tag{1}$$

The *i* component balance within the pores of the catalyst particles is:

$$\begin{aligned} 4\pi r^2 dr \cdot \varepsilon \cdot \frac{\partial c_i}{\partial t} &= +\frac{D_{im}}{\tau}\frac{\partial c_i}{\partial r}\bigg|_{r+dr} \cdot 4\pi(r+dr)^2 \cdot \varepsilon - \frac{D_{im}}{\tau}\frac{\partial c_i}{\partial r}\bigg|_{r} \cdot 4\pi r^2 \cdot \varepsilon \\ \varepsilon \cdot \frac{\partial c_i}{\partial t} &= \frac{D_{im}}{\tau \cdot r^2} \cdot \varepsilon \cdot \frac{\partial r^2 \cdot \frac{\partial c_i}{\partial r}}{\partial r} \end{aligned} \tag{2}$$

If the effective diffusion coefficient is defined as in equation (3), then the particle porosity cancels in the material balance as well as in the boundary condition:

$$D_{ieff} = \frac{D_{im}}{\tau} \tag{3}$$

However, if the effective diffusion coefficient is defined taking the catalyst porosity then the mass balance becomes:

$$\varepsilon \cdot \frac{\partial c_i}{\partial t} = \frac{D_{ieff}}{r^2} \cdot \frac{\partial r^2 \cdot \frac{\partial c_i}{\partial r}}{\partial r} \tag{4}$$

If now $c_{ic} = \varepsilon \cdot c_i$ is defined as the molar concentration within the catalyst particle at the macroscopic scale, the boundary condition (1) is modified as follows since the continuity of the fluid phase concentration has to be satisfied:

$$k_{if} \cdot \left(c_{i\ bulk} - \frac{c_{ic}|_{r=R_{particle}}}{\varepsilon}\right) \cdot \varepsilon = \frac{D_{im}}{\tau}\frac{\partial c_{ic}}{\partial r}\bigg|_{r=R_{particle}} \tag{5}$$

The material balance within the particles is now:

$$\begin{aligned} 4\pi r^2 dr \cdot \frac{\partial c_{ic}}{\partial t} &= +\frac{D_{im}}{\tau \cdot \varepsilon}\frac{\partial c_{ic}}{\partial r}\bigg|_{r+dr} \cdot 4\pi(r+dr)^2 \cdot \varepsilon - \frac{D_{im}}{\tau \cdot \varepsilon}\frac{\partial c_{ic}}{\partial r}\bigg|_{r} \cdot 4\pi r^2 \cdot \varepsilon \\ \frac{\partial c_{ic}}{\partial t} &= \frac{D_{im}}{\tau \cdot r^2} \cdot \frac{\partial r^2 \cdot \frac{\partial c_{ic}}{\partial r}}{\partial r} \end{aligned} \tag{6}$$

The particle porosity cancels in the material balance but remains in the boundary condition. However, the definition (3) of the effective diffusion coefficient can be used for this situation.

APPENDIX II

The discretization over time and space of the pore network is performed by using respectively, DASPK created by Petzold, L.R.; Brown, P. N.; Hindmarsh, A. C. and Ulrich C. W. and an orthogonal collocation method developed by Villadsen, J. and Michelsen, M., which is briefly described below.

The discretization over time uses the package DASPK. This is used to calculate large-scale systems with initial conditions, in the presence of differential algebraic equations (DAEs), as mentioned before. Indeed, this code solves non-linear or linear systems of DAEs using a combination of variable-order, variable-step size backward differentiation formula (BDF) for time stepping.

In summary, on each step taken by DASPK, a sequence of nonlinear algebraic systems arises. These are solved by one of two types of methods (Petzold, 1982):

- a Newton iteration with a direct method (dense or band matrix solvers) for the linear systems involved;
- a Newton iteration with a preconditioned Krylov iterative method for the linear systems involved.

We have opted for the direct method using band matrix solvers, since we consider we are in a small-scale project. Also, the direct method chosen will use an internal difference quotient Jacobian matrix.

DASPK solves the initial value problem for the DAE system $F(t, y, y') = 0$ with respect to a set of initial conditions $y(t_0) = y_0$ and $y'(t_0) = y'_0$. To solve $F(t, y, \alpha y + \beta) = 0$, DASPK follows, as mentioned before, the discretization by the BDF method. For each time step, where $\alpha = \alpha_0/h_n$, which changes whenever the steps or order change and β is a vector which depends on the solution at past times and finally, t, y, α and β are evaluated at time t_n, using therefore a modified version of Newton's method (Brenan and Campbell, 1996; Petzold, 1982):

$$y_n^{m+1} = y_n^m - c\left(\alpha\frac{\partial F}{\partial y'} + \frac{\partial F}{\partial y}\right)^{-1} \times F(t_n, y_k^m, \alpha y_k^m + \beta) \qquad (7)$$

In fact, the direct method computes and factorizes matrix A (defined in parentheses in the equation above – termed the iteration matrix) and then uses it, for as many time steps as possible. The iterative method (Krylov) would have used an approximation of A (a preconditioned matrix P).

Using the direct method implies that DASPK will determine the Jacobian of the system. It also implies that the Jacobian matrix will be considered as a full matrix.

In our case study and as expected, we will not be in the presence of a full Jacobian matrix. Therefore, we must determine the size of our matrix. For each pore we have $(NC-1)(Ncolloc-1)$ elements, to which we must multiply the maximum value found between the difference of the pores' labels connected to a given node in order to have our matrix size.

Concerning the spatial discretization, an orthogonal collocation method is applied, which is able to solve differential equations by polynomial approximations. It is called orthogonal collocation due to the fact that the collocation points are the zeros of orthogonal polynomials. It should be clear that this method is a system of distributed parameters, the collocation points that are located along the pore length correspond to the roots of a polynomial.

The domain is broken up into a fixed number of (relatively) large subdomains or elements, and high-order basis functions are used to construct a trial solution within each element. The polynomial functions passing through the collocation points are Jacobi polynomials, or more specifically shifted polynomials as they are ranged between [0,1] instead of [-1,1]. These polynomials can be easily constructed and increased to any desired degree $Ncolloc$. The Jacobi polynomials $P_n^{\alpha,\beta}$ of degree n are defined such, that they satisfy the orthogonality conditions (Villadsen and Stewart, 1967; Soliman *et al.*, 2014), which are:

$$\int_0^1 w(x) \times P_n^{\alpha,\beta}(x) \times P_m^{\alpha,\beta}(x)dx = 0 \tag{8}$$

With $n \neq m$ and,

$$\int_0^1 w(x) \times P_n^{\alpha,\beta}(x) \times P_m^{\alpha,\beta}(x)dx \ = C_n > 0 \tag{9}$$

With $n = m$ and where $w(x)$ is the weighting function of the orthogonality conditions and C_n is a constant. For Jacobi polynomials,

$$w(x) = (1-x)^{\alpha}x^{\beta};\ \alpha,\beta > -1 \tag{10}$$

Thus, α and β are the indices of the weight function $w(x)$. The Jacobi polynomials must satisfy some requirements, for more information we refer the reader to Soliman *et al.* (2014).

In the orthogonal collocation method, we represent the solution as a polynomial with unknown coefficients to be determined such that the differential equation is satisfied at certain points. The best way to write a polynomial approximation of a function in terms of its values (ordinates) at certain points is through the Lagrange interpolation formula that

allows to obtain the solution at the collocation points (Surjanhata, 1993). Secondly, we can easily derive formulae for the derivatives using the Lagrange interpolation formula. And finally, the same Lagrange formula can then be used to obtain the concentration values at any point $z \in [0,1]$. The Lagrange interpolation formula is given as follows (Villadsen and Michelsen, 1978):

$$c_i(z) = c_i(z_k) = \sum_{k=1}^{Ncolloc+1} l_k(z) \times c_i(z_k) \tag{11}$$

With the Lagrange polynomials,

$$\mathrm{l_k(z)} = \prod_{\mathrm{j=1,j\neq k}}^{\mathrm{Ncolloc+1}} \frac{\mathrm{z - z_j}}{\mathrm{z_k - z_j}} \tag{12}$$

With the help of equation (11), the first and second derivatives of any function $c(z)$ expressed in terms of Lagrange polynomials and at a collocation point $z = z_k$ can be easily obtain (Soliman *et al.*, 2014):

$$\left.\frac{\partial c_i}{\partial z}\right|_{z=z_k} = \sum_{k=1}^{Ncolloc+1} A_{k,j} \times c_{i_j} \tag{13}$$

$$\left.\frac{\partial^2 c_i}{\partial z^2}\right|_{z=z_k} = \sum_{k=1}^{Ncolloc+1} B_{k,j} \times c_{i_j} \tag{14}$$

With k and j, the collocation points and where,

$$A_{k,j} = l_j^{(1)}(z_k) \tag{15}$$

$$B_{k,j} = l_j^{(1)}(z_k) \tag{16}$$

Villadsen and Michelsen (1978) propose a good method to calculate these two vectors, $A_{k,j}$ and $B_{k,j}$.

Also, equations (13) and (14) must be in accordance with,

$$\int_{z=0}^{z=1/L_{ref}} c_i(z)dz = \sum_{j=1}^{Ncolloc} w_j \times c_{i_j} \tag{17}$$

with w the weighting matrix of integration.

APPENDIX III

In order to numerically validate the FORTRAN® code used in the mass transfer simulation, we intend in this section to present some pore networks with low complexity that may be helpful to validate the code by comparing concentration profiles.

At first, the concentration profiles obtained for simple networks of pores in series with an overall pore length L_p will be compared to the concentration profiles of a single pore with length L_p. We expect to obtain identical concentration profiles. Secondly, non-linear networks such as, triangles and stars will be put at test.

For all simulations, through the pore network will diffuse a binary mixture composed by species *A* and *B*. At time $t \leq t_0$, the network is immerged under a solution composed by species *B* and for time $t > t_0$, species *A* will start diffusing through the pore network from the external surface of the network and at concentration $c_o = 1\, mol \cdot m^{-3}$.

III.1 SIMULATION OF LINEAR SIMPLE NETWORKS USING THE FICK'S MODEL

The code validation can be outlined as follows:

1) Simulation of 1 single pore of radius and length, R_p and L_p(basis of comparison);
2) Simulation of 2 pores in series, sized R_p and $L_1 = L_2 = L_p/2$;
3) Simulation of 2 pores in series, sized R_p and $L_1 = L_p/3$ and $L_2 = 2L_p/3$;
4) Simulation of 3 pores in series, sized R_p and $L_1 = L_2 = L_3 = L_p/3$;
5) Simulation of 3 pores in series, sized R_p and $L_1 = L_p/6$, $L_2 = 2L_p/3$ and $L_3 = L_p/6$.

The pore radius and length used are: $R_p = 1 \times 10^{-7}$ and $L_p = 1 \times 10^{-6} m$.

III.1.1 SIMULATION OF A SINGLE PORE

In order to manage the code validation, it was important in a first step, to compare concentration profiles of simple networks. We have decided, for instance, to compare pores in series (having an overall length of L_p) to a single pore sized L_p (basis of comparison). For these case scenarios, both concentration profiles should be identical.

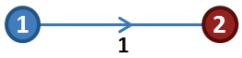


Fig. Ap. III-1. 1 single pore sized L_p with blue node at the external surface of the grain, with c_o.

Here follows the concentration profile of a single pore of size L_p (Fig. Ap. III-2):

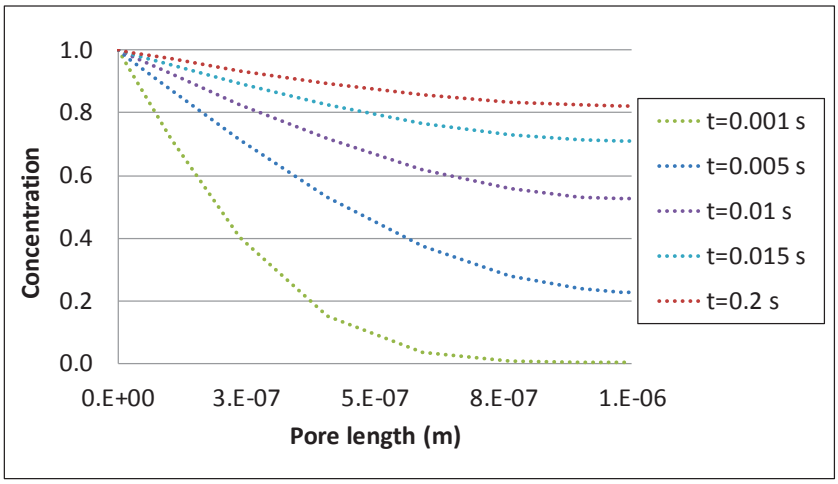


Fig. Ap. III-2. Concentration profile of a single pore sized R_p and L_p (dashed lines represent the basis of comparison).

III.1.2 SIMULATION OF 2 PORES IN SERIES WITH L1=L2=L_P /2

The graphical representation presented on Fig. Ap. III-4, gives us the comparison of the concentration profiles obtained from two different networks: 2 pores in series of size $L_p/2$ (continuous lines) and a single pore of size L (dashed lines) and at different simulation times.



Fig. Ap. III-3. 2 pores sized $L_p/2$, with node 1 open to the outer surface.

As we can see from Fig. Ap. III-4, the concentration profiles are identical, except at time $t = 0{,}001\ s$, where at the extremity of the pore a maximum relative error of 3.7×10^{-4} was found. Apart from time $t = 0{,}001\ s$, at all times and positions, the relative errors have an order of magnitude of 10^{-6} or even 10^{-7}.

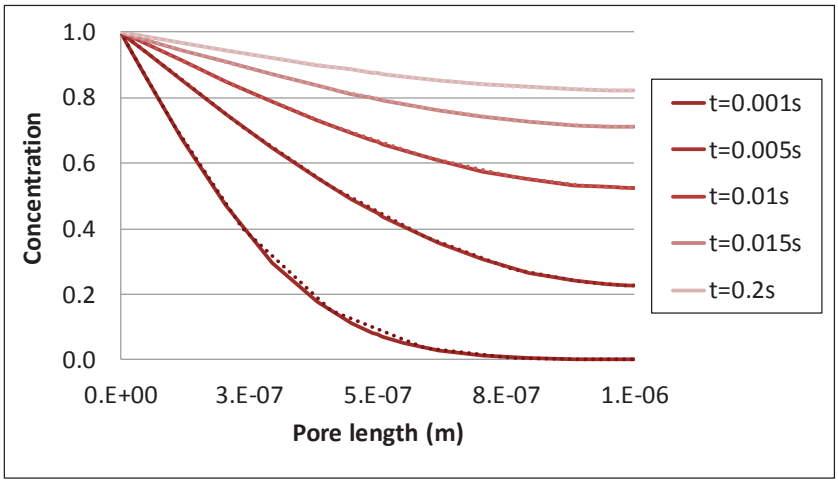


Fig. Ap. III-4. Concentration profiles at different times t obtained from one single pore L_p (dashed lines) and 2 pores in series $L_p/2$ (continuous lines).

III.1.3 SIMULATION OF 2 PORES IN SERIES WITH $L_1 = L_P/3$ AND $L_2 = 2L_P/3$

We proceed to an analogous comparison using once again two pores in series having different lengths, $L_p/3$ for the first pore and $2L_p/3$ for the second one. Node 1 is open and at concentration c_o for species *A*. Here follows an illustrative representation of the network.



Fig. Ap. III-5. 2 pores sized: $L_p/3$ and $2L_p/3$, with node 1 open.

Placing us at the end of the pore and looking for the maximum relative error, we have found once again the same order of magnitude 10^{-4}, followed by 10^{-6} and the majority of the relative errors present an order of magnitude of 10^{-7} or even 10^{-8}. The following figure represents the concentration profiles at different simulation times for the two pores in series (continuous lines) and for the single pore L_p (dashed lines).

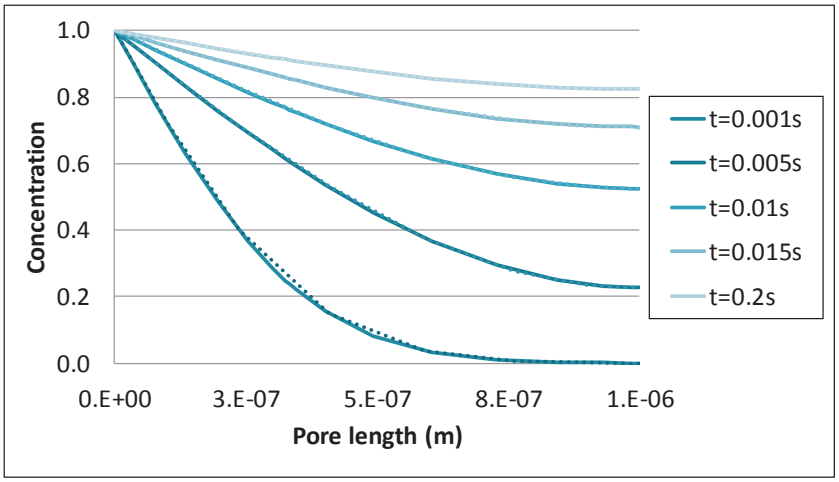


Fig. Ap. III-6. Concentration profiles at different times *t* obtained for one single pore L_p (dashed lines) and 2 pores in series of $L_p/3$and $2L_p/3$ (continuous lines).

III.1.4 SIMULATION OF 3 PORES IN SERIES $L_1 = L_2 = L_3 = L_P/3$

This time, we have simulated three pores in series sized $L_p/3$ with an overall network length of L_p, as shown illustratively below (Fig. Ap. III-7) and that we shall compare with the single pore concentration profile of size L_p.

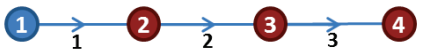


Fig. Ap. III-7. Illustrative representation of the network constituted by 3 pores sized $L_p/3$, with node 1 open.

For this comparison presented on Fig. Ap. III-8, we have calculated as well, the relative errors at the end of the network (node 4). For $t = 0.001\ s$, the order of magnitude has not changed 10^{-4}, for the following simulation times the order of magnitude of the relative errors alternates between 10^{-6} and 10^{-7}.

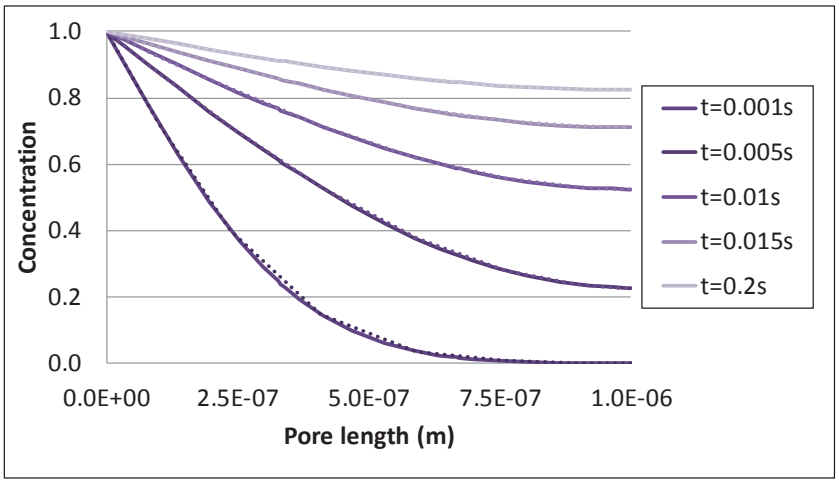


Fig. Ap. III-8. Concentration profiles at different times *t* obtained from one single pore L_p (dashed lines)and 3 pores in series of $L_p/3$ (continuous lines).

III.1.5 SIMULATION OF 3 PORES IN SERIES WITH $L_1 = L_P/6$, $L_2 = 2L_P/3$ AND $L_3 = L_P/6$

Last but not the least, we have simulated 3 pores in series with pores sized: $L_p/6$, $2L_p/3$ and finally $L_p/6$.

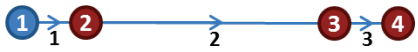


Fig. Ap. III-9. Illustrative representation of the network constituted by 3 pores sized $L_p/6$, $2L_p/3$ and $L_p/6$, with node 1 open.

The concentration profiles at different simulation times are shown in Fig. Ap. III-10, continuous lines for the 3 pores in series and dashed lines for the single pore of size L_p. The relative errors are rather low and the concentration profiles obtained simulating the 3 pores in series of different sizes match the concentration profiles obtained from the simulations using a single pore of size L_p.

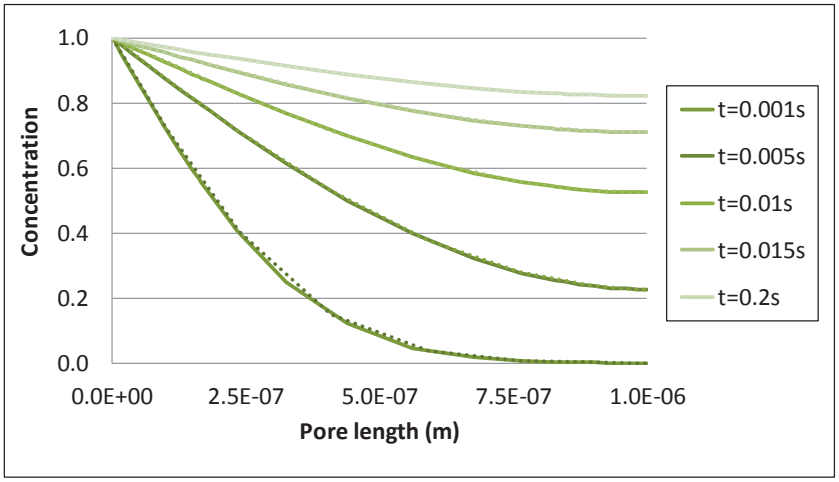


Fig. Ap. III-10. Concentration profiles at different times *t* obtained from one single pore L_p (dashed lines)and 3 pores in series of $L_p/6$, $2L_p/3$ and $L_p/6$ (continuous lines).

With the data presented above, we have shown that a good agreement is found for the comparisons performed. The code is able to numerically handle a series of pores. It should also be mentioned that different sizes of pores, length and radius, were also tested, and that we have found a good agreement as well. In the next subchapter, non-linear pore networks will be tested.

III.2 SIMULATION OF NON-LINEAR PORE NETWORKS USING THE FICK'S MODEL

After having validated the networks of pores in series presented above, we tested other kinds of network shapes, in order to understand the feasibility of the code. We present here simulations performed with pores in the form of a triangle and a star. The pore radius and length used are: $R_p = 1 \times 10^{-8}$ and $L_p = 1 \times 10^{-6} m$.

III.2.1 SIMULATION OF A TRIANGLE WITH DIFFERENT BOUNDARY CONDITIONS SCENARIOS

Fig. Ap. III-12 plots the concentration profiles at several simulation times of all three pores belonging to a triangle network (see Fig. Ap. III-11). All nodes of the triangle are placed at the external surface of the particle, they have therefore the same concentration c_o.

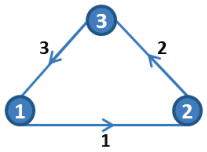


Fig. Ap. III-11. Schematic illustration of a triangle network having all nodes open. Blue nodes are open and at the external surface of the catalyst grain, with c_o.

To validate the calculations, the concentration profiles of each pore should be the same. It is exactly what is found in the graphical representation below (Fig. Ap. III-12).

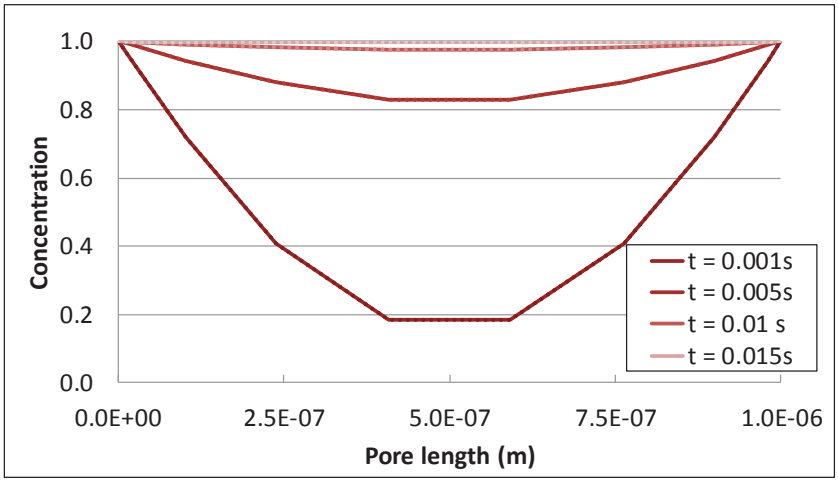


Fig. Ap. III-12. Concentration profiles of all 3 pores belonging to a triangle where all nodes are open. Dashed lines represent pores 2 and 3 and continuous lines, pore 1.

The following plots of Fig. Ap. III-14 and Fig. Ap. III-15 also refer to a triangle for which the node 3 is closed and nodes 1 and 2 open and with concentration c_o (Fig. Ap. III-13).

Therefore, the concentration profiles that we shall obtain have necessarily two pores with the exact same concentration profiles.

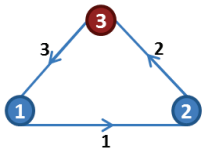


Fig. Ap. III-13. Schematic illustration of a triangle network having 1 only node closed. Blue nodes are open and at the external surface of the catalyst grain, with c_o. Red nodes are interior nodes.

Indeed, if we look to Fig. Ap. III-14 and Fig. Ap. III-15, representing the concentration profiles at times $t = 0.001$ and $t = 0.005s$ respectively, one observes two identical concentration profiles, corresponding to pores 2 and 3, as expected.

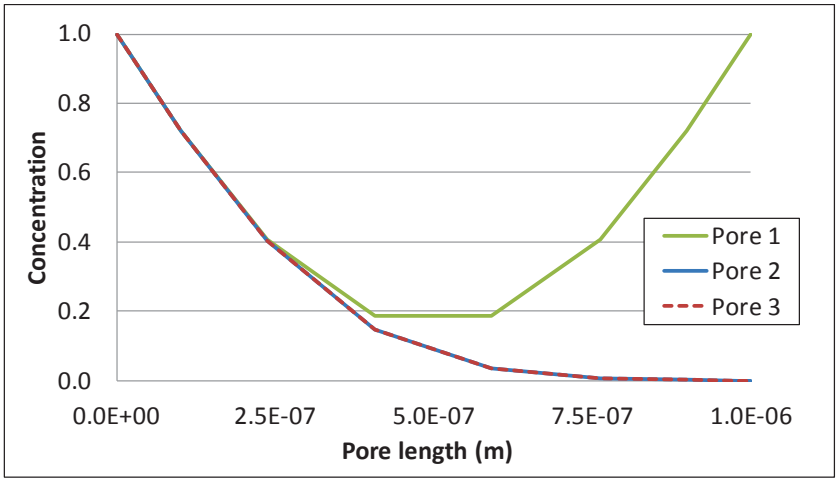


Fig. Ap. III-14. Concentration profiles extracted at time *t*=0.001s for 3 pores belonging to a triangle where one of the nodes is closed.

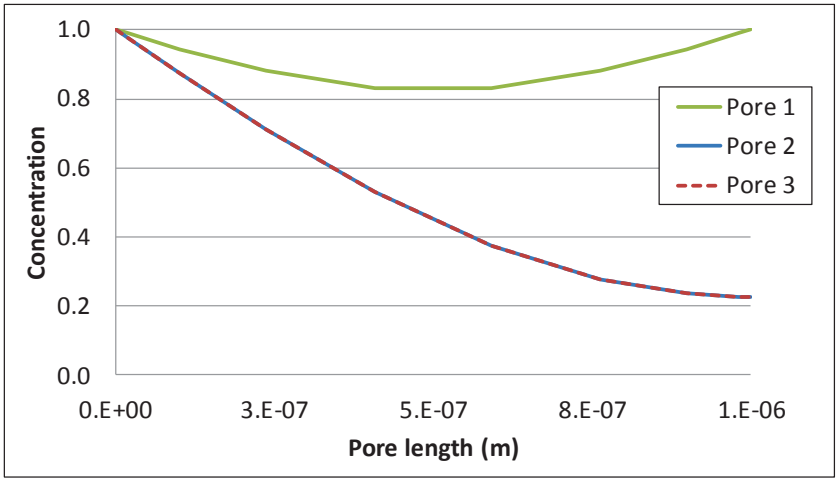


Fig. Ap. III-15. Concentration profiles extracted at time *t*=0.005s for 3 pores belonging to a triangle where one of the nodes is closed.

We have also tested instead of closing one only node of the triangle, closing two of them, as shown in the scheme below (Fig. Ap. III-16). Now, the concentration profiles of pores 1 and 3 should be equal.

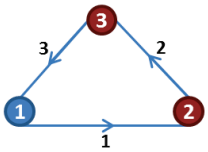


Fig. Ap. III-16. Schematic illustration of a triangle network having 2 nodes closed.

The following graphical representations, Fig. Ap. III-17 and Fig. Ap. III-18, confirm that the concentration profiles obtained at two different simulation times, $t = 0.001$ and $t = 0.005\ s$ for pores 1 and 3 completely match.

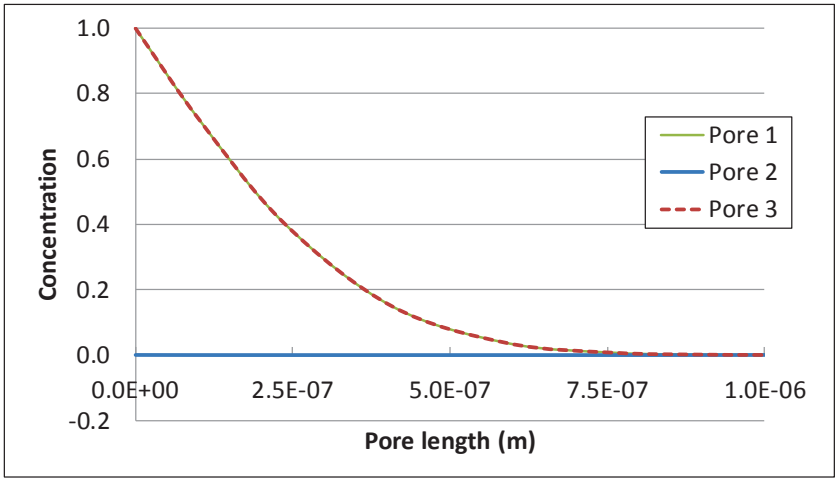


Fig. Ap. III-17. Concentration profiles at t = 0.001s for 3 pores belonging to a triangle where two of the nodes are closed.

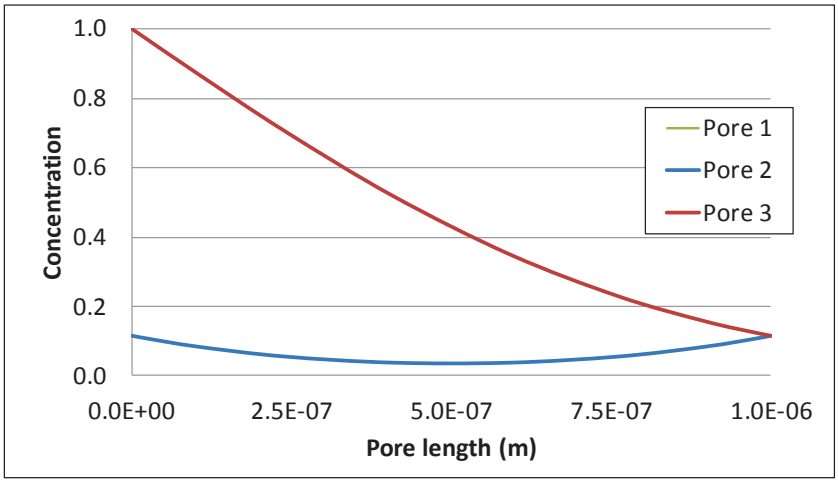


Fig. Ap. III-18. Concentration profiles at t = 0.005s for 3 pores belonging to a triangle where two of the nodes are closed.

III.2.2 SIMULATION OF A STAR TAKING DIFFERENT BOUNDARY CONDITIONS SCENARIOS

The star under consideration has three pores and contains four nodes (Fig. Ap. III-19). We have obtained for each pore their concentration profile. Assuming that only the middle pore is closed, we should obtain the exact same concentration profiles for each three pores.

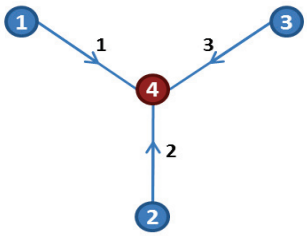


Fig. Ap. III-19. Schematic illustration of a star network, having the external nodes open. Blue nodes are open and so, at the external surface of the catalyst grain, with c_o. Red nodes are inner nodes.

Looking to Fig. Ap. III-20, we can confirm that all three pores have the same concentration profile.

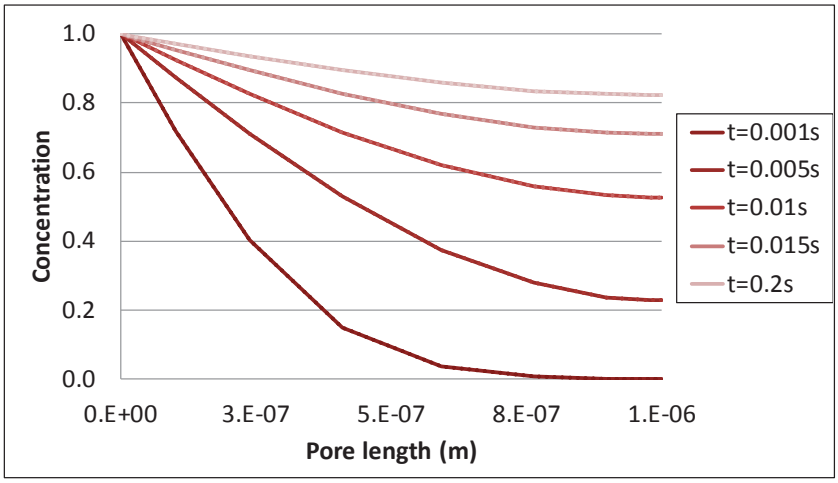


Fig. Ap. III-20. Concentration profiles referent to the pores of a star at different time simulations having the external nodes open and with c_o. Dashed lines represent pores 2 and 3 and the continuous line, pore 1.

Now, taking the middle node of the star open and with concentration c_o and all the external nodes closed as illustrated on Fig. Ap. III-21. With this case scenario, we should also find that all pores have the same concentration profiles.

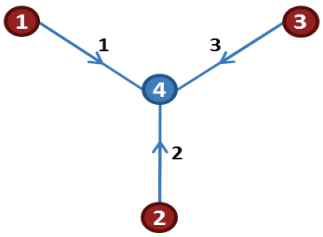


Fig. Ap. III-21. Schematic illustration of a star network, having the middle node open.

Fig. Ap. III-22 shows exactly this scenario. The concentration profiles were obtained at different simulation times, in continuous lines we have represented pore 1 and in dashed lines, pores 2 and 3. We may conclude from this data that there is a perfect match between the concentration profiles obtained for each pore, as expected.

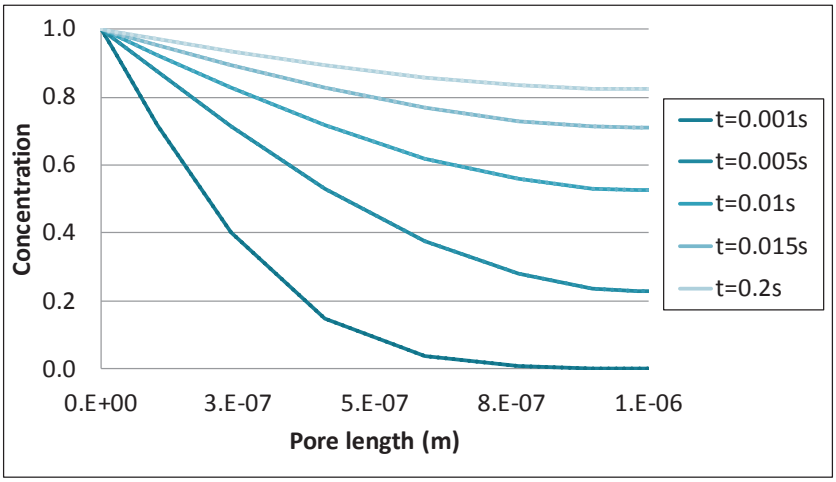


Fig. Ap. III-22. Concentration profiles referent to the pores of a star at different time simulations. External nodes are closed, and the middle node opened with c_o.

Taking another scenario, we have considered external nodes 1 and 2 to have concentration c_o and node 3 and 4 are not in contact with the external surface (inner nodes).

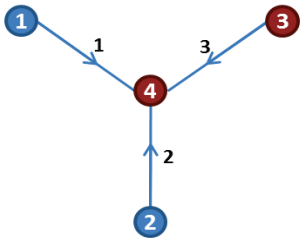


Fig. Ap. III-23. Schematic illustration of a star network, having 2 external nodes open. Blue nodes are open and at the external surface of the catalyst grain, with c_o. Red nodes have no contact with the grain surface.

The concentration profiles obtained are shown in Fig. Ap. III-24 and Fig. Ap. III-25 confirming that pores 1 and 2 have the same profiles.

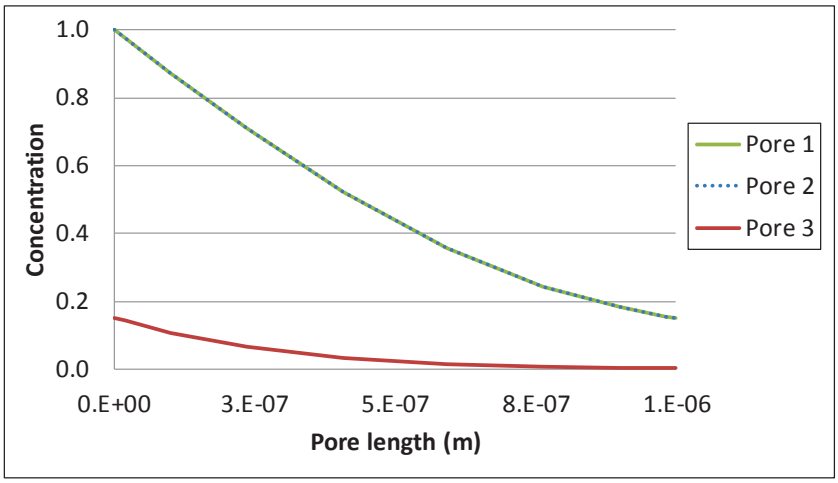


Fig. Ap. III-24. Concentration profiles referent to the pores of a star at time simulation t=0.005s. 2 external nodes are open and with c_o.

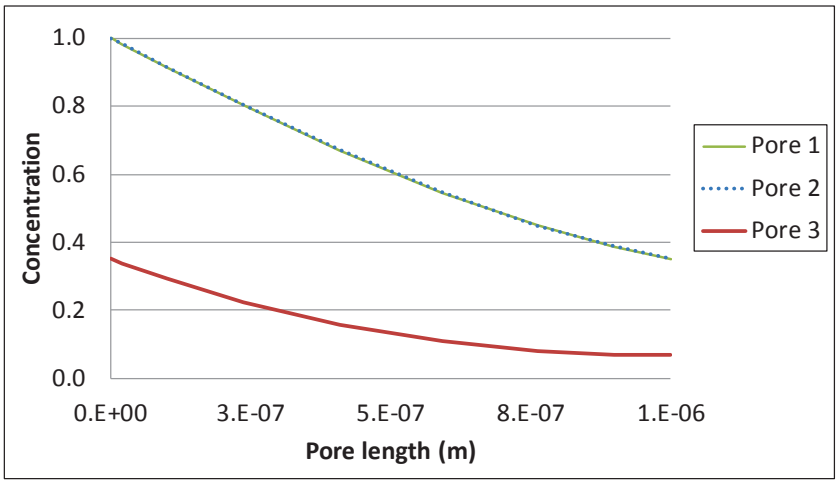


Fig. Ap. III-25. Concentration profiles referent to the pores of a star at time simulation t=0.01s. 2 external nodes are open and with c_o.

Taking now, one external node open (node 1) and therefore in contact with the external surface of the grain and with concentration c_o, we can represent the network as shown in Fig. Ap. III-26:

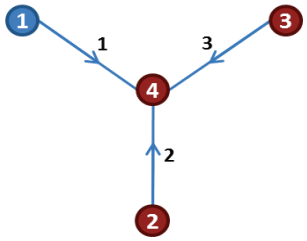


Fig. Ap. III-26. Schematic illustration of a star network, having one only external node open.

The simulations confirm that pores 2 and 3 have identical concentration profiles as can be seen on Fig. Ap. III-27 and Fig. Ap. III-28 respectively for times $t = 0.005$ and $t = 0.01s$.

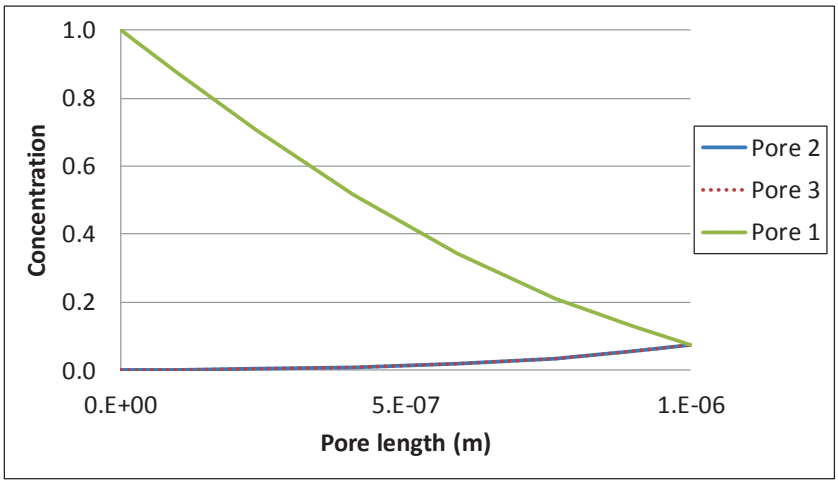


Fig. Ap. III-27. Concentration profiles referring to pores of a star at t=0.005s. 1 external node is open and with concentration c_o.

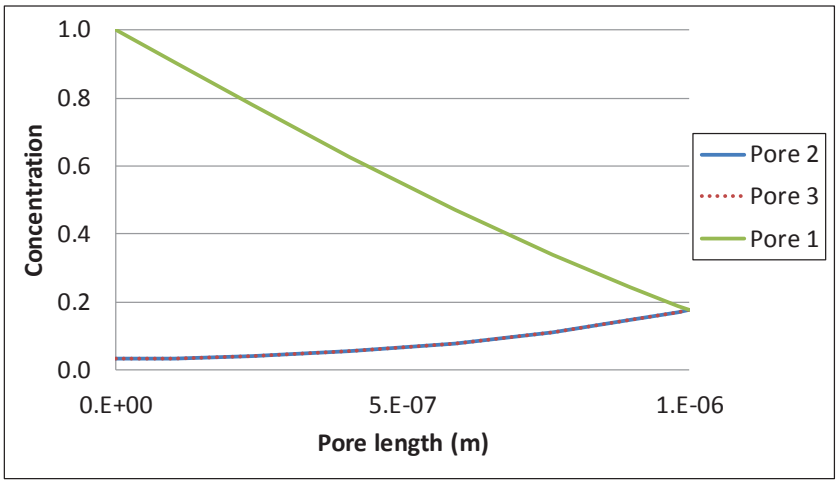


Fig. Ap. III-28. Concentration profiles referring to pores of a star at t=0.01s. 1 external node is open and with concentration c_o.

III.3 SIMULATION OF LINEAR SIMPLE NETWORKS USING THE MAXWELL-STEFAN'S MODEL

We present in this section simulations performed to validate the code using Maxwell-Stefan's law. All the simulations presented in the previous section were also performed using the Maxwell-Stefan's equation and all validations succeeded very well. However, for a matter of brevity and importance, we have decided that in this section we would only present two case scenarios. The reader also should know that the Maxwell-Stefan equation used is dedicated to isothermal, ideal and incompressible systems of a multicomponent mixture.

First, we performed a simulation for a binary mixture, where we compare the concentration profiles obtained from the Fick's and the Maxwell-Stefan equation, over one single pore.

The following graphical representations are relative to times T=0.005 and $0.015s$ (Fig. Ap. III-29 and Fig. Ap. III-30), using the given pore characteristics: R_p=1×10^{-7} and L=1×10^{-6}m. Having defined a diffusivity of D_{ij}=4×10^{-11} m^2/s, for i and j=1, 2 and 3. The simulations show a good agreement between the two laws, as expected. Given the fact that we are in the presence of a binary mixture.

Now, taking a pore network constituted by one single pore of $R_p = 1 \times 10^{-8}$ and $L = 1 \times 10^{-6}\, m$. And comparing it to two pores in series, each one of size $L/2$, we have compared the concentration profiles of these two simple networks using the Maxwell-Stefan model. We know for a fact that, the concentration profiles obtained from the two networks should match. Also, we should mention that we are still in the presence of a binary mixture. For simulation time $T = 0.01s$ we have, as expected, the profiles completely matching (see Fig. Ap. III-31).

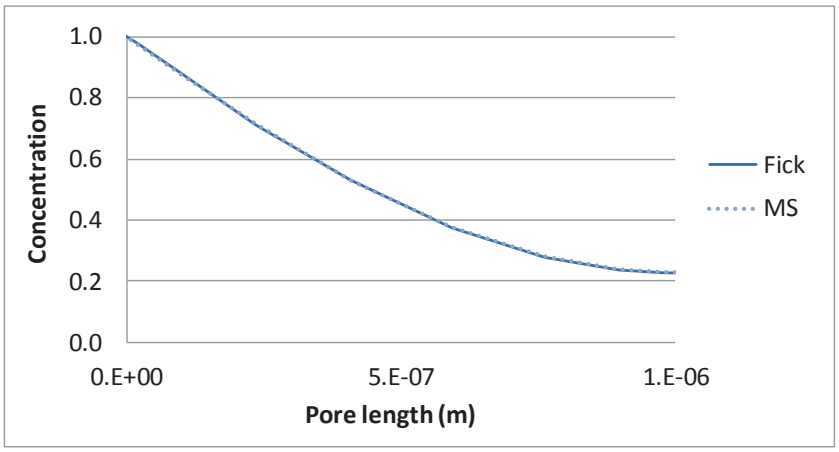


Fig. Ap. III-29. Concentration profiles comparing the use of the Maxwell-Stefan law with the Fick's law at time T=0.005s.

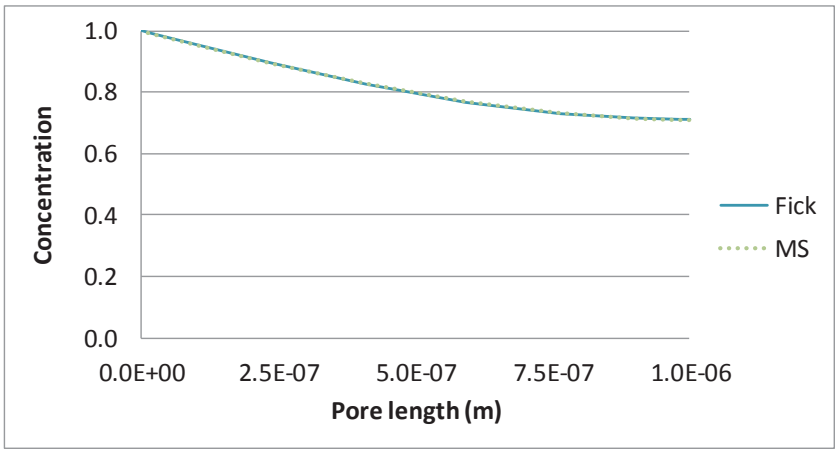


Fig. Ap. III-30. Concentration profiles comparing the use of the Maxwell-Stefan law with the Fick's law at time T=0.015s.

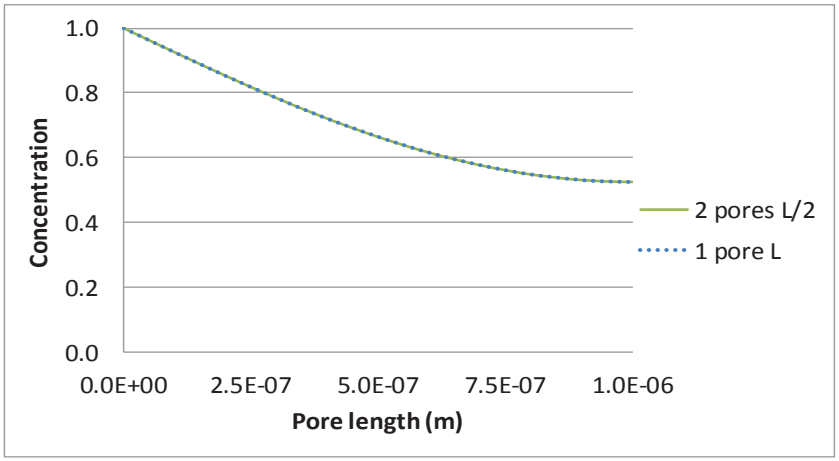


Fig. Ap. III-31. Concentration profiles obtained from a network of two pores in series, each sized L/2 and 1 single pore sized L.

III.4 OTHER CASE SCENARIOS USING THE MAXWELL-STEFAN'S MODEL

Another case scenario here proposed takes a binary mixture diffusing over the single pore, but this time we consider two mixtures with different species diffusivities. For one

of the binary mixtures we have $D_{ij} = 4 \times 10^{-11} m^2/s$ and for the other one, we have $D_{ij} = 8 \times 10^{-11} m^2/s$, for i and $j = 1, 2$ and 3. The following graphical representation contains the concentration profiles from both mixtures at two different simulation times (see Fig. Ap. III-32 and Fig. Ap. III-33).

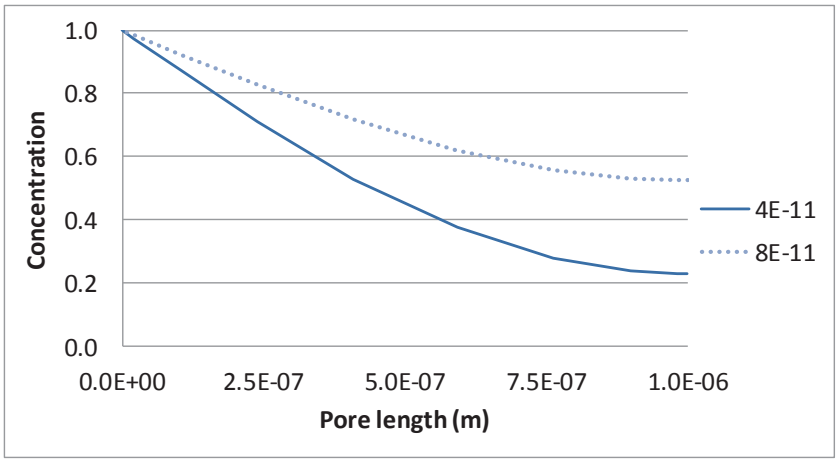


Fig. Ap. III-32. Concentration profiles comparing two different mixtures in terms of diffusivities and at time T=0.005s.

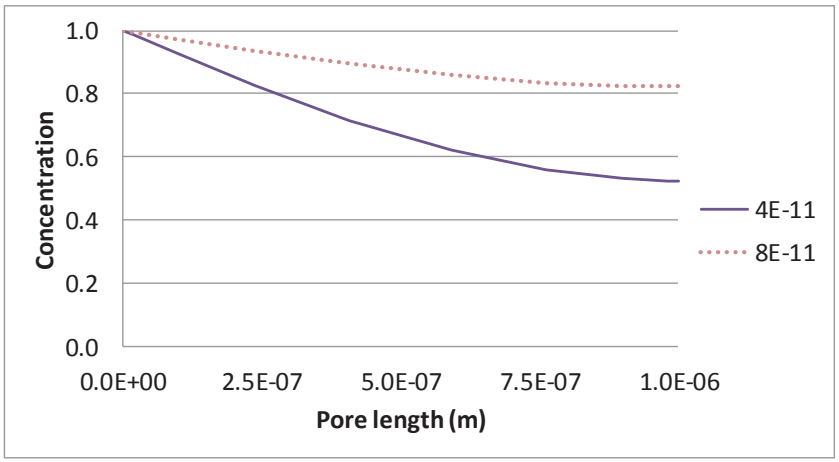


Fig. Ap. III-33. Concentration profiles comparing two different mixtures in terms of diffusivities and at time T=0.01s.

From the graphics presented above, it is clear that the mixture with lower values of diffusivities $(4 \times 10^{-11} m^2 \cdot s^{-1})$ has a delay compared to the other mixture with $D_{ij} = 8 \times 10^{-11} m^2 \cdot s^{-1}$, which is an expected result.

Last but not the least, we present here a simulation performed through a pore network defined by a star of three pores. The pores of the star network have respectively a pore radius and length of 1×10^{-8} and $1 \times 10^{-6}\, m$. The mixture diffusing is a ternary mixture and we have considered the situation where only two external nodes of the star are open (nodes 1 and 2 from Fig. Ap. III-34). One of these external nodes is only in contact with species 2 and the other, is only in contact with species 3 as shown in Fig. Ap. III-34 . At time $t < t_0$ only species 1 is present.

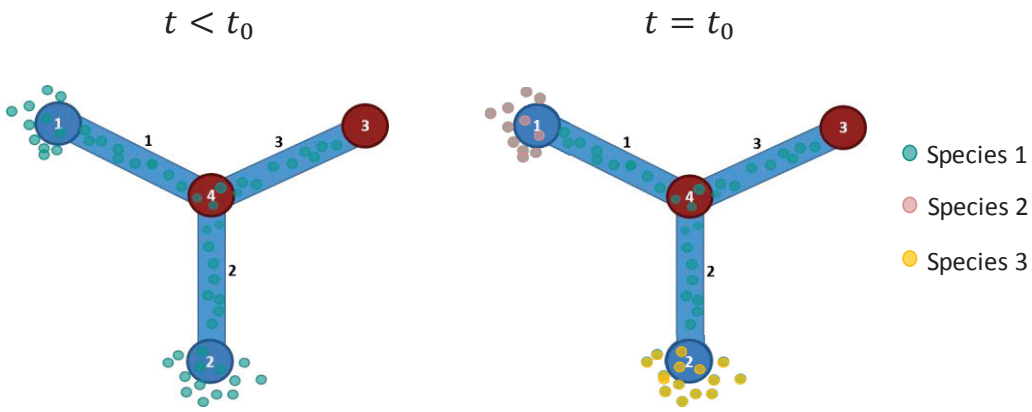


Fig. Ap. III-34. Simulation of a ternary mixture diffusing in a star network.

We have simulated this network with a mixture having all diffusivities taking the same value $D_{ij} = 4 \times 10^{-11} m^2 \cdot s^{-1}$, for i and $j = 1, 2$ and 3. The concentration profiles along pore 1 at a simulation time of $T = 0.015$ and $0.04s$ are represented graphically on the following figures:

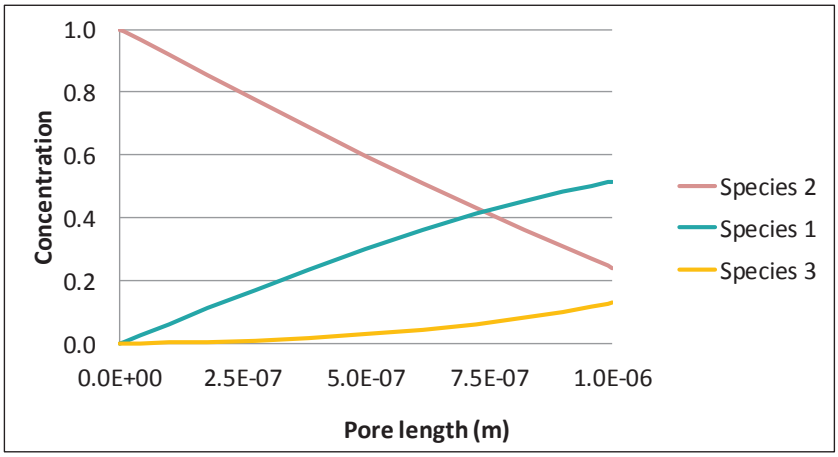


Fig. Ap. III-35. Concentration profiles of a ternary mixture over pore 1 at time T=0.015s.

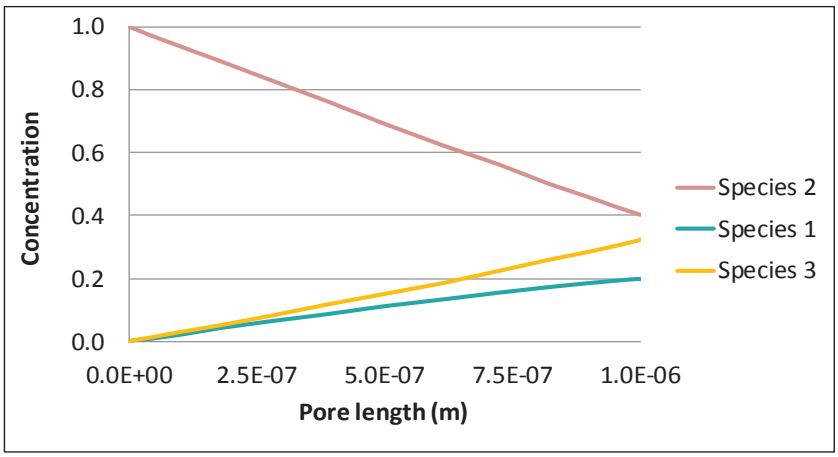


Fig. Ap. III-36. Concentration profiles over pore 1 of a ternary mixture over pore 1 at time T=0.04s.

The concentration of species 2 decreases from the entrance of the pore (node 1) until node 4, whereas for species 1 and 3 it increases, as expected. A similar behaviour is

observed in pore 2, as it can be seen on Fig. Ap. III-37 and Fig. Ap. III-38. With species 3 decreasing and species 1 and 2 increasing their concentration.

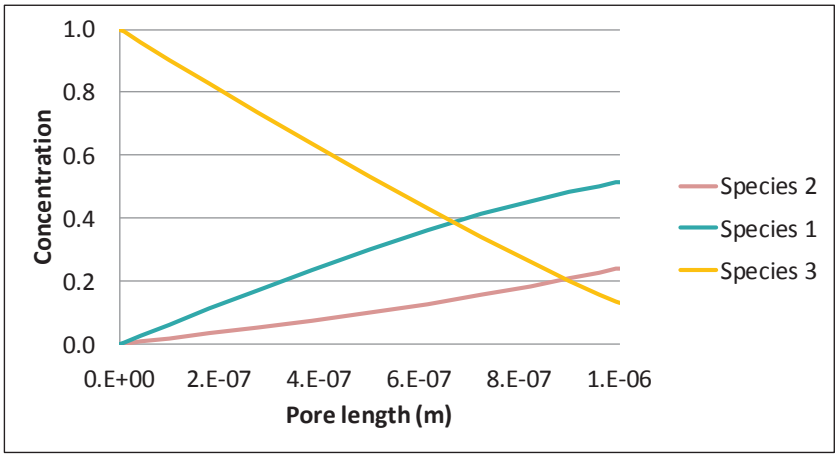


Fig. Ap. III-37. Concentration profiles of a ternary mixture over pore 2 at time t=0.015s.

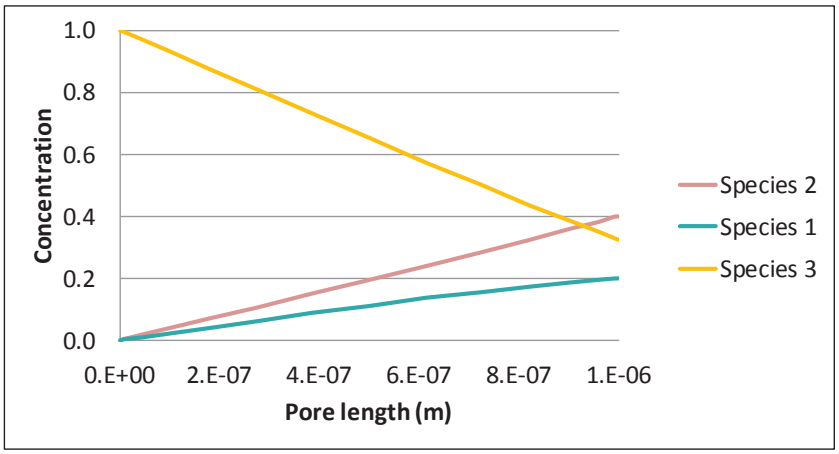


Fig. Ap. III-38. Concentration profiles of a ternary mixture over pore 2 at time t=0.04s.

Finally, the following graphics show the evolution of the concentration in pore 1: at the entrance of the pore (Fig. Ap. III-39), in the middle (Fig. Ap. III-40) and at the end of the pore (Fig. Ap. III-41):

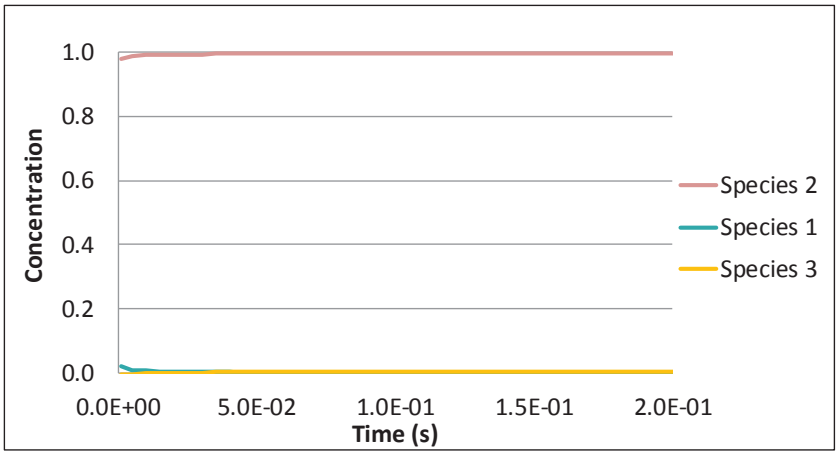


Fig. Ap. III-39. Concentration evolution at the entrance of the diffusing species in pore 1 of the star network.

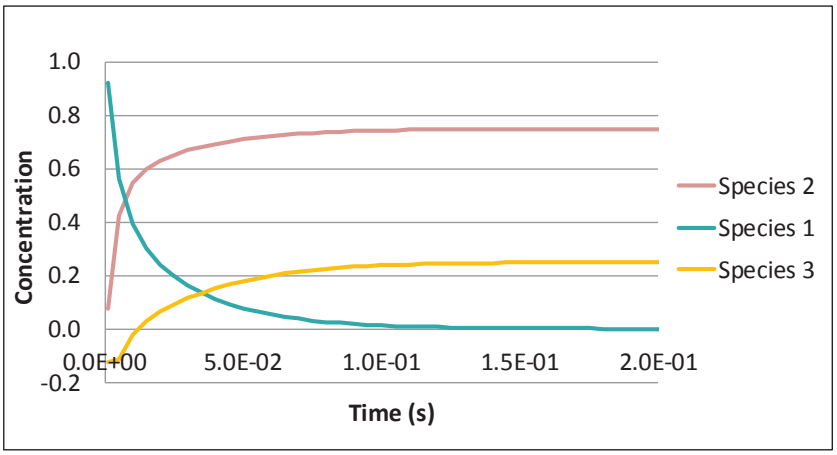


Fig. Ap. III-40. Concentration evolution in the middle of pore 1 of the star network.

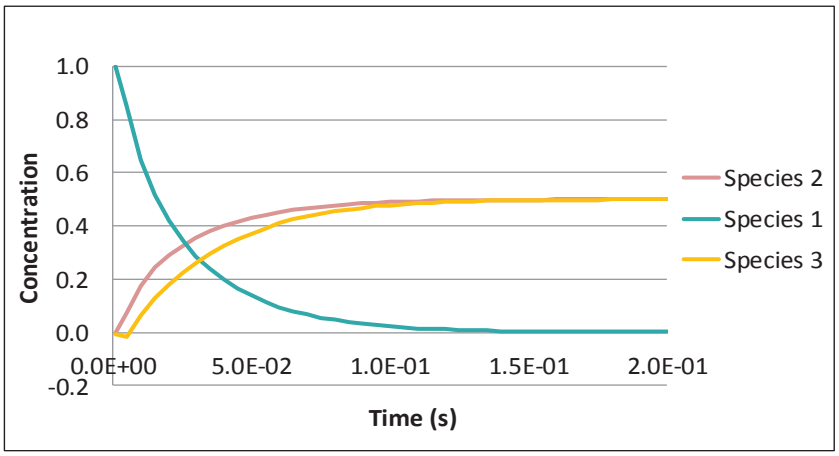


Fig. Ap. III-41. Concentration evolution in the outlet of pore 1 of the star network.

III.5 CONCLUSIONS

We developed a model where mass transfer by diffusion can be described through a pore network, using the Fick's and Maxwell-Stefan's laws and where the influence of the morphology of the network is taken into account, using a connectivity matrix. The code was validated numerically and theoretically through various cases using simple networks of: pores in series, stars and triangles.

This model is a valuable tool that helped us to define in each pore, a concentration profile at different simulation times. It also allows to make use of the node rule used in the work of Kirchhoff's and therefore to define as well the concentration at each node of the network. The mass transfer prediction proposed in the model can be of course extended to other phenomena that may be produced inside a porous structure, for instance chemical reactions or adsorption phenomena.

APPENDIX IV

Additional data related to the required minimum network size, where different network sizes are tested $N_x \times N_y \times N_z$ with $N_x=N_y$ and $N_z=1$.

The study was promoted on different kinds of networks, from 2D Z_{max}=4-6 to 3D Z_{max}=6-8.

IV.1 REQUIRED MINIMUM NETWORK SIZE FOR 2D SQUARE NETWORKS

Regarding the 2D square network (Z_{max}=4) several pore existence probabilities were studied $P = \{0.5, 0.7, 0.9\}$.

Taking P=0.5, we have:

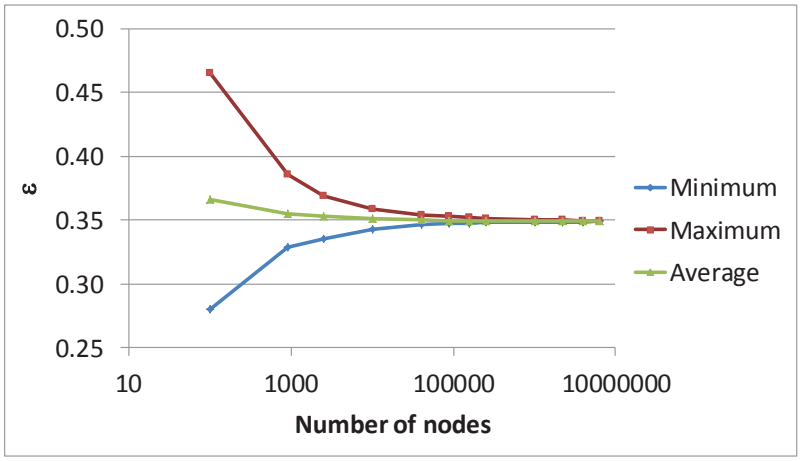


Fig. Ap. IV-1. Catalyst porosity obtained for different network sizes $N_x \times N_y \times N_z$ with $N_x=N_y$ and $N_z=1$. 2D Z_{max}=4 networks with P=0.5.

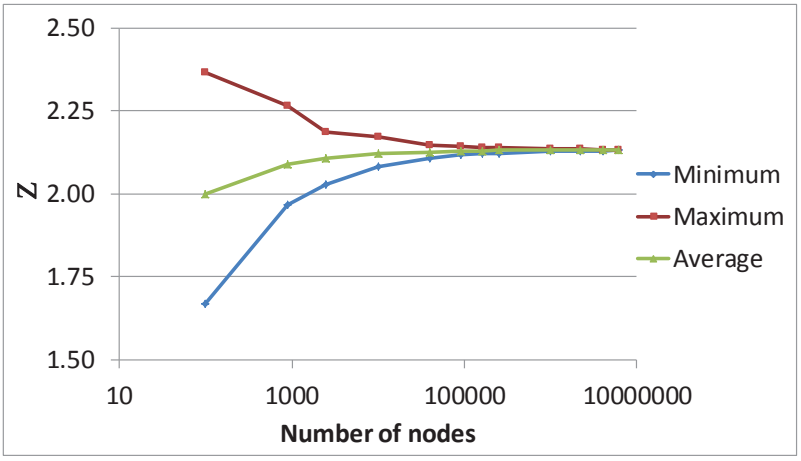


Fig. Ap. IV-2. Connectivity obtained for different network sizes $N_x \times N_y \times N_z$ with $N_x=N_y$ and $N_z=1$. 2D Z_{max}=4 networks with P=0.5.

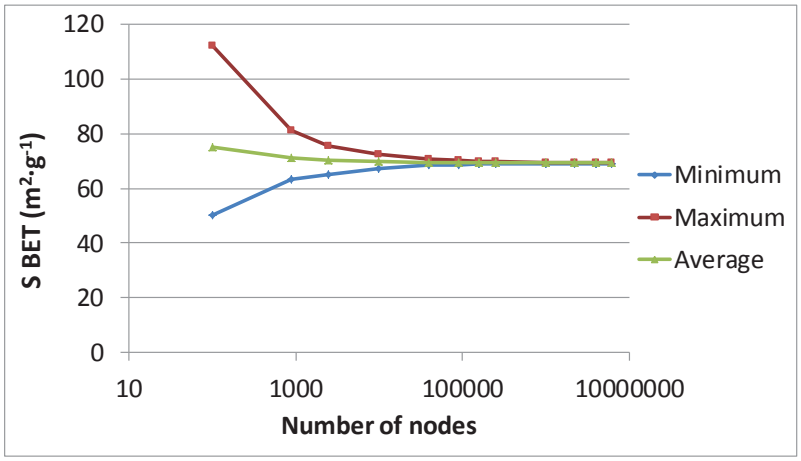


Fig. Ap. IV-3. Specific surface area obtained for different network sizes $N_x \times N_y \times N_z$ with $N_x=N_y$ and $N_z=1$. 2D $Z_{max}=4$ networks with $P=0.5$.

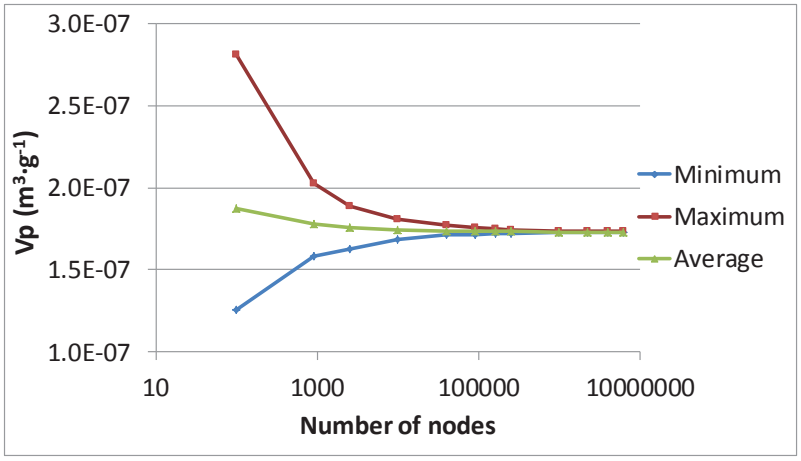


Fig. Ap. IV-4. Pore volume obtained for different network sizes $N_x \times N_y \times N_z$ with $N_x=N_y$ and $N_z=1$. 2D $Z_{max}=4$ networks with $P=0.5$.

For P=0.7, one has:

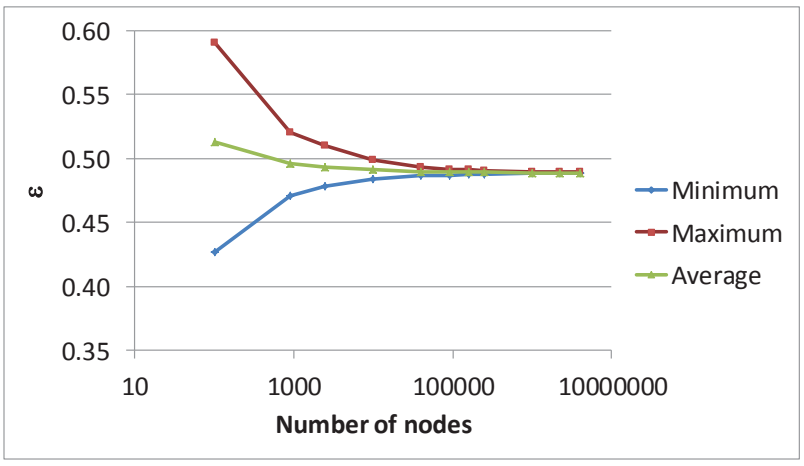


Fig. Ap. IV-5. Catalyst porosity obtained for different network sizes $N_x \times N_y \times N_z$ with $N_x=N_y$ and $N_z=1$. 2D $Z_{max}=4$ networks with $P=0.7$.

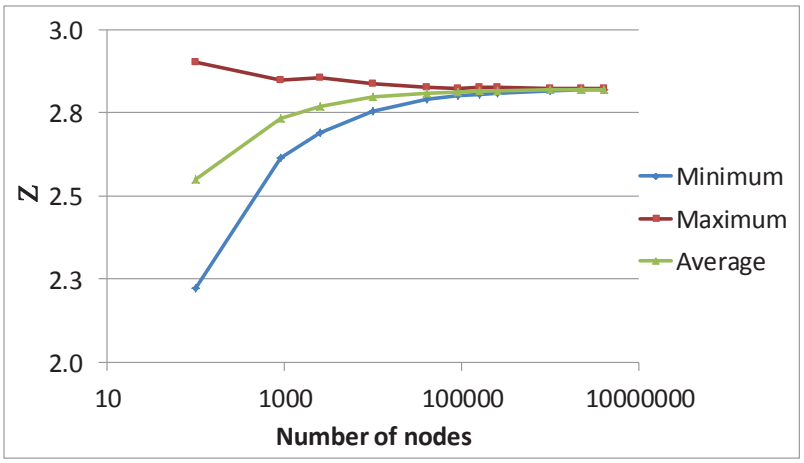


Fig. Ap. IV-6. Connectivity obtained for different network sizes $N_x \times N_y \times N_z$ with $N_x=N_y$ and $N_z=1$. 2D $Z_{max}=4$ networks with $P=0.7$.

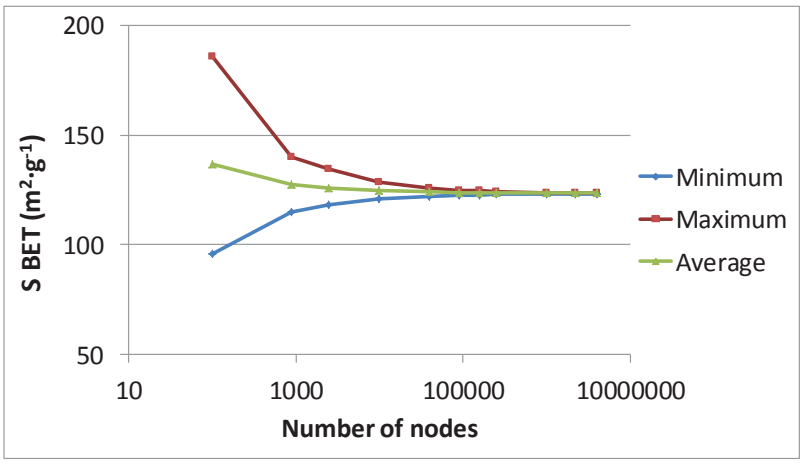


Fig. Ap. IV-7. Specific surface area obtained for different network sizes $N_x \times N_y \times N_z$ with $N_x=N_y$ and $N_z=1$. 2D $Z_{max}=4$ networks with $P=0.7$.

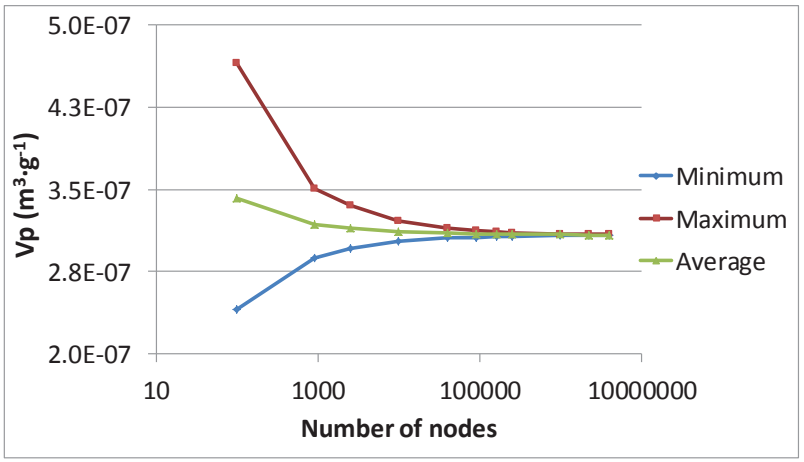


Fig. Ap. IV-8. Pore volume obtained for different network sizes $N_x \times N_y \times N_z$ with $N_x=N_y$ and $N_z=1$. 2D $Z_{max}=4$ networks with $P=0.7$.

And finally, for P=0.9:

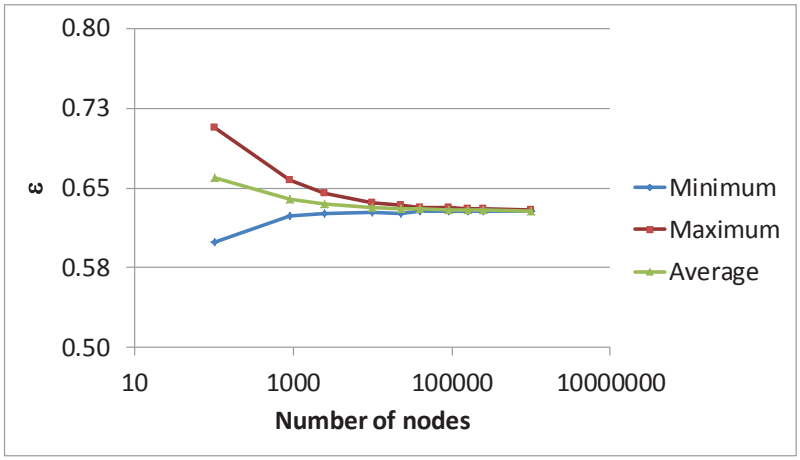


Fig. Ap. IV-9. Catalyst porosity obtained for different network sizes $N_x \times N_y \times N_z$ with $N_x=N_y$ and $N_z=1$. 2D $Z_{max}=4$ networks with $P=0.9$.

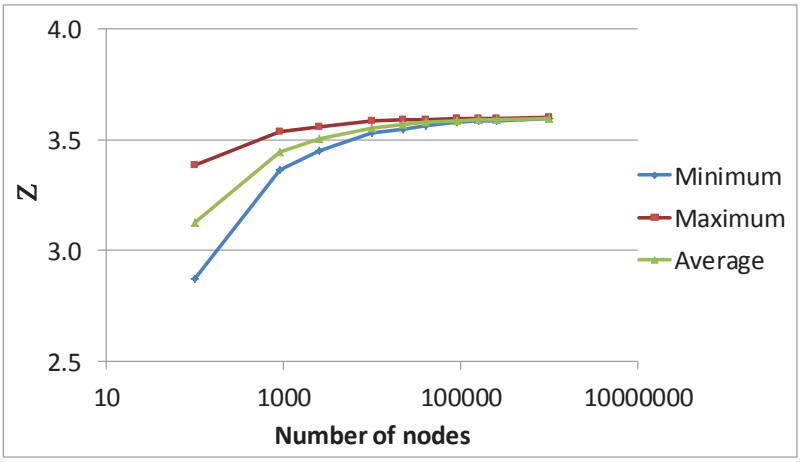


Fig. Ap. IV-10. Connectivity obtained for different network sizes $N_x \times N_y \times N_z$ with $N_x=N_y$ and $N_z=1$. 2D $Z_{max}=4$ networks with $P=0.9$.

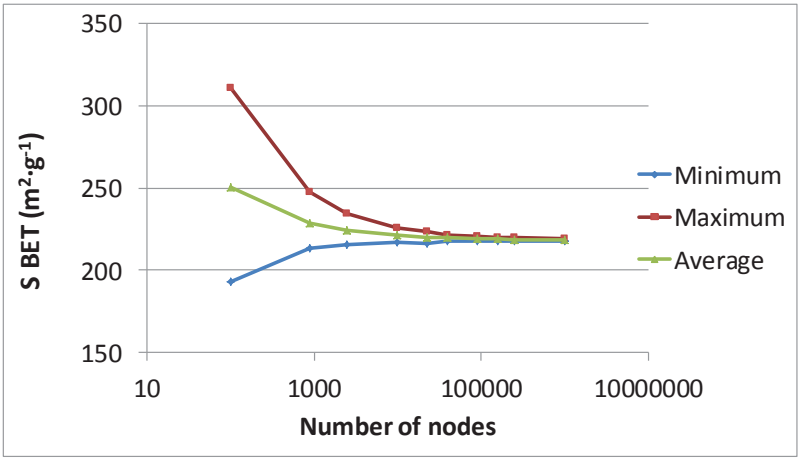


Fig. Ap. IV-11. Specific surface area obtained for different network sizes $N_x \times N_y \times N_z$ with $N_x=N_y$ and $N_z=1$. 2D $Z_{max}=4$ networks with $P=0.9$.

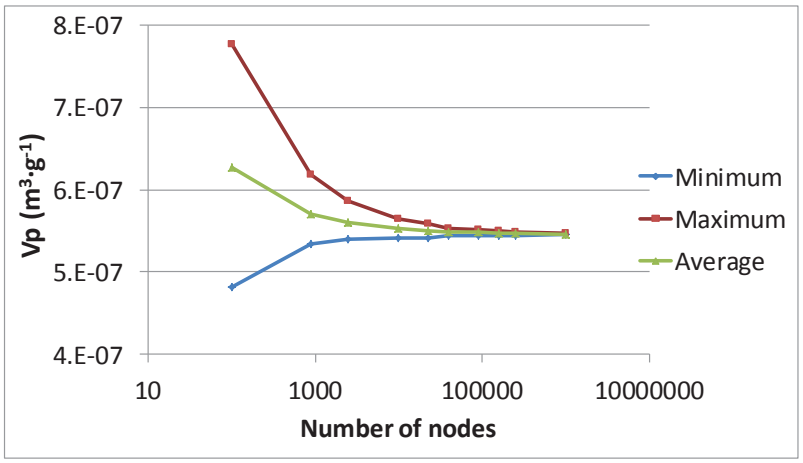


Fig. Ap. IV-12. Pore volume obtained for different network sizes $N_x \times N_y \times N_z$ with $N_x=N_y$ and $N_z=1$. 2D $Z_{max}=4$ networks with $P=0.9$.

IV.2 REQUIRED MINIMUM NETWORK SIZE FOR 2D TRIANGULAR NETWORKS

Concerning 2D triangular networks with $Z_{max}=6$ and taking P=0.5, we have:

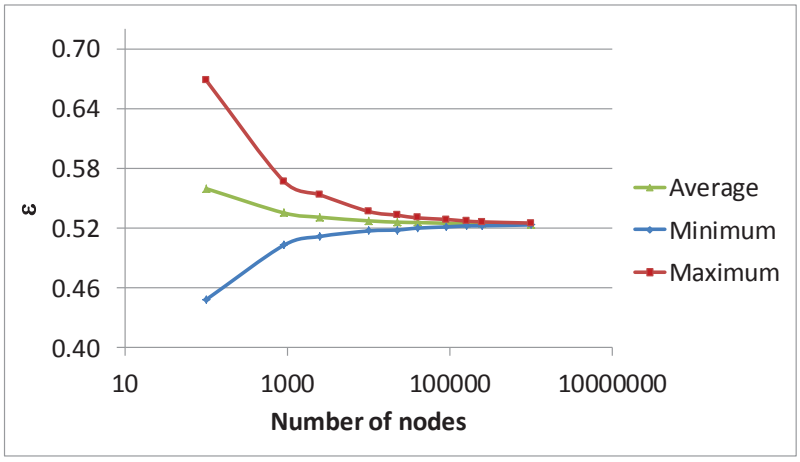


Fig. Ap. IV-13. Catalyst porosity obtained for different network sizes $N_x \times N_y \times N_z$ with $N_x=N_y$ and $N_z=1$. 2D $Z_{max}=6$ networks with $P=0.5$.

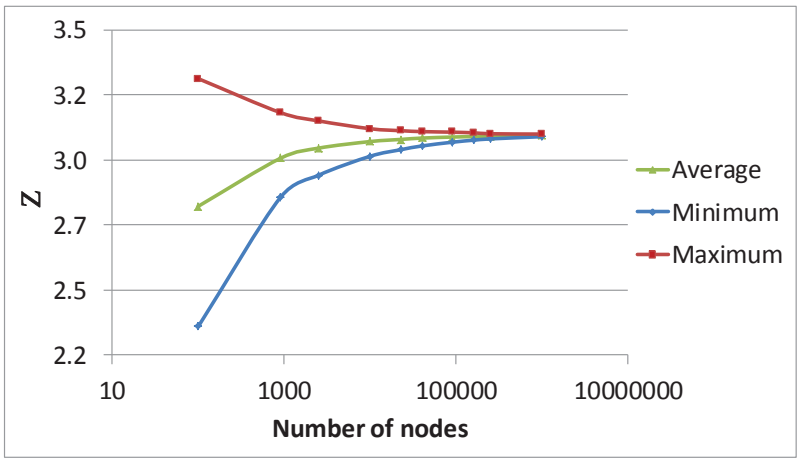


Fig. Ap. IV-14. Connectivity obtained for different network sizes $N_x \times N_y \times N_z$ with $N_x=N_y$ and $N_z=1$. 2D $Z_{max}=6$ networks with $P=0.5$.

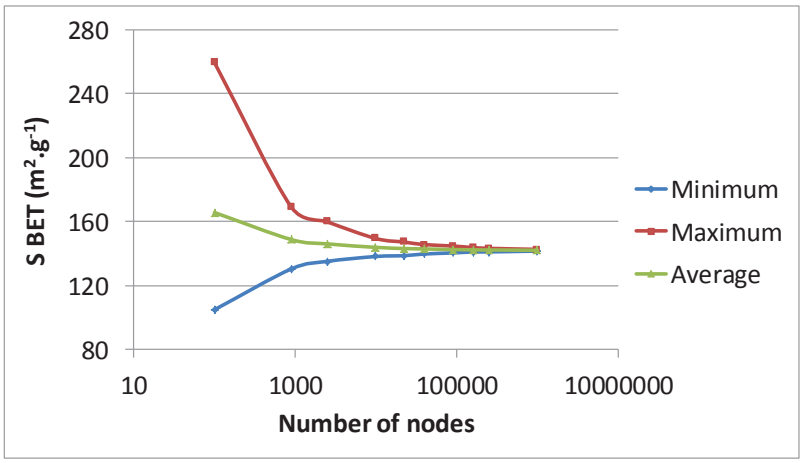


Fig. Ap. IV-15. Specific surface area obtained for different network sizes $N_x \times N_y \times N_z$ with $N_x=N_y$ and $N_z=1$. 2D $Z_{max}=6$ networks with $P=0.5$.

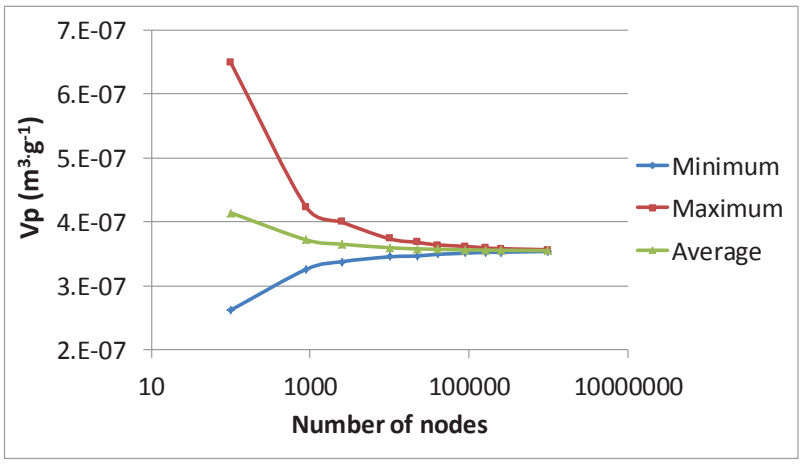


Fig. Ap. IV-16. Pore volume obtained for different network sizes $N_x \times N_y \times N_z$ with $N_x=N_y$ and $N_z=1$. 2D $Z_{max}=6$ networks with $P=0.5$.

For P=0.7 see section V.3.1. Finally, for P=0.9, we have:

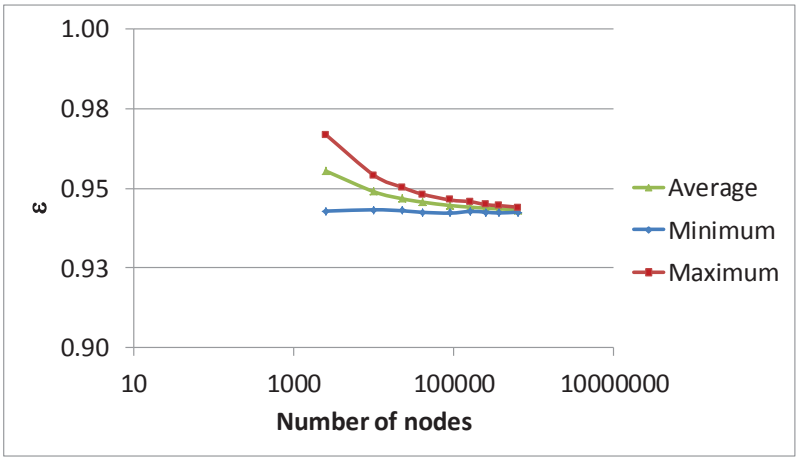


Fig. Ap. IV-17. Catalyst porosity obtained for different network sizes $N_x \times N_y \times N_z$ with $N_x=N_y$ and $N_z=1$. 2D $Z_{max}=6$ networks with $P=0.9$.

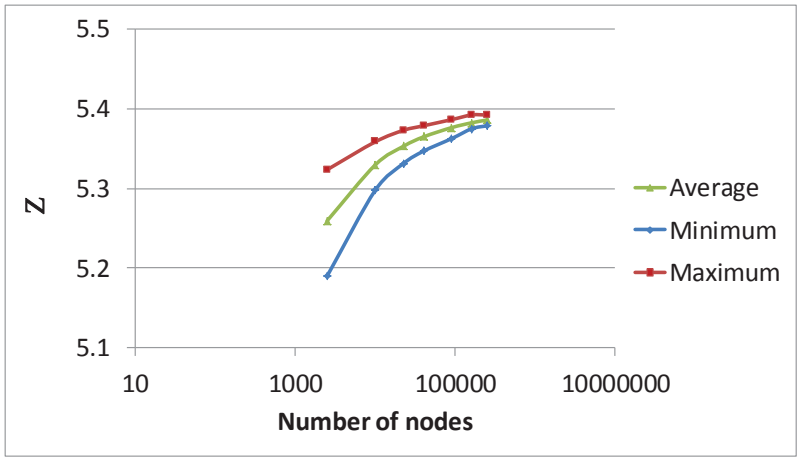


Fig. Ap. IV-18. Connectivity obtained for different network sizes $N_x \times N_y \times N_z$ with $N_x=N_y$ and $N_z=1$. 2D $Z_{max}=6$ networks with $P=0.9$.

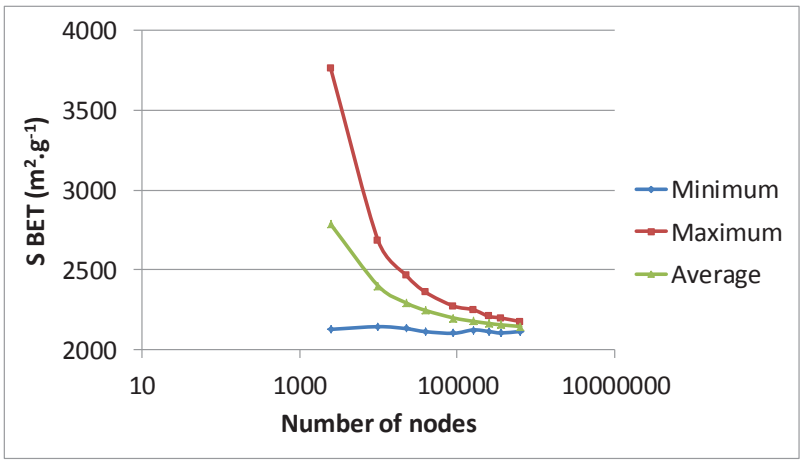


Fig. Ap. IV-19. Specific surface area obtained for different network sizes $N_x \times N_y \times N_z$ with $N_x=N_y$ and $N_z=1$. 2D $Z_{max}=6$ networks with $P=0.9$.

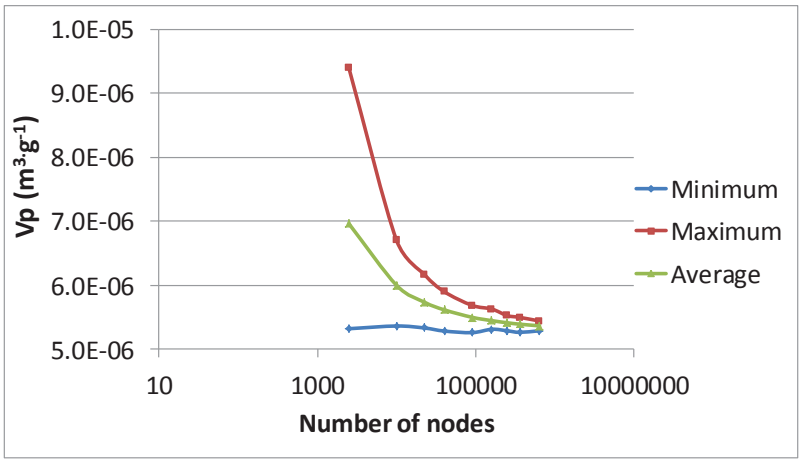


Fig. Ap. IV-20. Pore volume obtained for different network sizes $N_x \times N_y \times N_z$ with $N_x=N_y$ and $N_z=1$. 2D $Z_{max}=6$ networks with $P=0.9$.

IV.3 REQUIRED MINIMUM NETWORK SIZE FOR 3D CUBIC NETWORKS

For 3D pore networks of $Z_{max}=6$, three pore existence probabilities were studied $P = \{0.5, 0.7, 0.9\}$.

Taking P=0.5, we have:

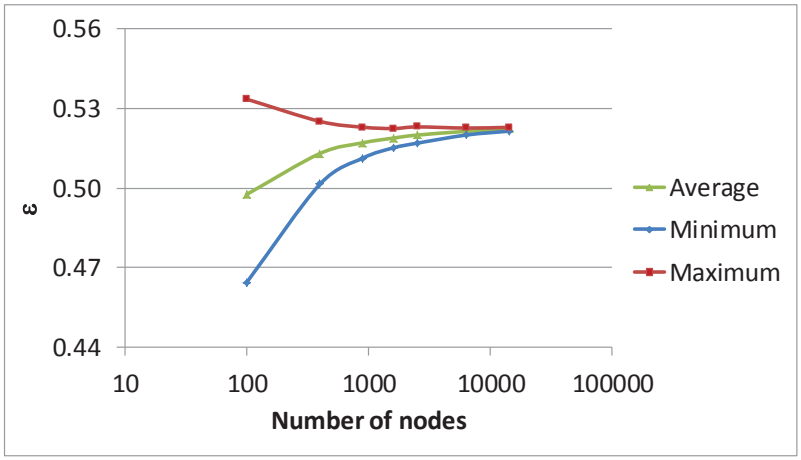


Fig. Ap. IV-21. Catalyst porosity obtained for different network sizes $N_x \times N_y \times N_z$ with $N_x=N_y=N_z$. 3D Z_{max}=6 networks with P=0.5.

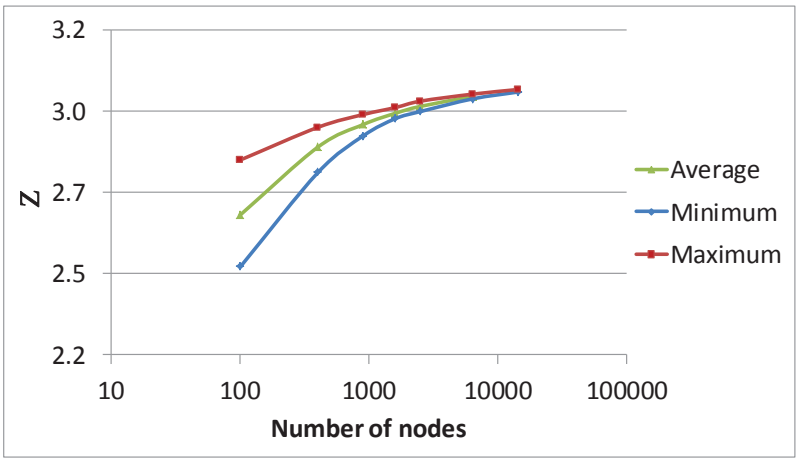


Fig. Ap. IV-22. Connectivity obtained for different network sizes $N_x \times N_y \times N_z$ with $N_x=N_y=N_z$. 3D Z_{max}=6 networks with P=0.5.

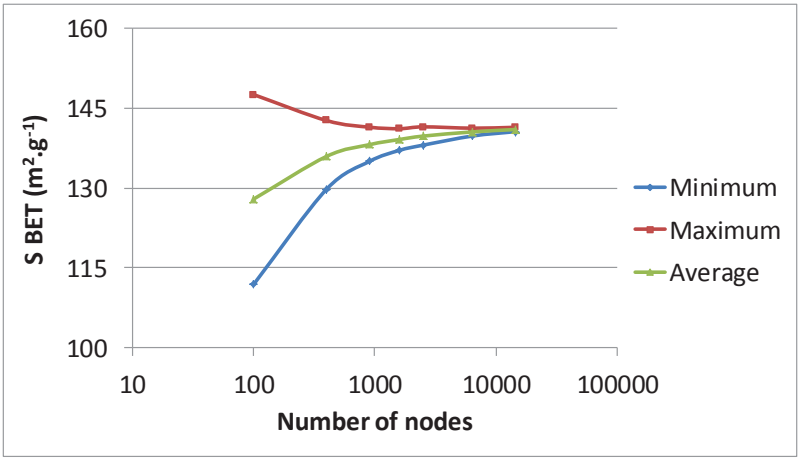


Fig. Ap. IV-23. Specific surface area obtained for different network sizes $N_x \times N_y \times N_z$ with $N_x=N_y=N_z$. 3D Z_{max}=6 networks with P=0.5.

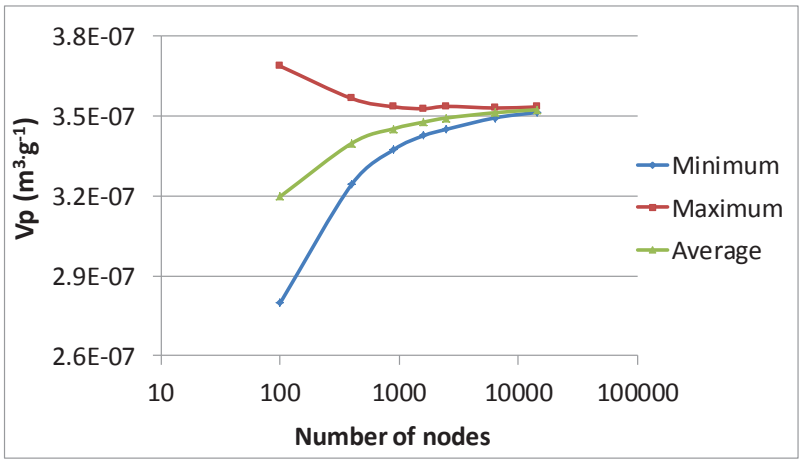


Fig. Ap. IV-24. Pore volume obtained for different network sizes $N_x \times N_y \times N_z$ with $N_x=N_y=N_z$. 3D Z_{max}=6 networks with P=0.5.

For P=0.7:

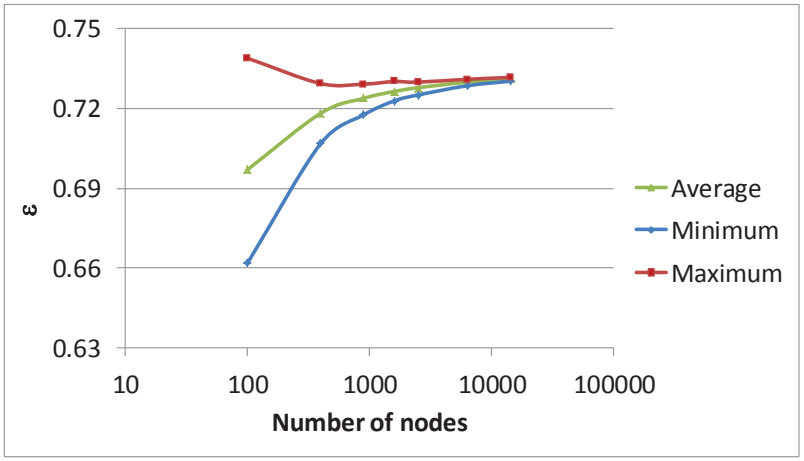


Fig. Ap. IV-25. Catalyst porosity obtained for different network sizes $N_x \times N_y \times N_z$ with $N_x=N_y=N_z$. 3D Z_{max}=6 networks with P=0.7.

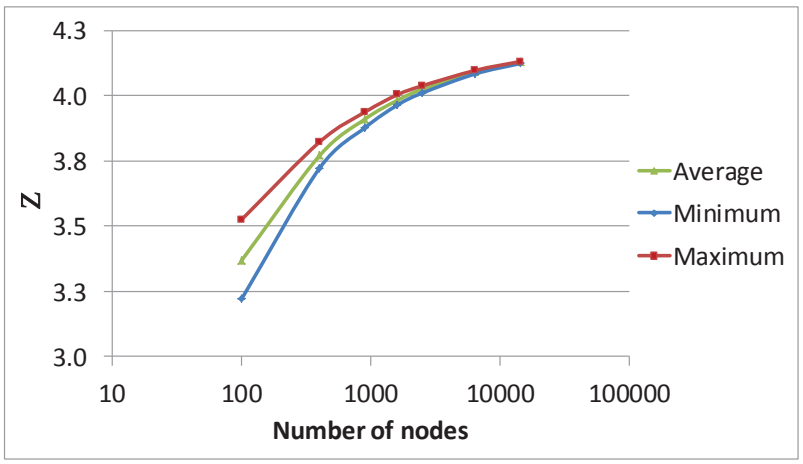


Fig. Ap. IV-26. Connectivity obtained for different network sizes $N_x \times N_y \times N_z$ with $N_x=N_y=N_z$. 3D Z_{max}=6 networks with P=0.7.

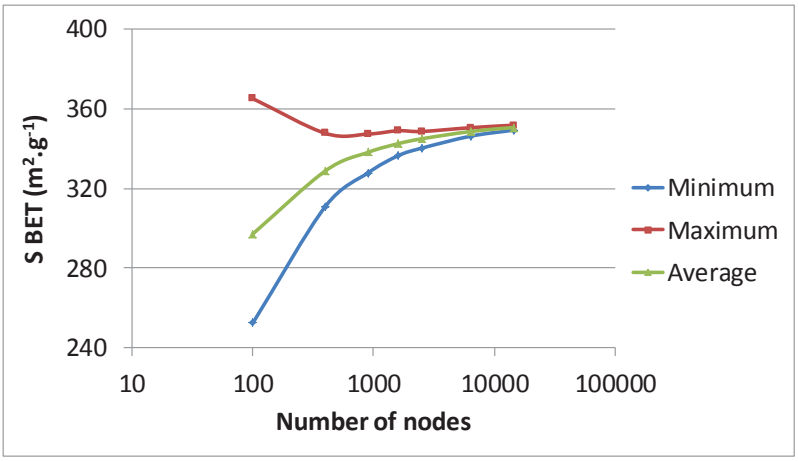


Fig. Ap. IV-27. Specific surface area obtained for different network sizes $N_x \times N_y \times N_z$ with $N_x=N_y=N_z$. 3D $Z_{max}=6$ networks with $P=0.7$.

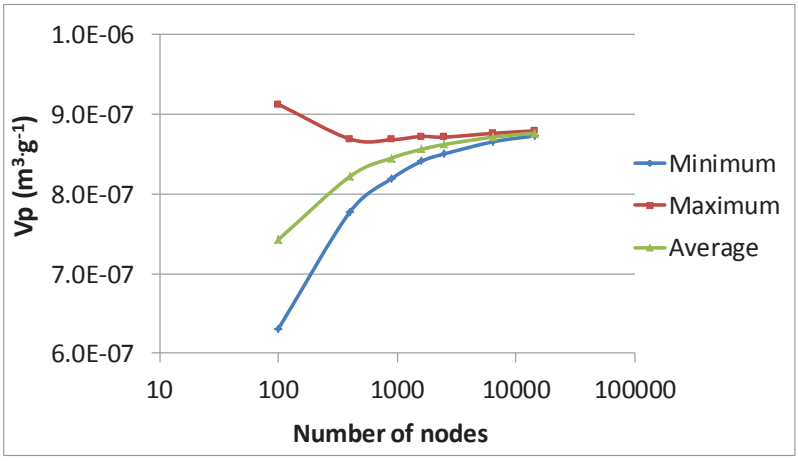


Fig. Ap. IV-28. Pore volume obtained for different network sizes $N_x \times N_y \times N_z$ with $N_x=N_y=N_z$. 3D $Z_{max}=6$ networks with $P=0.7$.

For P=0.9:

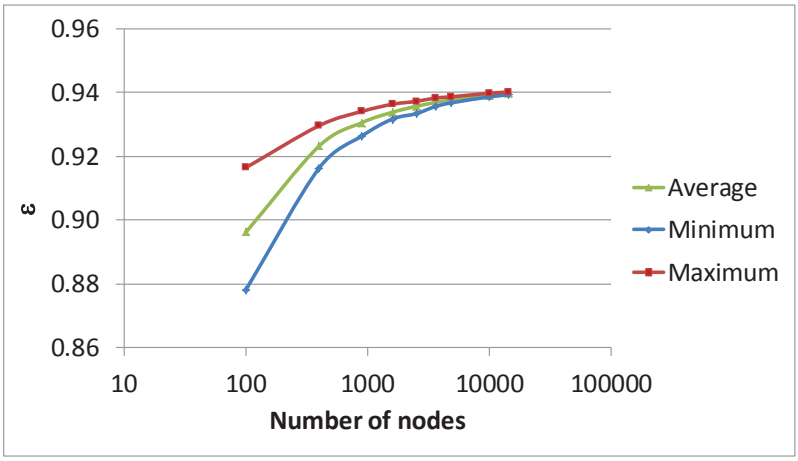


Fig. Ap. IV-29. Catalyst porosity obtained for different network sizes $N_x \times N_y \times N_z$ with $N_x=N_y=N_z$. 3D $Z_{max}=6$ networks with $P=0.9$.

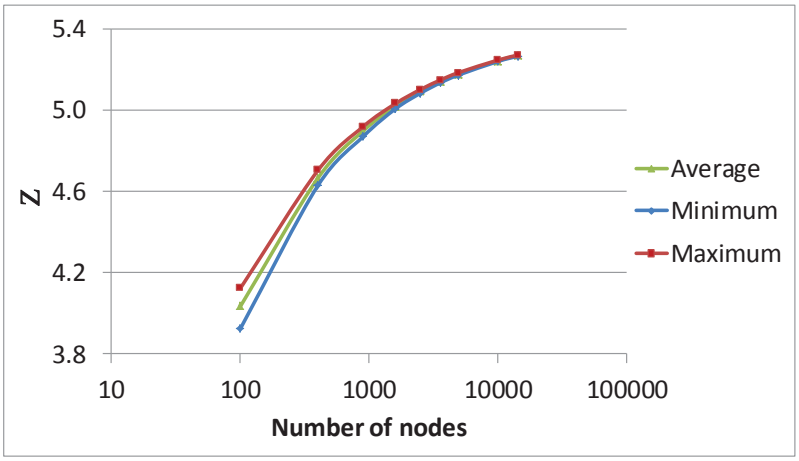


Fig. Ap. IV-30. Connectivity obtained for different network sizes $N_x \times N_y \times N_z$ with $N_x=N_y=N_z$. 3D $Z_{max}=6$ networks with $P=0.9$.

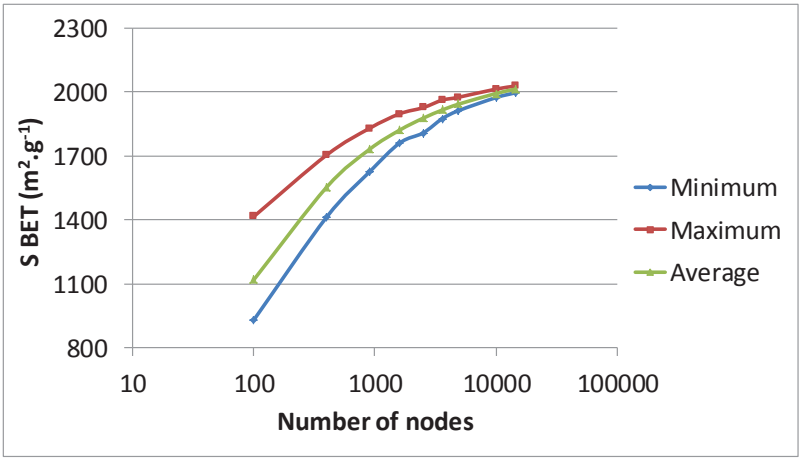


Fig. Ap. IV-31. Specific surface area obtained for different network sizes $N_x \times N_y \times N_z$ with $N_x=N_y=N_z$. 3D $Z_{max}=6$ networks with $P=0.9$.

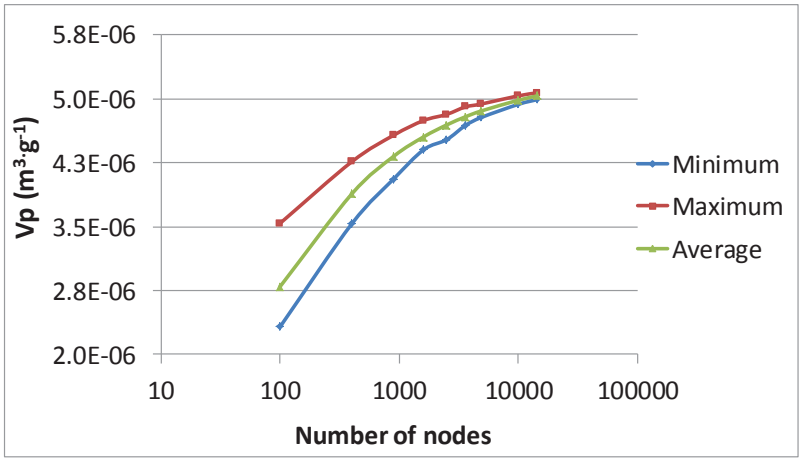


Fig. Ap. IV-32. Pore volume obtained for different network sizes $N_x \times N_y \times N_z$ with $N_x=N_y=N_z$. 3D $Z_{max}=6$ networks with $P=0.9$.

IV.4 REQUIRED MINIMUM NETWORK SIZE FOR 3D ZMAX=8 NETWORKS

Regarding 3D pore networks of $Z_{max}=8$, we obtained the following results for a pore existence probability of $P=0.5$ and of $P=0.7$.

For P=0.5, we have:

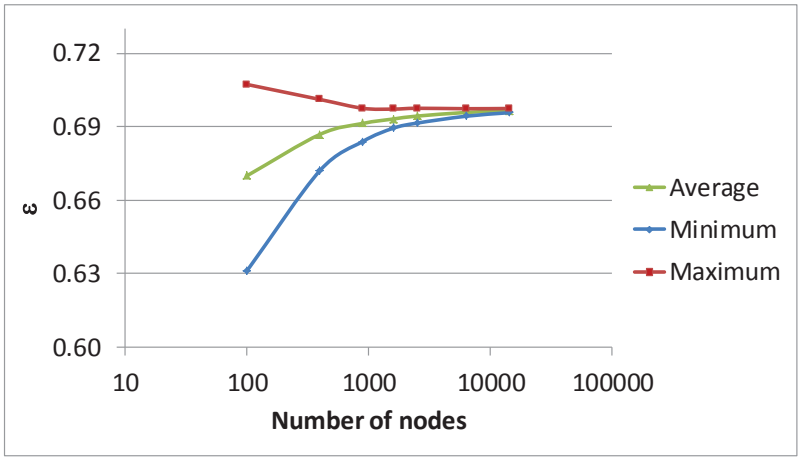


Fig. Ap. IV-33. Catalyst porosity obtained for different network sizes $N_x \times N_y \times N_z$ with $N_x=N_y=N_z$. 3D Z_{max}=8 networks with P=0.5.

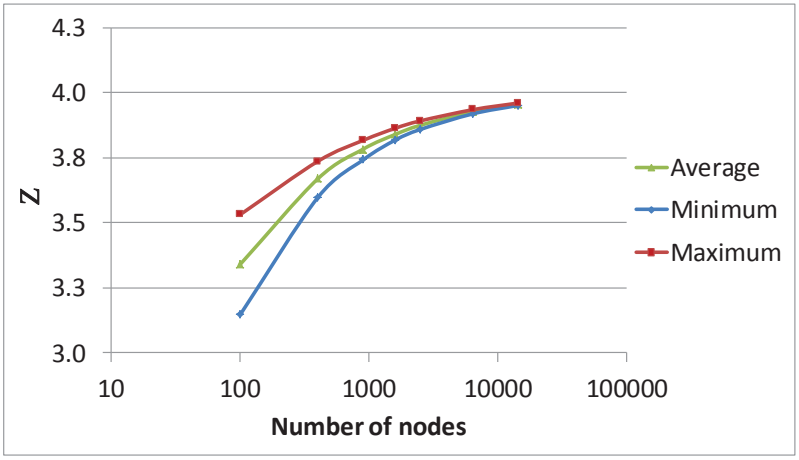


Fig. Ap. IV-34. Connectivity obtained for different network sizes $N_x \times N_y \times N_z$ with $N_x=N_y=N_z$. 3D Z_{max}=8 networks with P=0.5.

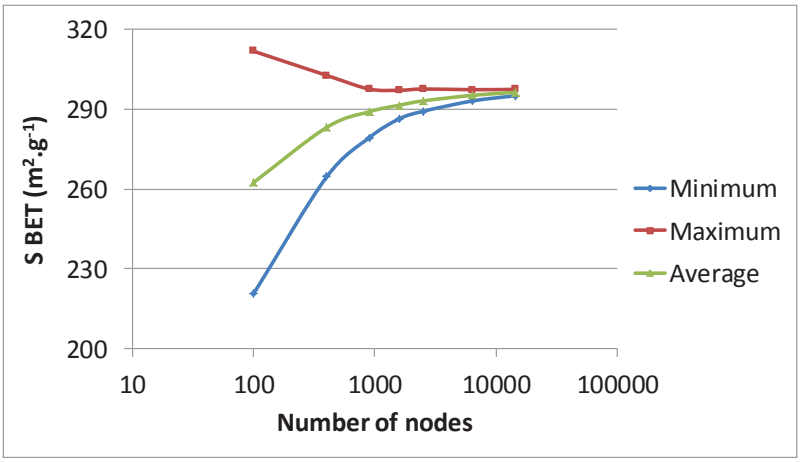


Fig. Ap. IV-35. Specific surface area obtained for different network sizes $N_x \times N_y \times N_z$ with $N_x=N_y=N_z$. 3D Z_{max}=8 networks with P=0.5.

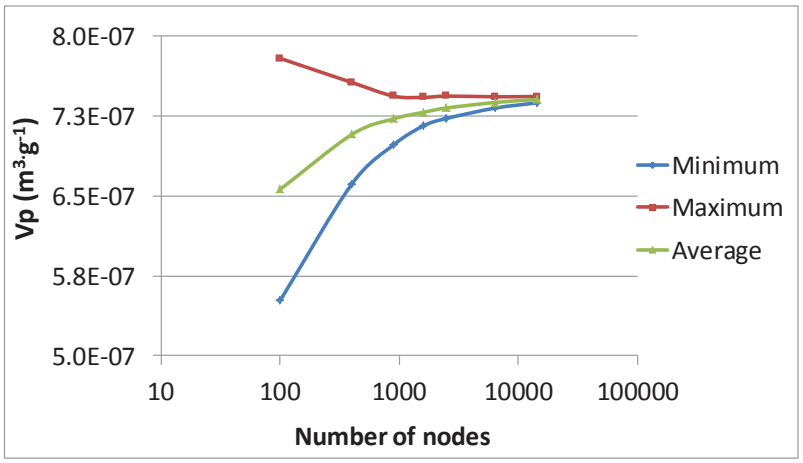


Fig. Ap. IV-36. Pore volume obtained for different network sizes $N_x \times N_y \times N_z$ with $N_x=N_y=N_z$. 3D Z_{max}=8 networks with P=0.5.

For P=0.7:

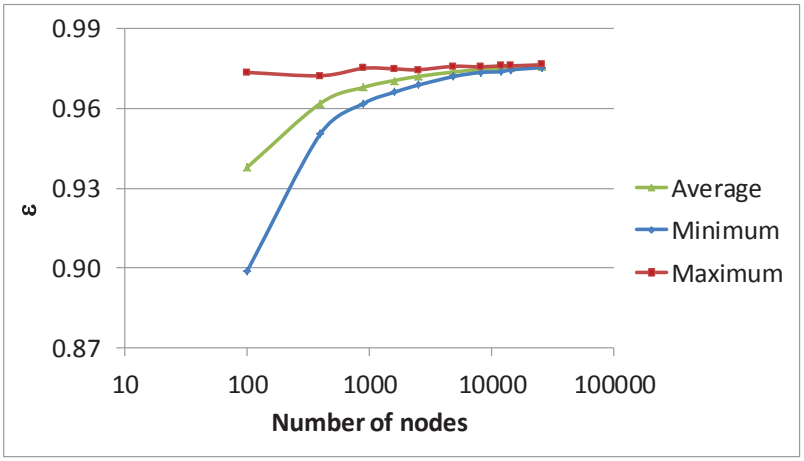


Fig. Ap. IV-37. Catalyst porosity obtained for different network sizes $N_x \times N_y \times N_z$ with $N_x=N_y=N_z$. 3D Z_{max}=8 networks with P=0.7.

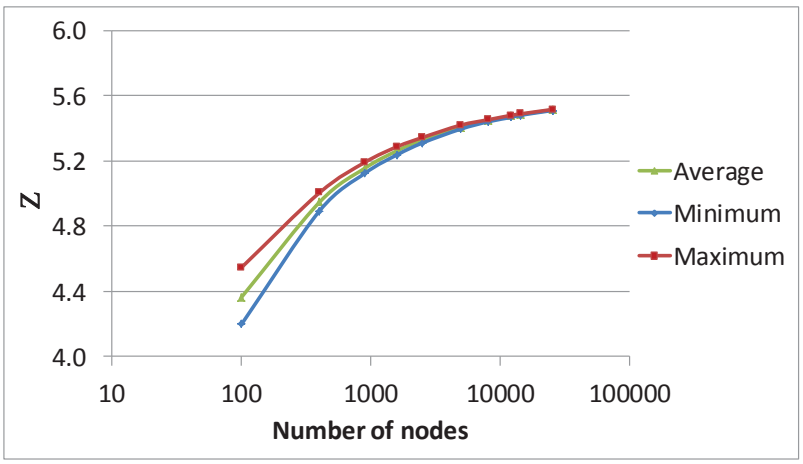


Fig. Ap. IV-38. Connectivity obtained for different network sizes $N_x \times N_y \times N_z$ with $N_x=N_y=N_z$. 3D Z_{max}=8 networks with P=0.7.

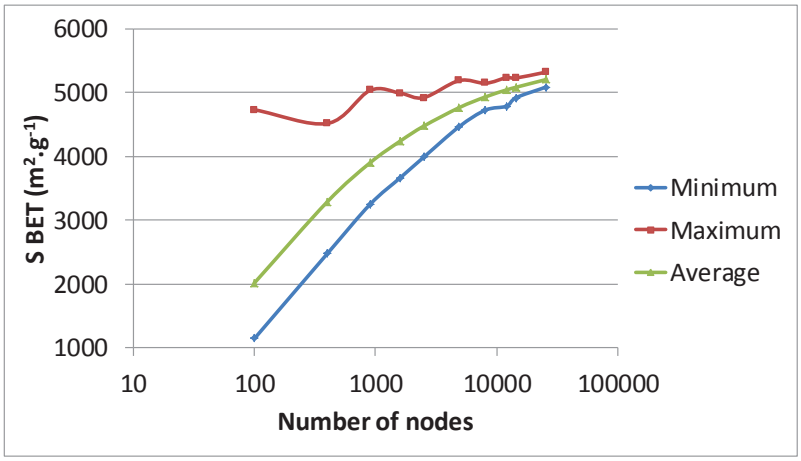


Fig. Ap. IV-39. Specific surface area obtained for different network sizes $N_x \times N_y \times N_z$ with $N_x=N_y=N_z$. 3D $Z_{max}=8$ networks with $P=0.7$.

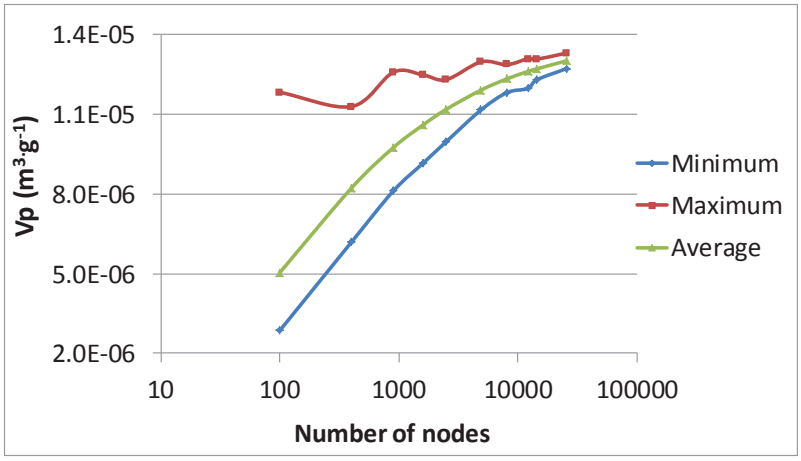


Fig. Ap. IV-40. Pore volume obtained for different network sizes $N_x \times N_y \times N_z$ with $N_x=N_y=N_z$. 3D $Z_{max}=8$ networks with $P=0.7$.

APPENDIX V

In this section, we first present the results obtained for 2D Z_{max}=4 (triangular) networks respective to the separate influence of N_x and N_y and then, we present the results obtained for 2D Z_{max}=4 networks on both the textural and mass transfer properties. A pore existence probability of P=0.98 is here used.

V.1 INFLUENCE OF N_X ON 2D TRIANGULAR NETWORKS (Z_{MAX}=6)

To study the sensitivity towards N_x, thirty 2D triangular networks of constant N_y and variable N_x were generated. The maximum network sizes used are: 10×1000, 20×1000, 30×1000, 40×1000, 50×1000 and 60×1000. The used pore existence probability is of 0.7. The networks generated at a maximum size of 10×1000 have a maximum number of nodes of 10,000 nodes and for example, the network size 50×1000, contains an average amount of nodes of 49,955 and an average number of pores of 104,805.

The influence of N_x on the mean and standard deviation of the catalyst porosity, connectivity, particle specific surface area and specific pore volume are represented graphically in Fig. Ap. V-1-Fig. Ap. V-4.

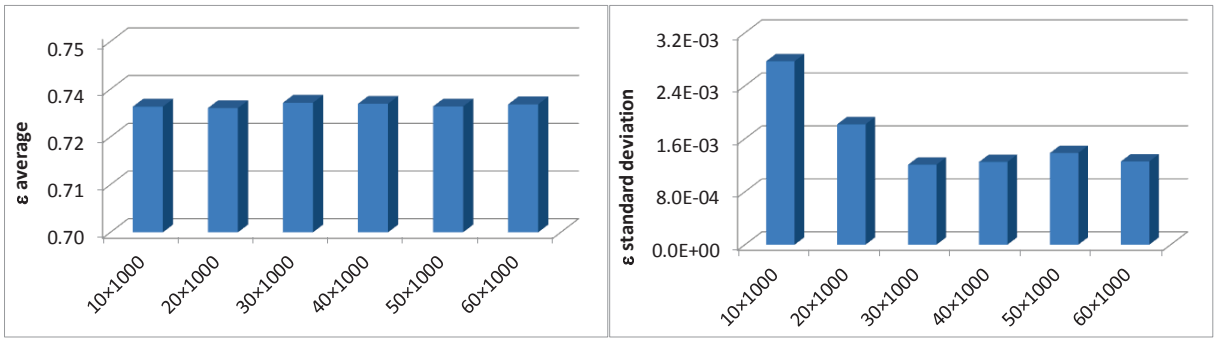


Fig. Ap. V-1. Porosity according to N_x with N_y=1000. 2D networks, Z_{max}=6 and P=0.7.

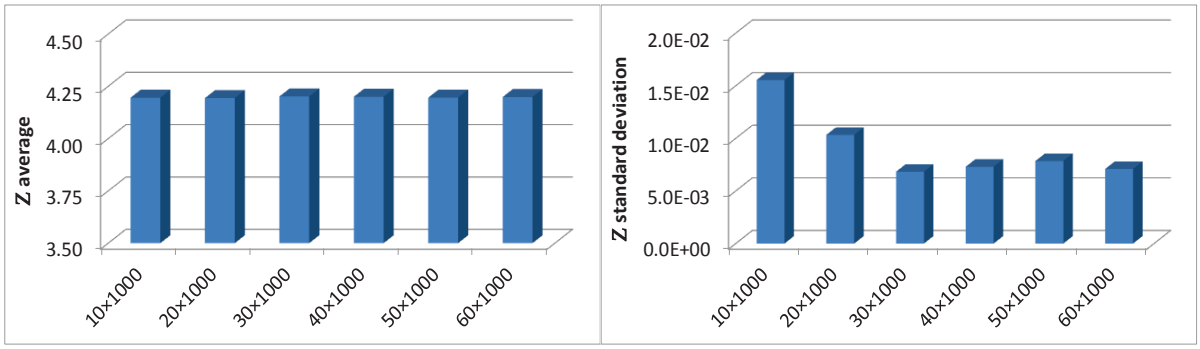


Fig. Ap. V-2. Connectivity according to N_x with N_y=1000. 2D networks, Z_{max}=6 and P=0.7.

On Fig. Ap. V-1, the porosity standard deviation globally decreases when increasing the particle dimension N_x while the average porosity takes a value of 0.73. The same trends are observed for the remaining textural properties (see Fig. Ap. V-1-Fig. Ap. V-4). The mean textural properties take rather constant values. The average connectivity is of

4.20, the specific surface area of 352 $m^2 \cdot g^{-1}$ and the pore volume around 8.81×10^{-7} $m^3 \cdot g^{-1}$.

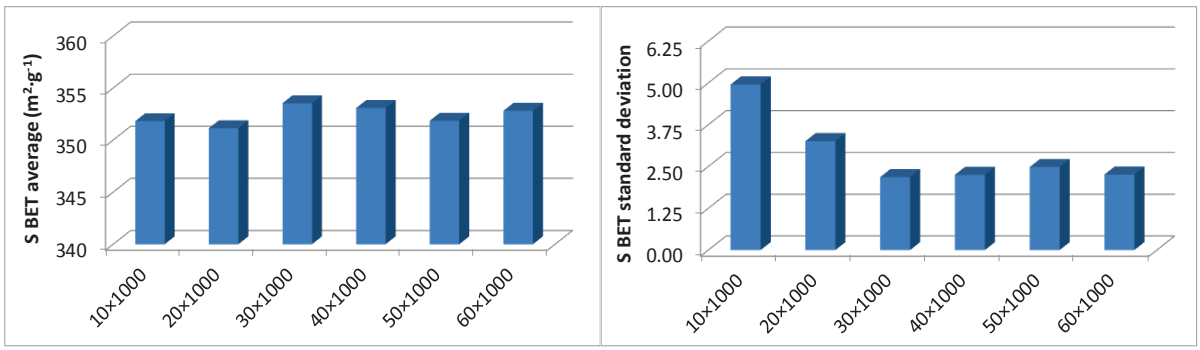


Fig. Ap. V-3. Specific surface area according to N_x with N_y=1000. 2D networks, Z_{max}=6 and P=0.7.

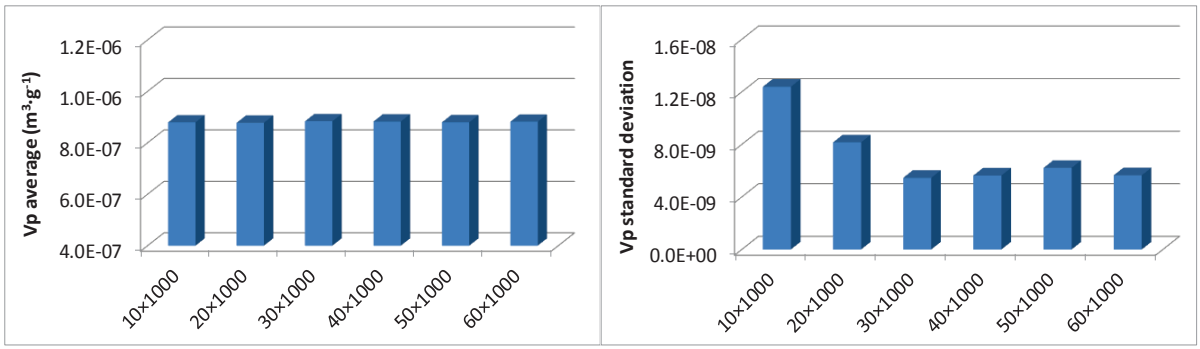


Fig. Ap. V-4. Pore volume according to N_x with N_y=1000. 2D networks, Z_{max}=6 and P=0.7.

In Fig. Ap. V-5 are graphically represented the tortuosities of all 30 networks generated for each network size and that have been previously studied in terms of the textural properties in Fig. Ap. V-1 to Fig. Ap. V-4.

Fig. Ap. V-5 gives a global apparatus on the average and dispersion of the tortuosity data at each network size, being necessary to graphically represent the average and standard deviation from all 30 networks simulated for each network size, as shown in Fig. Ap. V-6.

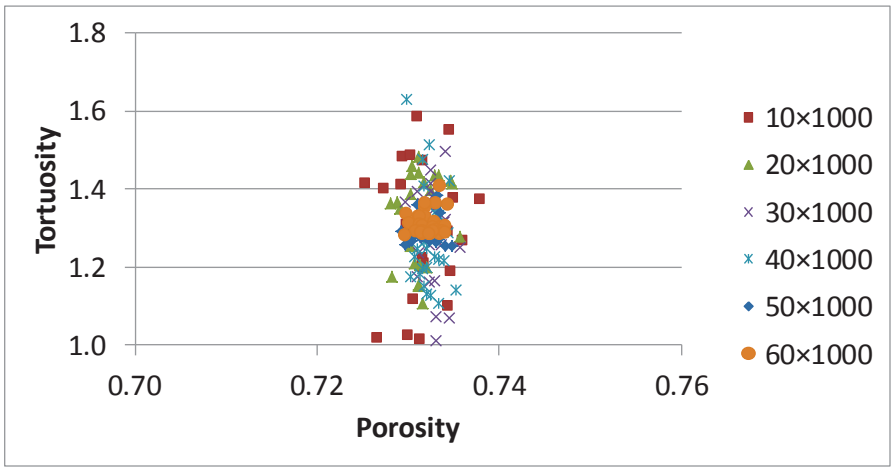


Fig. Ap. V-5. Tortuosity obtained per simulation as a function of the catalyst porosity for 6 different 2D Z_{max}=6 networks according to N_x with N_y=1000.

In Fig. Ap. V-6, on the left are represented graphically the average tortuosity from all 30 networks obtained for each network size and on the right, their corresponding standard deviation.

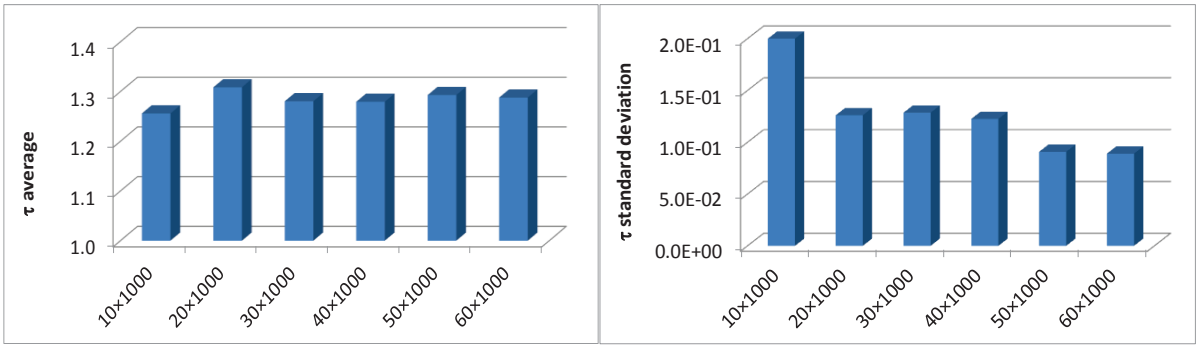


Fig. Ap. V-6. Tortuosity obtained for 6 different 2D Z_{max}=6 network sizes according to N_x with N_y=1000.

When looking to the mass transfer properties shown in Fig. Ap. V-6, a similar behaviour to that from the textural properties is here found. Indeed, we observe a decrease in the standard deviation as N_x increases in combination with a rather constant value of the average tortuosity (1.26 to 1.30) for an average value of the porosity of 0.73. We would expect that for greater N_x, the lower the probability to find paths with τ=1.0 and so, a tortuosity different from the average tortuosity becomes less exclusive and the standard deviation reduces. Also, with the increase in N_x, the network size also increases and the Monte Carlo variability is reduced hence, the standard deviation is also reduced.

V.1.1 INFLUENCE OF N_Y ON 2D TRIANGULAR NETWORKS (Z_{MAX}=6)

A similar study is provided according to the parallelepiped dimension N_y, with N_x being constant. Thirty 2D triangular networks (Z_{max}=6) were generated for different maximum network sizes: 50×200, 50×500, 50×1000 and 50×1500. The used pore existence probability is of 0.7. For the lowest initial network size (50×200), the maximum number of nodes is of 10,000 and for example, the 50×1500 network size contains an average number of nodes of 74,940 and an average number of pores of 157,385.

Looking at the mean and standard deviation of the main textural properties presented on Fig. Ap. V-7 to Fig. Ap. V-10, it can be concluded a reduction on the standard deviation as N_y increases. The preponderant reason is actually due to the reduction of the variability of Monte Carlo for greater network sizes. Regarding the catalyst porosity, the connectivity and the pore volume averages, they remain rather constant and taking values of 0.73, 4.2 and 8.75×10^{-7} $m^3 \cdot g^{-1}$, respectively. Whereas, the particle specific surface area varies between: 345 to 353 $m^2 \cdot g^{-1}$, with an average value of 350 $m^2 \cdot g^{-1}$.

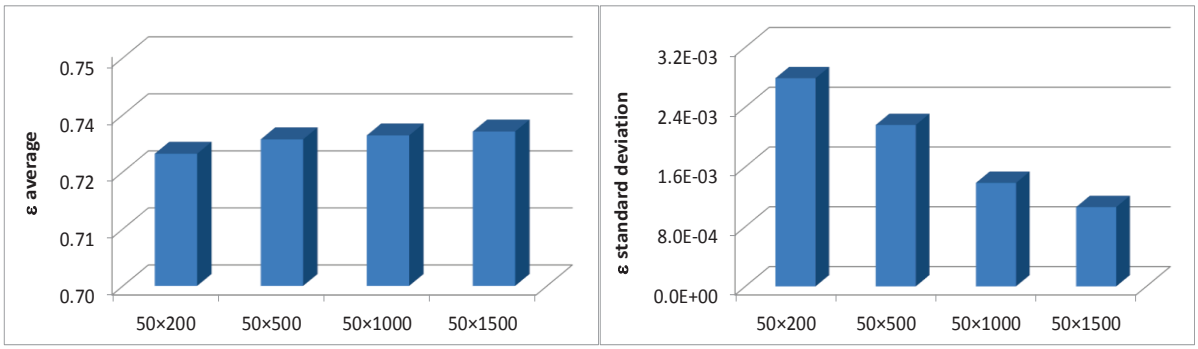


Fig. Ap. V-7. Porosity obtained according to N_y with N_x = 50. 2D networks, Z_{max} = 6, P = 0.7.

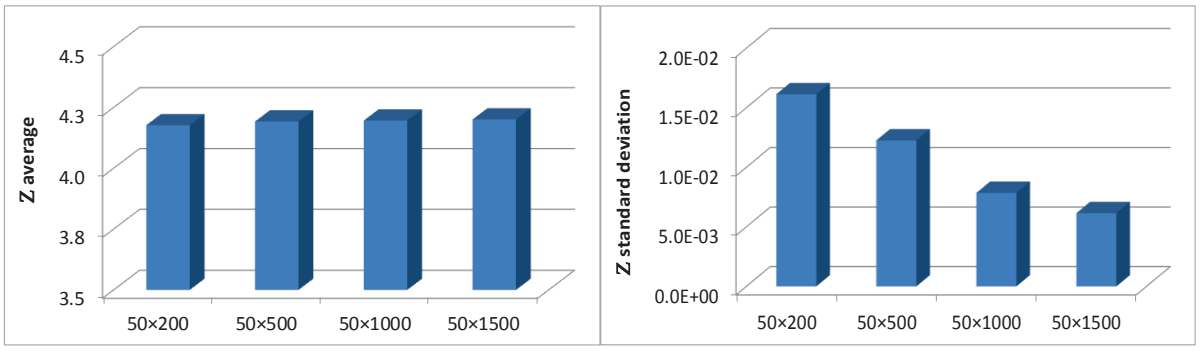


Fig. Ap. V-8. Connectivity according to N_y with N_x = 50. 2D networks, Z_{max} = 6, P = 0.7.

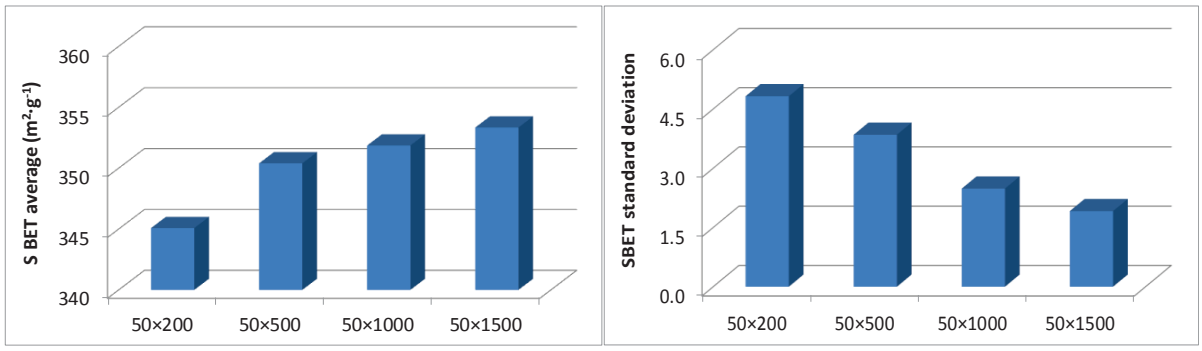


Fig. Ap. V-9. Specific surface area according to N_y with N_x = 50. 2D networks, Z_{max} = 6, P = 0.7.

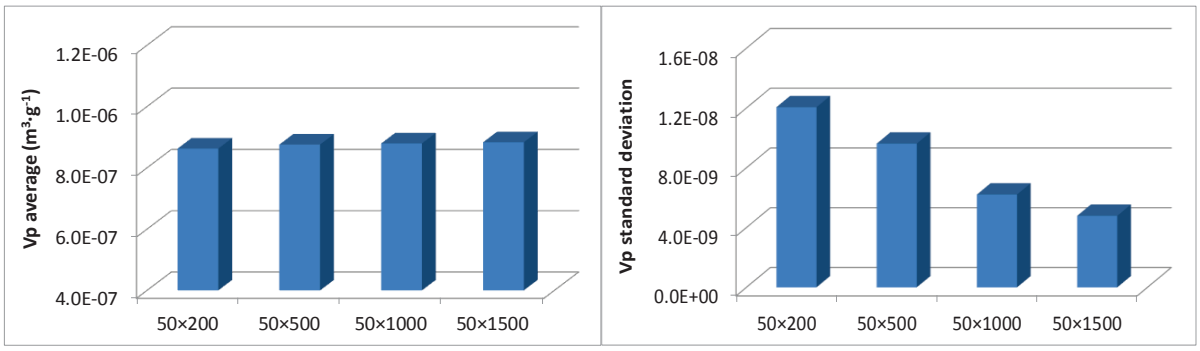


Fig. Ap. V-10. Pore volume according to N_y with N_x = 50. 2D networks, Z_{max} = 6, P = 0.7.

The 30 networks generated for each network size that were studied in terms of textural properties on Fig. Ap. V-7 to Fig. Ap. V-10 are now studied in terms of mass transfer properties. The tortuosity obtained for the 30 samples generated per network size is available on Fig. Ap. V-11 and ranges from 1.293 to 1.308. Concerning the average

tortuosity that is available on Fig. Ap. V-12, it takes a value of 1.30 for an average porosity of 0.73.

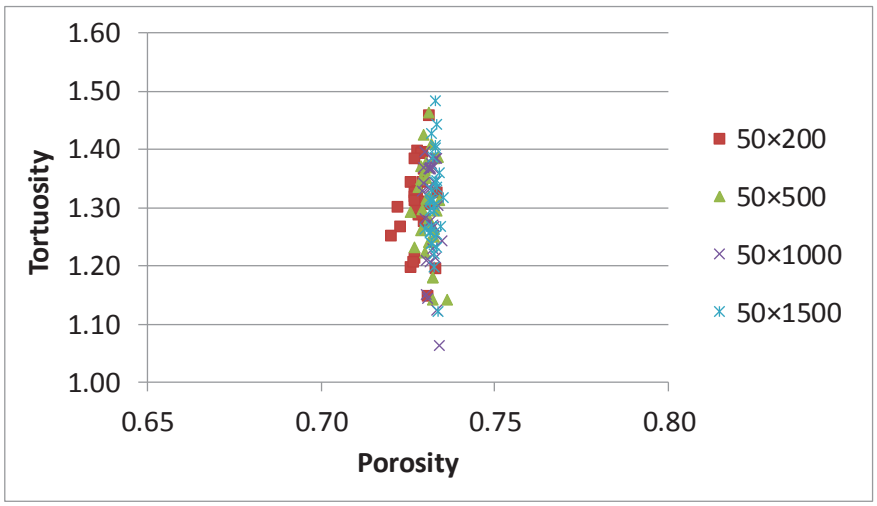


Fig. Ap. V-11. Predicted tortuosity per simulation as a function of the catalyst porosity for 4 different 2D Z_{max}=6 network sizes according to N_y with N_x =50.

The tortuosity standard deviations presented on the right hand side of Fig. Ap. V-12, do not have the same behaviour as the textural properties, that reduced with N_y. Indeed, the tortuosity standard deviation remains globally constant. As far as the average tortuosity is concerned, it remains rather constant with N_y.

We would expect that for greater N_y, the greater the dispersion since, the characteristic length of diffusion increases with N_y and with that the probability to find more heterogeneous paths increases as well. Yet, one should know that the standard deviations calculated for the variation of N_y can be misleading. Due to the Monte Carlo variability that gets an important role if the maximum network size is varied. For greater network sizes, the data dispersion reduces.

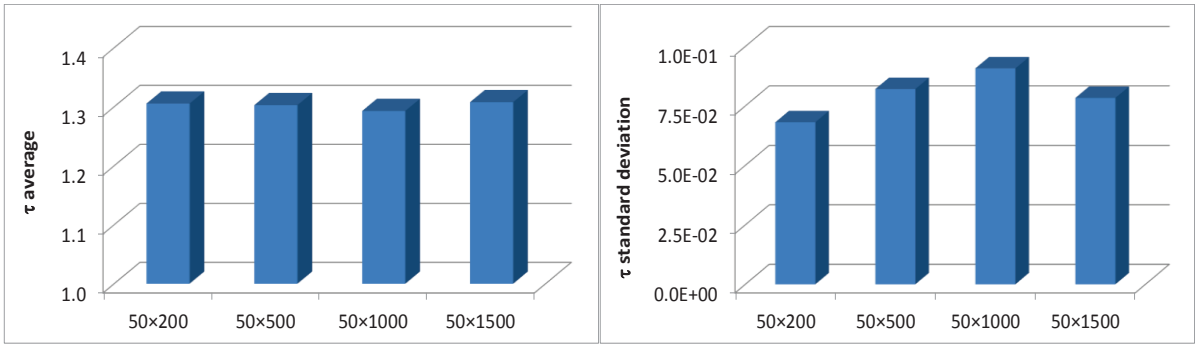


Fig. Ap. V-12. Predicted tortuosity according to N_y with N_x = 50. 2D networks, Z_{max} = 6, P = 0.7.

In order to get a clear understanding on the influence of both dimensions N_x and N_y one should bear in mind that the previous simulations were obtained keeping constant, one of the dimensions and varying the other one. Thus, we have compared pore networks containing a variable maximum number of nodes. Section VI.3.1 presented in the core of

the report will help clarifying since, we have simulated pore networks of equal number of nodes and $N_x \neq N_y$ according to N_x/N_y.

V.2 INFLUENCE OF N_X ON 2D SQUARE NETWORKS (Z_{MAX}=4)

The influence of N_x on the textural and mass transfer properties is here studied on 2D Z_{max}=4 pore networks with P=0.98.

As we can see from Fig. Ap. V-13 to Fig. Ap. V-16, the mean textural properties remain rather constant and the standard deviations are globally decreasing with increasing N_x due, essentially to the augmentation of the maximum network size that leads to a lower Monte Carlo variability.

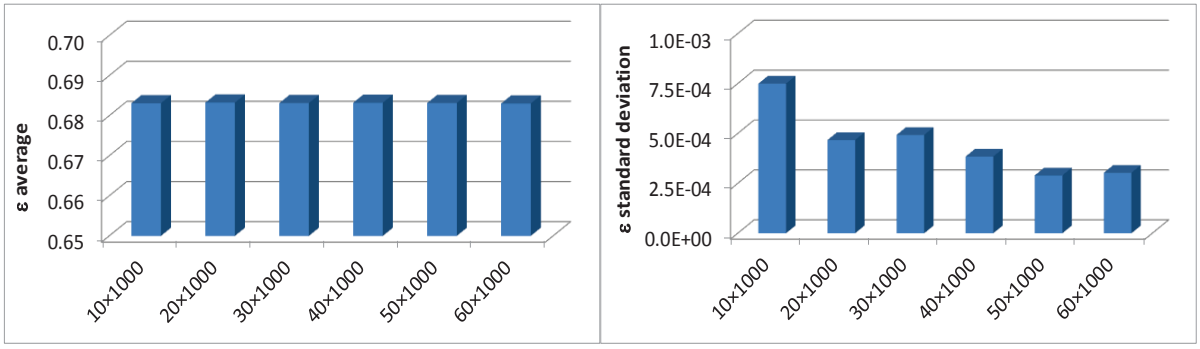


Fig. Ap. V-13. Porosity according to N_x with N_y=1000. 2D networks, Z_{max}=4 and P=0.98.

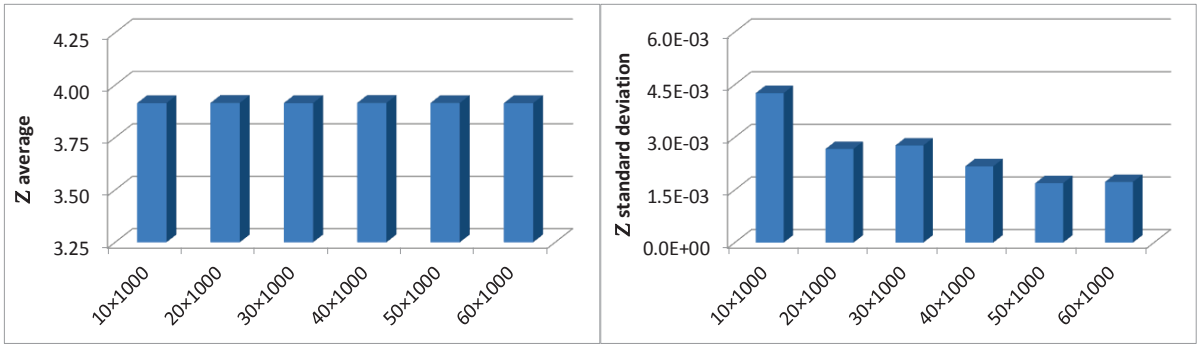


Fig. Ap. V-14. Connectivity according to N_x with N_y=1000. 2D networks, Z_{max}=4 and P=0.98.

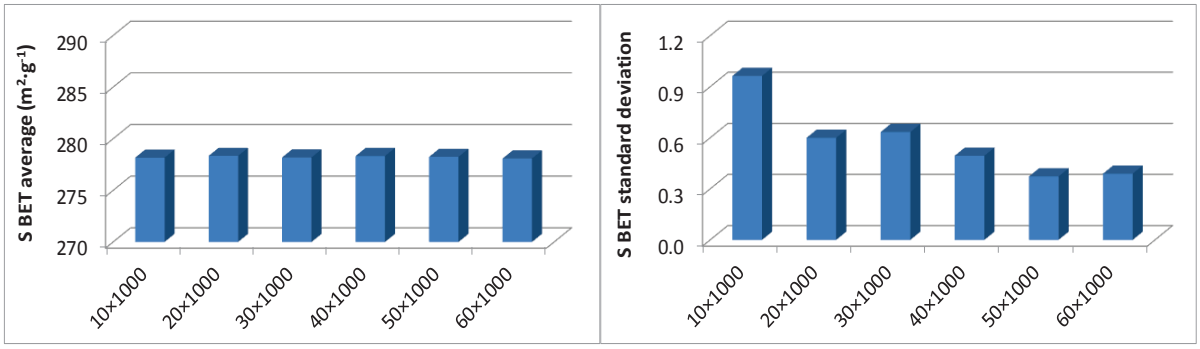


Fig. Ap. V-15. s_{BET} according to N_x with N_y=1000. 2D networks, Z_{max}=4 and P=0.98.

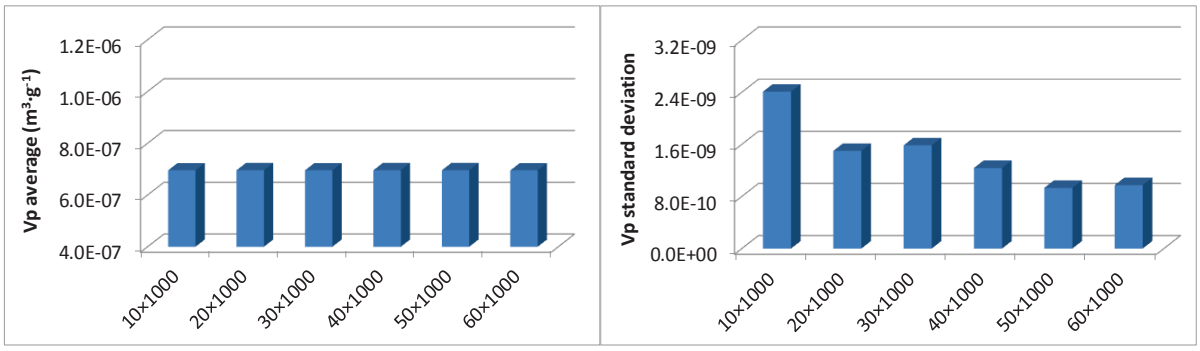


Fig. Ap. V-16. Pore volume according to N_x with N_y=1000. 2D networks, Z_{max}=4 and P=0.98.

The mean tortuosity is also rather constant with a similar behaviour on the standard deviation of that from the textural properties. I.e., a decrease in the standard deviation with the augmentation of N_x. Once again probably due to the variability of the Monte Carlo approach.

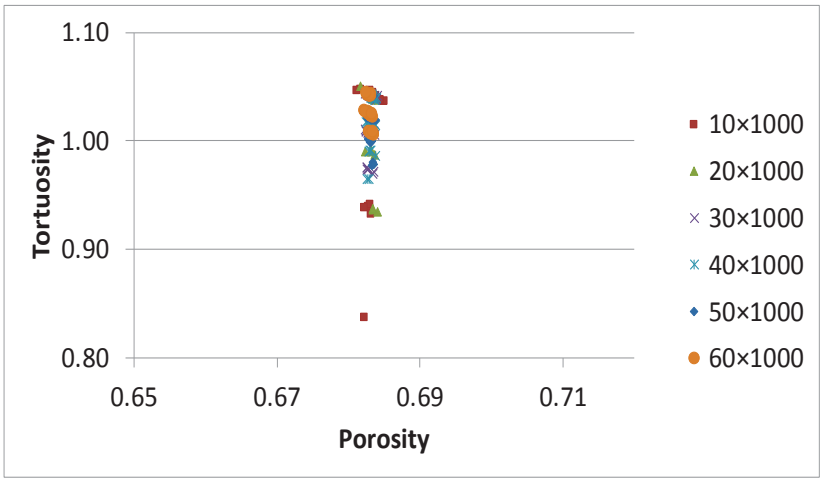


Fig. Ap. V-17. Tortuosity obtained per simulation as a function of the catalyst porosity for 6 different 2D Z_{max}=4 networks according to N_x with N_y=1000.

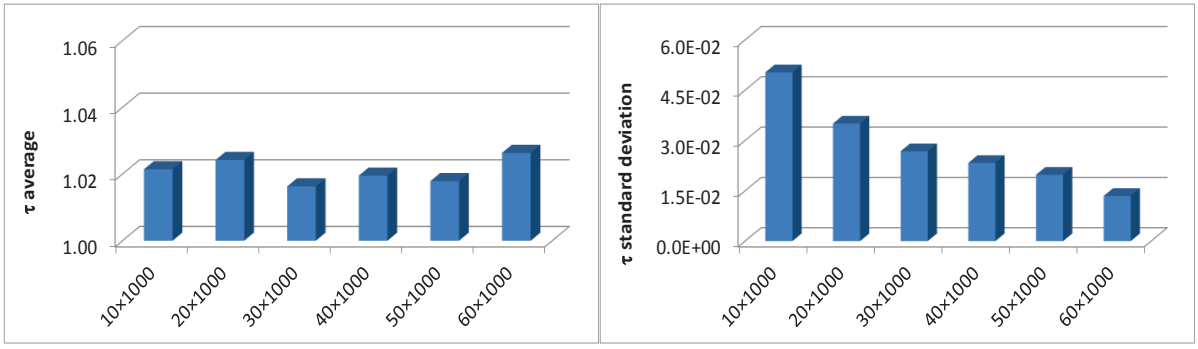


Fig. Ap. V-18. Tortuosity obtained for 6 different 2D Z_{max}=4 network sizes according to N_x with N_y=1000.

V.3 INFLUENCE OF N_Y ON 2D SQUARE NETWORKS (Z_{MAX}=4)

We have gathered in the figures below (Fig. Ap. VI-7 to Fig. Ap. VI-12) the mean and standard deviations from the textural and mass transport properties obtained for 2D Z_{max}=4 networks with P=0.98 according to N_y. As previously observed on the influence of N_x, herein the textural properties average remains globally constant with a decrease in

the standard deviation when N_y increases. Which we believe is merely due to the variability of Monte Carlo approaches. Since, for lower maximum network sizes the greater the results variability.

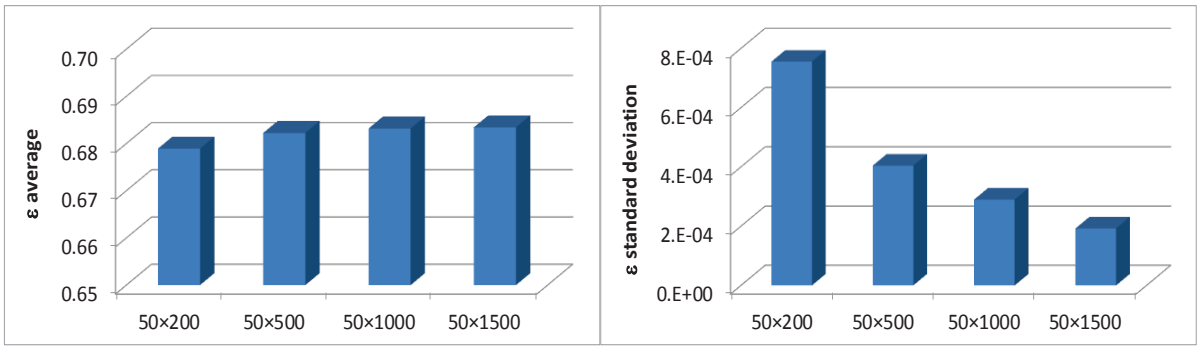


Fig. Ap. V-19. Catalyst porosity according to N_y with N_x=50. 2D networks, Z_{max}=4 and P=0.98.

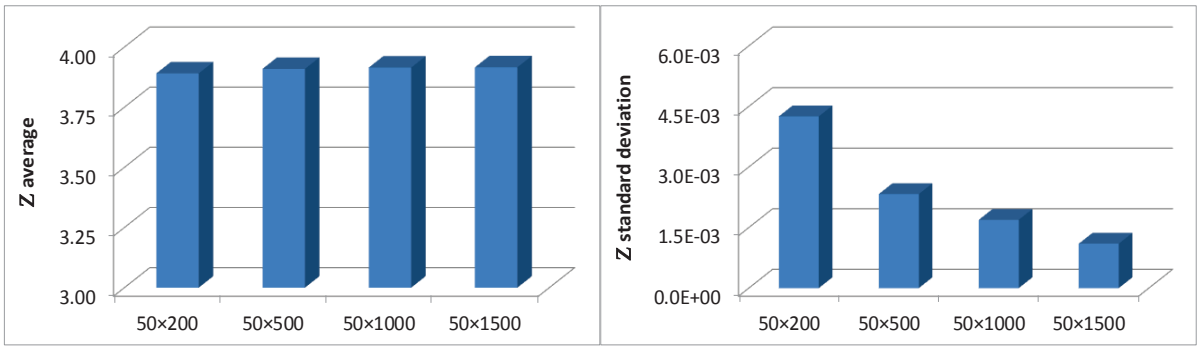


Fig. Ap. V-20. Connectivity according to N_y with N_x=50. 2D networks, Z_{max}=4 and P=0.98.

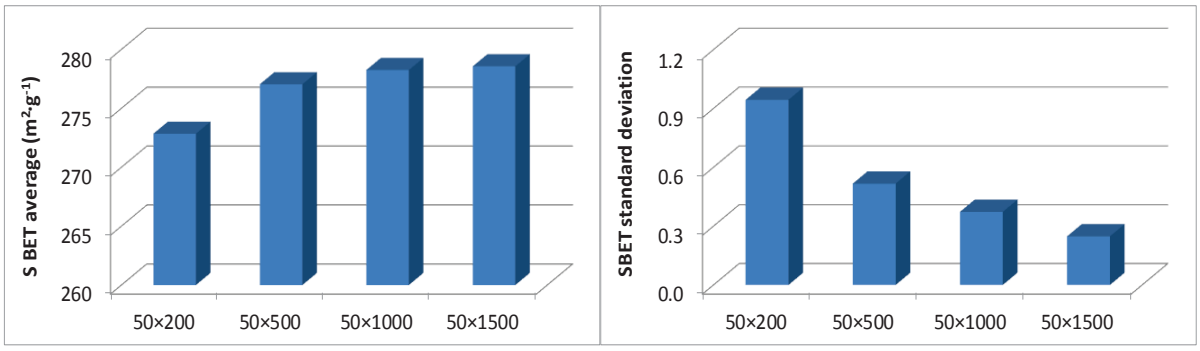


Fig. Ap. V-21. Specific surface area according to N_y with N_x=50. 2D networks, Z_{max}=4 and P=0.98.

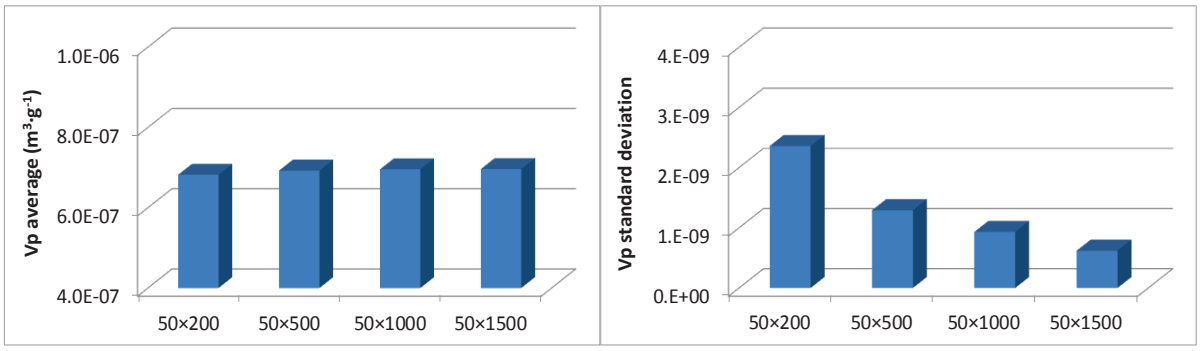


Fig. Ap. V-22. Pore volume according to N_y with N_x=50. 2D networks, Z_{max}=4 and P=0.98.

As for the averages of the tortuosity factor, they remain quite constant with values ranging from 1.018 to 1.032. On the other hand, the behaviour of the standard deviation of the mass transfer properties is quite different compared to that from the textural properties. It seems that, it keeps increasing with the augmentation of N_y. Yet, since the maximum network sizes of the different network sizes tested are different, any conclusions taken from these figures might be misleading. The reason why we have promoted the study on the influence of the parallelepiped dimensions taking networks with equal maximum number of nodes, as it is described in the next section.

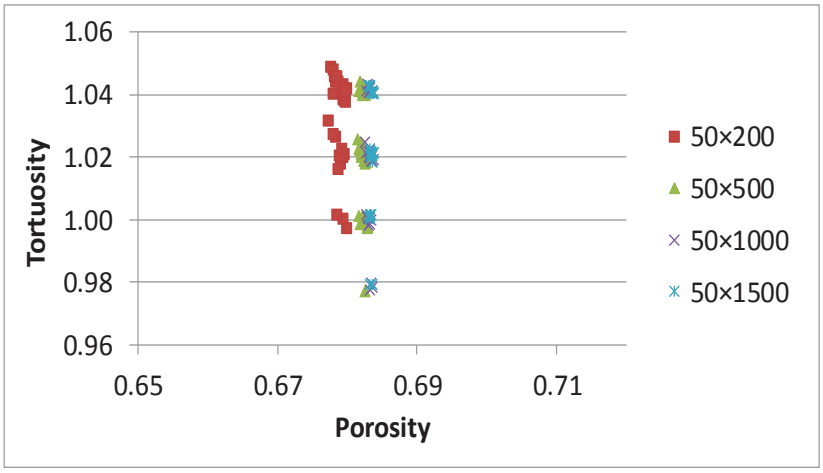


Fig. Ap. V-23. Tortuosity obtained per simulation as a function of the catalyst porosity for 6 different 2D Z_{max}=4 P=0.98 networks according to N_y with N_x=50.

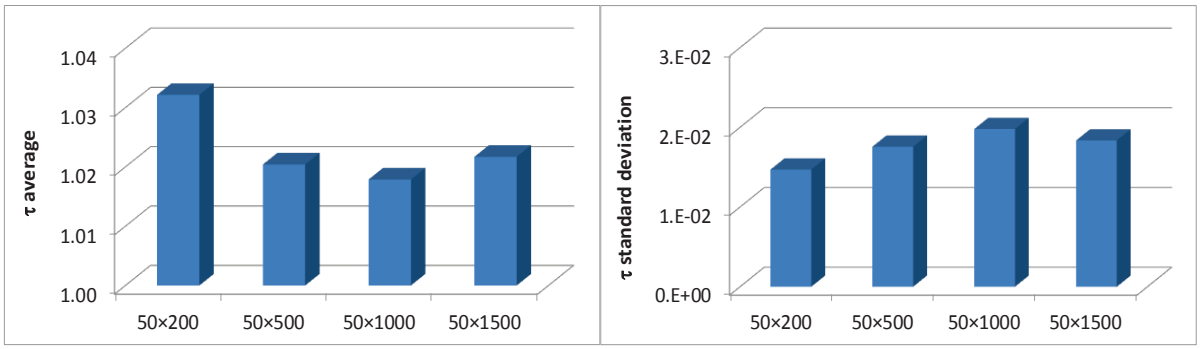


Fig. Ap. V-24. Tortuosity obtained for 4 different 2D Z_{max}=4 P=0.98 network sizes according to N_y with N_x=50.

V.4 INFLUENCE OF N_X/N_Y ON 2D SQUARE NETWORKS (Z_{MAX}=4)

The previous studies performed on the separate influence of N_x and N_y can be misleading due to the variability of Monte Carlo approaches. Therefore, we have extended the study to 2D networks with identical maximum network size. The mean and standard deviations obtained from the textural and mass transport properties are gathered in Fig. Ap. V-25 to Fig. Ap. V-30.

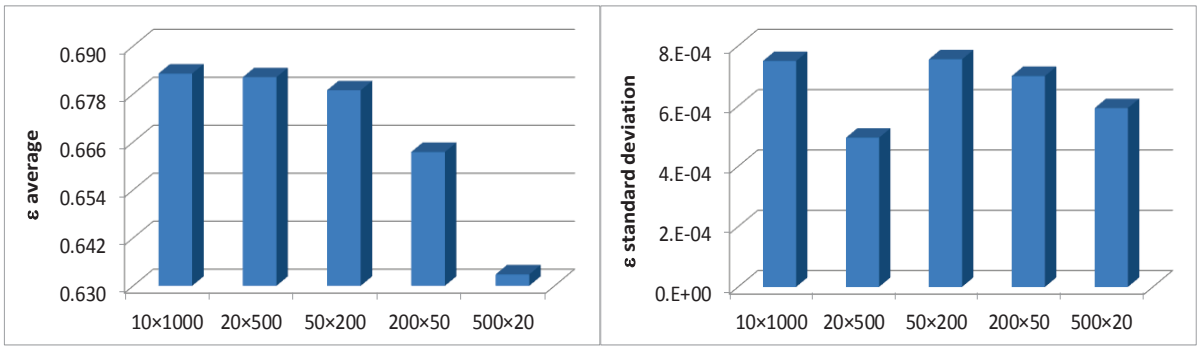


Fig. Ap. V-25. Porosity according to N_x/N_y. 2D networks, Z_{max} = 4, P = 0.98.

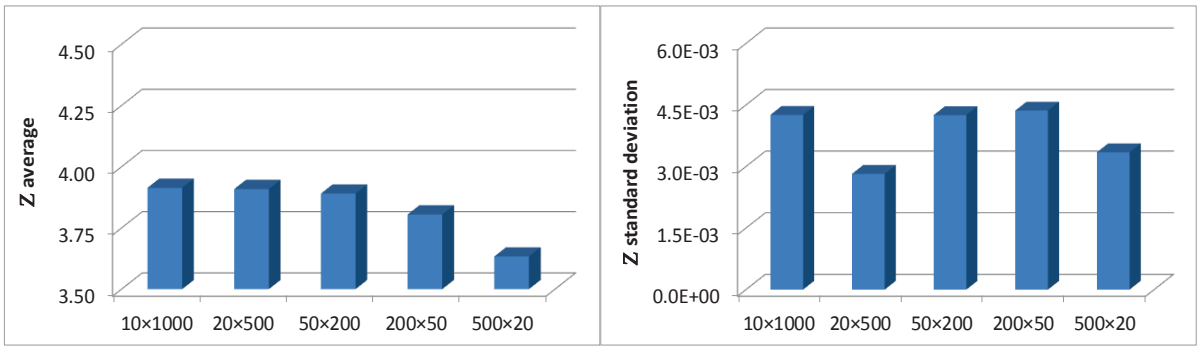


Fig. Ap. V-26. Connectivity according to N_x/N_y. 2D networks, Z_{max} = 4, P = 0.98.

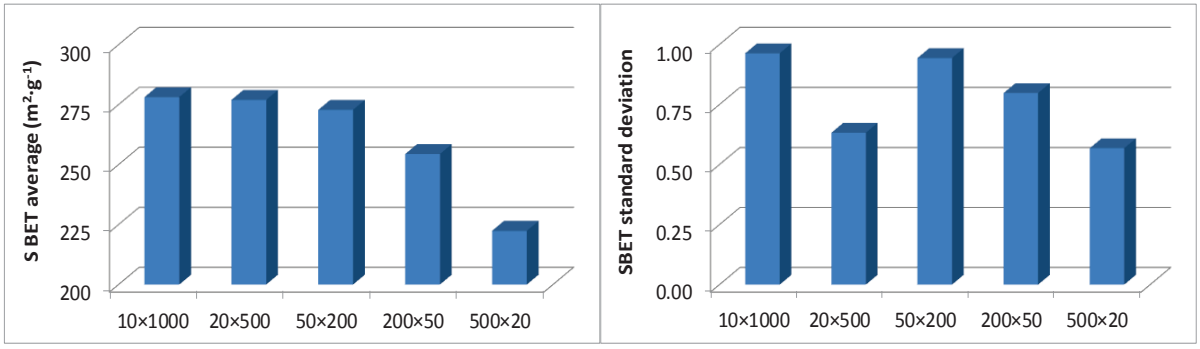


Fig. Ap. V-27. Specific surface area according to N_x/N_y. 2D networks, Z_{max} = 4, P = 0.98.

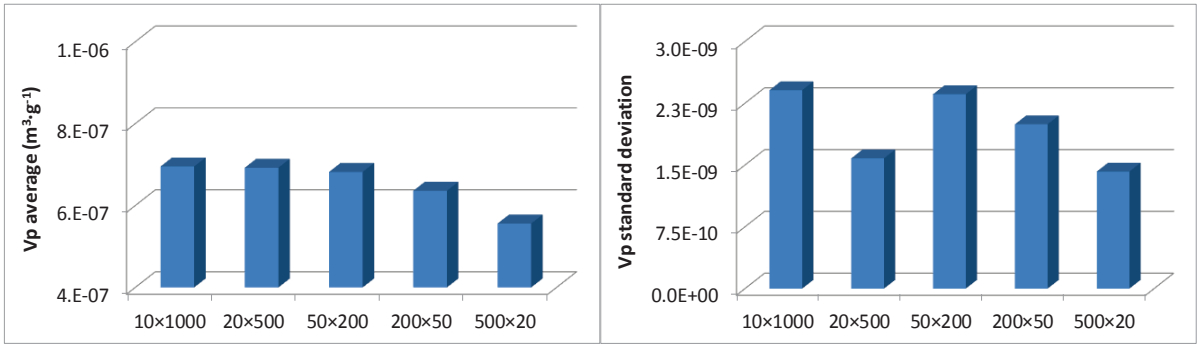


Fig. Ap. V-28. Pore volume according to N_x/N_y. 2D networks, Z_{max} = 4, P = 0.98.

From these figures, one may conclude that the mean textural properties slightly decrease with the augmentation of the ratio N_x/N_y. For the same reasons mentioned before on 2D Z_{max}=6 networks: the removal of the horizontal pores that gets more impact for greater

N_x. And, that the standard deviations from the textural properties take rather low and globally constant values.

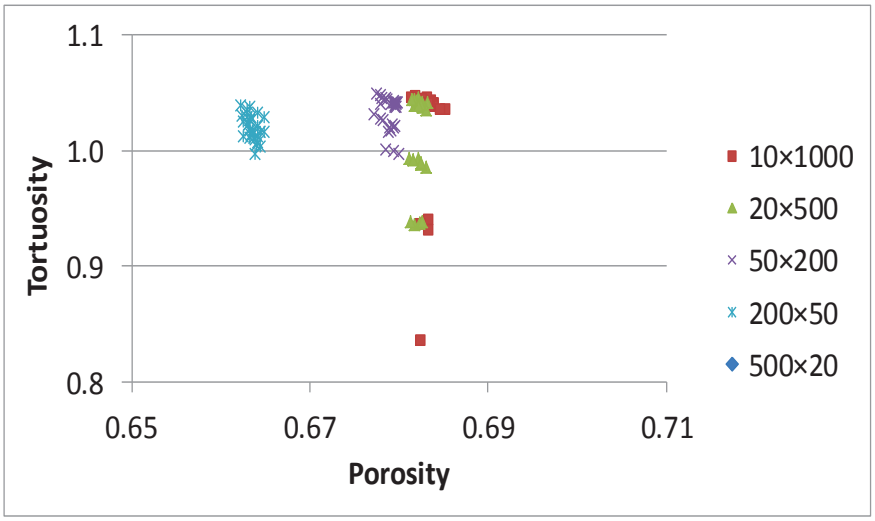


Fig. Ap. V-29. Predicted tortuosity from mass transfer simulations as a function of the catalyst porosity for 4 different 2D Z_{max}=4 P=0.98 networks according to N_x/N_y.

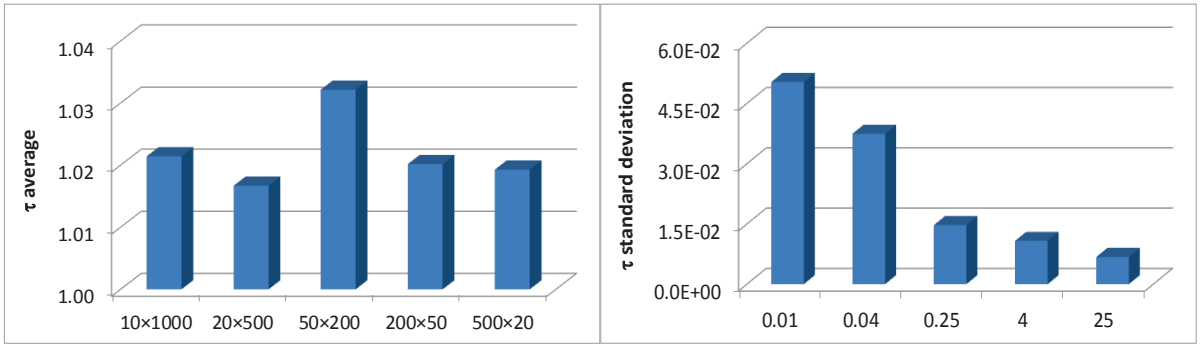


Fig. Ap. V-30. Predicted tortuosity for 5 different 2D Z_{max}=4 and P=0.98 networks according to N_x/N_y.

Concerning the tortuosity factor averages, it is observed a rather constant value from 1.017 to 1.032 with an average value from all tested network sizes of 1.022 and for an average porosity of 0.668. The standard deviations behave likewise to the 2D Z_{max}=6 network sizes with of course, a decrease in their values with the augmentation of N_x/N_y. The decrease in the standard deviation is related to the increase in N_x. If we take networks with N_x=500, the impact of extreme paths ($\tau = 1$ or τ very large) among the total amount of paths within a network is reduced. However, for a network with N_x=10, the diversity in terms of tortuous paths is reduced and so, the presence of an extreme path will have a large impact, increasing therefore the standard deviation. Moreover, if we increase the characteristic length of diffusion, that is if we increase N_y, the probability to find a given amount of bends along the y axis also increases and the dispersion of the results that is the standard deviation increases. In summary, the increase in N_x and the decrease in N_y tend to reduce the standard deviation of the tortuosity results. As explained before for the 2D Z_{max}=6 networks in section VI.3.1.

APPENDIX VI

This appendix contains extended data from section VI.3.2 regarding the variation of the textural and mass transport properties as a function of the number of generated pore networks, from 2 to 30 samples. 2D networks of size 100×100 with Z_{max}=6 were used. For 2D square networks (Z_{max}=4), the influence of the pore existence probability on the textural properties, as well as, on the tortuosity as a function of the catalyst porosity are presented.

VI.1 INFLUENCE OF THE PORE EXISTENCE PROBABILITY ON 2D TRIANGULAR NETWORKS

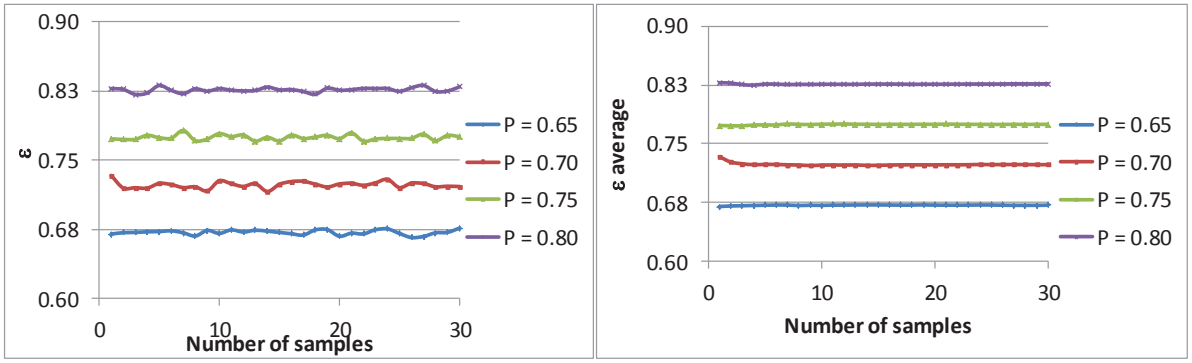


Fig. Ap. VI-1. Porosity per sample and cumulated average for different pore existence probabilities.

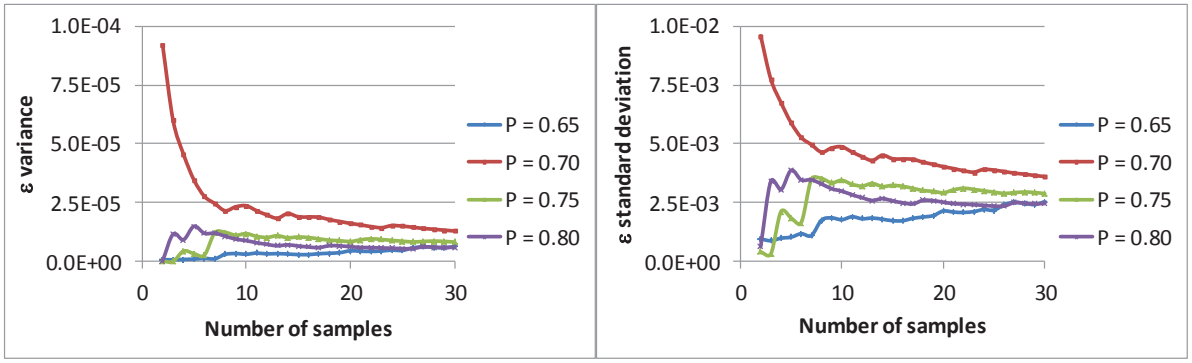


Fig. Ap. VI-2. Porosity variance and standard deviation from 2 to 30 samples of networks at different pore existence probabilities.

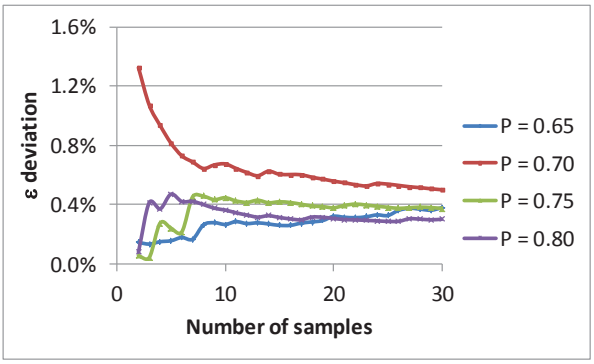


Fig. Ap. VI-3. Porosity deviation from 2 to 30 samples of networks at different pore existence probabilities.

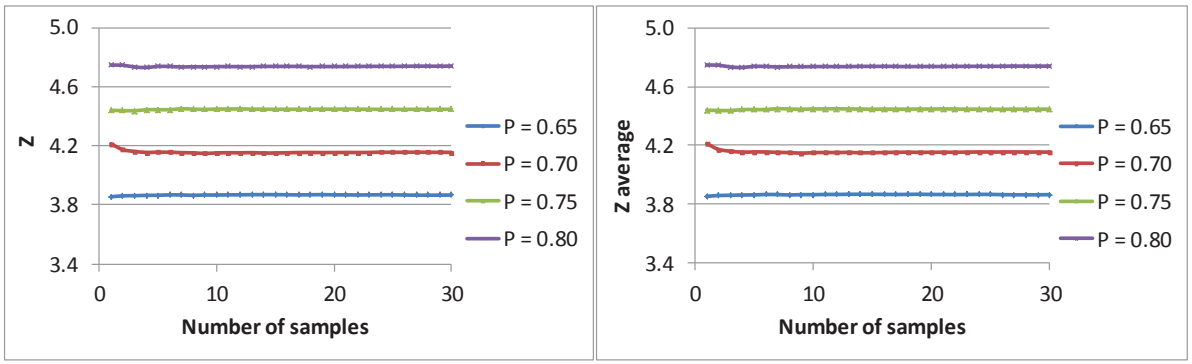


Fig. Ap. VI-4. Connectivity per sample and cumulated average for different pore existence probabilities.

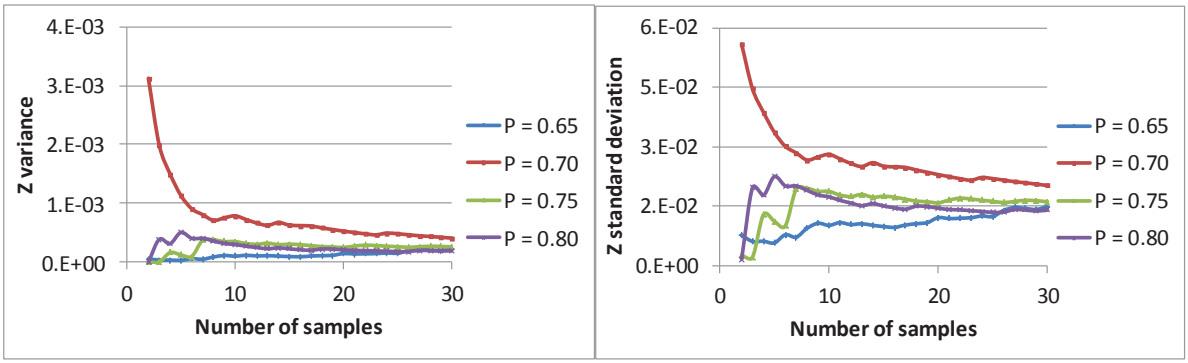


Fig. Ap. VI-5. Connectivity variance and standard deviation from 2 to 30 samples of networks at different pore existence probabilities.

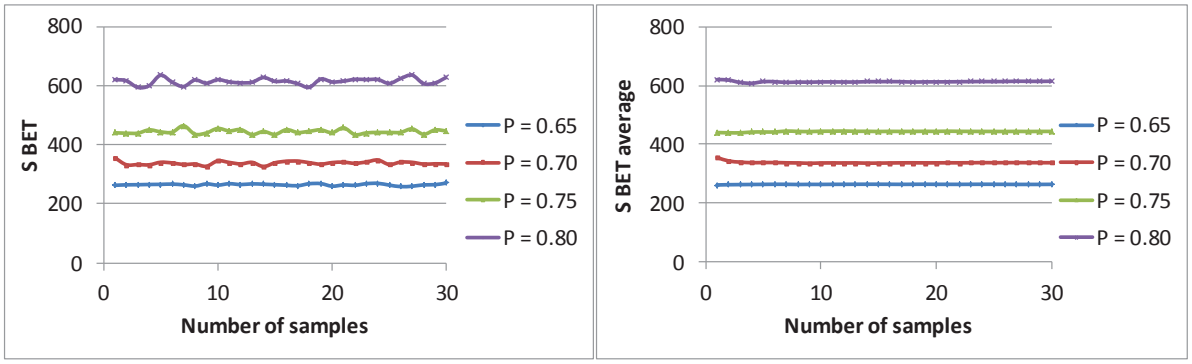


Fig. Ap. VI-6. Specific surface area per sample and cumulated average for different pore existence probabilities.

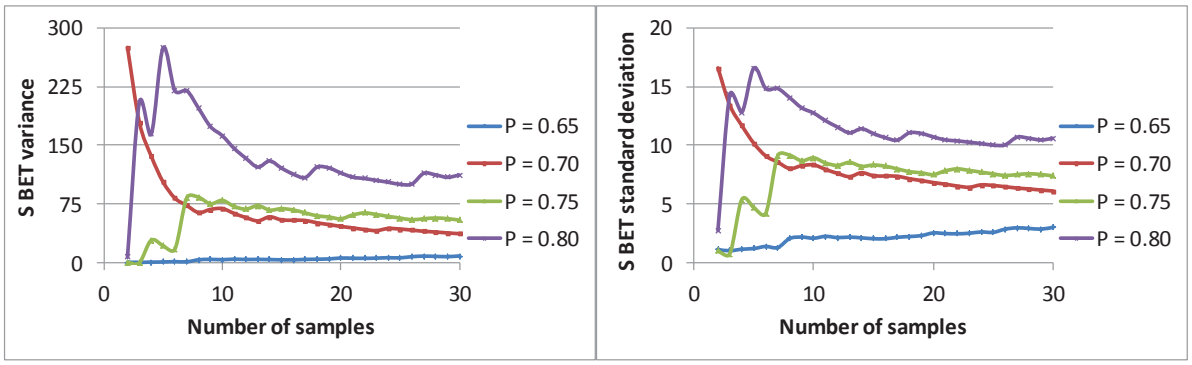


Fig. Ap. VI-7. Specific surface area variance and standard deviation from 2 to 30 samples of networks at different pore existence probabilities.

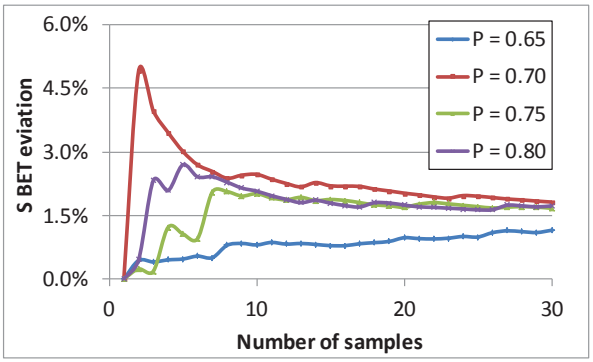


Fig. Ap. VI-8. Specific surface area deviation from 2 to 30 samples of networks at different pore existence probabilities.

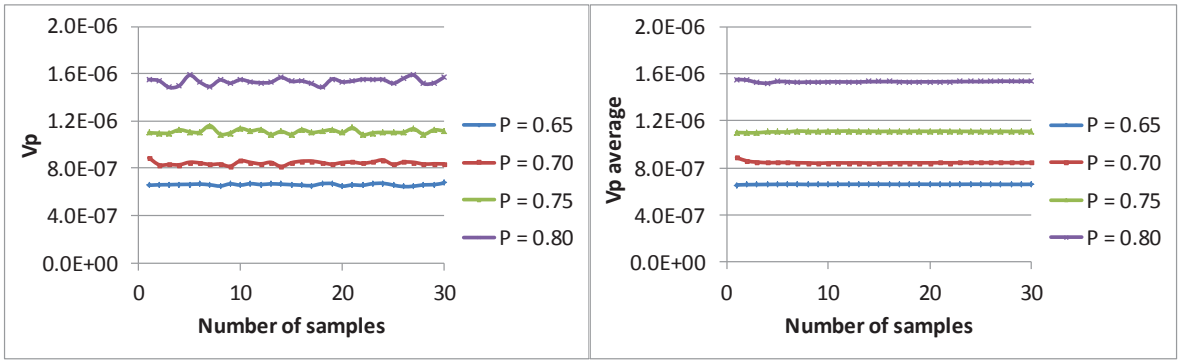


Fig. Ap. VI-9. Pore volume per sample and cumulated average for different pore existence probabilities.

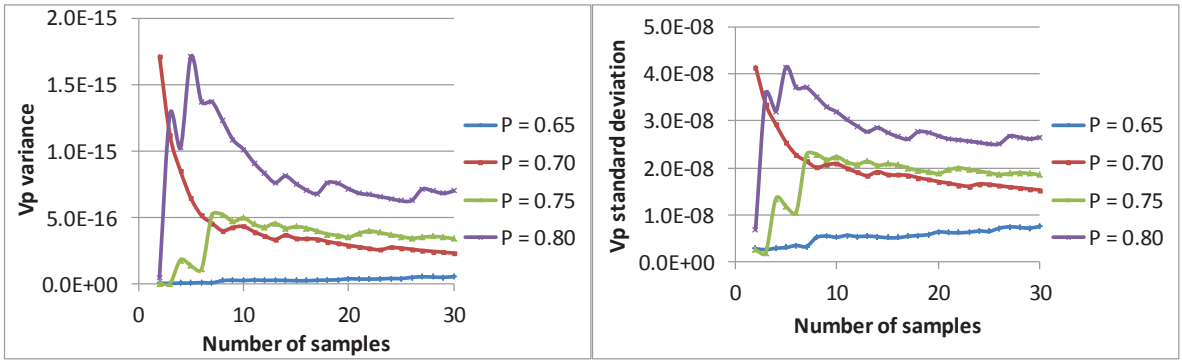


Fig. Ap. VI-10. Pore volume variance and standard deviation from 2 to 30 samples of networks at different pore existence probabilities.

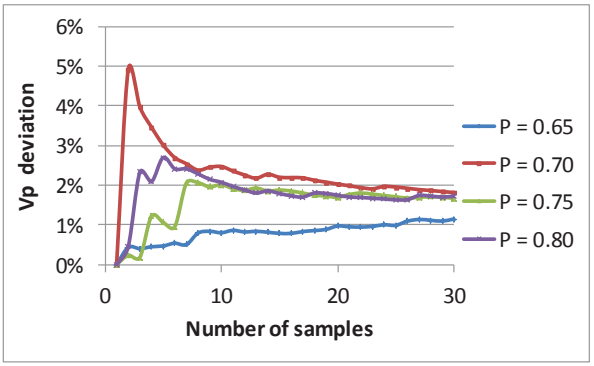


Fig. Ap. VI-11. Pore volume deviation from 2 to 30 samples of networks at different pore existence probabilities.

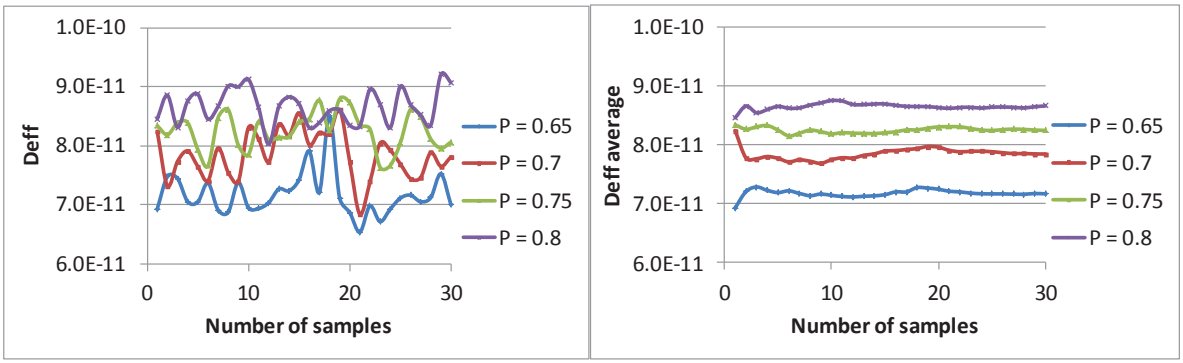


Fig. Ap. VI-12. Effective diffusion coefficient per sample and cumulated average for different pore existence probabilities.

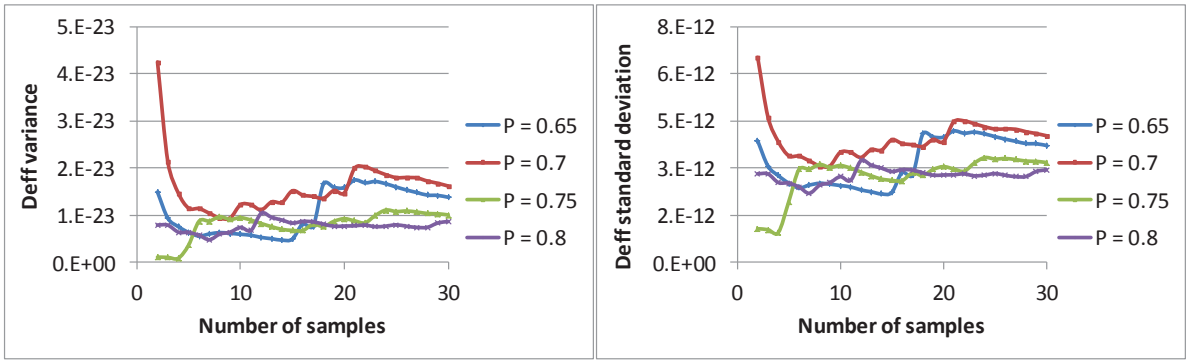


Fig. Ap. VI-13. Effective diffusion coefficient variance and standard deviation from 2 to 30 samples of networks at different pore existence probabilities.

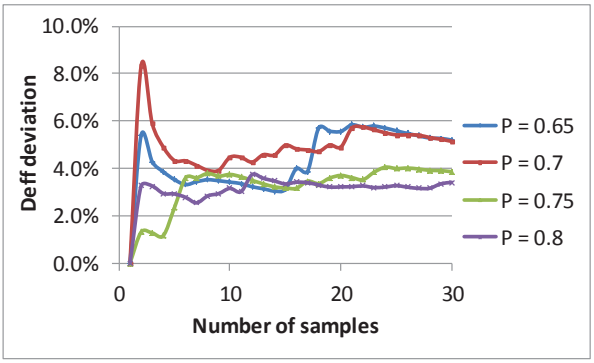


Fig. Ap. VI-14. Effective diffusion coefficient deviation from 2 to 30 samples of networks at different pore existence probabilities.

VI.2 INFLUENCE OF THE PORE EXISTENCE PROBABILITY ON 2D SQUARE NETWORKS

For 2D square pore networks (Z_{max}=4) of size 100×100 and 50×50, the following textural and mass transfer properties are obtained:

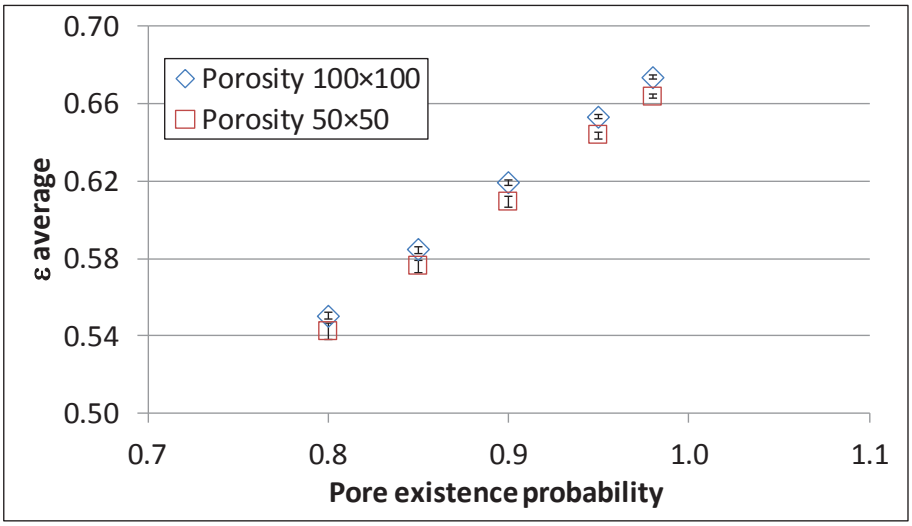


Fig. Ap. VI-15. Mean porosity according to the pore existence probability, *P*. 2D networks, Z_{max} = 4.

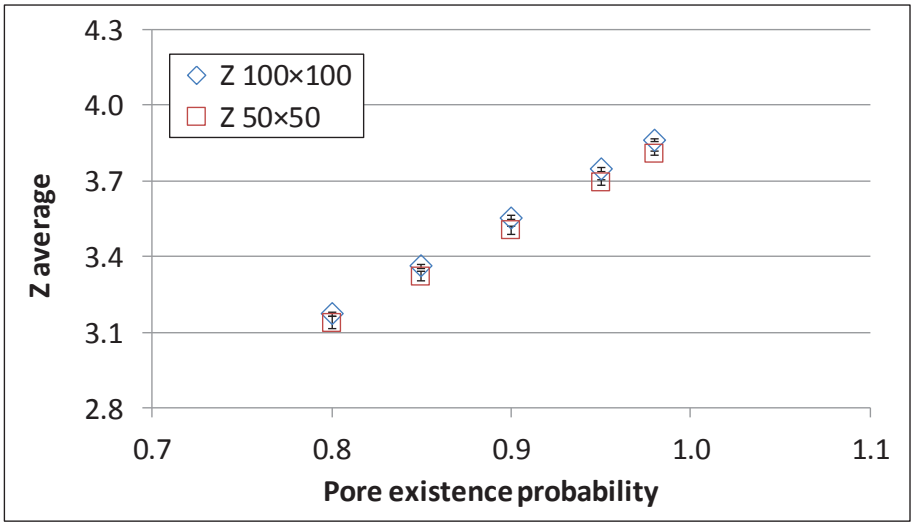


Fig. Ap. VI-16. Mean connectivity according to the pore existence probability, *P*. 2D networks, Z_{max} = 4.

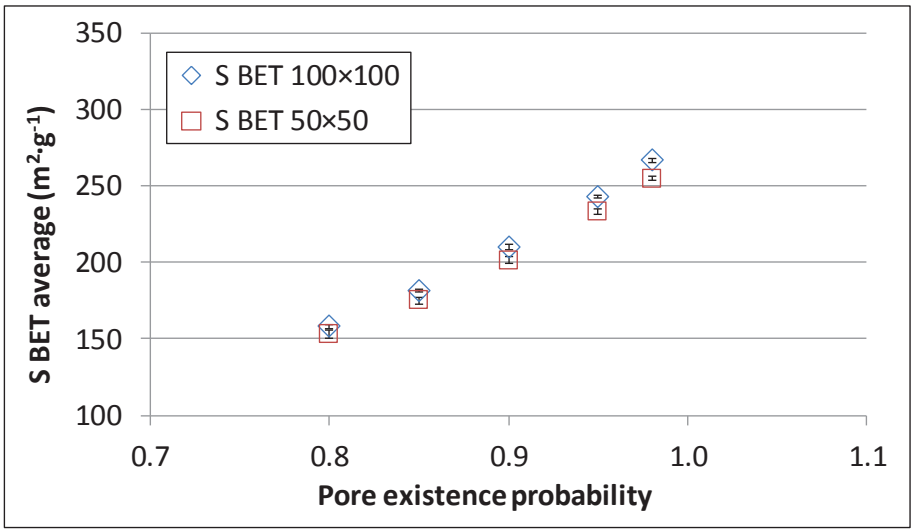


Fig. Ap. VI-17. Mean specific surface area according to the pore existence probability, *P*. 2D networks, Z_{max} = 4.

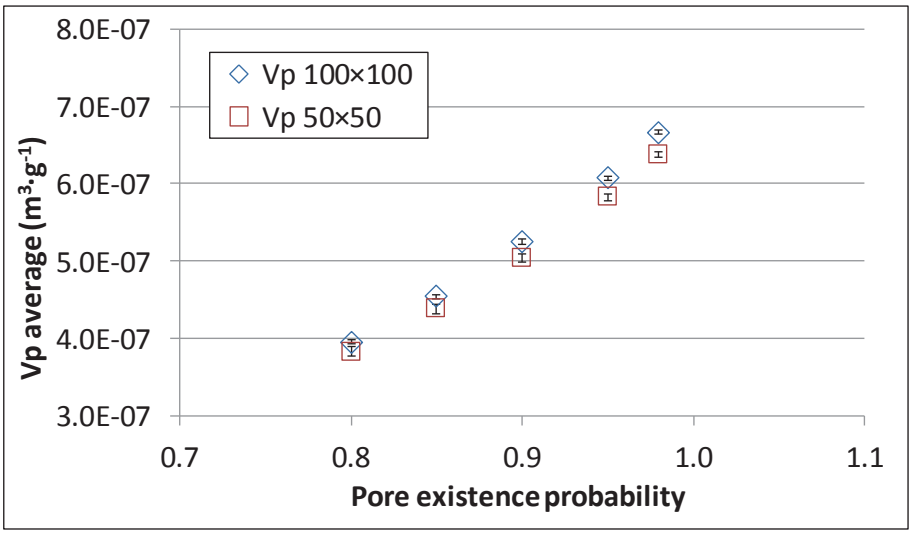


Fig. Ap. VI-18. Mean pore volume according to the pore existence probability, *P*. 2D networks, Z_{max} = 4.

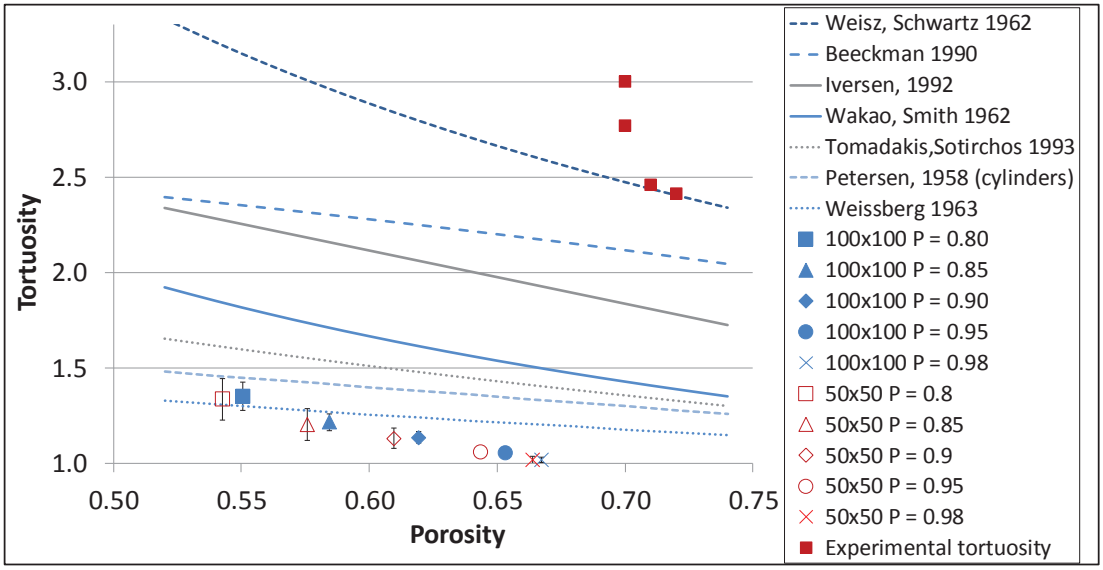


Fig. Ap. VI-19. Variation of the predicted tortuosities as a function of porosity for several pore existence probabilities and taking a 2D pore network with Z_{max}=4. Correlations taken from Akanni and Evans (1987), Beeckman (1990), and Shen and Chen (2007).

APPENDIX VII

Influence of the pore diameter on the textural and mass transfer properties for 2D pore networks of size 100×100 and 50×50 with Z_{max}=4 and P=0.97. Additional data from section VI.3.3.

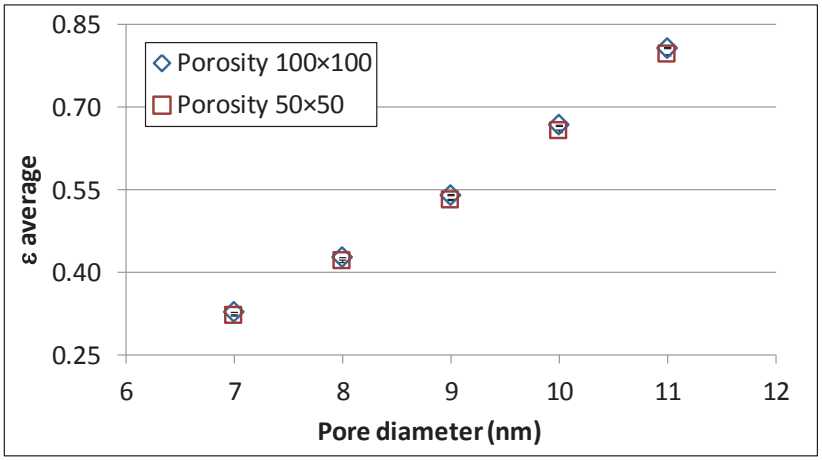


Fig. Ap. VII-1. Porosity according to the pore diameter. 2D networks with Z_{max}=4 and P=0.97.

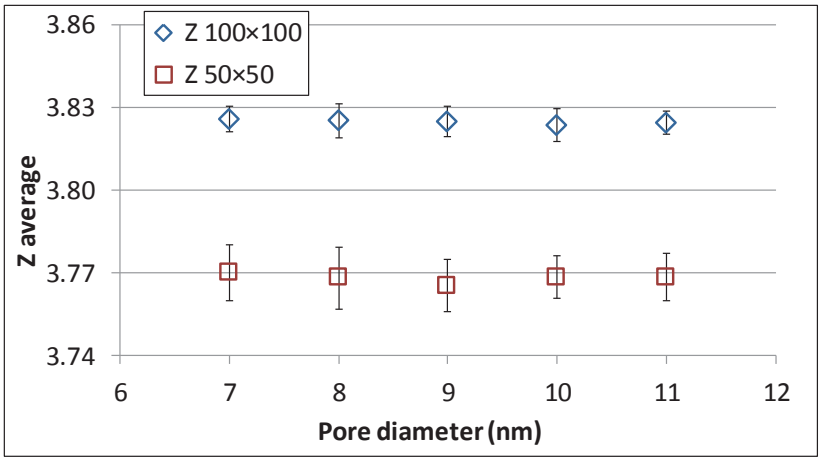


Fig. Ap. VII-2. Connectivity according to the pore diameter. 2D networks with Z_{max}=4 and P=0.97.

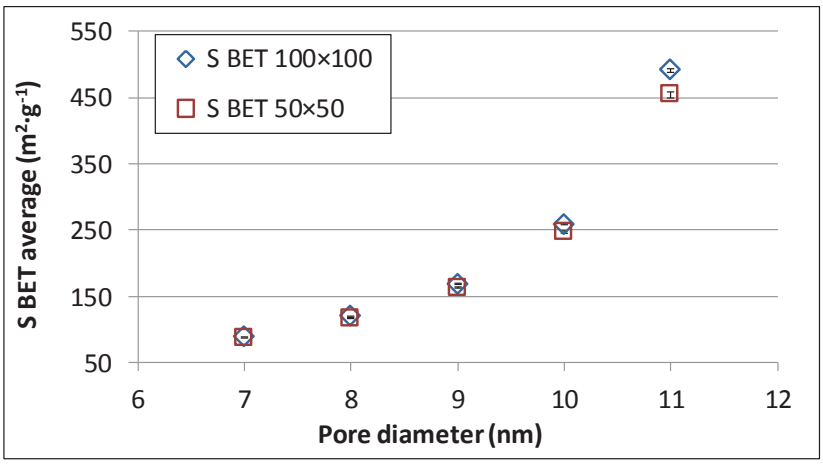


Fig. Ap. VII-3. Specific surface area according to the pore diameter. 2D networks with Z_{max}=4 and P=0.97.

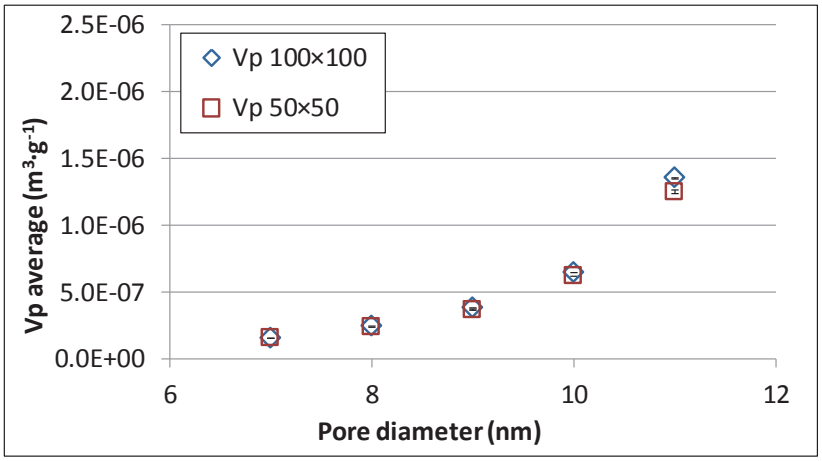


Fig. Ap. VII-4. Predicted pore volume according to the pore diameter. 2D networks with Z_{max}=4 and P=0.97.

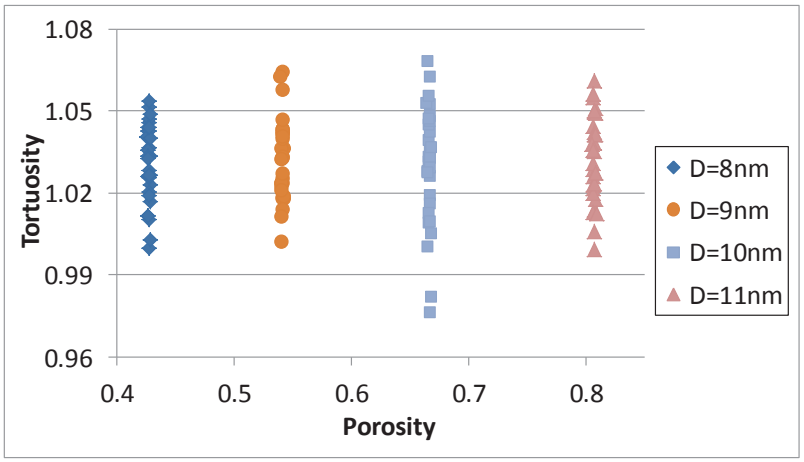


Fig. Ap. VII-5. Tortuosity per simulation as a function of porosity for several pore diameters. 2D pore network with Z_{max}=4 and P=0.97.

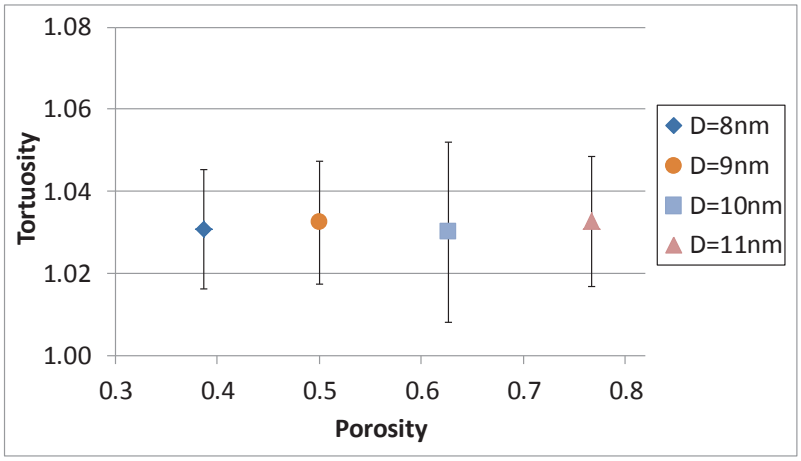


Fig. Ap. VII-6. Variation of the average predicted tortuosities as a function of porosity for several pore diameters. 2D pore networks Z_{max}=4 and P=0.97.

APPENDIX VIII

Influence of the pore length on the textural and mass transfer properties for 2D pore networks having a maximum connectivity of Z_{max}=4 and a pore existence probability of P=0.97.

A similar behaviour is found to that shown on section V.4.4, being the example present on this section referent to 2D triangular pore networks having Z_{max}=6. The porosity, the specific surface area and the pore volume decrease with the augmentation of the pore length.

Concerning the tortuosity factor (Fig. Ap. VII-5 and Fig. Ap. VII-6), we could say that a slight increase with the pore length is observed. Nevertheless, one has to keep in mind that the error bars follow this increase.

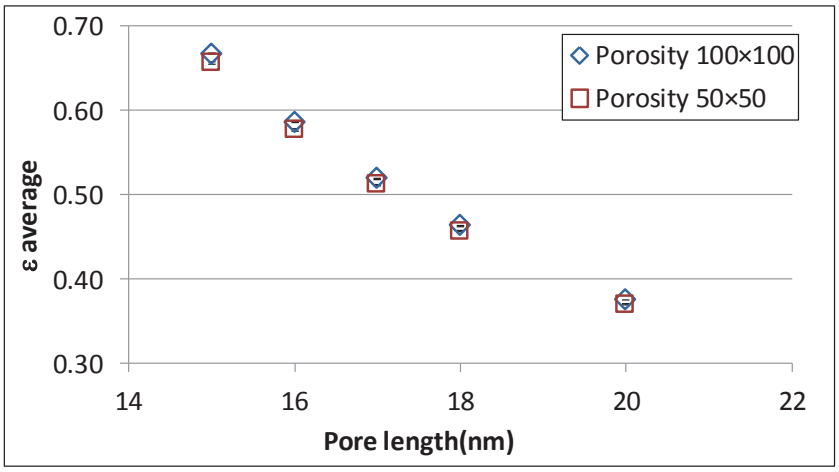


Fig. Ap. VIII-1. Porosity according to the pore length. 2D networks with Z_{max}=4 and P=0.97.

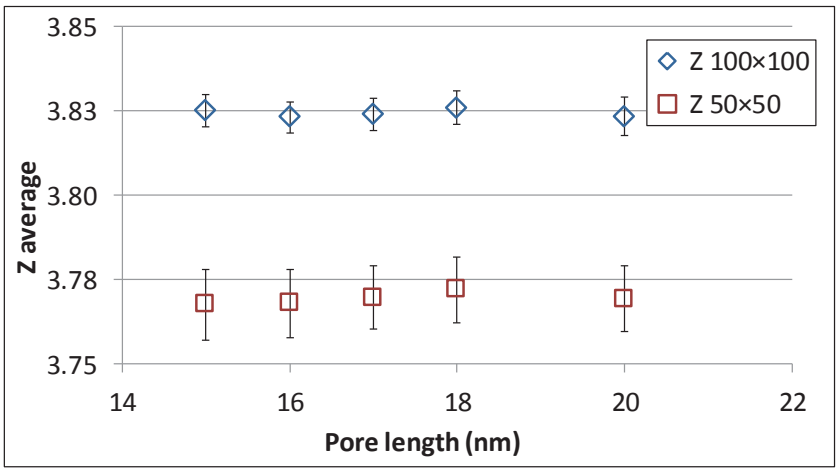


Fig. Ap. VIII-2. Connectivity according to the pore length. 2D networks with Z_{max}=4 and P=0.97.

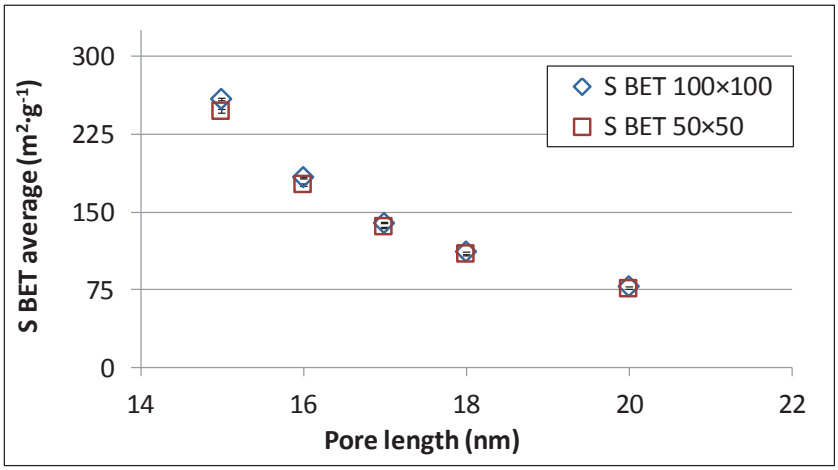


Fig. Ap. VIII-3. Specific surface area according to the pore length. 2D networks with Z_{max}=4 and P=0.97.

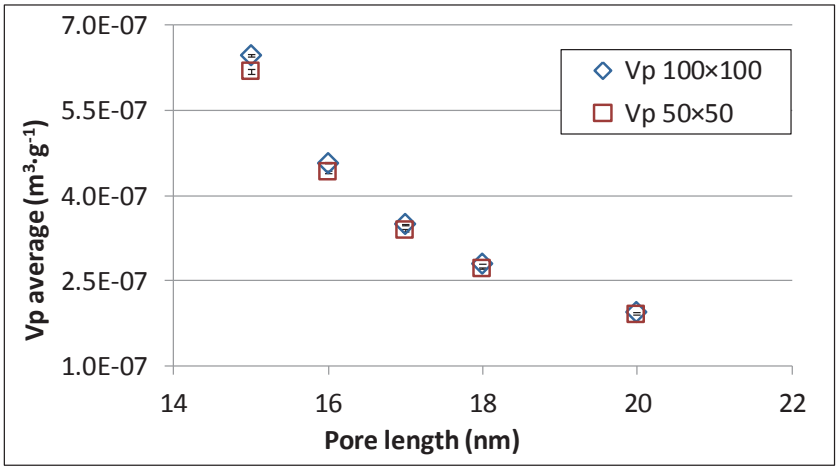


Fig. Ap. VIII-4. Pore volume according to the pore length. 2D networks with Z_{max}=4 and P=0.97.

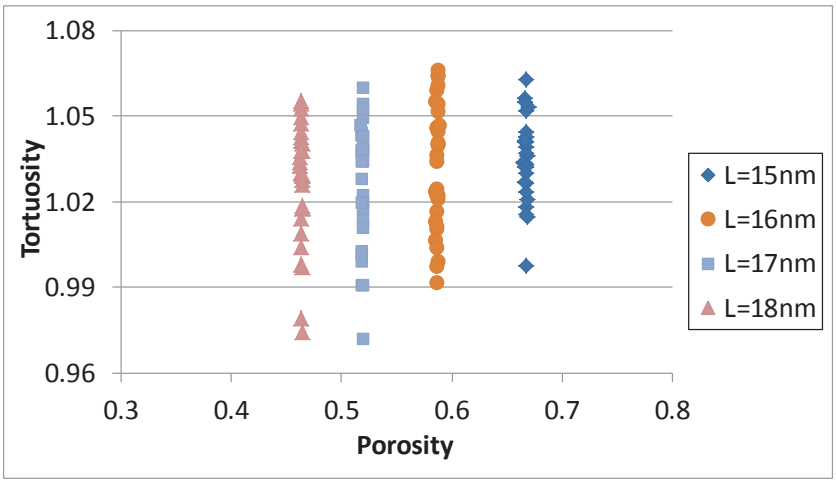


Fig. Ap. VIII-5. Tortuosity per simulation as a function of porosity for several pore lengths. 2D pore networks with Z_{max}=4 and P=0.97.

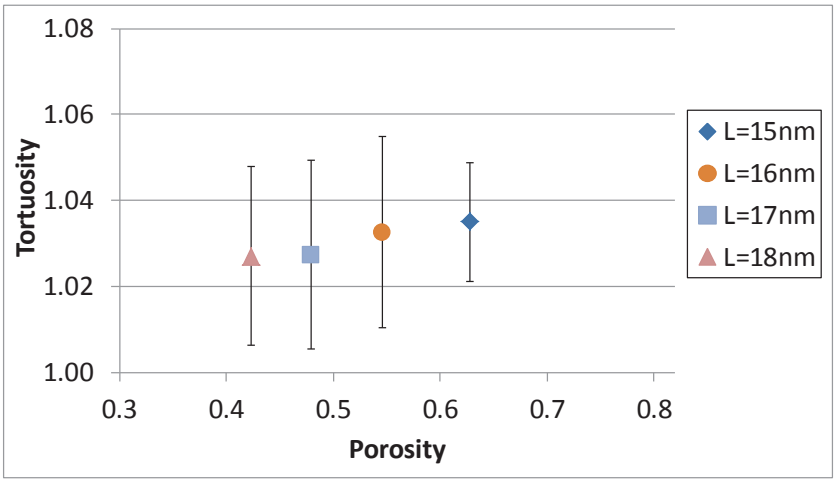


Fig. Ap. VIII-6. Variation of the average predicted tortuosities as a function of porosity for several pore lengths. 2D pore networks with Z_{max}=4 and P=0.97.

APPENDIX IX

Study related to the dynamic response of the mass transfer model. At first, the dynamic response from the discrete model on the effect of the initial conditions is evaluated. Then, the effect of the dead volume on the purge process is discussed similarly to the presented filling process on section 0.

The extra case studies presented in this appendix refer to the simple case studies of pore networks without and with a dead volume (see sections VII.2 and VII.2.2).

IX.1 DYNAMIC EFFECTS FOR THE DISCRETE MODEL

IX.1.1 THE EFFECT OF THE INITIAL CONDITIONS

At $t > 0$, the networks are either going to be filled with species *A* and therefore, the initial condition is: $c_A(l, t = 0) = 0$ or, the networks may be purged and so, $c_A(l, t = 0) = 1$. The usual boundary conditions have been kept: at the inlet and outlet nodes we have respectively, 1 and $0\ mol \cdot m^{-3}$ for the concentration of species *A*.

Looking at the dynamic responses of CS 1 testing the filling and the purge process (cf. Fig. Ap. IX-1), we can see that the inlet and the outlet flux are reversed that is the expected behaviour since we are in the presence of a linear model.

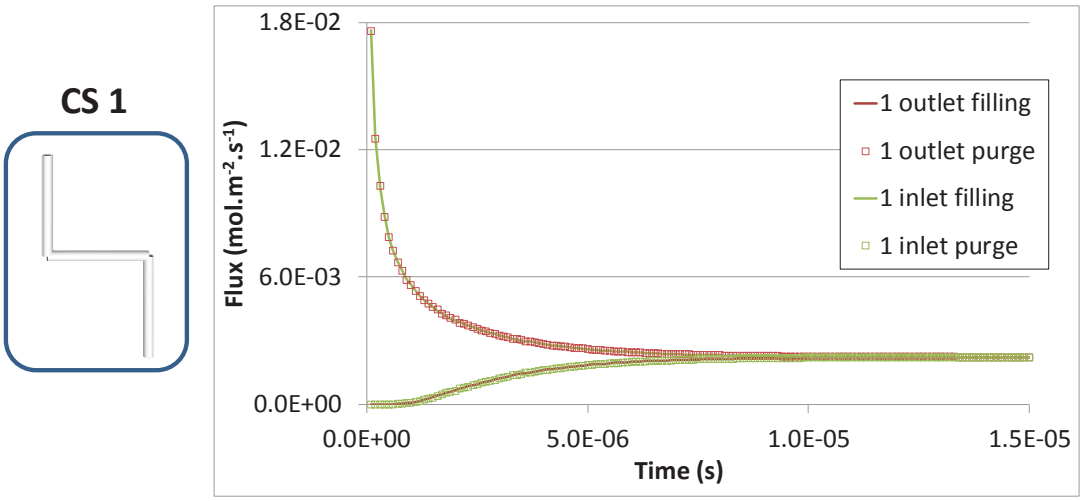


Fig. Ap. IX-1. Dynamic response for CS 1 during the filling and the purge.

After adding a dead volume to CS 1, we have obtained CS 11 and 11b that differ only on where the dead volume is placed as shown in Fig. Ap. IX-2 and Fig. Ap. IX-3. Again, the inlet and outlet flux are inversed for the filling and purge. Yet, for CS 11 the outlet flux from the purge is delayed compared to the inlet flux of the filling process and for CS 11b the inlet flux from the filling process is delayed compared to the outlet of the purge.

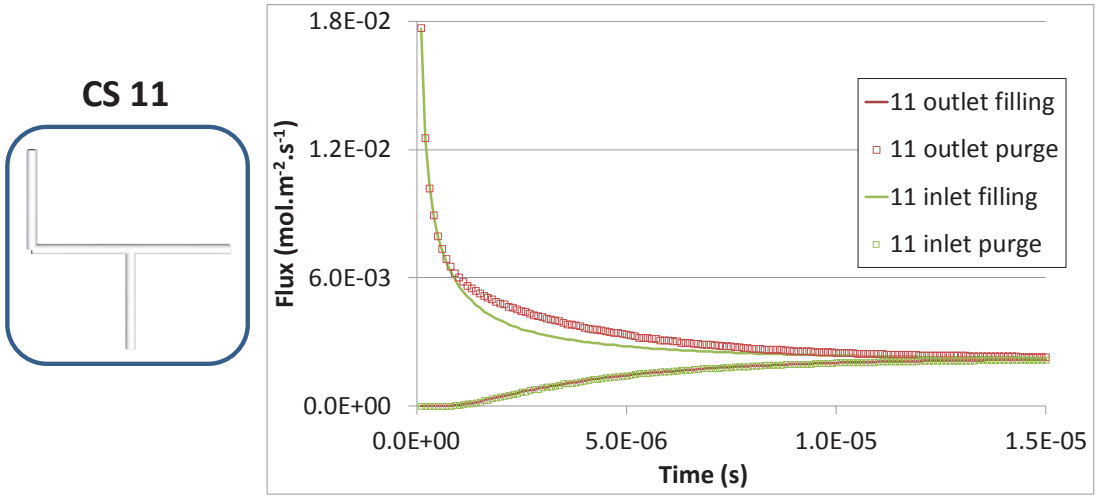


Fig. Ap. IX-2. Dynamic response for CS 11 during the filling and the purge.

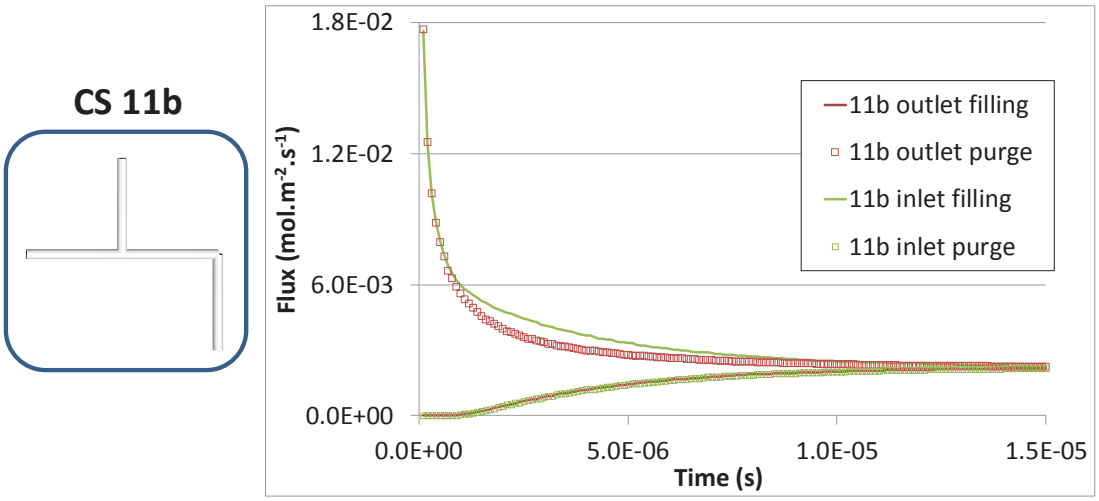


Fig. Ap. IX-3. Dynamic response for CS 11b during the filling and the purge.

The delay observed in the dynamic responses from CS 11 and CS 11b can be explained by the number of moles that must be purged or filled out of the two types of volume, percolating and capacitive. We know that the percolating volume contains the same amount of molecules that must be purged or filled so, we must take special interest on the dead volume. Which plays an important role in the capacitive volume. So, for CS 11, at the steady state, the concentration of the dead volume is uniform and we observe that it is equal to $c_A = 0.33\, mol \cdot m^{-3}$. Taking the filling process with $c_A(l, t = 0) = 0\, mol \cdot m^{-3}$, we know that in the end, we must fill $n_A(mol) = 0.33 \cdot V_{DV}$. While during the purge, where $c_A(l, t = 0) = 1\, mol \cdot m^{-3}$ we must purge $n_A(mol) = (1 - 0.33) \cdot V_{DV}$. Which is greater than the number of moles used during the filling process explaining therefore the delay observed in Fig. Ap. IX-2.

A similar behaviour is found for CS 11b (Fig. Ap. IX-3), during steady state the concentration of the dead volume is $c_A = 0.67\, mol \cdot m^{-3}$. Therefore, during the filling process, we must fill the dead volume with $n_A(mol) = 0.67 \cdot V_{DV}$ and during the purge we

must remove $n_A(mol) = (1 - 0.67) \cdot V_{DV}$. The purge clearly has a lower number of moles to purge than the filling process has to fill hence, the latter is delayed.

IX.1.2 THE EFFECT OF THE DEAD VOLUME

The effect of the dead volume during a purge is observed taking the dynamic inlet and outlet flux and for CS 1, 11 and 11b (see Fig. Ap. IX-4). Equal steady states are found as the percolating volume is identical.

Comparing the filling process presented on (Fig. VII-2), we can see that the inlet and outlet flux from the purge were inversed. Similarly to what happened in the filling process, where the outlet flux from CS 11 and 11b are identical, herein the inlet flux are as well identical. The perturbation implicating the dead volume is therefore observed on the outlet flux. For the same reasons previously explained in section IX.1.1, dealing with the initial conditions effect, the sequence of delay in the dynamic inlet flux must be: CS 1, 11b and 11. Since a greater amount of moles needs to be purged in CS 11.

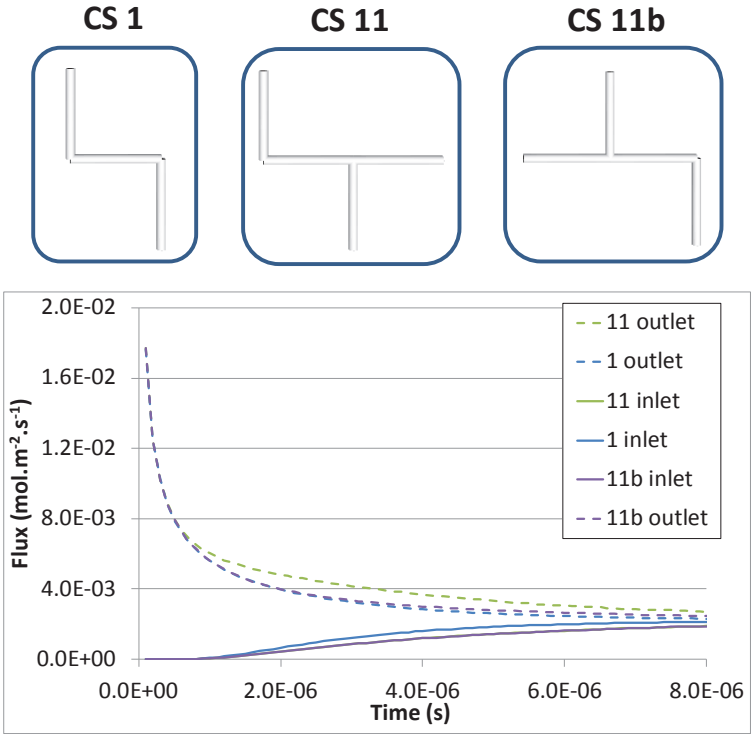


Fig. Ap. IX-4. Dynamic response of CS 1, 11 and 11b, observation of the dead volume effect during a purge.

IX.2 SIMPLE CASE STUDIES COMPARING THE DYNAMIC RESPONSES OF THE DISCRETE AND CONTINUUM MODELS

Fig. Ap. IX-5 that contains the response from CS 3 and 4 shows an identical behaviour as observed for CS 1 and 2. Indeed, we reach the same steady state for both the discrete and the pseudo-homogeneous approaches, whereas the two steady states of CS 3 and 4

differ, due to the difference on the percolating volume. The flux for case study 3 and 4 are respectively: $F_{CS3} = 1.33 \times 10^{-3}$ and $F_{CS4} = 9.52 \times 10^{-4}\, mol \cdot m^{-2} \cdot s^{-1}$, with the following effective diffusion coefficients: $D_{eff\ CS\ 3} = 6.00 \times 10^{-11}$ and $D_{eff\ CS\ 4} = 4.28 \times 10^{-11}\, m^2 \cdot s^{-1}$ and the diffusion tortuosities of $\tau_3 = 1.67$ and $\tau_4 = 2.33$, which are identical to the geometric tortuosities.

Concerning the dynamic response of the pseudo-homogeneous approach available on Fig. Ap. IX-5, it is well described when using the right correction factor applied to the accumulation term. Case studies 3 and 4 use the following correction factors 5/3=1.67 and 7/3=2.33, respectively. These corrections manage to take into account the adequate capacitive volume. Otherwise, a time lapse is observed between the dynamic responses of the discrete and continuum models.

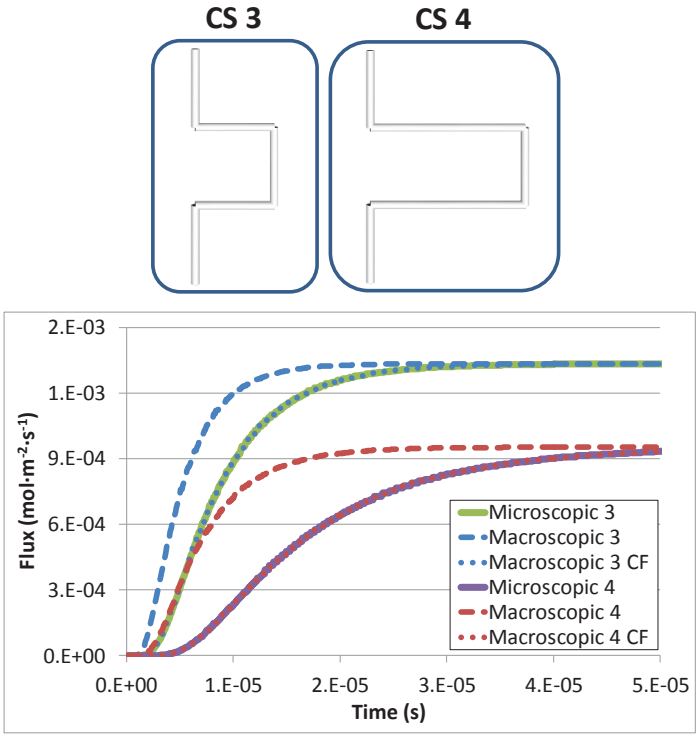


Fig. Ap. IX-5. Comparison of the predicted outlet flux in transient regime by discrete (microscopic) and continuum (macroscopic) models for case studies 3 and 4.

We have contibued our study by case study 5 and 6 presented in Fig. Ap. IX-6 that shows a similar behaviour as observed for CS 1 and 2 (Fig. VII-5). Indeed, we reach the same steady state for both the discrete and the continuum approach, whereas the steady states from CS 5 and 6 differ. The flux for case study 5 and 6 are respectively: $F_{CS5} = 8.33 \times 10^{-4}$ and $F_{CS6} = 6.66 \times 10^{-4}\, mol \cdot m^{-2} \cdot s^{-1}$, with the following effective diffusion coefficients: $D_{eff\ CS\ 5} = 5.00 \times 10^{-11}$ and $D_{eff\ CS\ 6} = 4.00 \times 10^{-11}\, m^2 \cdot s^{-1}$. The steady states differ from the two case studies due to the difference on the percolating volume, as mentioned in the comparison of CS 1 to CS2. Regarding the predicted diffusional tortuosities, we have for case study 5 and 6 respectively, $\tau_5 = 2.0$ and $\tau_6 = 2.5$. These

tortuosities are identical to the geometric tortuosities and to the correction factors. This is also true for every case study from 1 to 10.

Concerning the dynamic response of the continuum model available on Fig. Ap. IX-6, it can be seen that a correction on the accumulation term is required in order to establish identical transient regimes. Otherwise, a time delay is observed between the dynamic responses of the discrete and continuum model. The correction factors taken for case study 5 and 6 are respectively, *CF*=8/4=2.0 and *CF*=10/4=2.5.

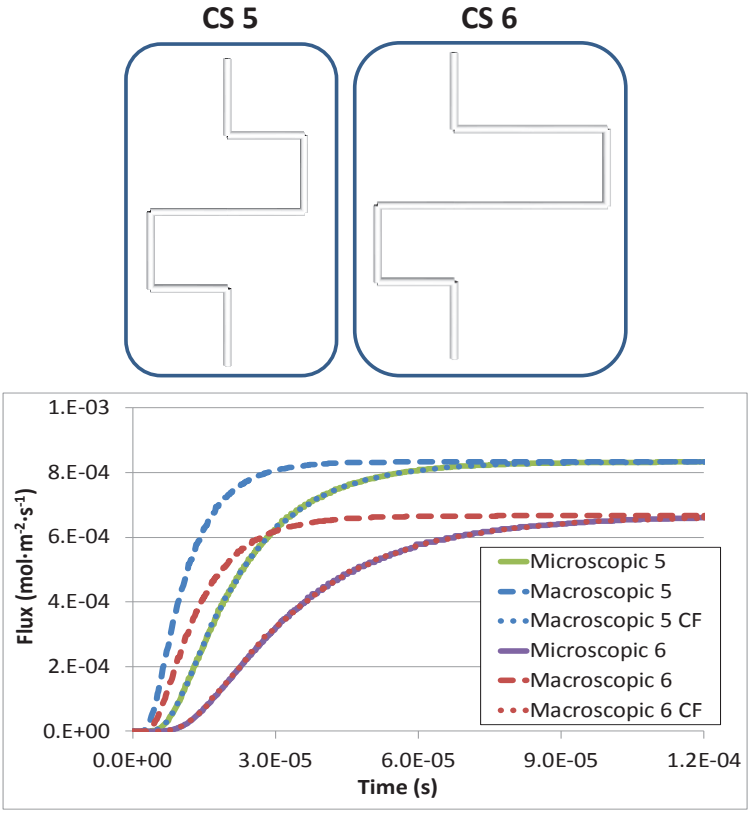


Fig. Ap. IX-6. Comparison of the predicted outlet flux in transient regime by discrete (microscopic) and continuum (macroscopic) models for case studies 5 and 6.

Regarding case studies 7 and 8, illustrated on Fig. Ap. IX-7, we found once again an equal steady state flux for both approaches yet different between CS 7 and 8: $F_{CS7} = 1.11 \times 10^{-3}$ and $F_{CS8} = 8.33 \times 10^{-4}\, mol \cdot m^{-2} \cdot s^{-1}$. With the following effective diffusion coefficients: $D_{eff\,CS\,7} = 6.67 \times 10^{-11}$ and $D_{eff\,CS\,8} = 5.00 \times 10^{-11}\, m^2 \cdot s^{-1}$ and $\tau_7 = 1.5$ and $\tau_8 = 2.0$.

Concerning the transient response, the corrected continuum model is able to correctly describe the response of the discrete model. A correction factor of 1.5 and 2.0 is used respectively for CS 7 and 8.

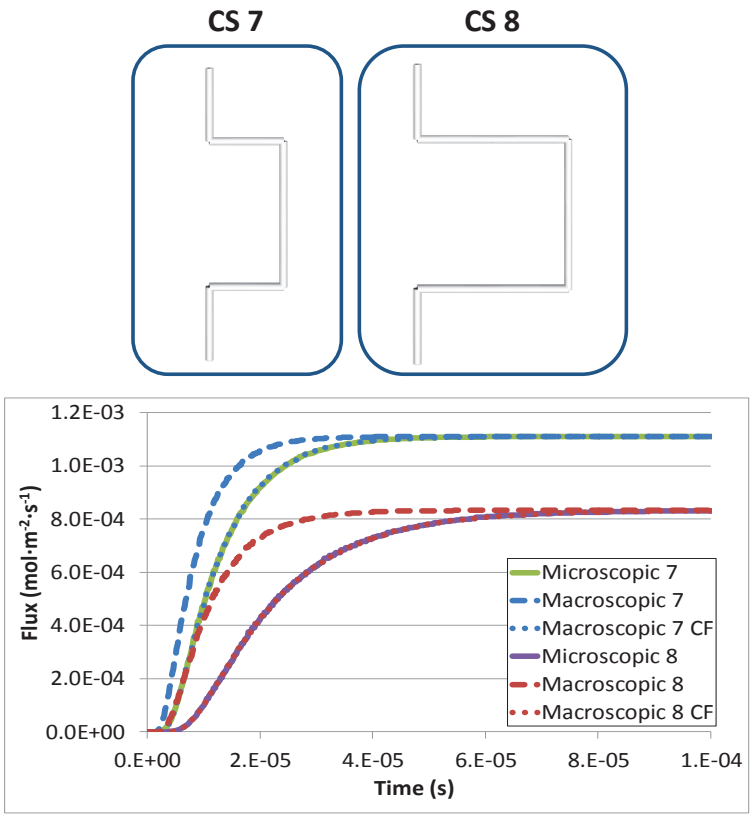


Fig. Ap. IX-7. Comparison of the predicted outlet flux in transient regime by discrete (microscopic) and continuum (macroscopic) models for case studies 7 and 8.

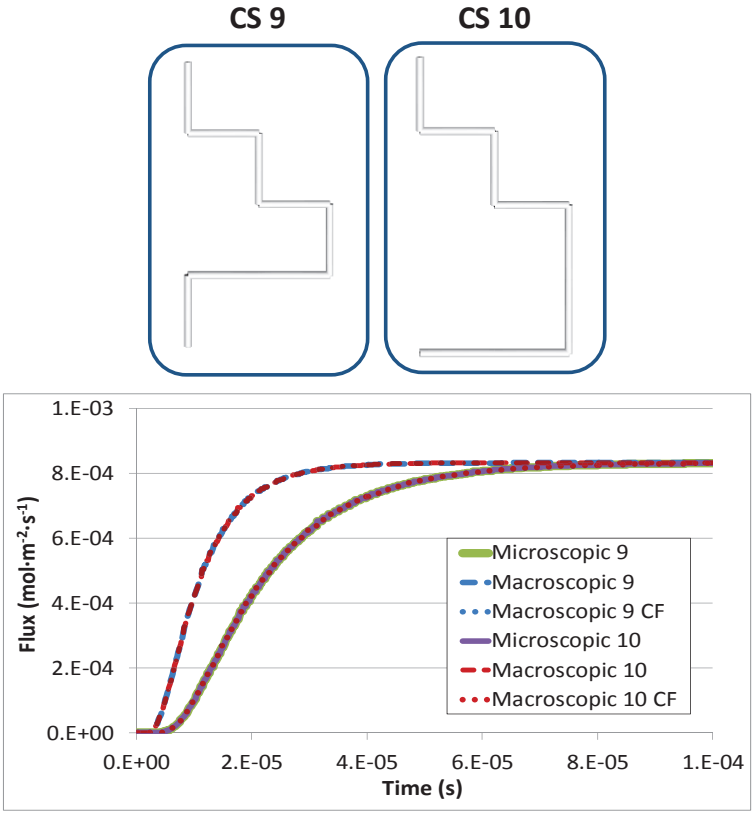


Fig. Ap. IX-8. Comparison of the predicted outlet flux in transient regime by discrete (microscopic) and continuum (macroscopic) models for case studies 9 and 10.

Finally, the information related to case studies 9 and 10 is gathered on Fig. Ap. IX-8. We have obtained equal steady state flux and effective diffusion coefficients: $F_{CS\,9/10} = 8.33 \times 10^{-4}$ and $D_{eff\,CS\,9/10} = 5.0 \times 10^{-11}\, m^2 \cdot s^{-1}$. An expected result since the percolating volumes are equal for both case studies. With the diffusional and geometric tortuosities also identical and predicted at a value of $\tau_{geom_{9/10}} = 2.0$, as expected as well.

Case studies 9 and 10 also have an identical transient response. A predictable result due, respectively, to the identical percolating and capacitive volumes. A correction factor of 2.0 is used for both pore networks in order to shift the dynamic response of the pseudo-homogeneous model to the right-hand side.

IX.3 SIMPLE CASE STUDIES WITH DEAD VOLUMES COMPARING THE DYNAMIC RESPONSES OF THE DISCRETE AND CONTINUUM MODELS

The following case studies are related to case studies 11 to 20 that result from CS 1 to 10 by adding a dead volume.

The simulated data comparing case study 2 with case study 12 is graphically represented onFig. Ap. IX-9. Case study 2 and 12 reproduce the same behaviour observed when comparing case study 1 and 11 from section VII.2.2.

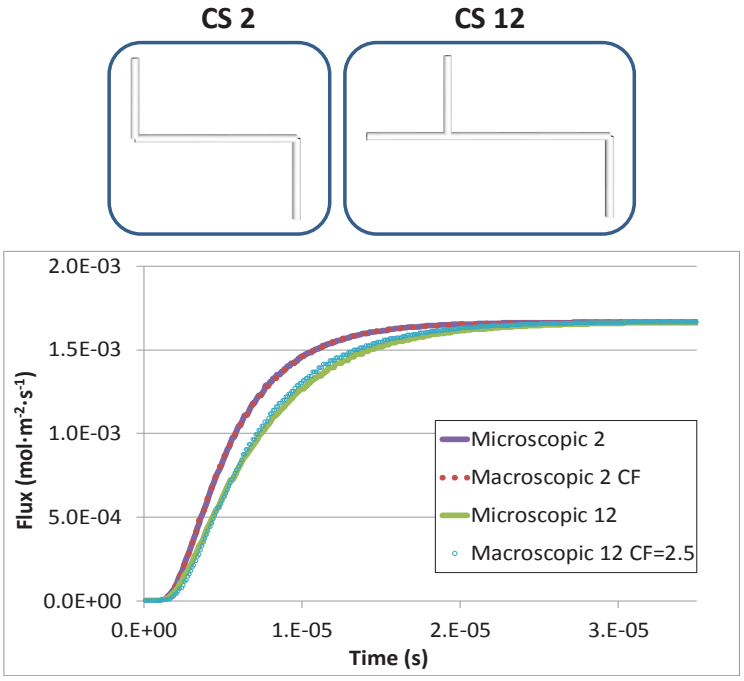


Fig. Ap. IX-9. Comparison of the discrete (microscopic) and continuum (macroscopic) models in transient regime for CS 2 and 12.

The steady states are identical as they have equal percolating volumes. And concerning the dynamic responses, case study 12 is delayed compared to case study 2, due to the augmentation of the capacitive volume. Comparing the responses of the discrete model and the corrected continuum model from case study 12 also indicates a difference between the two plots.

Fig. Ap. IX-10 contains the information regarding case study 3 and 13, where the tortuosity factor of case study 13 remains of course equal to that from case study 3, $\tau_{13} = \tau_3 = 1.67$.

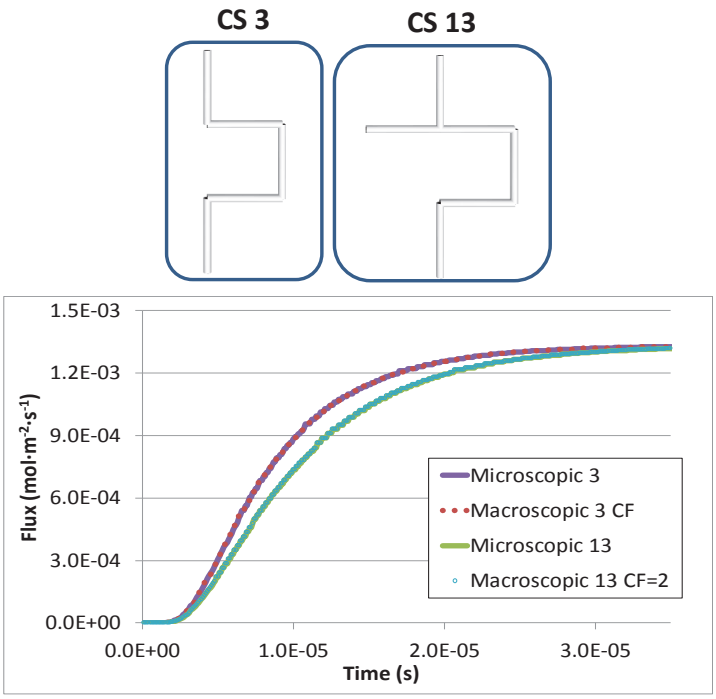


Fig. Ap. IX-10. Comparison of the discrete (microscopic) and continuum (macroscopic) models in transient regime for CS 3 and 13.

A slight difference between the transient responses for the discrete and the pseudo-homogeneous simulations of case study 13 is observed and taking the correction factor of 6/3=2.0. Case study 3, on the other hand is well represented by its correction factor of 5/3=1.67. The dead volume must be correctly taken into account on the continuum representation, as mentioned before. Moreover, the dynamic response of case study 13 is delayed compared to case study 3, due to the presence of the dead volume that delays the mass transfer behaviour by diffusion.

The information related to case study 4 and 14 is represented on Fig. Ap. IX-11. The tortuosity factor of case study 14 is equal to that from case study 4, $\tau_{14} = \tau_4 = 2.33$.

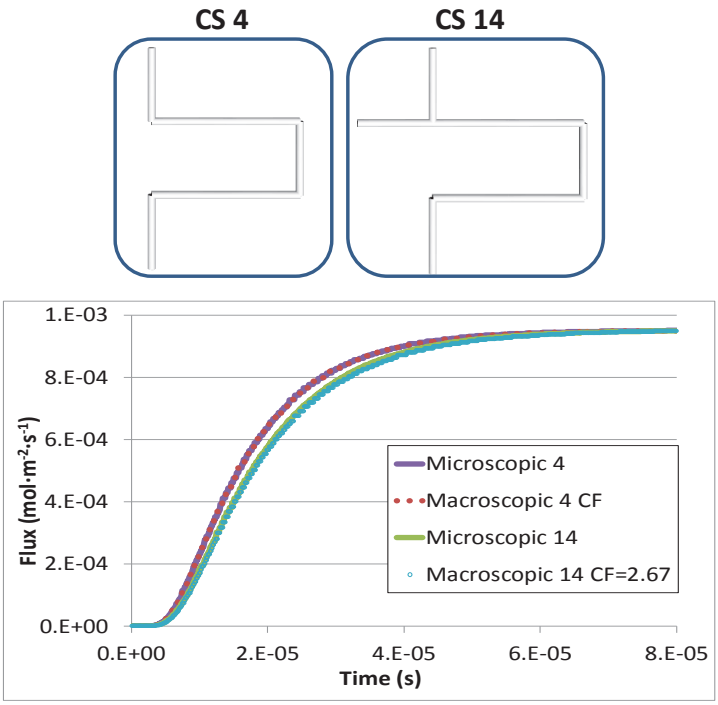


Fig. Ap. IX-11. Comparison of the discrete (microscopic) and continuum (macroscopic) models in transient regime for CS 4 and 14.

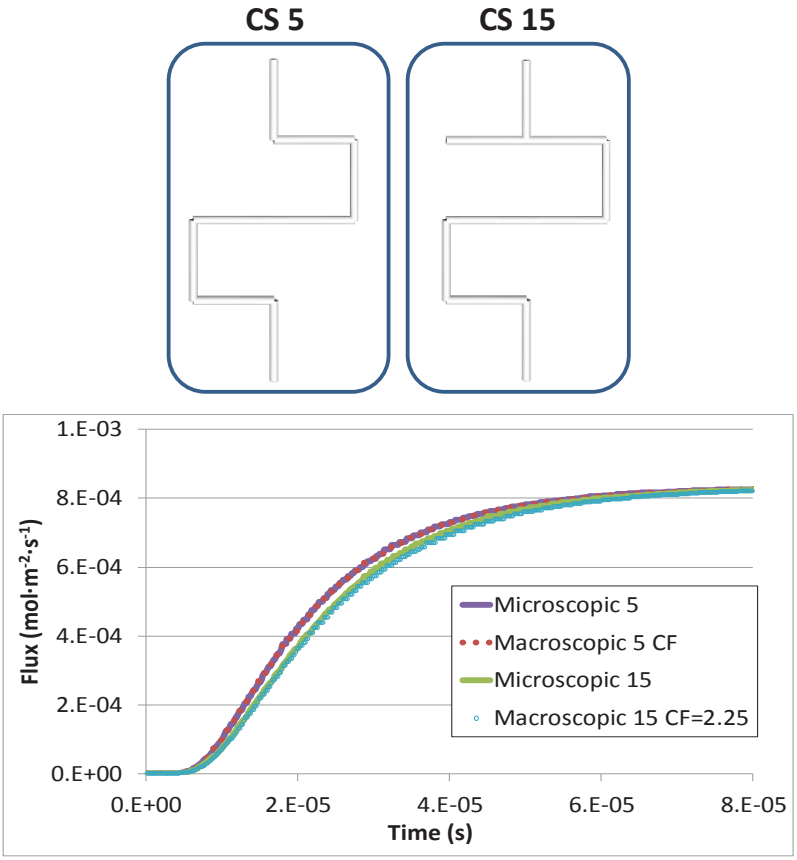


Fig. Ap. IX-12. Comparison of the discrete (microscopic) and continuum (macroscopic) models in transient regime for CS 5 and 15.

The dynamic response of the discrete simulation of case study 4 is faster than case study 14 (see Fig. Ap. IX-11), the dead volume present in the pore network from case study 14 is responsible for this delay since it increases the capacitive volume. The correction factor used in the continuum simulation of case study 14 is not in accordance with the response of the discrete simulation.

In conclusion, the corrected continuum model seems to be incapable of correctly describing the dynamic response of the discrete model.

Taking Fig. Ap. IX-12 and case study 15, a slight deviation on the response of the continuum approach is observed compared to the response of the discrete model. The dead volume should once again be correctly accounted for.

Given the predicted outlet flux present on Fig. Ap. IX-13, one observes an equal steady state for both case studies 6 and 16 and therefore the diffusional tortuosity of case study 16 is equal to that from case study 6, $\tau_{16} = \tau_6 = 2.5$.

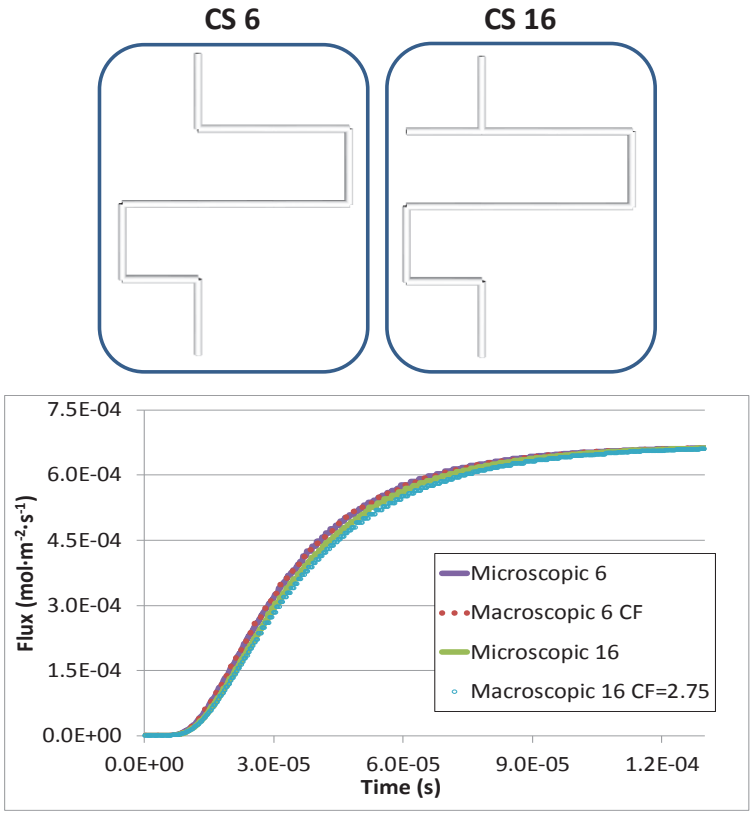


Fig. Ap. IX-13. Comparison of the discrete (microscopic) and continuum (macroscopic) models in transient regime for CS 6 and 16.

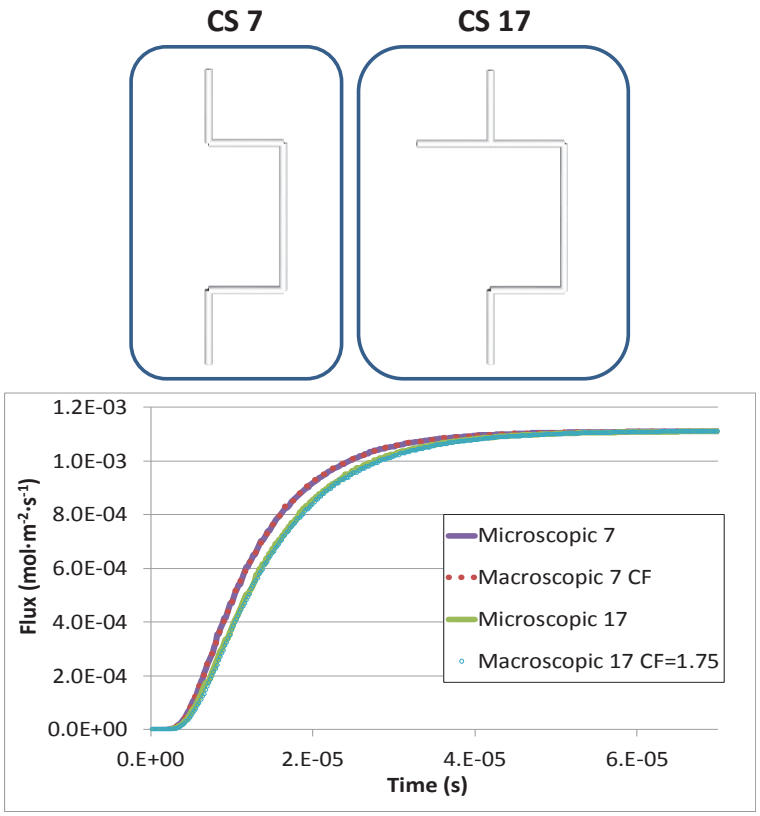


Fig. Ap. IX-14. Comparison of the discrete (microscopic) and continuum (macroscopic) models in transient regime for CS 7 and 17.

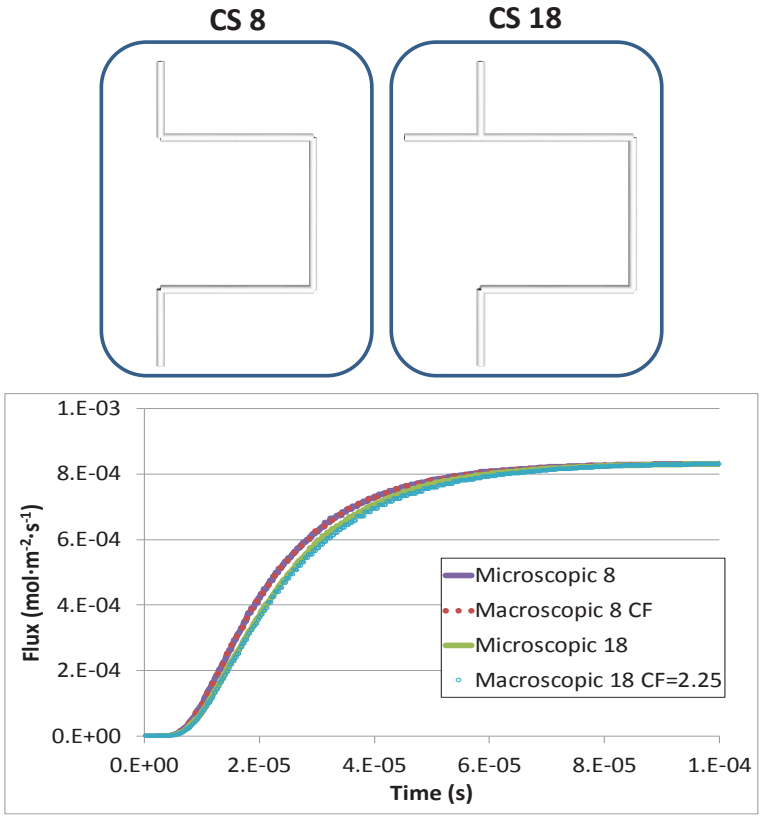


Fig. Ap. IX-15. Comparison of the discrete (microscopic) and continuum (macroscopic) models in transient regime for CS 8 and 18.

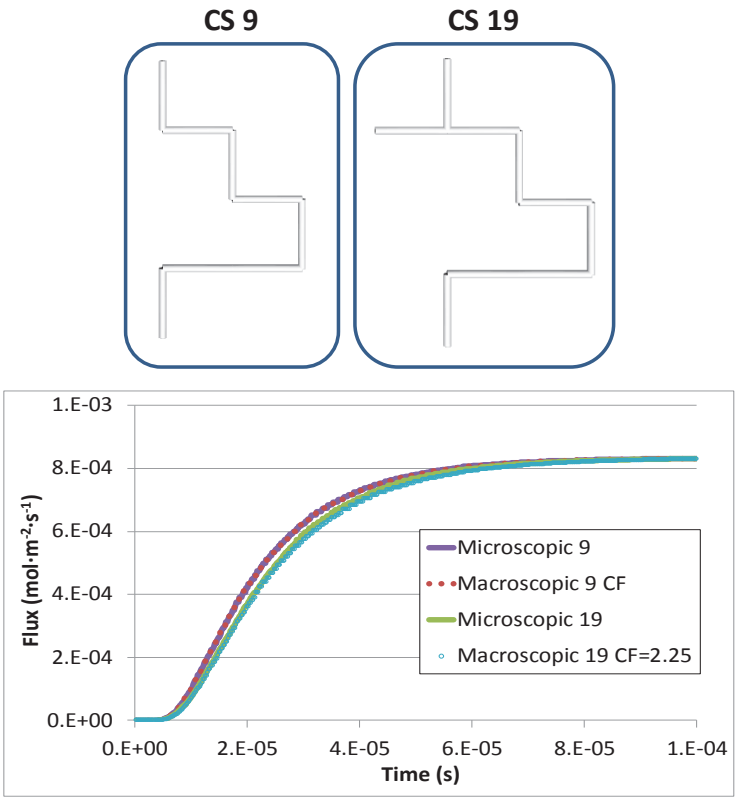


Fig. Ap. IX-16. Comparison of the discrete (microscopic) and continuum (macroscopic) models in transient regime for case study 9 and 19.

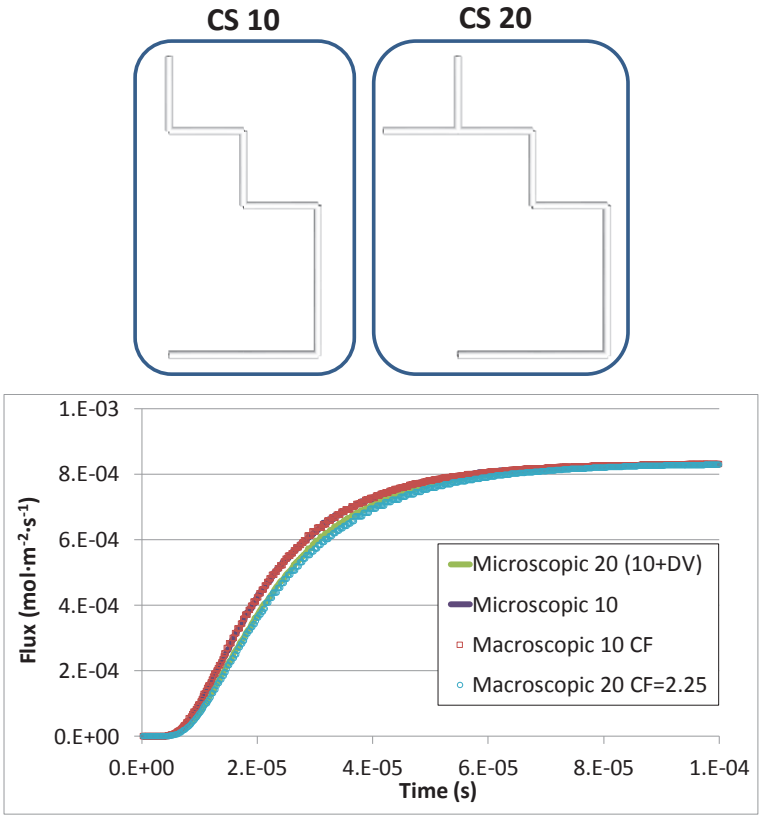


Fig. Ap. IX-17. Comparison of the discrete (microscopic) and continuum (macroscopic) models in transient regime for case study 10 and 20.

The discrepancy between the dynamic responses of case study 6 and 16 continues to reduce compared to case study 5 and 15 as well as, case study 3 and 13. The effect of a single dead volume gets less significant with the increase in the overall capacitive volume.

Similar behaviour are observed on the remaining case studies shown in Fig. Ap. IX-14 to Fig. Ap. IX-17.

Fig. Ap. IX-18 regroups the diffusional tortuosities as a function of the geometric tortuosity for the simple case studies from 1 to 10 and those from case study 11 to 20, where a dead volume was added to each first 10 case studies. As expected all data points coincide with the bisector.

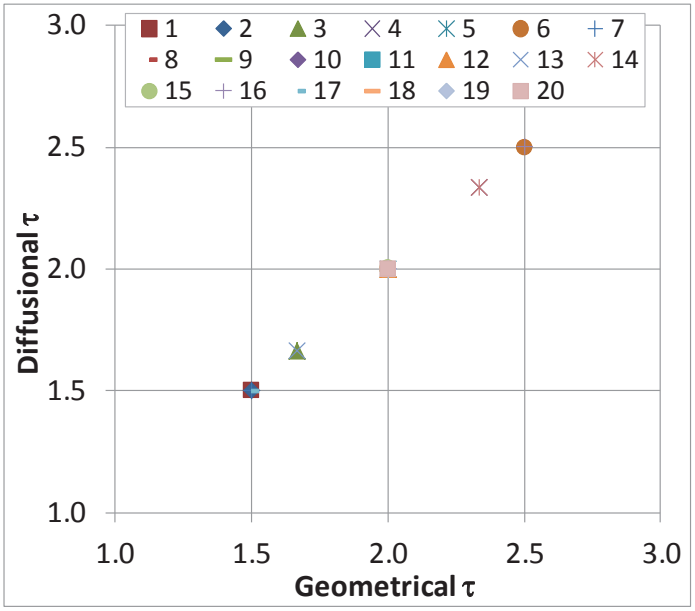


Fig. Ap. IX-18. Diffusional tortuosity as a function of the geometric tortuosity from case studies 1 to 20.

APPENDIX X

X.1 INFLUENCE OF THE PORE EXISTENCE PROBABLITY: P_1 AND P_2

Extended data on the catalyst porosity (Fig. Ap. X-1) and network connectivity (Fig. Ap. X-2) for the first configuration used, where L_2 is obligatorily greater than D_2.

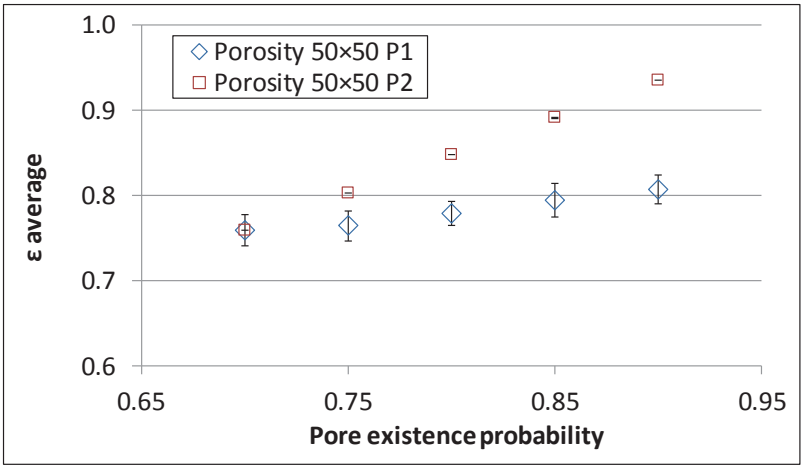


Fig. Ap. X-1. Influence of the pore existence probabilities P_1 (dotted blue plot) and P_2 (dotted red plot) on the catalyst porosity for a two-level network using the 1st configuration.

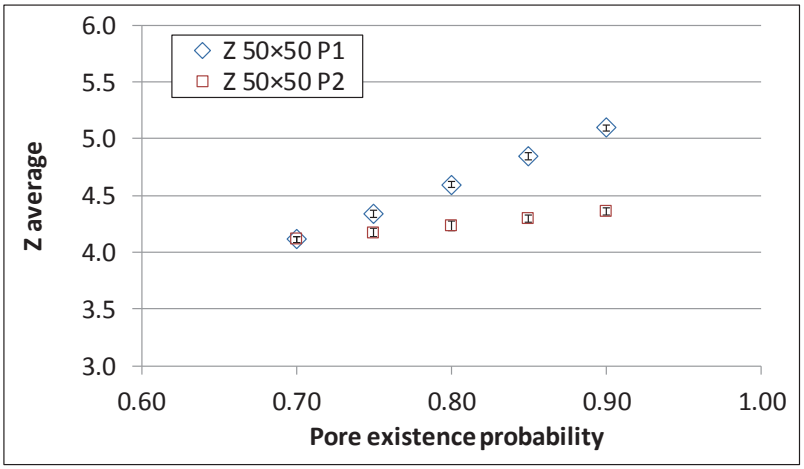


Fig. Ap. X-2. Influence of the pore existence probabilities P_1 (dotted blue plot) and P_2 (dotted red plot) on the network connectivity for a two-level network using the 1st configuration.

Extended data on the textural properties for the 2nd configuration can be found in Fig. Ap. X-3 to Fig. Ap. X-6.

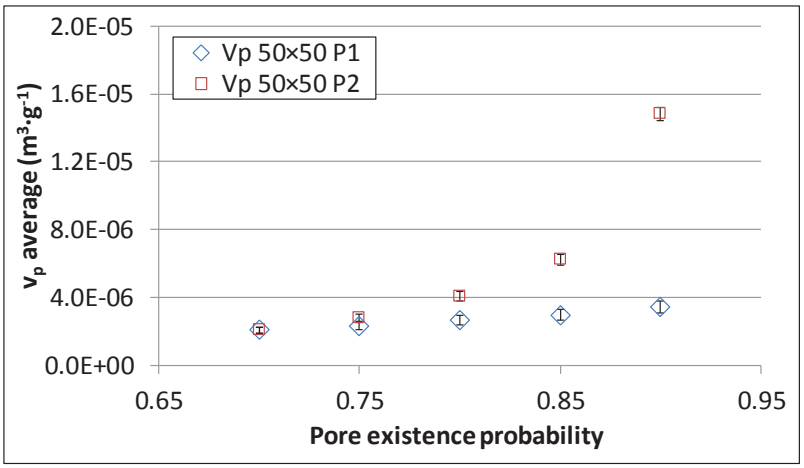


Fig. Ap. X-3. Influence of the pore existence probabilities P_1 (dotted blue plot) and P_2 (dotted red plot) on the specific pore volume for a two-level network using the 2nd configuration.

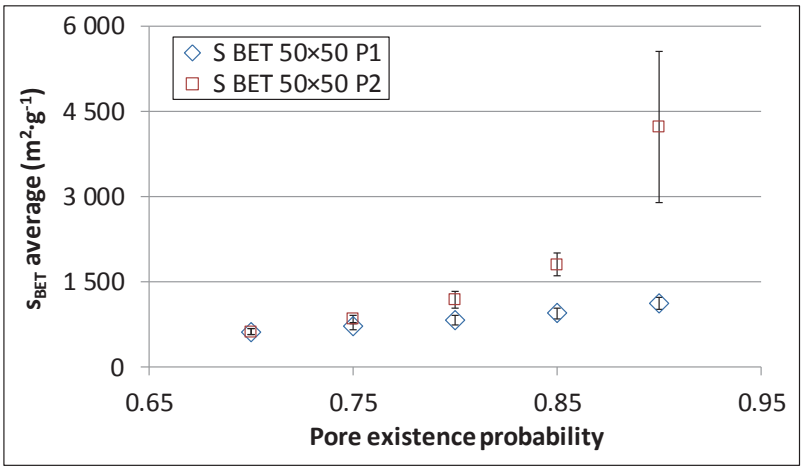


Fig. Ap. X-4. Influence of the pore existence probabilities P_1 (dotted blue plot) and P_2 (dotted red plot) on the specific surface area for a two-level network using the 2nd configuration.

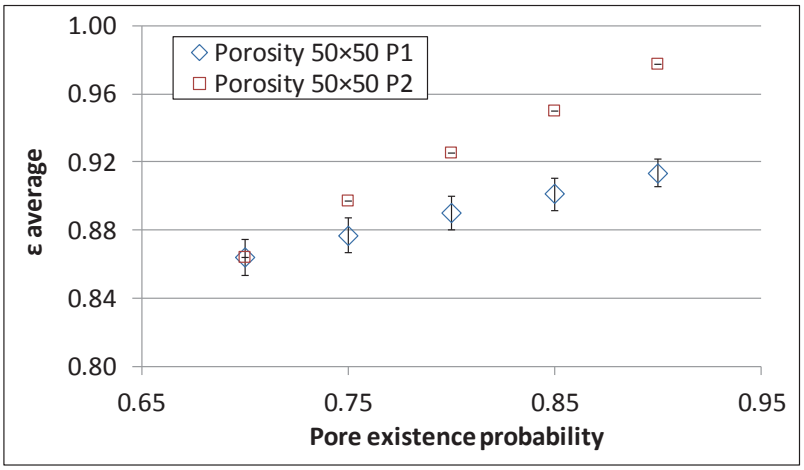


Fig. Ap. X-5. Influence of the pore existence probabilities P_1 (dotted blue plot) and P_2 (dotted red plot) on the catalyst porosity for a two-level network using the 2nd configuration.

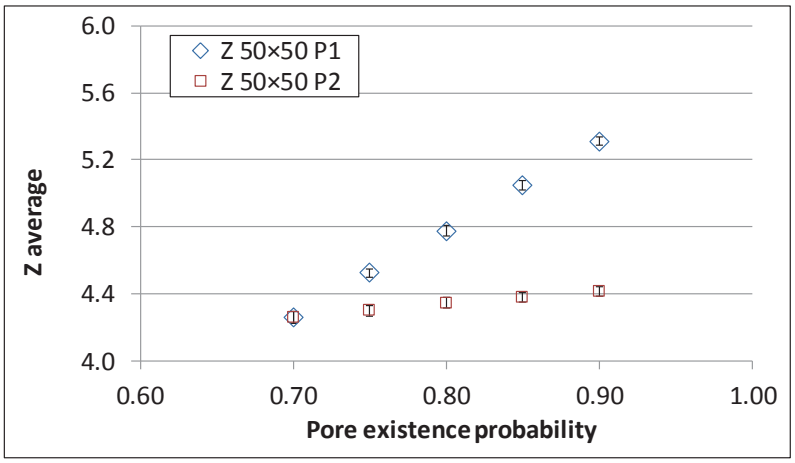


Fig. Ap. X-6. Influence of the pore existence probabilities P_1 (dotted blue plot) and P_2 (dotted red plot) on the network connectivity for a two-level network using the 2nd configuration.

X.2 INFLUENCE OF THE PORE DIAMETER: D_1 AND D_2

Extended data on the catalyst porosity (Fig. Ap. X-7) and network connectivity (Fig. Ap. X-8) for the first configuration used, where L_2 is obligatorily greater than D_2.

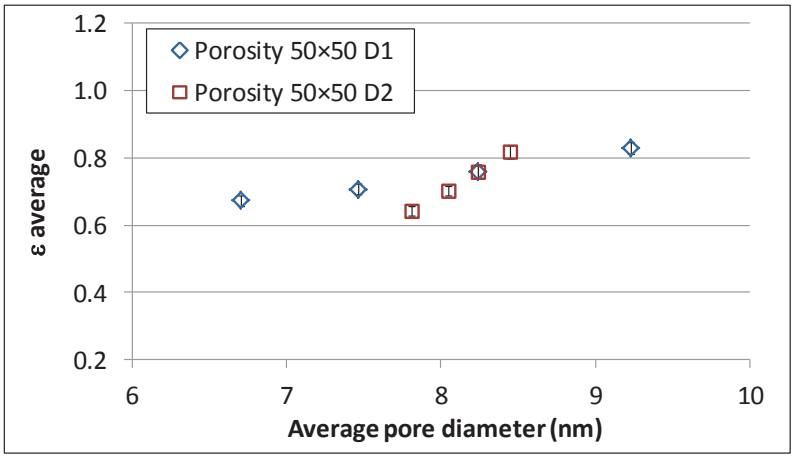


Fig. Ap. X-7. Influence of the pore diameters D_1 (dotted blue plot) and D_2 (dotted red plot) on the catalyst porosity for a two-level network using the 1st configuration.

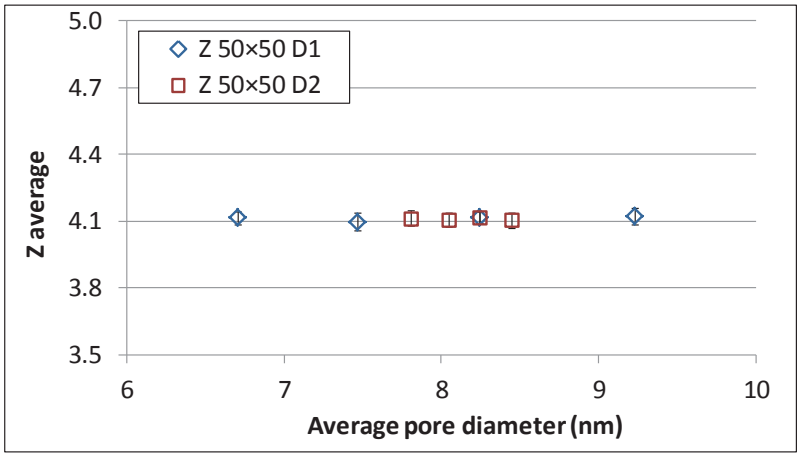


Fig. Ap. X-8. Influence of the pore diameters D_1 (dotted blue plot) and D_2 (dotted red plot) on the network connectivity for a two-level network using the 1st configuration.

Regarding the second configuration the following figures (from Fig. Ap. X-9 to Fig. Ap. X-13) contain the textural properties as a function of the pore diameters.

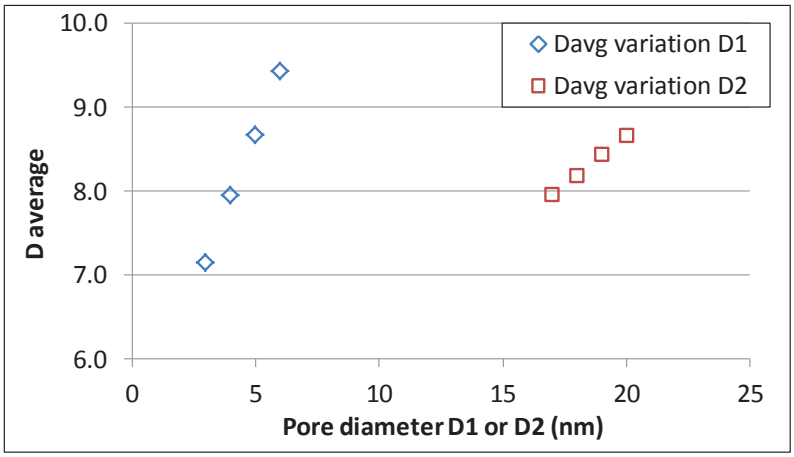


Fig. Ap. X-9. Influence of the pore diameters D_1 (dotted blue plot) and D_2 (dotted red plot) on the average pore diameter for a two-level network using the 2nd configuration.

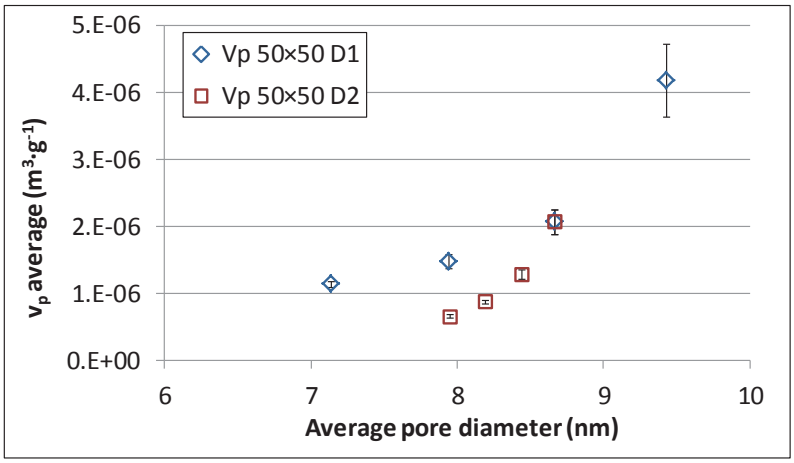


Fig. Ap. X-10. Influence of the pore diameters D_1 (dotted blue plot) and D_2 (dotted red plot) on the specific pore volume for a two-level network using the 2nd configuration.

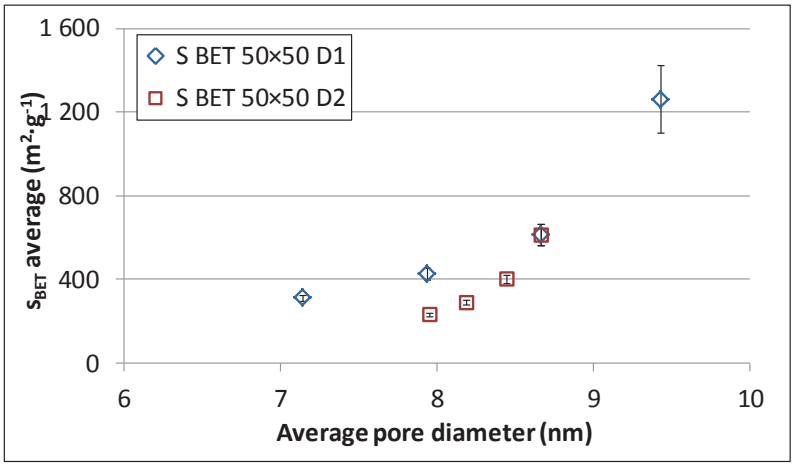


Fig. Ap. X-11. Influence of the pore diameters D_1 (dotted blue plot) and D_2 (dotted red plot) on the specific surface area for a two-level network using the 2nd configuration.

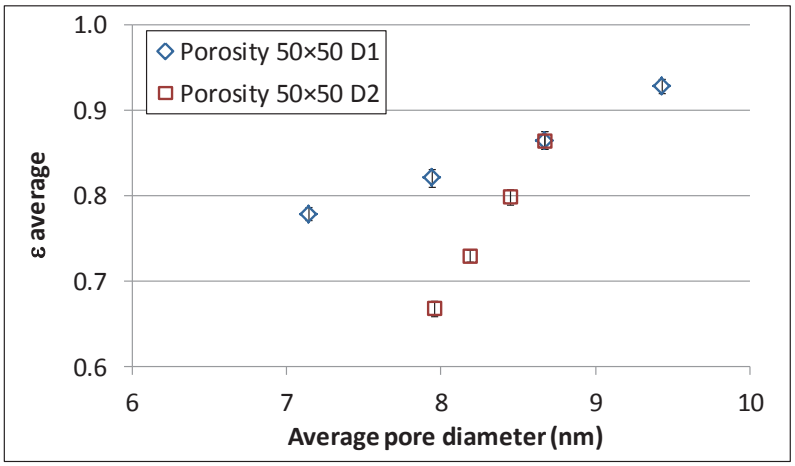


Fig. Ap. X-12. Influence of the pore diameters D_1 (dotted blue plot) and D_2 (dotted red plot) on the catalyst porosity for two-level network using the 2nd configuration.

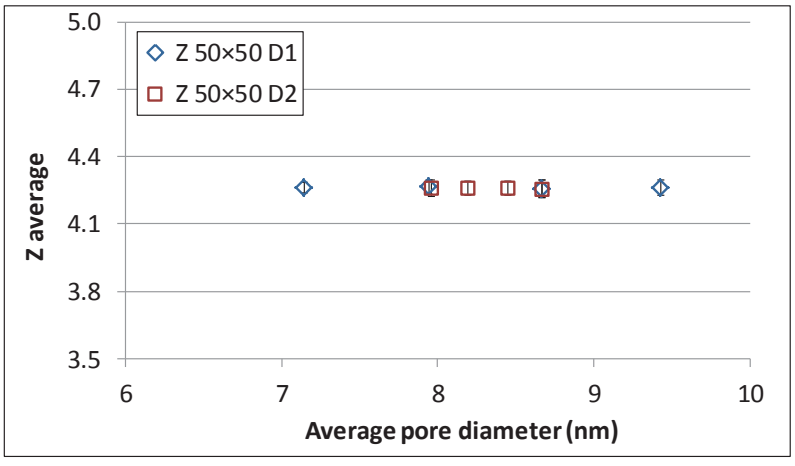


Fig. Ap. X-13. Influence of the pore diameters D_1 (dotted blue plot) and D_2 (dotted red plot) on the network connectivity for a two-level network using the 2nd configuration.

X.3 INFLUENCE OF THE PORE DIAMETER: L_1 AND L_2

Extended data on the catalyst porosity (Fig. Ap. X-14) and network connectivity (Fig. Ap. X-15) for the first configuration used, where L_2 is obligatorily greater than D_2.

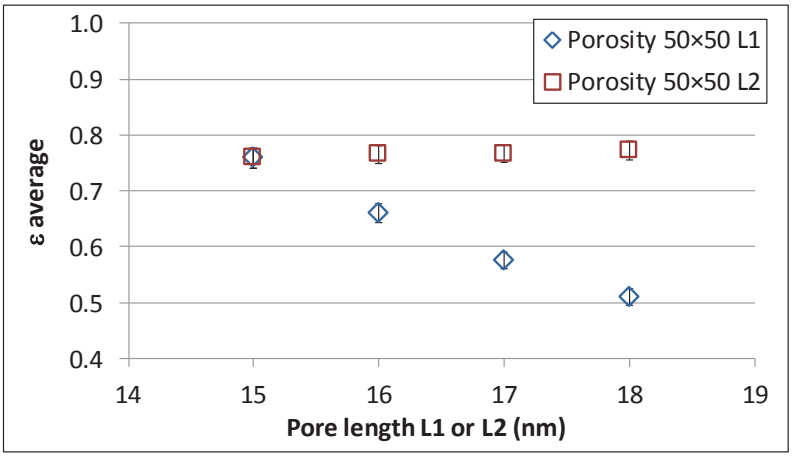


Fig. Ap. X-14. Influence of the pore lengths L_1 (dotted blue plot) and L_2 (dotted red plot) on the catalyst porosity for a two-level network using the 1st configuration.

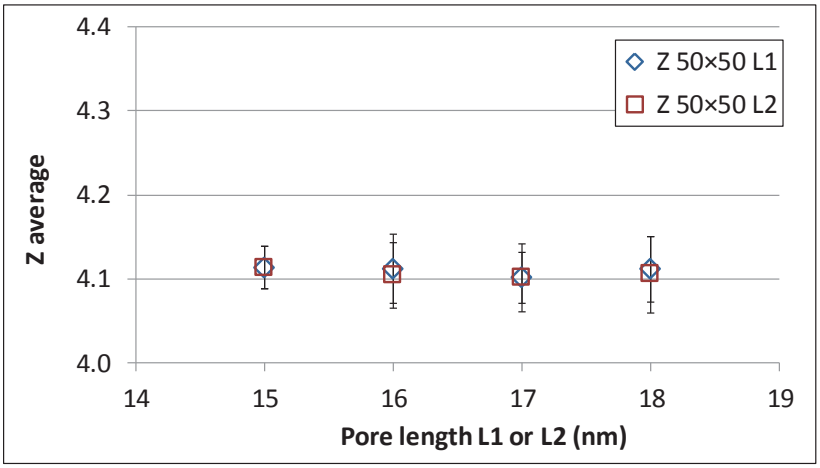


Fig. Ap. X-15. Influence of the pore lengths L_1 (dotted blue plot) and L_2 (dotted red plot) on the network connectivity for a two-level network using the 1st configuration.

Regarding the second configuration the following figures (from Fig. Ap. X-16 to Fig. Ap. X-19) contain the evolution of the textural properties as a function of the pore lengths.

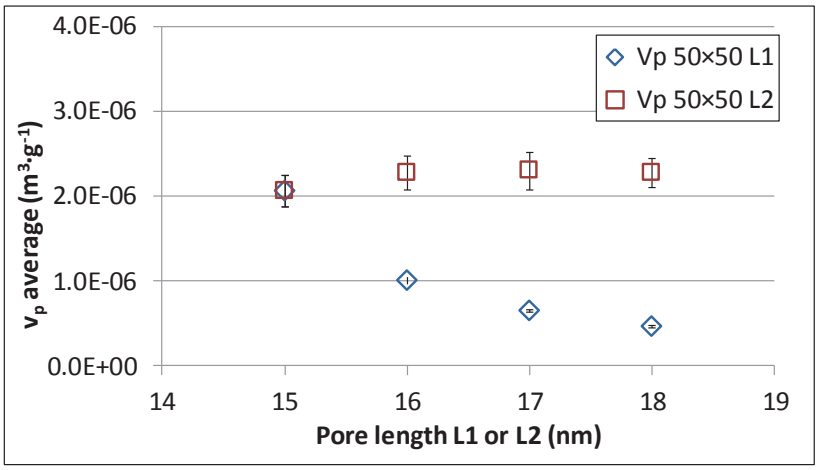


Fig. Ap. X-16. Influence of the pore lengths L_1 (dotted blue plot) and L_2 (dotted red plot) on the specific pore volume for a two-level network using the 2nd configuration.

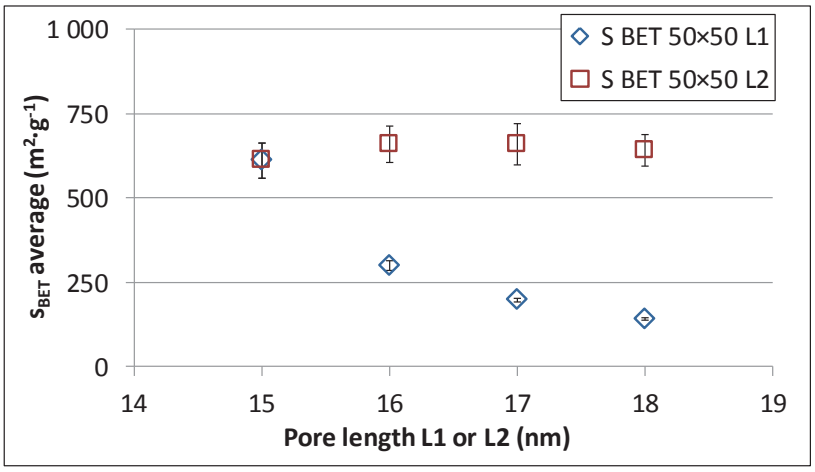


Fig. Ap. X-17. Influence of the pore lengths L_1 (dotted blue plot) and L_2 (dotted red plot) on the specific surface area for a two-level network using the 2nd configuration.

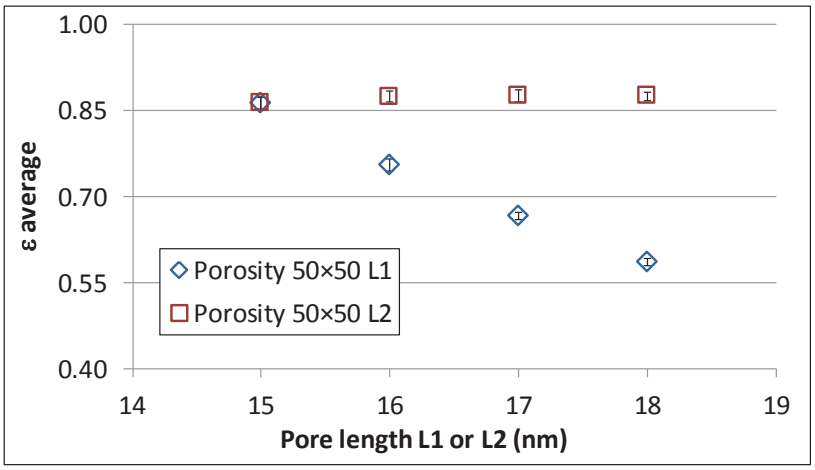


Fig. Ap. X-18. Influence of the pore lengths L_1 (dotted blue plot) and L_2 (dotted red plot) on the catalyst porosity for a two-level network using the 2nd configuration.

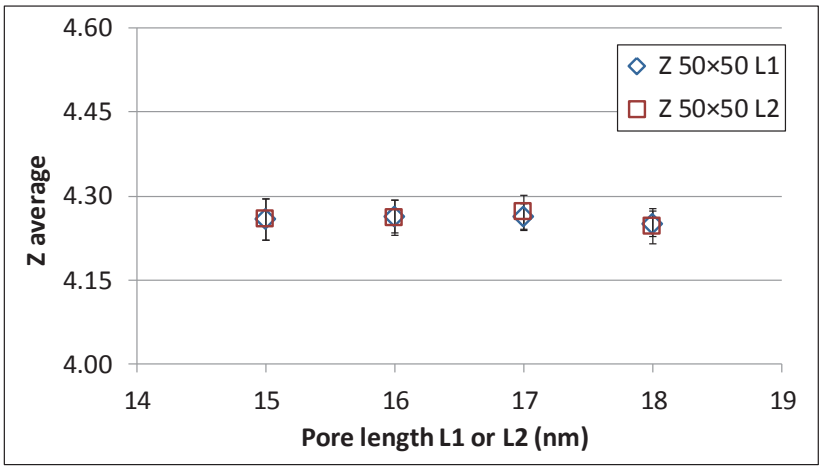


Fig. Ap. X-19. Influence of the pore lengths L_1 (dotted blue plot) and L_2 (dotted red plot) on the connectivity network for a two-level network using the 2nd configuration.